

# **High Peak, Perishable Energy Recovery**

**– Foundation Phase –**



Thesis submitted for the degree of  
**Doctor of Philosophy in Engineering**

By

**Haydeé Guadalupe Martínez-Zavala**

School of Engineering  
College of Physical Sciences and Engineering  
Cardiff University

February 2022

## **Acknowledgements**

This research was partially financed by The Mexican National Council on Science and Technology (CONACYT) and The Secretariat of Energy in Mexico (SENER) [Grant Number 327757/460766]. I would like to express my gratitude to my PhD supervisors, Dr Agustin Valera-Medina, Dr Samuel Bigot and Dr Debajyoti Bhaduri, for their guidance during this investigation and to the staff of the School of Engineering, Research Office, Student Support & Wellbeing Division, International Office, Advanced Research Computing at Cardiff (ARCCA) and Finance AP Office for their support. Special acknowledgement is due to Mr Karl Jones for his professional programming advice in the CFD code and to Mr Anuraag Saxena (CEng and MCIBSE) for his guidance in the construction of the experimental apparatus for the condensation heat transfer experiments. My sincere appreciation and gratitude go to my family and friends in Mexico for their support and for believing in me. Finally, thanks to the friends I made here, especially Karl, you made the UK feel like home.

This work is dedicated to my family, especially to my parents Gerardo and Glafira.

# Summary

Climate change negatively affects the natural environment, human society, and the worldwide economy. The primary reasons for climate change are unsustainable energy consumption and greenhouse gases emissions due to fossil fuels being the major energy resource over the past centuries. Because of the fossil fuels' finite nature and role in the greenhouse effect and global warming, research into renewable and sustainable energy alternatives has significantly grown, becoming a topic of interest to the scientific community in recent decades. However, the contribution of renewable resources has only moderately increased each year due to increasing global energy demand and ongoing consumption as well as investment in new fossil fuels. Therefore, futuristic alternative high energy sources, such as gales, hurricanes, floods and other highly energetic meteorological phenomena, could be added to the pool of resources to support the reduction of fossil fuel consumption.

The High Peak, Perishable Energies – Foundation Phase (HPPE-FP) project aims to create the fundamentals for developing new technologies for HPPE recovery. The results will support further research to enhance thermal and energy production processes, in addition to the development of industrial systems capable of decarbonising the electrical grid. One of the fundamental concepts of the HPPE-FP is the enhancement of condensation heat transfer. For this reason, the present doctoral research explores an alternative passive mechanism for surface topographical modification via fabricating microstructured surfaces in order to enhance heat transfer.

This doctoral investigation is divided into four stages. The first three stages focus on designing, fabricating, and testing hydrophobic and hydrophilic microstructures/textures produced via wire-electro discharge machining and laser micromachining. Stage four, based on the performance of the microstructured surfaces in the first three stages in terms of boundary layer control and thermal properties of the structured surfaces, involves designing, manufacturing, and testing novel biphilic (composed of hydrophobic and hydrophilic characteristics) microstructured surfaces to enhance condensation heat transfer for energy recovery purposes.

As a result, hydrophobic, hydrophilic and biphilic wetting states were obtained by manufacturing different micro-geometries on the surface topography without the need for chemical treatments. An experimental apparatus for the condensation heat transfer evaluation was successfully designed and built. The results indicate that hydrophobic, hydrophilic and biphilic microstructured surfaces achieve up to 17.45% boundary layer thickness reduction and up to 27% drag force reduction. Regarding the thermal evaluation, hydrophobic and hydrophilic microstructured surfaces exhibit up to 30.91% enhancement, while the novel biphilic textured surfaces exhibit a considerable increase in the overall heat transfer by 56.8-62.6%, when compared to untextured surfaces.

# Contents

<b>Acknowledgements .....</b>	<b>i</b>
<b>Summary .....</b>	<b>ii</b>
<b>List of Publications .....</b>	<b>viii</b>
Journal Publications .....	viii
Peer-reviewed Conference Publications .....	viii
Conference Presentations .....	viii
Other Presentations .....	ix
Papers under Preparation .....	ix
<b>List of Figures .....</b>	<b>x</b>
<b>List of Tables .....</b>	<b>xix</b>
<b>Nomenclatures .....</b>	<b>xxi</b>
Acronyms .....	xxi
Symbols .....	xxii
Latin Letters .....	xxii
Greek Letters .....	xxiv
<b>Chapter 1: Introduction .....</b>	<b>1</b>
1.1 Climate Change: Origin and Consequences .....	2
1.2 Renewable Energy .....	7
1.2.1 Direct Solar Energy .....	8
1.2.2 Hydropower .....	9
1.2.3 Bioenergy (Biomass) .....	9
1.2.4 Wind Energy .....	9
1.2.5 Ocean Energy .....	10
1.2.6 Geothermal Energy .....	10
1.3 Alternative Energy Sources: High Peak Perishable Energy Recovery .....	11
1.4 Enhancement of Heat Transfer via Microstructured Surfaces .....	13
1.5 Aims and Objectives .....	14
1.6 Thesis Structure .....	15

<b>Chapter 2: Literature Review .....</b>	<b>16</b>
2.1 Alternative Energy Sources: High Peak Perishable Energy Recovery .....	16
2.2 Condensation Heat Transfer Theory .....	22
2.2.1 Heat and Momentum Transfer Relationship: Boundary Layers .....	23
2.2.2 Nusselt's Theory .....	34
2.2.3 Flow Regimes .....	38
2.3 Types of Condensation .....	40
2.3.1 Filmwise Condensation .....	41
2.3.2 Dropwise Condensation .....	44
2.3.3 Jumping-droplet Condensation .....	45
2.4 Droplet Life Cycle .....	49
2.4.1 Surface Wettability .....	52
2.5 Heat Transfer Enhancement Techniques .....	56
2.5.1 Passive Techniques for Condensation Enhancement .....	57
2.6 Research on Condensation Heat Transfer Enhancement .....	59
2.6.1 Coated Surfaces .....	59
2.6.2 Hydrophobic and Superhydrophobic Surfaces .....	59
2.6.3 Superhydrophobic Nanostructured Surfaces .....	60
2.6.4 Hierarchical Superhydrophobic Surfaces .....	61
2.6.5 Hydrophilic Surfaces .....	61
2.6.6 Biphilic Surfaces .....	61
2.6.7 Wetting Gradient .....	64
2.6.8 Hybrid Wetting Gradient .....	65
2.7 Microstructured Surfaces: An Innovative Passive Technique .....	67
2.7.1 Considerations for Design and Manufacturing .....	67
2.7.1.1 Micro-geometry Design and Dimensions .....	67
2.7.1.2 Wetting State .....	68
2.7.2 Biphilic Microstructured Surfaces .....	69
2.7.3 Microstructured Surfaces without Chemical Treatment .....	71
2.7.4 Summary and Identified Knowledge Gaps.....	72
 <b>Chapter 3: Methodology .....</b>	 <b>73</b>
3.1 Research Structure .....	73
3.1.1 Research Stages .....	73
3.1.2 Evaluation Phases .....	76
3.2 Phase 1: Design .....	76
3.2.1 Previous Work .....	77
3.2.2 Computational Fluids Dynamics (CFD) Analysis .....	79

3.3 Phase 1: Manufacture of the Microstructured Surfaces .....	86
3.3.1 Insert Manufacturing Techniques .....	86
3.3.1.1 Casting .....	86
3.3.1.2 Laser Powder Bed Fusion .....	87
3.3.2 Texturing Techniques .....	89
3.3.2.1 Micro-Wire Electrical Discharge Machining ( $\mu$ -WEDM) .....	89
3.3.2.2 Laser Texturing .....	90
3.3.3 Cleaning Procedure .....	91
3.4 Phase 1: Characterisation of the Microstructured Surfaces .....	92
3.4.1 Area Scanning (3D Optical Profiler) .....	92
3.4.1.1 Software Set-up .....	92
3.4.1.2 Sample Collection .....	93
3.4.2 Characterisation Data and CFD Link Program .....	95
3.4.3 High-Resolution Surface Topography Analysis .....	98
3.4.4 Wettability Characterisation .....	99
3.5 Phase 2: Fluids Dynamics Evaluation (Momentum Transfer) .....	102
3.5.1 Experimental Apparatus .....	102
3.5.2 Experimental Design .....	104
3.5.3 Swirl Flow Rig Set-up .....	105
3.6 Phase 3: Heat Transfer Evaluation .....	107
3.6.1 Experimental Apparatus .....	107
3.6.2 Experimental Design .....	108
3.7 Experimental Uncertainty Analysis .....	110
3.8 Assessment Criteria .....	112

<b>Chapter 4: Performance Evaluation Results of Hydrophobic and Hydrophilic Microstructured Surfaces (Stages 1, 2 and 3) .....</b>	<b>113</b>
4.1 Stage 1: Microstructured Surfaces Produced via $\mu$ -WEDM on Cast Specimens .....	114
4.1.1 Phase 1: Design, Manufacture and Characterisation .....	114
4.1.1.1 Design .....	114
4.1.1.1.1 Previous Work .....	114
4.1.1.1.2 Computational Fluids Dynamics (CFD) Results .....	117
4.1.1.2 Manufacture and Characterisation of the Microstructured Surfaces .....	129
4.1.2 Phase 2: Fluids Dynamics Evaluation Results (Momentum Transfer) .....	132
4.1.3 Phase 3: Heat Transfer Evaluation .....	134
4.1.4 Assessment Summary .....	139

4.2 Stage 2: Microstructured Surfaces Produced via Laser Micro-Processing on Cast Specimens .....	140
4.2.1 Phase 1: Design, Manufacture and Characterisation .....	140
4.2.1.1 Design .....	140
4.2.1.1.1 Previous Work .....	140
4.2.1.2 Manufacture and Characterisation of the Microstructured Surfaces .....	141
4.2.2 Phase 2: Fluids Dynamics Evaluation Results (Momentum Transfer) .....	144
4.2.3 Phase 3: Heat Transfer Evaluation .....	146
4.2.4 Assessment Summary .....	149
4.3 Stage 3: Microstructured Surfaces Produced via Laser Micro-Processing on Selective Laser Melted Specimens .....	150
4.3.1 Phase 1: Design, Manufacture and Characterisation .....	150
4.3.1.1 Design .....	150
4.3.1.1.1 Previous Work .....	150
4.3.1.2 Manufacture and Characterisation of the Microstructured Surfaces .....	151
4.3.2 Phase 2: Fluids Dynamics Evaluation Results (Momentum Transfer) .....	154
4.3.3 Phase 3: Heat Transfer Evaluation .....	156
4.3.4 Assessment Summary .....	158
4.4 Swirl Flow Experimental Results .....	159
<b>Chapter 5: Performance Evaluation Results of Novel Biphilic Microstructured Surfaces (Stage 4) .....</b>	<b>161</b>
5.1 Phase 1: Design, Manufacture and Characterisation .....	162
5.1.1 Design .....	162
5.1.1.1 Previous Work .....	162
5.1.2 Manufacture .....	165
5.1.3 Characterisation .....	166
5.1.3.1 Section 1: Hydrophobic Features .....	168
5.1.3.2 Section 2: Hierarchical Structures .....	169
5.1.3.3 Section 3: Hydrophilic Features .....	172
5.1.3.4 Wettability Characterisation .....	175
5.2 Phase 2: Fluids Dynamics Evaluation Results (Momentum Transfer) .....	177
5.3 Phase 3: Heat Transfer Evaluation .....	179
5.4 Assessment Summary .....	184

<b>Chapter 6: Discussion .....</b>	<b>185</b>
6.1 Design Challenges and Approach .....	185
6.2 Manufacture and Characterisation of the Textured Workpieces .....	186
6.3 Numerical and Experimental Adaptation in Fluids Dynamics .....	188
6.4 Wettability Effect in Condensation Heat Transfer Performance .....	190
<b>Chapter 7: Conclusions .....</b>	<b>194</b>
7.1 Findings .....	195
7.2 Recommendations for Future Work .....	197
<b>References .....</b>	<b>200</b>
<b>Appendix A .....</b>	<b>212</b>
<b>Appendix B .....</b>	<b>215</b>
<b>Appendix C .....</b>	<b>222</b>
<b>Appendix D .....</b>	<b>224</b>



# List of Publications

## Journal Publications

- **Haydee Martinez-Zavala**, Debajyoti Bhaduri, Petko Petkov, Agustin Valera-Medina, and Samuel Bigot. 2020. “Effects of Laser Microtextured Surfaces in Condensation Heat Transfer.” *Procedia CIRP* 95:927–32. <https://doi.org/10.1016/j.procir.2020.01.184>.

## Peer-reviewed Conference Publications

- **Haydee Martinez-Zavala**, Debajyoti Bhaduri, Agustin Valera-Medina, and Samuel Bigot. 2019. “Experimental Study on Heat Transfer Enhancement during Condensation Using Microstructured Surfaces.” in *International Conference on Applied Energy 2019*. Västerås, Sweden.

## Conference Presentations

- **Haydee Martinez-Zavala**, Agustin Valera-Medina, Debajyoti Bhaduri, and Samuel Bigot. 2019. “Evaluation of Surface Topography Following Different Texturing Techniques on Microstructured Surfaces.” in *Cardiff School of Engineering PGR Research Conference*. Gregynog, Wales, UK.
- **Haydee Martinez-Zavala**, Agustin Valera-Medina, Samuel Bigot, Robert Winter, and Mohammed Al-fahham. 2018. “Experimental Study on Drag Reduction Using Different Microstructured Surfaces at Different Angles.” in *The European Conference on Fuel and Energy Research and its Applications*. Cardiff, Wales, UK.
- **Haydee Martinez-Zavala**, Agustin Valera-Medina, Samuel Bigot, Robert Winter, and Mohammed Al-fahham. 2018. “Experimental Study on Drag Reduction Using Different Microstructured Surfaces in Energy Engineering.” in *Cardiff School of Engineering PGR Research Conference*. Gregynog, Wales, UK.

## Other Presentations

- **Haydee Martinez-Zavala.** 2020. “An Unstructured Surface.” in Doctoral Academy: Images of Research. Cardiff, Wales, UK.
- **Haydee Martinez-Zavala.** 2019. “Micro-Art in Engineering.” in Doctoral Academy: Images of Research. Cardiff, Wales, UK.
- **Haydee Martinez-Zavala.** 2018. “The Spectacle of the Microstructure Borealis.” in Doctoral Academy: Images of Research. Cardiff, Wales, UK.

## Papers under Preparation

- **Haydee Martinez-Zavala,** Debajyoti Bhaduri, Mohammed Al-fahham, Agustin Valera-Medina, and Samuel Bigot. “A proposed method for enhancing the thermal characteristics of bio-inspired microstructured surfaces for energy sector applications”.
- **Haydee Martinez-Zavala,** Debajyoti Bhaduri, Petko Petkov, Agustin Valera-Medina, and Samuel Bigot. “Performance evaluation of novel biphilic microstructured surfaces for energy sector applications”.

## List of Figures

<b>Figure 1.1.</b> Global GHG emissions by gas and global GHG emissions by economic sector [6].	3
<b>Figure 1.2.</b> Carbon dioxide level in parts per million in the last 400,000 years [7].	3
<b>Figure 1.3.</b> History of global temperature change [9].	4
<b>Figure 1.4.</b> Climate change impacts in the UK [12].	5
<b>Figure 1.5.</b> Countries with selected climate change policies [3].	6
<b>Figure 1.6.</b> Estimated renewable energy share of total final energy consumption in 2009 and 2019 [3].	7
<b>Figure 1.7.</b> Renewable energy in total final energy consumption in 2018 by final energy use [3].	8
<b>Figure 2.1.</b> Tropical cyclone structure in the southern hemisphere [21].	17
<b>Figure 2.2.</b> Historical Storms Tracks (1851-2019). Adaption from the National Oceanic and Atmospheric Administration (NOAA) [20] and Saffir-Simpson hurricane scale [23].	17
<b>Figure 2.3.</b> Increase in Hurricanes in the Atlantic [27].	19
<b>Figure 2.4.</b> Development of velocity, thermal, and concentration boundary layers over a surface and differential control volume ( $dx.dy.1$ ) analysis. Adaption from [37].	23
<b>Figure 2.5.</b> Transition from a laminar to a turbulent boundary layer and flow in viscous sublayer near rough and smooth surfaces. Adaption from [41].	26
<b>Figure 2.6.</b> Filmwise condensation on a vertical plate. Adaption from [37,38,40].	35
<b>Figure 2.7.</b> Flow regimes for film condensation on a vertical plate. Adaption from [37].	39
<b>Figure 2.8.</b> Dropwise condensation with a large droplet contact angle and filmwise condensation with a small droplet contact angle. Adaption from [39].	40
<b>Figure 2.9.</b> Dropwise condensation and filmwise condensation on a copper plate. Photographs by Professor J. W. Westwater, University of Illinois, Urbana. Adaption from [40].	41
<b>Figure 2.10.</b> Condensate flow in a horizontal tube. Adaption from [37,46].	42
<b>Figure 2.11.</b> Comparison of experimental results and theoretical results of filmwise condensation heat transfer coefficients [47].	43
<b>Figure 2.12.</b> Experimental results from the study “Jumping-droplet-enhanced condensation on scalable superhydrophobic nanostructured surfaces” [49].	46

<b>Figure 2.13.</b> Heat flux during dropwise condensation and jumping droplet condensation on a tube sample for saturated vapour pressures $P_v$ of (a) 2.2 kPa, (b) 2.7 kPa. Adaptation from [36].....	46
<b>Figure 2.14.</b> Condensation modes and droplet behaviours on the three test surfaces [54]. .....	47
<b>Figure 2.15.</b> Condensation heat transfer performance. Heat flux and heat transfer coefficient as a function of surface subcooling [54]. .....	48
<b>Figure 2.16.</b> Schematic the droplet life cycle stages (a) nucleation (b) growth by direct steam condensation (c) growth by coalescences (d) droplet departure [58].....	49
<b>Figure 2.17.</b> Drop-size distributions from experiments after 3000 seconds and simulations (left). Average drop sizes (right). Adaptation from [59].....	51
<b>Figure 2.18.</b> Leach's experiments on small drops growth (R, T, S) in terms of the vicinity with larger drops. Time $t = 0$ corresponds to the coalescence event responsible for the nucleation of the three small drops. Adaptation from [59].....	51
<b>Figure 2.19.</b> Schematic of Young's equation. Adaptation from [63].....	52
<b>Figure 2.20.</b> (a) High contact angle hysteresis ( $\theta_{adv} - \theta_{rec}$ ), and (b) low contact angle hysteresis. Adaptation from [63]. .....	54
<b>Figure 2.21.</b> Different wetting states. Adaptation from [46,61,63].....	55
<b>Figure 2.22.</b> Orientation of alternating hydrophilic and hydrophobic strips (left). SEM image of a micropatterned fluoroalkylsilane monolayer surface with hydrophilic/hydrophobic area (right). Adaptation from [77,78]. .....	62
<b>Figure 2.23.</b> Comparison of the condensation behaviour on a hybrid surface consisting of hydrophobic posts with hydrophilic tops (left) and a superhydrophobic surface consisting of hydrophobic posts (right). Adaptation from [80].....	62
<b>Figure 2.24.</b> Environmental scanning electron microscope (ESEM) images of condensation of water vapour on a superhydrophobic surface (left) and on a surface with alternating hydrophobic and hydrophilic segments (right). Adaptation from [80].....	63
<b>Figure 2.25.</b> Superhydrophobic Hierarchical Porous Alumina Surfaces' fabrication process integrates micro-contact printing and chemical bath deposition [72]. .....	63
<b>Figure 2.26.</b> Wetting microstructured gradient surface for droplet motion. Adaptation from [84].	64

<b>Figure 2.27.</b> Shastry’s diagram of a droplet slice of width $dy$ shows moving a length $dx$ down a contact angle gradient: (left) top view and (right) side view (the previous location of the droplet is shown in light grey). Adaptation from [86].	65
<b>Figure 2.28.</b> Sliding behaviour of a 10 mg water droplet on the roughness gradient surface reported by Sun et al. [85].	65
<b>Figure 2.29.</b> Comparison of condensation heat flux on straight patterns vs a wettability gradient. Adaptation from [48].	66
<b>Figure 2.30.</b> Preferable parameters for heat transfer based on the wetting state [99].	68
<b>Figure 2.31.</b> Schematic image of a hybrid or biphilic condensing surface with wettability gradient. Adaptation from [48].	69
<b>Figure 2.32.</b> Condensation on a biphilic surface with wettability gradient. Adaptation from [48].	70
<b>Figure 2.33.</b> Lotus-leaf microstructured surface [101].	71
<b>Figure 3.2.</b> Research stages summary and ID procedure.	75
<b>Figure 3.1.</b> Evaluation phases summary.	76
<b>Figure 3.3.</b> (a) SEM images of lotus leaf, consisting of microstructures formed by papillose epidermal cells covered with three-dimensional epicuticular wax tubules on the surface (nanostructures). (b) Image of a water droplet sitting on a lotus leaf [109].	77
<b>Figure 3.4.</b> Environmental scanning electron microscope (ESEM) images of the bonnethead shark ( <i>Sphyrna tiburo</i> ) skin surface at different body locations. Green scale bars, 200 $\mu\text{m}$ ; white scale bars, 100 $\mu\text{m}$ [112].	78
<b>Figure 3.5.</b> Computer-aided drawing (CAD) for the microstructure geometries (a) Lotus, (b) Scallop, (c) Sharkskin and (d) Diamond [113].	79
<b>Figure 3.6.</b> Computational meshed domain divided into 36 sub-domains and microstructured surface location.	80
<b>Figure 3.7.</b> Local Mesh Refinement (LMR) of the computational domain and grid resolution.	81
<b>Figure 3.8.</b> Ghost cell method (a) pressure locations, velocities (b) tangential (c) normal to the interface. Adaptation from [119].	82
<b>Figure 3.9.</b> Riblet parameters for the Hydro3D validation. Where $s$ , $h$ , and $t$ , denote riblet space, riblet height, riblet thickness.	83

<b>Figure 3.10.</b> Validation of the code through drag reduction as a function of $s^+$ . (a) Approach 1: Varying velocity with $h/s=0.5$ . (b) Approach 2: Varying space between riblets with constant height $h$ . Adaptation from [19,113,117]. .....	84
<b>Figure 3.11.</b> Shear stress ( $N/m^2$ ) near the wall for (a) unstructured surface (b) microstructured surface (blade geometry of height = 200 $\mu m$ and width = 280 $\mu m$ ). Adaptation from [19,113,117]......	85
<b>Figure 3.12.</b> Grade 316L stainless steel insert manufactured via casting (Unstructured surface). ..	86
Figure 3.13. Conventional turning and facing operations © CustomPartNet. Adaptation from [126]. .....	87
<b>Figure 3.14.</b> Perspective and top view of the stainless steel inserts.....	87
<b>Figure 3.15.</b> (a) Renishaw AM250 machine (b) Laser parameters (c) AM process parameters (d) Powder material specifications. Adaptation from [127,128]. .....	88
<b>Figure 3.16.</b> Representation of micro-wire electrical discharge machining ( $\mu$ -WEDM). Adaptation from [129]. .....	89
<b>Figure 3.17.</b> Laser micro-processing diagram. Adaptation from [101]. .....	90
<b>Figure 3.18.</b> DMG-Lasertec 40. (a) Exterior view and (b) interior view. ....	91
<b>Figure 3.19.</b> Cleaning apparatus.....	91
<b>Figure 3.20.</b> Sensofar Smart equipment [131]. .....	92
<b>Figure 3.21.</b> SensoSCAN set-up. ....	93
<b>Figure 3.22.</b> Representation of the insert's top view with the scanned areas (left) for stages 1, 2 and 3; (right) for stage 4. ....	93
<b>Figure 3.23.</b> Representation of the measurement points in the scanned area.....	94
<b>Figure 3.24.</b> Groove characteristics. ....	94
<b>Figure 3.25.</b> Representation of the characteristics of the hydrophobic features (holes). ....	95
<b>Figure 3.26.</b> Hydro3D point cloud requirements. ....	95
<b>Figure 3.27.</b> Sensofar point cloud characteristics. ....	96
<b>Figure 3.28.</b> C# application for Sensofar point cloud file processing.....	96
<b>Figure 3.29.</b> Point cloud before and after are duplication. ....	97
<b>Figure 3.30.</b> Point cloud before and after processing the empty spaces. ....	97
<b>Figure 3.31.</b> Point cloud before and after points reduction.....	97

<b>Figure 3.32.</b> Scanning Electron Microscope (a) diagram [134], (b) back view, and (c) front view.	98
<b>Figure 3.33.</b> Shadowgraph configuration diagram.....	99
<b>Figure 3.34.</b> DropSnake technique for contact angles (CA) analysis. ....	100
<b>Figure 3.35.</b> Low-Bond Axisymmetric Drop Shape Analysis (LBADSA) for contact angles (CA). .....	101
<b>Figure 3.36.</b> Virtual protractor technique used to calculate contact angles (CA). ....	101
<b>Figure 3.37.</b> Angles of action against the flow direction (a) Lotus, (b) Scallop, (c) Sharkskin and (d) Diamond. Adaptation from [113].....	102
<b>Figure 3.38.</b> Air Duct Test Rig.....	103
<b>Figure 3.39.</b> Experimental set-up for the swirl evaluation from different views. ....	106
<b>Figure 3.40.</b> Experimental apparatus for the condensation heat transfer experiments. Adaptation from [143].....	107
<b>Figure 4.1.</b> Evaluation phases summary. ....	113
<b>Figure 4.2.</b> Summary of the microstructured surfaces in Stage 1. ....	114
<b>Figure 4.3.</b> (a-b) SEM images of the lotus' pyramidal configuration, adaptation from [151,152]. (c) Lotus and (d) Scallop Computer-aided designs (CAD) [113,143]. ....	115
<b>Figure 4.4.</b> (a-b) ESEM images of the shark skin surface configuration, adaptation from [112]. (c) Sharkskin and (d) Diamond Computer-aided designs (CAD) [113,140].....	116
<b>Figure 4.5.</b> Velocity distribution near the wall of an unstructured surface. ....	117
<b>Figure 4.6.</b> Velocity distribution near the wall of the microstructured surfaces from stage 1. ....	118
<b>Figure 4.7.</b> Flow velocity in the z-direction and vorticity behaviour on different microstructured surfaces. ....	120
<b>Figure 4.8.</b> Flow velocity in the z-direction and vorticity behaviour on an unstructured surface..	121
<b>Figure 4.9.</b> Turbulence kinetic energy (TKE) near the wall of an unstructured surface.....	121
<b>Figure 4.10.</b> Turbulence kinetic energy (TKE) near the wall of the Lotus and Scallop microstructured surfaces. ....	122
<b>Figure 4.11.</b> Turbulence kinetic energy (TKE) near the wall of the Sharkskin and Diamond microstructured surfaces. ....	123
<b>Figure 4.12.</b> Shear stress ( $N/m^2$ ) near the wall of an unstructured surface. ....	124

<b>Figure 4.13.</b> Shear stress ( $N/m^2$ ) near the wall of the Lotus and Scallop microstructured surfaces. .....	125
<b>Figure 4.14.</b> Shear stress ( $N/m^2$ ) near the wall of the Lotus and Scallop microstructured surfaces. .....	126
<b>Figure 4.15.</b> Comparison of relative drag reduction between numerical results, experimental results and previous studies [19]. .....	128
<b>Figure 4.16.</b> CAD designs, manufactured workpieces top view images and 3D scans (Sensofar) of the Lotus, Scallop, Sharkskin, Diamond and unstructured surfaces [113,140]. .....	130
<b>Figure 4.17.</b> Contact angles between water droplets and the unstructured and microstructured surfaces of stage 1. ....	131
<b>Figure 4.18.</b> Velocity profiles of the stage 1 microstructured surfaces and unstructured surface. ....	132
<b>Figure 4.19.</b> (a) Experimental Drag Reduction, (b) Experimental Boundary Layer Thickness Reduction. ....	133
<b>Figure 4.20.</b> Surface temperature differential ( $\Delta T_s$ ), specific heat absorbed by the insert ( $Q$ ), heat rate ( $\dot{Q}$ ), heat flux ( $q$ ) and heat transfer coefficient ( $h$ ) results with percentages of improvement with respect to an unstructured surface (Stage 1). .....	134
<b>Figure 4.21.</b> Condensation heat transfer performance. Heat flux ( $q$ ) and heat transfer coefficient ( $h$ ) as a function of the surface subcooling temperature differential ( $\Delta T$ ). ....	135
<b>Figure 4.22.</b> Formation of condensates on the unstructured and microstructured surfaces of stage 1. ....	136
<b>Figure 4.23.</b> Surface temperature differential ( $\Delta T_s$ ) vs time, showing droplet life cycles. ....	137
<b>Figure 4.24.</b> Summary of the microstructured surfaces in Stage 2. ....	140
<b>Figure 4.25.</b> Schematic of hydrophobic holes manufactured by laser pulses [165]. ....	141
<b>Figure 4.26.</b> Characterisation data of (a) HLC-1 and (b) HLC-2. ....	142
<b>Figure 4.27.</b> Manufactured workpieces images, 3D scans (Sensofar) and SEM images of the SLC-1, SLC-2, HLC-1 and HLC-2 [166]. ....	143
<b>Figure 4.28.</b> Contact angles between water droplets and the unstructured and microstructured surfaces of stage 2. ....	144
<b>Figure 4.29.</b> Velocity profiles of stage 2 microstructured surfaces and unstructured surface. ....	144



<b>Figure 4.30.</b> (a) Experimental boundary layer thickness (mm), boundary layer thickness reduction (%). (b) Drag force (N) and drag reduction (%) with respect to an unstructured surface (Stage 2). .....	145
<b>Figure 4.31.</b> Stage 2 condensation heat transfer performance. Surface temperature differential ( $\Delta T_s$ ), specific heat absorbed by the insert ( $Q$ ), heat rate ( $\dot{Q}$ ), heat flux ( $q$ ), heat transfer coefficient ( $h$ ) results with percentage of improvement with respect to an unstructured surface, and Heat flux ( $q$ ) and heat transfer coefficient ( $h$ ) as a function of the surface subcooling temperature differential ( $\Delta T$ ). .....	146
<b>Figure 4.32.</b> Formation of condensates on the unstructured and microstructured surfaces of stage 2. .....	147
<b>Figure 4.33.</b> Surface temperature differential ( $\Delta T_s$ ) vs. time, showing droplet life cycles (Stage 2). .....	148
<b>Figure 4.34.</b> Summary of the microstructured surfaces in Stage 3. ....	150
<b>Figure 4.35.</b> Manufactured workpieces images, 3D scans (Sensofar) and SEM images of the SLS-1, HLS-1 and HLC-S [166]. ....	151
<b>Figure 4.36.</b> Characterisation data of (a) HLS-1 and (b) HLS-2. ....	153
<b>Figure 4.37.</b> Contact angles between water droplets and the unstructured and microstructured surfaces of stage 3. ....	154
<b>Figure 4.38.</b> Velocity profiles of the stage three microstructured surfaces and unstructured surface. .....	154
<b>Figure 4.39.</b> (a) Experimental boundary layer thickness (mm), boundary layer thickness reduction (%). (b) Drag force (N) and drag reduction (%) with respect to an unstructured surface (Stage 3). .....	155
<b>Figure 4.40.</b> Stage 3 condensation heat transfer performance. Surface temperature differential ( $\Delta T_s$ ), specific heat absorbed by the insert ( $Q$ ), heat rate ( $\dot{Q}$ ), heat flux ( $q$ ), heat transfer coefficient ( $h$ ) results with percentage of improvement with respect to an unstructured surface, and Heat flux ( $q$ ) and heat transfer coefficient ( $h$ ) as a function of the surface subcooling temperature differential ( $\Delta T$ ). .....	156

<b>Figure 4.41.</b> Surface temperature differential ( $\Delta T_s$ ) vs time, showing droplet life cycles (Stage 3). .....	157
<b>Figure 4.42.</b> Formation of condensates on the unstructured and microstructured surfaces of stage 3. .....	158
<b>Figure 4.43.</b> (a) Tested swirler. (b) Velocity profile of each blade in the swirl flow experiment the stage. ....	159
<b>Figure 4.44.</b> Boundary layer thickness and drag force of each blade. ....	160
<b>Figure 5.1.</b> Summary of the microstructured surfaces in Stage 4. ....	162
<b>Figure 5.2.</b> Concept design. ....	163
<b>Figure 5.3.</b> Dimensions of the hydrophobic features in sections 1 and 2.....	164
<b>Figure 5.4.</b> Dimensions of the hydrophilic features in sections 2 and 3. ....	165
<b>Figure 5.5.</b> Manufactured biphilic wettability gradient. Specimen WLS-1 (left) Specimen WLS-2 (right). ....	166
<b>Figure 5.6.</b> Scanned areas representation for characterisation using Sensofar (left). Section 1-A on the insert (right).....	167
<b>Figure 5.7.</b> Top view scan of section 1, taken with Sensofar.....	168
<b>Figure 5.8.</b> Perspective view scan of section 1, taken with Sensofar.....	168
<b>Figure 5.9.</b> Characterisation of section 1 representation. ....	169
<b>Figure 5.10.</b> Perspective view (a) and top view (b) scans of WLS-1's section 2.....	170
<b>Figure 5.11.</b> Perspective view (a) and top view (b) scans of WLS-2's section 2.....	171
<b>Figure 5.12.</b> Section 2 characterisation of WLS-1. ....	172
<b>Figure 5.13.</b> Section 2 characterisation of WLS-2. ....	172
<b>Figure 5.14.</b> Perspective view scan of section 3 (a) WLS-1 and (b) WLS-2. ....	173
<b>Figure 5.15.</b> Top view scan of section 3 (a) WLS-1 and (b) WLS-2. ....	174
<b>Figure 5.16.</b> Contact angles between water droplets and the unstructured and microstructured surfaces of stage 4. ....	175
<b>Figure 5.17.</b> Top view of the wettability test. ....	176
<b>Figure 5.18.</b> Velocity profiles of the stage 4 microstructured surfaces and unstructured surfaces. .....	177

<b>Figure 5.19.</b> Surface temperature differential ( $\Delta T_s$ ), specific heat absorbed by the insert ( $Q$ ), heat rate ( $\dot{Q}$ ), heat flux ( $q$ ) and heat transfer coefficient ( $h$ ) results with percentage of improvement with respect to an unstructured surface (Stage 4). .....	180
<b>Figure 5.20.</b> Condensation heat transfer performance. Heat flux ( $q$ ) and heat transfer coefficient ( $h$ ) as a function of the surface subcooling temperature differential ( $\Delta T$ ). .....	181
<b>Figure 5.21.</b> Formation of condensates on the unstructured and microstructured surfaces of stage 4. ....	182
<b>Figure 5.22.</b> Surface temperature differential ( $\Delta T_s$ ) vs time, showing droplet life cycles. ....	183
<b>Figure B.1.</b> Global Protect. ....	215
<b>Figure B.2.</b> WinSCP interface. ....	215
<b>Figure B.3.</b> PuTTY interface. ....	216
<b>Figure B.4.</b> Hawk supercomputer interface. ....	216
<b>Figure B.5.</b> Notepad++ interface. ....	217
<b>Figure B.6.</b> Permissions set-up. ....	217
<b>Figure B.7.</b> Submission job script. ....	218
<b>Figure B.8.</b> Modules. ....	219
<b>Figure B.9.</b> Job submission. ....	219
<b>Figure B.10.</b> sacct. ....	220
<b>Figure B.11.</b> squeue. ....	220
<b>Figure B.12.</b> slurmtop. ....	220
<b>Figure B.13.</b> scancel jobnumber. ....	220
<b>Figure C.1.</b> C# application for Sensofar point cloud file processing. ....	222
<b>Figure C.2.</b> Cloudcompare interface before data processing. ....	223
<b>Figure C.3.</b> Cloudcompare interface after data processing. ....	223

## List of Tables

<b>Table 2.1.</b> Dropwise condensation enhancement techniques. Adapted from [23]-[25], [38].....	58
<b>Table 3.1.</b> Cases tested numerically using Hydro3D for code validation. Adaptation from [19,113,117].....	84
<b>Table 3.2.</b> Assessment criteria example. ....	112
<b>Table 4.1.</b> Nominal dimensions of the micro-geometries (Stage 1).....	115
<b>Table 4.2.</b> Characterisation data of the microstructured surfaces and percentage difference with respect to the nominal dimensions. ....	129
<b>Table 4.3.</b> Wettability characterisation data for the microstructured surfaces of stage 1, margin and standard errors.....	131
<b>Table 4.4.</b> Assessment summary of stage one.....	139
<b>Table 4.5.</b> Nominal dimensions of the micro-geometries based on Scallop (Stage 2).....	141
<b>Table 4.6.</b> Characterisation data of the unstructured surface, scallop (stage 1 for comparison), SCL-1, SCL-2 and percentage difference with respect to the nominal dimensions. ....	142
<b>Table 4.7.</b> Wettability characterisation data for the microstructured surfaces of stage 2, margin and standard errors.....	143
<b>Table 4.8.</b> Assessment summary of stage two.....	149
<b>Table 4.9.</b> Nominal dimensions of the micro-geometry based on Scallop (Stage 3). * For comparison purposes. ....	151
<b>Table 4.10.</b> Characterisation data of the unstructured surface, scallop, SLC-1, SLS-1 and percentage difference with respect to the nominal dimensions. * For comparison purposes. ....	152
<b>Table 4.11.</b> Wettability characterisation data for the microstructured surfaces of stage 3, margin and standard errors.....	153
<b>Table 4.12.</b> Assessment summary of stage three.....	158
<b>Table 5.1.</b> Roughness values of WLS-1 and WLS-2 (Stage 4).....	166
<b>Table 5.2.</b> Characterisation data of the microstructured surfaces and percentage difference with respect to the nominal dimensions (Stage 4). ....	167

<b>Table 5.3.</b> Wettability characterisation data for the microstructured surfaces of stage 4, margin and standard errors.....	176
<b>Table 5.4.</b> Experimental Boundary layer thickness, boundary layer thickness reduction, drag force and drag reduction of stage 4. ....	178
<b>Table 5.5.</b> Heat transfer results. Surface temperature differential ( $\Delta T_s$ ), specific heat absorbed by the insert ( $Q$ ), heat rate ( $\dot{Q}$ ), heat flux ( $q$ ) and heat transfer coefficient ( $h$ ) results with percentage of improvement with respect to an unstructured surface (Stage 4). ....	179
<b>Table 5.6.</b> Assessment summary of stage four. ....	184
<b>Table 6.1.</b> Summary of the results of this study. ....	193
<b>Table A.1.</b> Summary of the current research on surface wettability modification. Adaptation from Edalatpour, et al. [53].....	212
<b>Table D.1.</b> Experimental Boundary layer thickness, boundary layer thickness reduction, drag force and drag reduction of stage 1. ....	224
<b>Table D.2.</b> Experimental Boundary layer thickness, boundary layer thickness reduction, drag force and drag reduction of stage 2. ....	226
<b>Table D.3.</b> Experimental Boundary layer thickness, boundary layer thickness reduction, drag force and drag reduction of stage 3. ....	227
<b>Table D.4.</b> Repeatability analysis based on boundary layer thickness and drag force (swirl flow experiments).....	227

# Nomenclatures

## Acronyms

$\mu$ -WEDM	Micro-Wire Electro Discharge Machining
ARCCA	Advanced Research Computing at Cardiff
CA	Static Contact Angle
CAD	Computer-Aided Design
CCRA	Climate Change Risk Assessment
CEng	Chartered Engineer
CFD	Computational Fluid Dynamics
CONACYT	Mexican National Council on Science and Technology
COVID-19	Coronavirus Disease 2019
DWC	Dropwise Condensation
ESEM	Environmental Scanning Electron
FWC	Filmwise Condensation
GFDL	Geophysical Fluid Dynamics Laboratory
GHG	Greenhouse Gases
HDR	High Dynamic Range
HPPE	High Peak Perishable Energy Recovery
HPPE-FP	High Peak, Perishable Energies – Foundation Phase
IBM	Immersed Boundary Method
ID	Identification
IPCC	Intergovernmental Panel on Climate Change
LBADSA	Low-Bond Axisymmetric Drop Shape Analysis
LDA	Laser Doppler Anemometry
LED	Light-Emitting Diode
LES	Large-Eddy Simulation
LMR	Local Mesh Refinement
MCIBSE	Member of the Chartered Institution of Building Services Engineers
MPI	Message Passing Interface
MOE	Margin of Error
NASA	National Aeronautics and Space Administration
NOAA	National Oceanic and Atmospheric Administration
PhD	Doctor of Philosophy
SDK	Software Development Kit
SEM	Scanning Electron Microscope
SEM	Standard Error of the Mean
SEM	Synthetic-Eddy-Method
SENER	Secretariat of Energy in Mexico
SGS	Subgrid Scale
SLM	Selective Laser Melting
TKE	Turbulence Kinetic Energy
UNEP	United Nations Environment Programme
WALE	Wall-Adapting Local Eddy-Viscosity
WMO	World Meteorological Organisation
XPS	X-ray Photoelectron Spectroscopy

# Symbols

## Latin Letters

$A$	Surface area on which the condensate occurs
$A$	Average or arithmetic mean
$A_c$	Cross-sectional area of the condensate flow at the lowest part of the flow
$b$	Width of the plate
$Bi$	Biot number
$c_f$	Skin friction coefficient
$Co$	Condensation number
$c_p$	Specific heat capacity
$c_{pl}$	Specific heat capacity of the liquid at the average film temperature
$D$	Diameter of the tube
$D$	Drag force
$D_h$	Hydraulic diameter of the condensate flow
$e$	Internal energy
$Ec$	Eckert number
$f_1$	Area in contact with droplet / projected surface area
$f_2$	Area in contact with air beneath the droplet / projected surface area
$g$	Gravitational acceleration
$\dot{g}$	The rate at which energy is generated per unit volume
$Gr$	Grashof number
$h$	Condensation heat transfer coefficient
$h$	Height
$h$	Riblet height
$h^+$	Dimensionless height
$\bar{h}$	Average value of the heat-transfer coefficient
$h_{fg}$	Latent heat of vaporisation
$h^*_{fg}$	Modified latent heat of vaporisation
$h_m$	Mass transfer convection coefficient
$h_x$	Heat transfer coefficient at location $x$
$hy$	Height
$H$	Heat transfer coefficient
$k$	Thermal conductivity (conduction)
$k_l$	Thermal conductivity of the liquid film
$l$	Length of the plate

$L$	Characteristic length
$\dot{m}$	Mass flow rate
$n$	Number of elements in the list
$N$	Number of horizontal tubes in the condenser
$Nu$	Nusselt number
$Nu_x$	Nusselt number at location $x$
$p^*$	Dimensionless pressure
$p$	Static pressure
$P$	Wetted perimeter of the condensate
$Pr$	Prandtl number
$q$	Heat flux
$Q$	Specific heat
$\dot{Q}$	Heat transfer rate
$\dot{Q}_x$	Heat transfer rate at location $x$
$r$	Roughness = actual surface area / projected surface area
$Re$	Reynolds number
$Re_x$	Critical Reynolds number
$s$	Riblet space
$S_a$	Surface roughness
$s^+$	Dimensionless space
$St$	Stanton number
$t$	Riblet thickness
$t^+$	Dimensionless thickness
$T_\infty$	Temperature of the freestream flow
$T_\theta$	Dimensionless temperature
$T_f$	Film temperature
$T_s$	Temperature of solid surface
$T_{sat}$	Temperature of vapour saturation
$T_v$	Vapour temperature
$u$	Velocity
$u^*$	Dimensionless velocity component
$u'$	Instantaneous velocity components that give rise to the eddies in the $x$ -direction
$\bar{u}$	Steady (mean) velocity component in the $x$ -direction
$U_\infty$	Freestream velocity of the flow
$v^*$	Dimensionless velocity component
$v'$	Instantaneous velocity components that give rise to the eddies in the $y$ -direction



$V^2/2$	Kinetic energy (advected)
$\bar{V}_l$	Average velocity of the condensate at the lowest part of the flow
$V_v$	Velocity of the vapour
$w$	Width of the plate
$x^*$	Dimensionless length x
$x_l$	Value of each element in the list
$X$	Body force in the x-direction
$y^*$	Dimensionless length y
$Y$	Body force in the y-direction
$z_\gamma$	Quantile or z-score

### Greek Letters

$\alpha$	Thermal diffusivity
$\beta$	Volumetric thermal expansion coefficient
$\gamma$	Confidence level
$\gamma_{sv}$	Solid/vapour surface tension
$\gamma_{sl}$	Solid/liquid surface tension
$\gamma_{lv}$	Liquid/vapour surface tension
$\delta$	Film thickness
$\delta^*$	Displacement boundary thickness
$\delta(x)$	Velocity boundary layer
$\delta_t(x)$	Thermal boundary layer
$\delta_c(x)$	Concentration boundary layer
$\Delta T$	Surface subcooling temperature differential
$\Delta T_s$	Surface temperature differential
$\varepsilon$	Eddy viscosity
$\theta$	Angle
$\theta^*$	New apparent contact angle on the roughened surface
$\theta_1$	Contact angle of the smooth solid surface
$\theta_2$	Contact angle for air
$\theta_{adv}$	Advancing contact angle
$\theta_{rec}$	Receding contact angle
$\mu_l$	Viscosity of the liquid
$\mu_v$	Viscosity of the vapour
$\nu$	Kinematic viscosity = momentum diffusivity
$\nu_l$	Kinematic viscosity of the fluid at liquid phase

$\rho_\infty$	Freestream flow density
$\rho_l$	Density of the liquid
$\rho_v$	Density of the vapour
$\sigma$	Standard deviation
$\sigma_{ii}$	Normal stress
$\tau_{ij}$	Shear stress
$\tau_w$	Shear stress at the wall

# Chapter 1 : Introduction

This introductory chapter presents a general review of the origin and consequences of climate change, including the relationship between the greenhouse effect, global warming, and climate change. It also includes a review of available renewable energy resources with their advantages and disadvantages. The project ‘High Peak, Perishable Energies - Foundation Phase’ (HPPE-FP) is described to understand its role in reducing the use of fossil fuels and to outline the aims and objectives of this doctoral research that focuses on enhancing heat transfer via microstructured surfaces for energy recovery purposes. Finally, this chapter will close by presenting the aims and objectives of this research, followed by the thesis structure.

The adverse effects of climate change have been widely apprehended recently, with detrimental consequences especially noted on the natural environment, human society, and worldwide economy. The primary reasons for climate change have been identified as unsustainable energy consumption and greenhouse gases (GHG) emissions, which are highly reliant on the evolution of many factors, such as economic and population growth, energy demand, energy resources and the costs and performance of energy supply and end-use technologies.

Over the past centuries, fossil fuels have been the primary energy source. However, due to their finite nature and role in the greenhouse effect and global warming, research into renewable and sustainable energy alternatives has increased exponentially, becoming a topic of interest to the scientific community in recent decades. Sustainable energy requires secure and affordable access to sources that can provide essential and sustainable services with low environmental impacts to meet basic human needs and serve productive processes. Renewable energy sources play an essential role in sustainably providing energy services while mitigating climate change by reducing GHG emissions. Renewable and sustainable energy technologies can also offer benefits concerning air pollution and health compared to fossil fuels [1,2]. According to the latest Global Status Report on Renewable Energy [3], modern renewable accounted for an estimated 11.2% of total final energy consumption in 2019, up from 8.7% a decade earlier. Notwithstanding significant growth in some renewable energy sectors, the contribution of renewables has only moderately increased each year due to increasing global energy demand and ongoing consumption of and investment in new fossil fuels [3,4].

Consequently, futuristic alternative high peak perishable energy sources, such as hurricanes, gales, floods and other highly energetic meteorological phenomena could be added to the mix of resources to support the reduction of fossil fuels consumption.

However, most of these alternative sources have not been extensively explored because they are located far from the grid or present extremely short-lasting, perishable and random natures, making their proliferation even more restrictive than current renewable energy technologies. This opens up the possibility of exploring the recovery of High Peak, Perishable Energies (HPPE) as part of future technologies into the 21<sup>st</sup> century. The High Peak, Perishable Energies - Foundation Phase (HPPE-FP) project aims to create the fundamentals for developing new technologies for the recovery of HPPE [5]. The results will support further research to enhance thermal and energy production processes, in addition to the development of industrial systems capable of decarbonising the electrical grid. One of the fundamental concepts of the HPPE-FP project to recover energy from sources such as hurricanes is the enhancement of heat transfer between the meteorological phenomenon and the equipment. For this reason, the present doctoral research explores an alternative passive mechanism for surface topographical modification via fabricating microstructured surfaces in order to enhance condensation heat transfer.

## **1.1 Climate Change: Origin and Consequences**

In recent decades, climate change has become a point of discussion in science and engineering due to its numerous effects on the world. In order to understand its origin and consequences, the difference between the greenhouse effect, global warming and climate change has to be defined.

The greenhouse effect is a natural mechanism that provides conditions suitable for life on the planet through the heating of the earth's atmosphere by the presence of greenhouse gases trapping radiation from the sun, which would otherwise be reflected back into space. The global climate system receives energy radiated by the sun in the visible spectrum (shortwave radiation), owing to the albedo (reflectivity of a surface), 31% of this energy is reflected by the atmosphere and by the different surfaces; the rest of the radiation enters and heats the terrestrial climate system. Subsequently, the earth's hot surface, due to solar radiation, radiates energy in the infrared spectrum (long-wave radiation), greenhouse gases (GHG) trap long-wave energy radiated by the earth and re-radiate energy in the same infrared spectrum returning it to the surface of the earth where it is absorbed again. Thus, the earth's surface receives constant energy from the atmosphere and the sun. This repetitive process allows the earth to maintain a temperature between 33°C to 36°C, higher than it would have without the presence of greenhouse gases. The main greenhouse gases are carbon dioxide (CO<sub>2</sub>), methane (CH<sub>4</sub>), nitrous oxide (N<sub>2</sub>O), water vapour (H<sub>2</sub>O), ozone (O<sub>3</sub>), halocarbons (CFC, HCFC, PFC, HFC) and sulphur hexafluoride (SF<sub>6</sub>). In the last decade, the Intergovernmental Panel on Climate Change (IPCC) reported the global greenhouse gas emissions by gas and the global greenhouse gas emissions by the economic sector (Figure 1.1) [6].

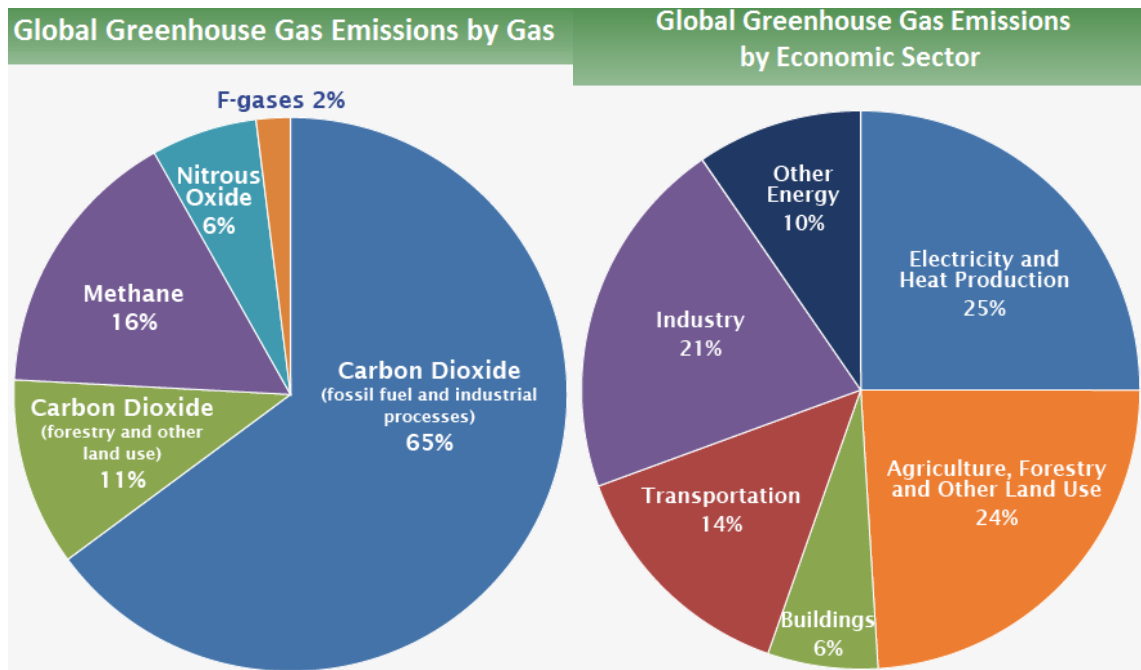


Figure 1.1. Global GHG emissions by gas and global GHG emissions by economic sector [6].

The following graph (Figure 1.2), developed by the National Aeronautics and Space Administration (NASA), shows how the atmospheric CO<sub>2</sub> has increased since the industrial revolution based on atmospheric samples contained in ice cores and recent direct measurements by J.R. Petit (Vostok ice core data) and the National Oceanic and Atmospheric Administration (NOAA) Mauna Loa CO<sub>2</sub> record [7]. Furthermore, the IPCC, established by the United Nations Environment Programme (UNEP) and the World Meteorological Organisation (WMO) as the leading authority on global climate change, states that “the total anthropogenic GHG emissions have risen more rapidly from 2000 to 2010 than in the previous three decades, in addition, CO<sub>2</sub> emissions from fossil fuel combustion and industrial processes contributed about 78% to the total GHG emissions increase from 1970 to 2010, with similar percentage contribution for the period 2000-2010” [8].

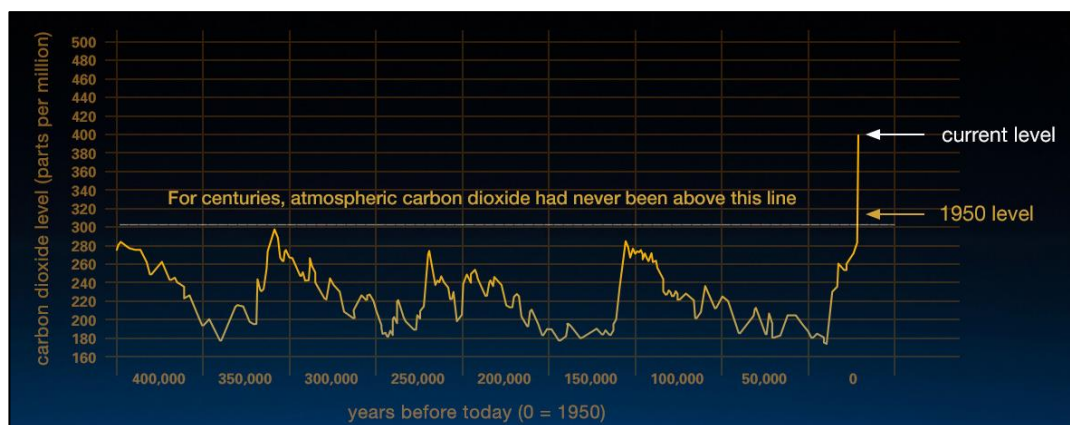
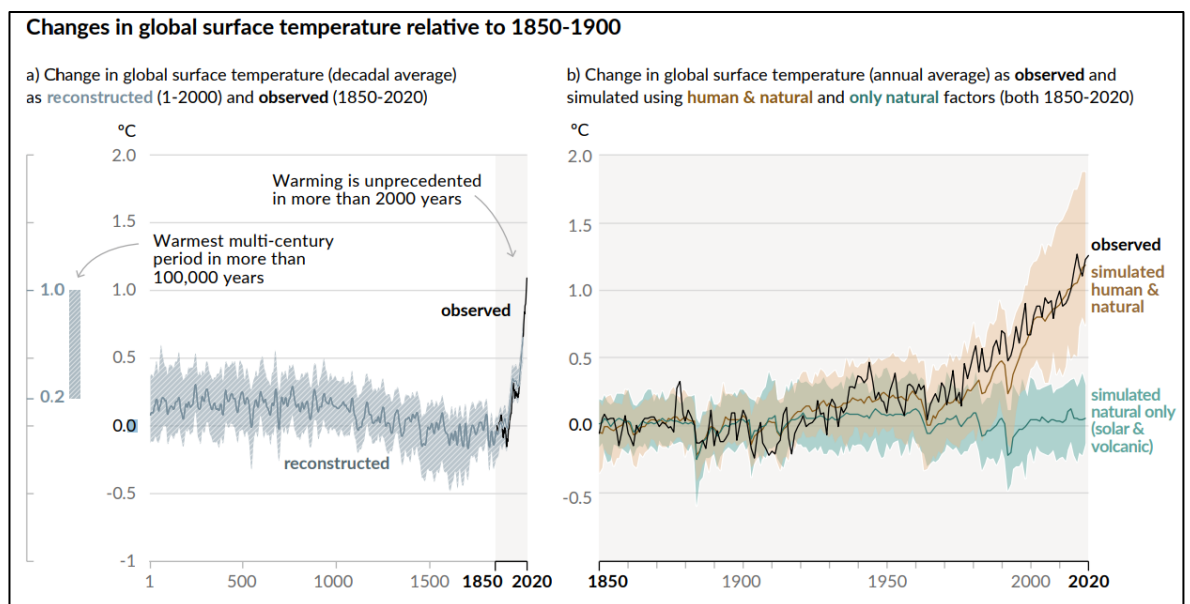


Figure 1.2. Carbon dioxide level in parts per million in the last 400,000 years [7].

Global warming is defined by the IPCC as an increase in combined surface air and sea surface temperatures averaged over the globe and over a 30-year period, and is mainly caused by anthropogenic greenhouse gas emissions, such as the burning of fossil fuels for industrial processes and energy production [9]. The global temperature change (Figure 1.3), based on long-term average temperature from 1850 to 2020, indicates that the observed temperature has been warmer every year since 1980, rendering a rise in the average global temperature [9]. Furthermore, according to The National Aeronautics and Space Administration (NASA), 97% of actively publishing climate scientists agree that climate-warming trends over the past century are extremely likely due to human activities [10]. According to information provided by the National Oceanic and Atmospheric Administration in the United States, the global average temperature has fluctuated during the 4.54-billion-year history of the earth. The planet has experienced long cold periods called ice ages and warm periods known as interglacials on 100,000-year cycles for at least the last million years. Previous warming periods were caused by small increases in how much sunlight reached the earth's surface and then amplified by significant carbon dioxide releases from the oceans as they warmed. The current global average temperature is increasing faster than at any point since modern civilisation and agriculture developed in the past 11,000 years as a result of the rise in greenhouse gases emissions [11].



**Figure 1.3. History of global temperature change [9].**

Climate change originates due to the alteration in long-term global weather patterns. According to the IPCC, *climate change refers to a change in the state of the climate that can be identified (e.g., by using statistical tests) by changes in the mean and/or the variability of its properties and that persists for an extended period, typically decades or longer* [3].

While global warming refers only to the earth’s rising surface temperature due to the increase in greenhouse gases, climate change includes all the variations of the climate that have occurred during the history of the planet, resulting from different factors such as global warming, persistent anthropogenic changes in the composition of the atmosphere or in land use, deforestation, modulations of the solar cycles and orbital variations, ocean circulation and volcanic or geological activity. The consequences are the changes in precipitation and snow patterns, melting glaciers, sea-level rise and risk of intense hurricanes, storms, tsunamis and droughts. These phenomena are likely to have a much greater impact on society with extreme weather conditions, altered habitats, health issues, and water and food scarcity than the temperature change alone.

The main consequences of climate change in the United Kingdom are presented in Figure 1.4, identified by the UK Climate Change Risk Assessment (CCRA). The CCRA reports the UK and Devolved Governments' views on the key climate change risks and opportunities that the UK faces, giving a detailed assessment of the following six areas: natural environment & assets, infrastructure, people & the built environment, business & industry, international dimensions, and cross-cutting issues [12,13].

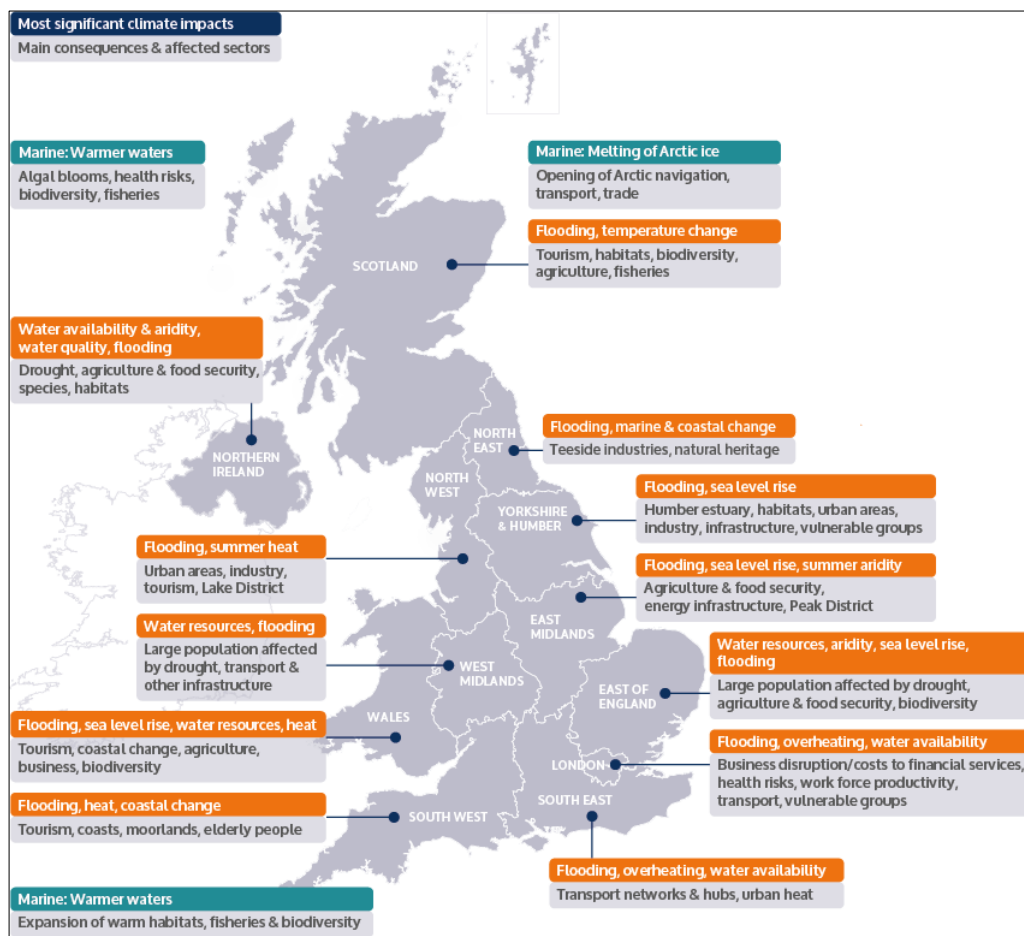


Figure 1.4. Climate change impacts in the UK [12].

Consequently, by early 2021, several countries worldwide implemented policies to help mitigate climate change (Figure 1.5). For instance, setting greenhouse gas emission targets, adopting carbon pricing or emission trading programmes, announcing fossil fuel bans or phase-outs; can directly or indirectly support and stimulate renewable energy deployment [3].

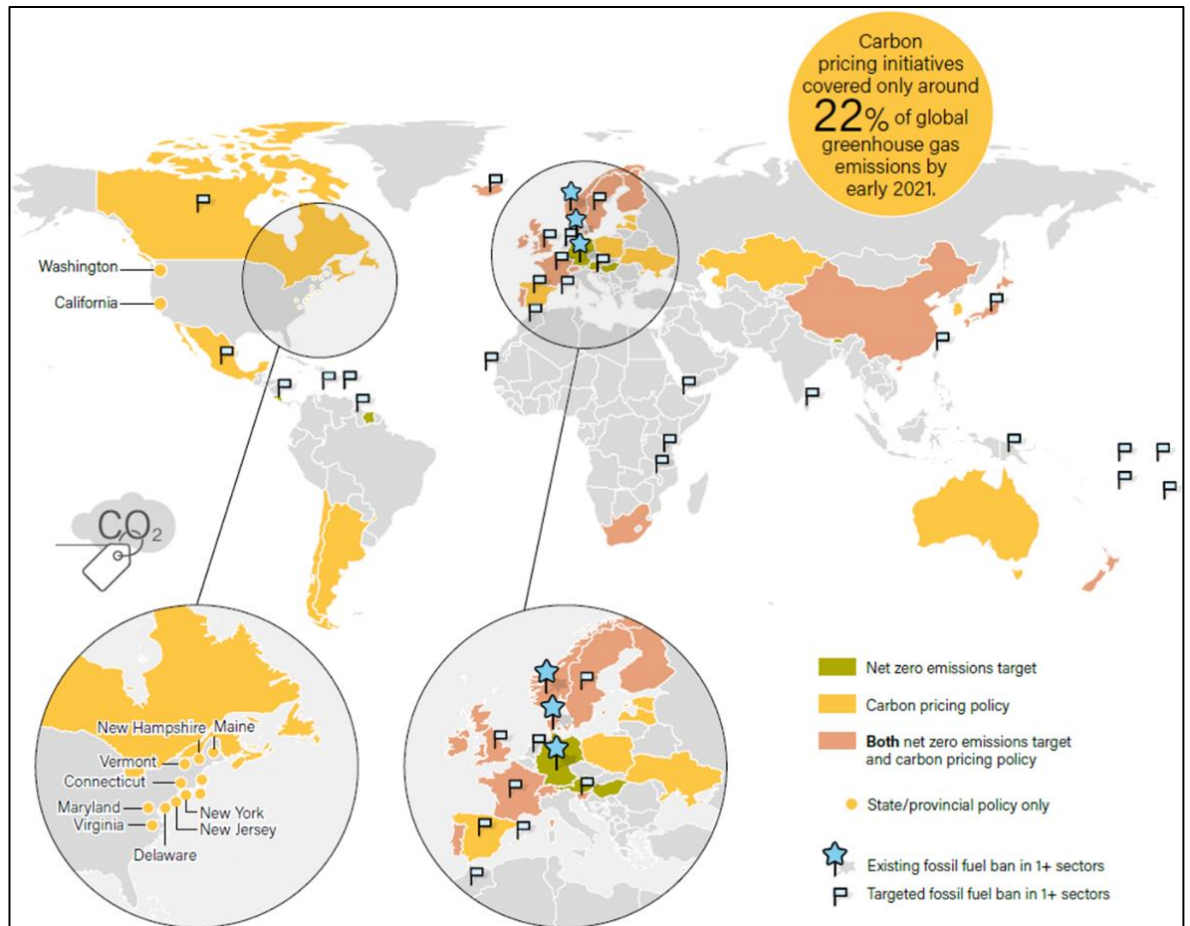


Figure 1.5. Countries with selected climate change policies [3].



## 1.2 Renewable Energy

Climate change is a global problem that entails the need for international cooperation. In order to mitigate the effects of climate change, it is necessary to reduce greenhouse gases emissions. In this way, the solution can be focused on carbon dioxide, the gas with the most significant impact on the greenhouse effect. From an engineering point of view, CO<sub>2</sub> emissions are mainly originated from energy production processes through the burning of fossil fuels (non-renewable energy). Therefore, a sustainable solution to decrease CO<sub>2</sub> emissions in the area is the use of renewable energy.

Renewable energy is generated from virtually inexhaustible natural resources using technology which ensures that the energy stores are naturally replenished, either by the immense amount of energy they contain, or because they are regenerated by natural means. The main resources for renewable energy are hydropower (tide and waves), sun, biomass, wind, ocean, thermal energy and geothermal power. Figure 1.6 shows a comparison between the shares of energy sources in the total global energy consumption across a 10-year span from 2009 to 2019, whereas Figure 1.7 presents renewable energy in total final energy consumption in 2018 by final energy use [3].

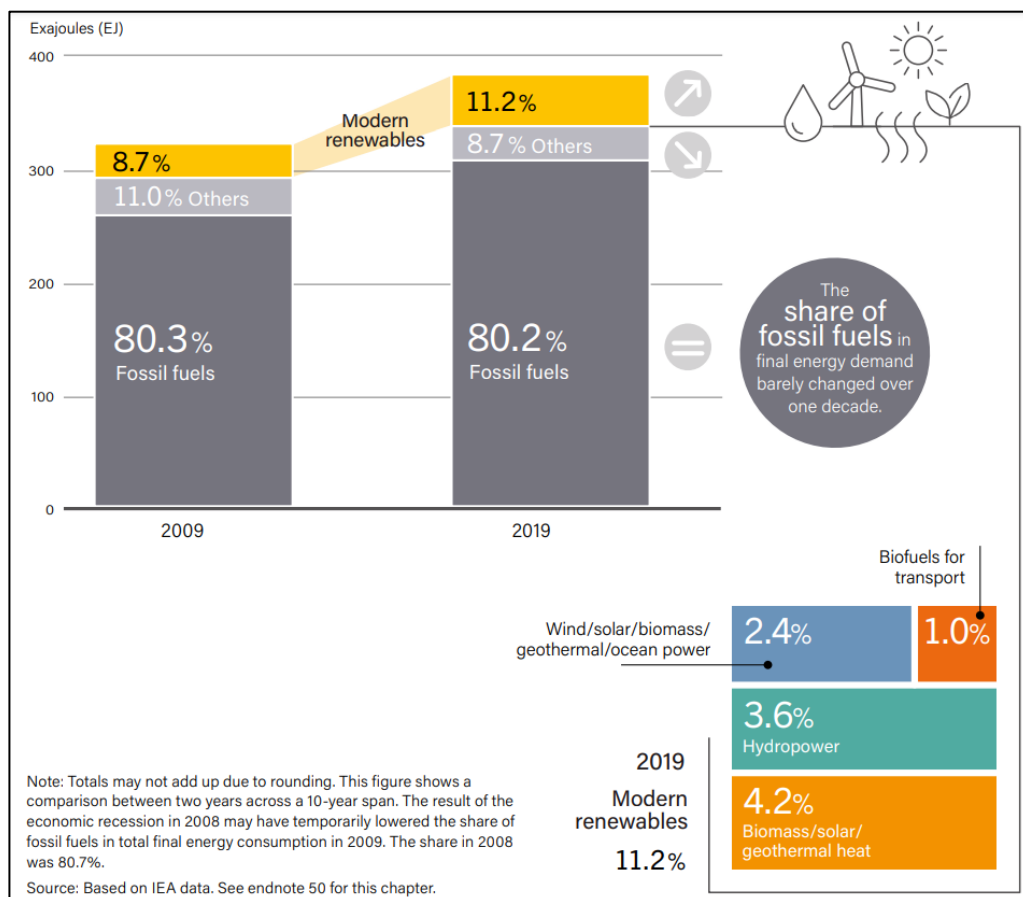


Figure 1.6. Estimated renewable energy share of total final energy consumption in 2009 and 2019

[3].

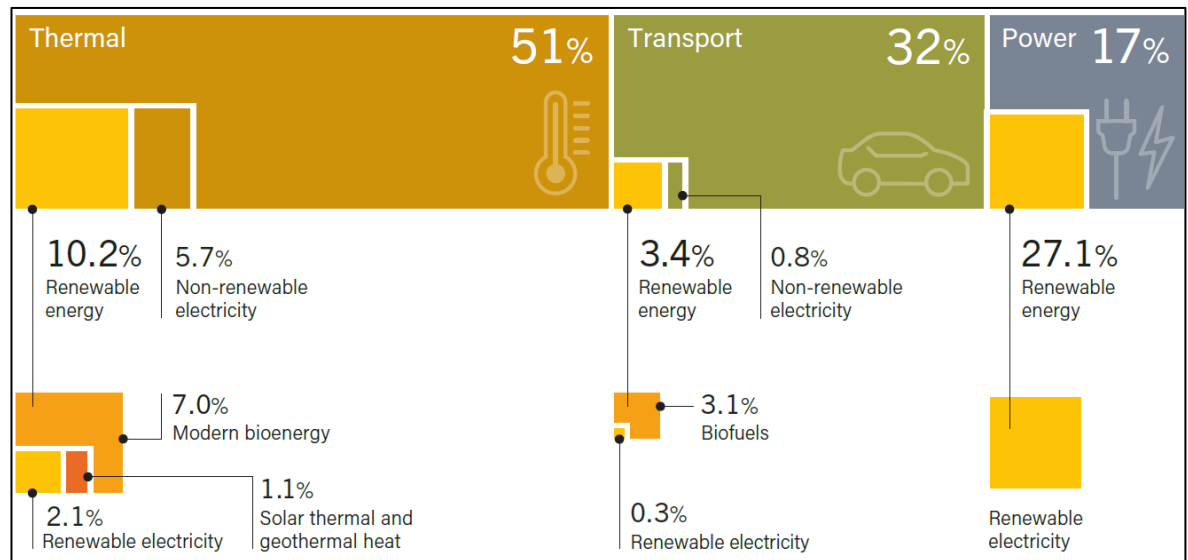


Figure 1.7. Renewable energy in total final energy consumption in 2018 by final energy use [3].

### 1.2.1 Direct Solar Energy

Direct solar energy represents 1% of all electricity used worldwide [14]. This type of renewable technology is based on the sun's energy directly. However, other technologies (wind and ocean thermal) only use solar energy after it has been absorbed on the earth and converted to other forms. The main types of direct solar energy are [2]:

- Photovoltaic (PV): Electricity generation via direct conversion of sunlight to electricity by photovoltaic cells.
- Solar Thermal: Active and passive heating of buildings, domestic and commercial solar water heating, swimming pool heating and process heat for industry.
- Concentrated Solar Power (CSP): Electricity generation by optical concentration of solar energy to obtain high-temperature fluids or materials to drive heat engines and electrical generators.
- Solar Fuels Production Methods: Fuels production using solar energy.

The main advantages of direct solar energy are electricity supply in areas where connection to the main grid is cost-prohibitive. Greenhouse gases and pollutants (particulates and toxic gases) reduction from fossil fuel plants that it replaces. Although the cost of solar energy varies widely by technology, application, location and other factors, costs have been reduced significantly during the past 30 years, and technical advances and supportive public policies continue to offer the potential for additional cost reductions [2].

### **1.2.2 Hydropower**

Hydropower is derived from the energy of water moving from higher to lower levels. According to the world energy resources report, hydropower is the principal renewable source for electricity generation worldwide [14]. The International Energy Agency also states that hydropower is expected to remain the world's largest source of renewable electricity generation and play a critical role in decarbonising the power system and improving system flexibility with a global annual generation of 4,418 TWh in 2020 [15]. Hydropower is a foreseeable and economically competent technology that offers a wide range of benefits such as: near- and long-term GHG emissions reduction; flood control, water conservation during droughts or dry seasons by hydropower facilities; impacts on the living conditions of local communities and the regional economy through the creation of freshwater storage systems for irrigation, navigation, tourism, fisheries and sufficient water supply to communities and industries. Even though the initial investment is higher than other renewable energy technologies, the operation and maintenance cost is considerably low with a long lifespan [2,14].

### **1.2.3 Bioenergy (Biomass)**

Bioenergy is obtained from organic matter (biomass) that is not embedded in geological formations (fossilised). Due to its nature, it can be used as fuel in its original state or be processed into different types of solid, gaseous or liquid biofuels. Biofuels are frequently used in all sectors of society for electricity production, transportation, heating and cooling purposes and industrial processes [16]. Bioenergy plays an important role in the daily livelihoods of billions of people in developing countries. Furthermore, expanding its production requires sophisticated land and water use management; global feedstock productivity increases for food, fodder, fibre, forest products and energy; substantial conversion technology improvements; and a refined understanding of the complex social, energy and environmental interactions associated with bioenergy production and usage [2].

### **1.2.4 Wind Energy**

Wind Energy is the technology by which wind turbines transform the kinetic energy present in the wind into mechanical power or electricity. According to the Global Wind Report 2021, global wind power generation capacity reached 743 GW [13]. This capacity helps to avoid over 1.1 billion tonnes of CO<sub>2</sub> globally, equivalent to the annual carbon emissions of South America. Additionally, it has a reasonably smaller environmental footprint than other electricity supply technologies. The main challenge is the variability of the wind power output over multiple time scales due to the nature of the resource [2].

### 1.2.5 Ocean Energy

According to the IPCC's special report on renewable energy sources and climate change, ocean energy is obtained from technologies that utilise seawater as their motive power or harness the water's chemical or heat potential. Electricity generation from marine technologies increased an estimated 400 GWh (+33%) from 2019 to 2020 [17]. The renewable energy resource in the ocean comes from six distinct sources, each with different origins and each requiring different technologies for conversion. These sources are [2]:

- Tidal Currents: Obtained from water flow that results from filling and emptying of coastal regions associated with tides.
- Ocean Currents: Obtained from wind-driven and thermohaline ocean circulation.
- Salinity Gradients (osmotic power): Obtained from salinity differences between fresh and ocean water at river mouths.
- Wave Energy: Obtained from the transfer of the wind's kinetic energy to the ocean's upper surface.
- Tidal Range (tidal rise and fall): Obtained from gravitational forces of the earth-moon-sun system.
- Ocean Thermal Energy Conversion: Obtained from temperature differences from solar energy stored as heat in upper ocean layers and colder seawater, generally below 1,000 m.

### 1.2.6 Geothermal Energy

Geothermal technology uses the heat from the earth's interior stored in both rock and trapped steam or liquid water. The earth's thermal energy, in an active reservoir, is continuously restored by natural conduction and convection from surrounding hotter regions, while the extracted geothermal fluids are replenished by natural recharge and by reinjection of the cooling fluids. The main applications are electricity generation and agro-industrial applications requiring heat [2]. Geothermal electricity generation increased an estimated 2% in 2020, falling below average growth of the previous five years, with a capacity increase of ~200 MW [18]. Nevertheless, geothermal could meet roughly 3% of the global electricity demand and 5% of the global demand for heating and cooling by 2050, according to the IPCC report on renewable energy sources and climate change [2,14]. One of the advantages is that the earth's natural heat reserves are immense, and climate change has no significant impact on its effectiveness. Geothermal energy can be integrated into all types of electrical power supply systems, from large, interconnected continental transmission grids to onsite use in small, isolated villages or autonomous buildings [2,14]. Due to natural processes, discharge of gases mixed with steam from surface features, minerals dissolved in water from hot springs, micro-earthquakes, hydrothermal steam eruptions, seismic events are a main concern for this technology in addition to higher installation costs and more extended development periods [2].

### **1.3 Alternative Energy Sources: High Peak Perishable Energy Recovery**

Even though significant actions have been successfully taken to reduce the use of non-renewable resources, the different challenges that current renewable energy technologies present limit their effectiveness in completely replacing fossil fuels. This could be solved by adding alternative high energy resources to the energy mix. Examples of such alternative energy sources are hurricanes, gales, tropical storms, floods, tornados, monsoons and other highly energetic meteorological phenomena. However, most of these alternative sources have not been explored exhaustively because they are either stranded far from the grid or present extremely short-lasting, perishable, and random natures, limiting their proliferation. Exploring the possibility of recovering High Peak, Perishable Energies (HPPE) could provide alternative and innovative technologies capable of supporting worldwide energy consumption.

This doctoral research is part of the “Foundation Phase (FP)” of the HPPE project, led by Dr Agustín Valera-Medina at the School of Engineering of Cardiff University, which was originally part of the Carbon-Free Ammonia programme, in collaboration with The Katholieke Universiteit Leuven (Belgium), National Autonomous University of Mexico (Mexico), Delft University of Technology (Netherlands), Royal Institute of Technology (Sweden), London School of Economics (UK), The Institute of Atmospheric Sciences and Climate (Italy), Cambresis (UK), CENAPRED (Mexico), MET Office (UK), Vortex Bladeless (Spain) and Siemens (Germany). The “HIGH PEAK, PERISHABLE ENERGY RECOVERY - FOUNDATION PHASE (FP) PART B” proposal (FETOPEN-01-2016-2017) is presented in this section with the intention of understanding the aim and objectives of this individual PhD project.

Extreme weather events carry an enormous amount of energy that can be harvested with the right technology. However, a series of potential impacts are yet to be fully determined and should be considered to develop these technologies in a socially and ethically responsible way. Despite the fact of numerous challenges arising from the high energy production in an extremely short period of time, such as the lack of affordable and highly advanced devices capable of recovering and storing this energy; the environmental, economic and social benefits that are related to the development of HPPE recovery systems would be more significant due to the reduction of energy production via fossil fuels and reduction of negative impacts that come with extreme meteorological events. For example, regions where hurricanes touch land would be more safeguarded as the energy produced by the hurricane would be consumed for energy generation whilst diverting the fast winds that cause destruction. Also, the population in countries where energy is recovered will benefit from the energy produced by these phenomena. Since more energy sources will be available, greater development is expected in these regions.

Most energy harvesting devices get rapidly overloaded with high-speed winds; as a result, devices such as classical bladed wind turbines are impractical to use in the event of high loads. Additionally, the duration of hurricanes or tropical storms is too short and hard to predict to enable continuous operation in one single location; consequently, they will require mobile devices to capture energy efficiently. Therefore, the mission of the general project is to develop the foundations of a new research area for harnessing high peak, perishable energy from extremely energetic meteorological phenomena. Manufacturing, deployment and maintenance of new energy-harnessing devices will create a new industry, ensuring that more energy is recovered efficiently and safely for the benefit of the communities and stakeholders involved. Industries related to heat transfer will also benefit from the outcomes of the new HPPE technology, developing more efficient devices for heat transfer ranging from small heaters and medium economisers to large cooling towers for power generation due to the transfer of the HPPE-FP knowledge [5].

The consortium offers a combination of innovation and skills that can provide the foundation, knowledge, techniques and facilities for more research in the field and the creation of new systems whilst positioning Europe as a worldwide leader and contributing to the decarbonisation and decentralisation of energy networks in the Caribbean.

Desiccant Resonant Swirling Tubes can be used to recover energy from large kinematic and heat sources, promoting their implementation not only in highly energetic events but also for the usage of stranded energy in warm humid flows. This HPPE recovery system consists of portable venturi cone shape cylinders of  $\sim 0.2\text{-}0.5$  m in diameter and  $\sim 0.6$  m in length, with the in-and outflow of air along the same axis, they work as centrifugal separators while absorbing the moisture from the humid air entering the system. The development of the HPPE recovery system, e.g. desiccant resonant swirling tubes, could be achieved by combining the following concepts (more detailed information is presented in Chapter 2):

- Droplet-solid material barriers
- Venturi channels
- Vortex tubes and swirl generators
- Wake effect
- Resonance of standing wave
- Enhancement of heat transfer via microstructured surfaces

Considering the facilities and experience of the team at Cardiff University, this doctoral project only focuses on enhancing heat transfer via microstructured surfaces, while the rest of the concepts will be developed by other teams in the consortium.

## 1.4 Enhancement of Heat Transfer via Microstructured Surfaces

Considering the vast amount of energy, origin and self-sustaining physics behind a hurricane, heat recovery from a highly energetic weather event can provide the energy necessary for ammonia production, whilst the high-speed wind can drive the flows to ensure better recovery. Thus, some fundamental studies need to be carried out to develop a system capable of recovering heat from fast-flowing wind [5]. It is envisaged that systematically designed microstructured surfaces would ensure high heat transfer from the moisture latent heat of the hurricane to the surface of the device instead of transferring the energy to the drier air. This phenomenon is based on the surface characteristics that can improve droplet nucleation, droplet growth, and droplet drainage depending on the wetting state. Thus, increasing heat transfer during condensation. Moreover, microstructured surfaces have shown positive effects on boundary layer control [19], which can widen this research's applications. This theory lays the foundation of the aim of the present PhD research that focuses on enhancing heat transfer via microstructured surfaces.

In order to define the most appropriate micro-geometry for condensation heat transfer enhancement, this PhD research is divided into four stages to evaluate different micro-geometries. The micro-geometries' designs are based on previous work and computational fluid dynamics (CFD) analysis at Cardiff University for the first stage, while the following stages are based on the performance of the corresponding subsequent stage. The different micro-geometries are generated either by micro-wire electro discharge machining ( $\mu$ -WEDM) or laser micro-processing on two types of base surfaces/bodies (hereinafter referred as inserts) made either via casting or metal additive manufacturing. The evaluation of the microstructured surfaces is divided into three phases: Phase 1: Design, manufacture and characterisation; Phase 2: Fluid dynamics evaluation (momentum transfer); and Phase 3: Condensation heat transfer evaluation. The characterisation phase is carried out using a 3D optical scanning profiler and a scanning electron microscope (SEM), while a shadowgraph configuration is used for the wettability assessment. Velocity experiments are carried out to validate numerical simulation results and to analyse the effects of micro-geometries at different angles of action against the flow direction in terms of boundary layer control and drag reduction. Finally, differential temperature measurement experiments are carried out in a condensation chamber to evaluate the extent of heat transfer during matter's phase change.

## 1.5 Aims and Objectives

This PhD research **aims** to explore an alternative passive mechanism for surface topographical modification via fabricating microstructured surfaces in order to enhance heat transfer for energy recovery purposes.

To achieve this aim, the selection and fabrication of the suitable microstructure geometry are established as the **general objective**, which is further broken down to the following **specific objectives**:

- To undertake an extensive literature review on condensation heat transfer.
- Selection of various microstructure designs based on previous work on biomimetic engineering, hydrophobic/hydrophilic characteristics and CFD analysis at Cardiff University.
- To undertake the manufacture of the selected microstructure geometries.
- To carry out characterisations of the fabricated microstructured surfaces via  $\mu$ -WEDM and laser micro-processing.
- To carry out fluid velocity profile experiments to evaluate the effect of different geometries, angles of action and manufacturing techniques on surface characteristics for boundary layer control and drag reduction.
- To conduct condensation experiments to analyse the effects of different micro-geometries and their wetting state on surface characteristics for heat transfer enhancement.
- To design, manufacture and test a novel biphilic, that which is comprised of hydrophobic and hydrophilic characteristics, with higher performance.



## 1.6 Thesis Structure

The thesis is divided into seven chapters:

### *Chapter 1: Introduction*

This chapter gives a summary of the relationship between the greenhouse effect, global warming and climate change. It also includes the consequences of burning fossil fuels and how renewable energy is a sustainable solution for energy production. A summary of available renewable energy resources is presented, along with their advantages and disadvantages. The concept of High Peak Perishable Energy Recovery (HPPE) is defined to understand the aims and objectives of this doctoral research that focuses on enhancing heat transfer via microstructured surfaces for energy recovery purposes.

### *Chapter 2: Literature Review*

This chapter provides a comprehensive review of condensation heat transfer, previous work on heat transfer enhancement, and principles for using microstructured surfaces as a passive mechanism for surface topographical modification for energy sector applications.

### *Chapter 3: Methodology*

This chapter explains the approaches and procedures used in each of the four stages and three evaluation phases of this study with the purpose of achieving the aim and objectives.

### *Chapter 4. Performance Evaluation Results of Hydrophobic and Hydrophilic Microstructured Surfaces (Stages 1, 2 and 3)*

In this chapter, the results of each evaluation phase from stages 1, 2 and 3 are presented. This is with the objective of understanding how each stage is linked and how they contribute to the novel biphilic wettability gradient approach used in stage 4 for condensation heat transfer enhancement via microstructured surfaces.

### *Chapter 5. Performance Evaluation Results of Novel Biphilic Microstructured Surfaces (Stage 4)*

In this chapter, the results of the novel microstructured surface design (stage 4) are presented.

### *Chapter 6. Discussion*

In this chapter, a summary of the results is presented, together with a discussion of the findings from each stage and phase, as well as challenges faced during this research.

### *Chapter 7. Conclusions*

This chapter presents conclusions and recommendations for future work.

## Chapter 2 : Literature Review

In this chapter, the concepts behind the High Peak Perishable Energy Recovery (foundation phase) project are presented in the first section in order to understand the relevance of the condensation phenomenon; followed by an extensive review of condensation heat transfer theory, types of condensation and the relationship between the life cycle of the condensed droplets with the surface wettability. Heat transfer enhancement techniques are reviewed, and current research on condensation enhancement is discussed concerning surface modification. The last section of the literature review chapter presents various considerations and concepts associated with microstructured surfaces as a passive technique for surface modification in heat transfer performance.

### 2.1 Alternative Energy Sources: High Peak Perishable Energy Recovery

Extremely energetic meteorological phenomena with humid environments, such as gales, floods, tornados, monsoons and tropical cyclones, contain an enormous amount of energy that could easily exceed the worldwide electrical generating capacity. For example, tropical cyclones, also known as hurricanes, cyclones, or typhoons depending on where they originate, are the most violent storms on Earth and can released up to  $5.2 \times 10^{19}$  Joules per day, equivalent to 200 times the worldwide electrical generating capacity [20]. For a hurricane to form it is required warm water with a temperature of at least  $26.5^{\circ}\text{C}$ , over a depth of 46 m to induce instability in the atmosphere and feed the storm, a sharp temperature gradient to enable latent heat to be released during water vapour condensation and high humidity for the formation a large number of cumulonimbus clouds [20,21].

As seen in Figure 2.1, the hot and humid air above the ocean moves upwards the eye in an anticlockwise direction, creating a low-pressure area near the water's surface. From the high air-pressure area, around the low-pressure area, air sinks towards the low point of the eye, where it warms up and becomes more humid, it moves upwards, forming rain bands where the warm rising air cools down and condenses into clouds and rain that feeds up the process to repeats itself. Meanwhile, "new" cooler air is sucked into the low-pressure area to continue with the cycle. The hurricane spins due to momentum conservation and the Coriolis force, and can only be stopped when one or more of the following scenarios happen: the water cools down, the temperature differences in the air decrease, the humidity level drops or when the hurricane reaches land stopping the warm water supply [22]. Even though hurricanes have a highly perishable nature, they have recently become more prevalent and stronger, representing a considerable environmental, social and economic risk for the places they could hit, as shown in Figure 2.2.

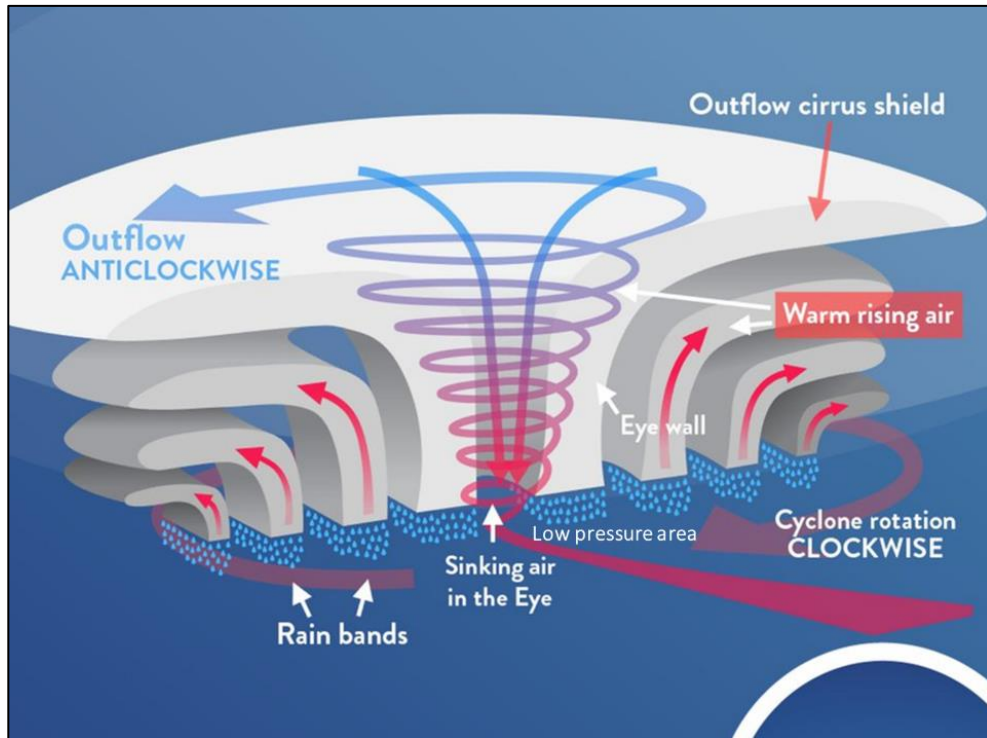


Figure 2.1. Tropical cyclone structure in the southern hemisphere [21].

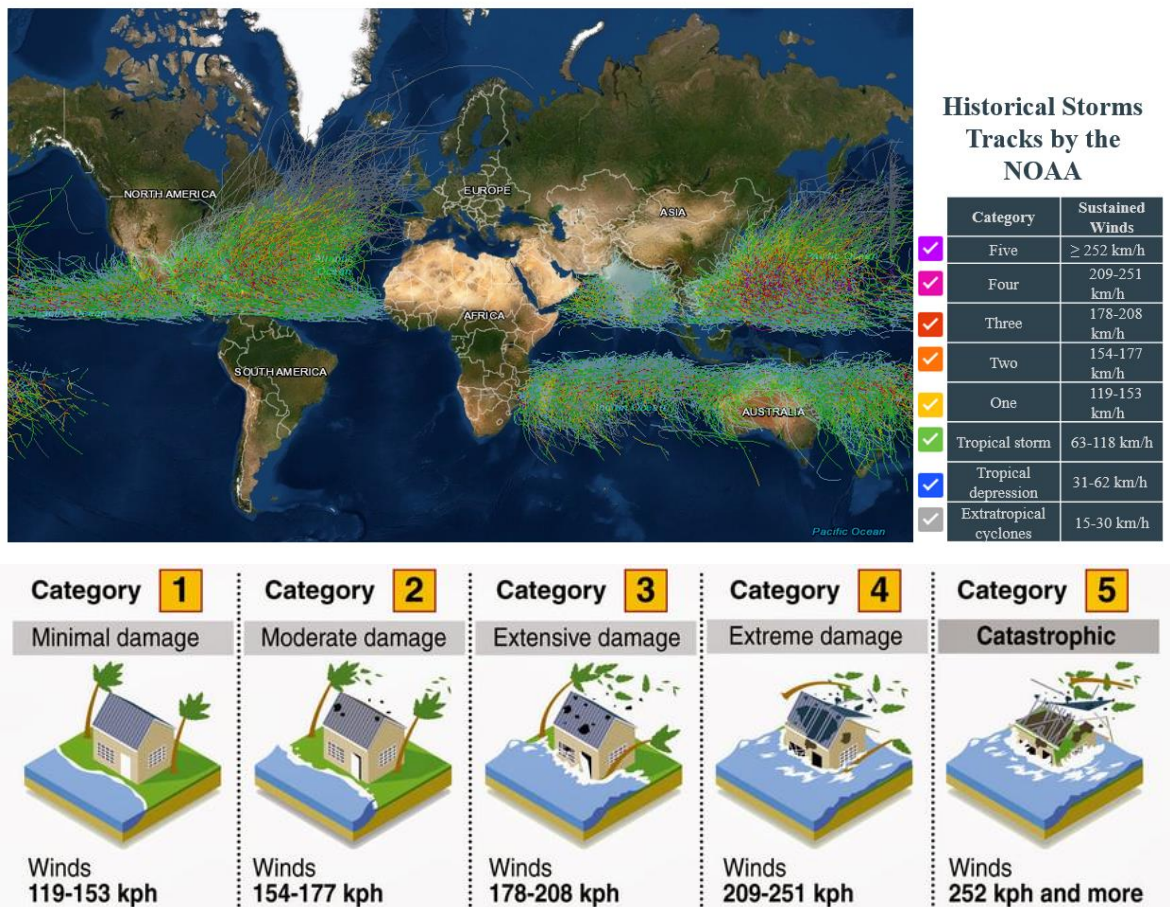


Figure 2.2. Historical Storms Tracks (1851-2019). Adaption from the National Oceanic and Atmospheric Administration (NOAA) [20] and Saffir-Simpson hurricane scale [23].

From a thermodynamic and engineering point of view, hurricanes work as heat engines. Through condensation, the heat from the warm, humid air of the tropical ocean transforms into heavy storms while the amount of kinetic energy generated maintains the strong swirling winds [20]. If the energy from a hurricane could be extracted and carefully managed, regions where hurricanes touch land would be more safeguarded as the energy produced by the hurricane would be consumed for energy production whilst diverting the fast winds that cause destruction. These fast winds that cause destruction are usually seen as the most energetic part of the hurricane. However, only a small portion of the energy in a hurricane drives the storm's horizontal winds (kinetic energy). In a mature hurricane, the amount of kinetic energy generated is equal to that being dissipated due to friction [23]; hence, the wind dissipation rate or wind generation rate is  $1.3 \times 10^{17}$  Joules/day, which is equivalent to about half the world-wide electrical generating capacity [20].

The latent heat from condensation is the energetic process that feeds a hurricane's momentum through convection or rising motions in the storms. An average hurricane with an eyewall of 665 km radius produces  $2.1 \times 10^{16}$  cm<sup>3</sup>/day of rain. Consequently, the total energy released from condensation through cloud and rain formation is  $5.2 \times 10^{19}$  Joules/day, equivalent to 200 times the worldwide electrical generating capacity [20]. With more than 13,000 storms recorded since 1842, studies indicate an increase in the number of hurricanes and their intensity in past decades [24]. Furthermore, the Intergovernmental Panel on Climate Change (IPCC) reported that an increase of 2°C in the global temperatures will affect this meteorological phenomenon as follows: Tropical cyclone rainfall rates will likely increase by 10% to 15%. Tropical cyclone intensity is likely to globally increase by up to 10%. Consequently, assuming no reduction in storm size, the level of storm destruction will be higher. In addition, the global proportion of tropical cyclones that reach very intense levels, such as Category 4 and 5, will likely increase [25].

The Geophysical Fluid Dynamics Laboratory (GFDL), through direct model simulations of hurricane activity under climate change scenario (Figure 2.3), concluded that greenhouse warming would cause hurricanes in the coming century to be more intense and have higher rainfall rates than present-day hurricanes [25]. For instance, in 2015, Hurricane Patricia produced sustained winds of up to 320 km/h, leading experts to reconsider if the current Saffir-Simpson hurricane wind scale with five categories is still appropriate [26]. Although not all energy can be recovered, it is clear that the potential of this source is extremely vast, and new innovative ideas are required to access this resource, as only a 1% recovery constitutes an enormous amount of energy that several countries could have access to.

## Atlantic Hurricanes (1980-2012): Simulated vs. Observed

Correlation = 0.73; Linear trends: +0.18 storms/yr (model) and +0.13 storms/yr (observed)

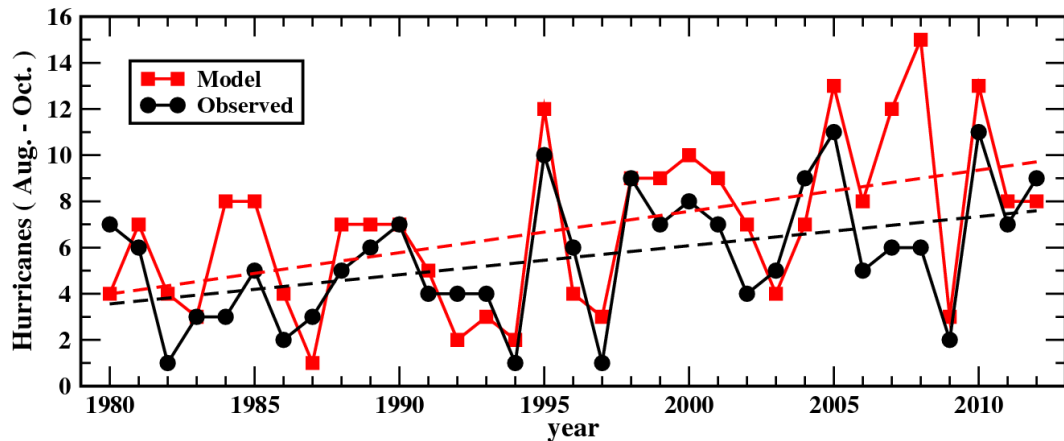


Figure 2.3. Increase in Hurricanes in the Atlantic [27].

A major challenge of any development towards harnessing such large amounts of energy would be its storage beyond the short lifetime of the extreme weather event. This can be overcome by producing ammonia that can be moved around alongside any energy-capturing technology to not only capture hurricanes touching land but also to be flexible and mobile enough to increase capture along their pathway.

For energy production, hurricane winds are far stronger than the turbine's cut-out speed (88.5-112.65 km/h [27]); thus, making classical bladed wind turbines would not be feasible for the task. Additionally, the paths of fast, warm winds (tropical storms or hurricanes) are difficult to predict and therefore would require mobile devices to capture energy efficiently, making more restrictive and challenging their development. One development that could potentially recover fast winds is the Vortex Bladeless Technology, which uses vortex generators to recover wind energy [28,29]. However, these systems are still relatively small, and their power outputs are low to subtract the energy from these fast, warm winds. Moreover, the devices do not recover any potential heat in the moisture associated with these heavy storms. Hence, this research will be the first venturing in this field to develop larger-scale systems.

The main source of energy in a hurricane is the heat released when water condenses in a rising air current. It is also known that 20% of the heat taken from the sea during a hurricane is converted into mechanical energy according to the 'Total energy equation method for calculating hurricane intensity' article developed by Michaud in 2001. This explains why hurricanes quickly fade away when they touch dry land [30].

The HPPE recovery system (confidential) concept is based on the same physics ruling over the production and self-sustaining of a hurricane [5]. The idea of this system, *Desiccant Resonant Swirling Tubes*, is based on the following fundamental concepts:

1. *Droplet-solid material barriers*: Hurricanes bring considerable moisture, which produces clouds and extremely high precipitation containing big droplets and other unwanted solids that can be detrimental for the device [31]. It is necessary to develop new concepts of droplet-solid material barriers to mitigate the impact of these small but high momentum bodies. Droplet-Solid Material barriers would stop unwanted bodies inside the Desiccant Swirling Tube, leaving only wet air. These barriers could also serve as flow straighteners [5].
2. *Venturi channels*: These devices increase velocity while reducing pressure and temperature. This can be used to establish a temperature differential for heat transfer between the cold drier air at the shroud of the device and the moisture latent heat in the wet air to produce an electric current from thermoelectric materials. An increase of velocity from 90 m/s to 330 m/s (before choking) can reduce almost 650 mbar pressure. Considering an isenthalpic process with no changes in enthalpy, this will produce temperatures in the range of 240K. In the interim, a higher velocity at the system's core would produce high swirling flows, increasing the wet air's residence time [5].
3. *Vortex tubes and swirl generators*: In essence, Vortex Tubes use an induced vortex that, due to motion and energy conversion (i.e. kinetic to internal), allow the production of two streams, one hot the other cold, at different ends of the tube [32–34]. On the other hand, swirl generators establish a swirling pattern with a central recirculation zone that, if properly handled, can elongate to the outlet of a swirling device.

Thus, combining these concepts can impose a high swirl stream that effectively increases the residence time of the wet air for moisture recovery whilst generating regions of recirculation of dry backflow for use in the venturi channels. This will also serve to establish a colder, drier inner core at the swirl generator, and the colder, drier flow will be redirected to the shroud of the system [5].

4. *Wake effect*: As a consequence of the redirection of the air stream, a wake will be established at the back of the device to improve and increase the pressure differential for the venturi flows. The phenomenon can produce sub-atmospheric pressures that can drive the incoming air at higher velocities for the movement of the flow [5].

5. *Resonance of standing wave*: Sound is essentially the propagation of waves that compress and expand air. Suppose a standing wave can be imposed in a system. In that case, compression effects could allow further contact between the microstructured surfaces and the flow while establishing nodes where condensed water can be recovered [5].
  
6. *Microstructured surfaces*. Enhanced microstructured surfaces will ensure high heat transfer from the moisture latent heat to the surface of the device instead of passing the energy to the drier air. The concept promotes the formation of micro-vortical tubes that, due to rotation, keep a continuous exchange of energy whilst just keeping a single point in contact with a solid surface. Research in this area demonstrated that specific surfaces increase heat transfer whilst reducing pressure losses and drag [35]. Additionally, microstructures can improve droplet nucleation and drainage by utilising the correct topographical modification, which increases heat transfer coefficients during condensation.

Considering the facilities and experience of the team at Cardiff University, this PhD research is specifically focused on enhancing heat transfer via microstructured surfaces for the HPPE recovery system, making the microstructure's geometry selection the main objective. Whereas the rest of the concepts will be investigated by other teams in the consortium. Foundations of heat transfer and fluids dynamics will be revised to determine the best path on the microstructure's geometry selection from their design to their manufacture, characterisation and evaluation.

## 2.2 Condensation Heat Transfer Theory

Understanding the mechanisms governing water condensation on surfaces is crucial to this project. In addition to the HPPE recovery system, this research has a wide range of applications that have significant social and environmental impacts, such as energy conversion, water harvesting, water desalination, thermal management systems, and environmental control [36].

Newton's law of cooling shows that condensation is a convection heat transfer process involving phase change in a fluid from vapour to liquid. Condensation occurs when the vapour temperature is reduced below its saturation temperature ( $T_{sat}$ ) due to the contact between the vapour and a solid surface whose temperature ( $T_s$ ) is lower than the  $T_{sat}$  of the vapour. It can also take place on the free surface of a liquid or gas when their temperature is below the  $T_{sat}$  of the vapour; in this case, the liquid droplets suspended in the gas form a fog. The condensation heat transfer coefficient ( $h$ ) is several times higher than those associated with other forms of convection heat transfer processes that involve only a single-phase due to the latent heat released by the substance as it is converted from vapour to liquid without changing its temperature [37,38]. The latent heat of vaporisation or condensation ( $h_{fg}$ ) represents the heat transfer per unit mass of condensate formed during condensation [37].

During condensation, the solid surface has two major roles: (1) it cools the vapour in contact with it so that it becomes supersaturated, and (2) it provides nucleation sites for droplets to form. Once condensation has started, it can continue at an exceedingly high rate, as long as the latent heat is carried away and the necessary vapour supply is maintained. Consequently, heat transfer is mainly limited by the rate at which the condensate can drain from the condensing surfaces. Condensate flows down on the surface under the influence of gravity and accumulates as a pool of ever-increasing thickness that insulates the surface. Since the thermal conductivity of liquids is lower than that of solids, the temperature gradient existing in the film represents a thermal resistance that reduces heat transfer by condensation because the heat flux must pass through this liquid before it can reach the surface. For this reason, in any process using condensation, arrangements must take place to remove the condensate as quickly as possible; otherwise, the surfaces will become waterlogged and ineffective [39]. There are different types of condensation, known as "filmwise" and "dropwise", that will be discussed in the next section with a recent term known as "Jumping-droplet condensation".



### 2.2.1 Heat and Momentum Transfer Relationship: Boundary Layers

According to Holman [40], the heat transfer coefficient can be determined by making measurements of the frictional drag on a plate under conditions in which no heat transfer is involved. For this reason, it is important to understand how momentum transfer takes place and the role of the drag force in the convection boundary layers. The velocity boundary layer  $\delta(x)$ , the thermal boundary layer  $\delta_t(x)$ , and the concentration boundary layer  $\delta_c(x)$  are convection boundary layers.

The velocity boundary layer is characterised by the presence of velocity gradient or shear stress, the thermal boundary layer by temperature gradient and heat transfer, while the concentration boundary layer is characterised by concentration gradient and species transfer. According to Rathakrishnan, for engineering applications, the key parameters associated with the velocity, thermal, and concentration boundary layers are the skin friction coefficient  $c_f$ , the heat transfer coefficient  $h$ , and the mass transfer convection coefficient  $h_m$ , respectively.

The velocity boundary layer will always exist because of the fluid flow viscosity and surface friction. Nonetheless, a thermal boundary layer and the associated heat transfer will prevail only when the plate surface and the freestream are at different temperatures. Similarly, a concentration boundary layer will only exist when the concentration of a species at the plate surface differs from its freestream concentration.

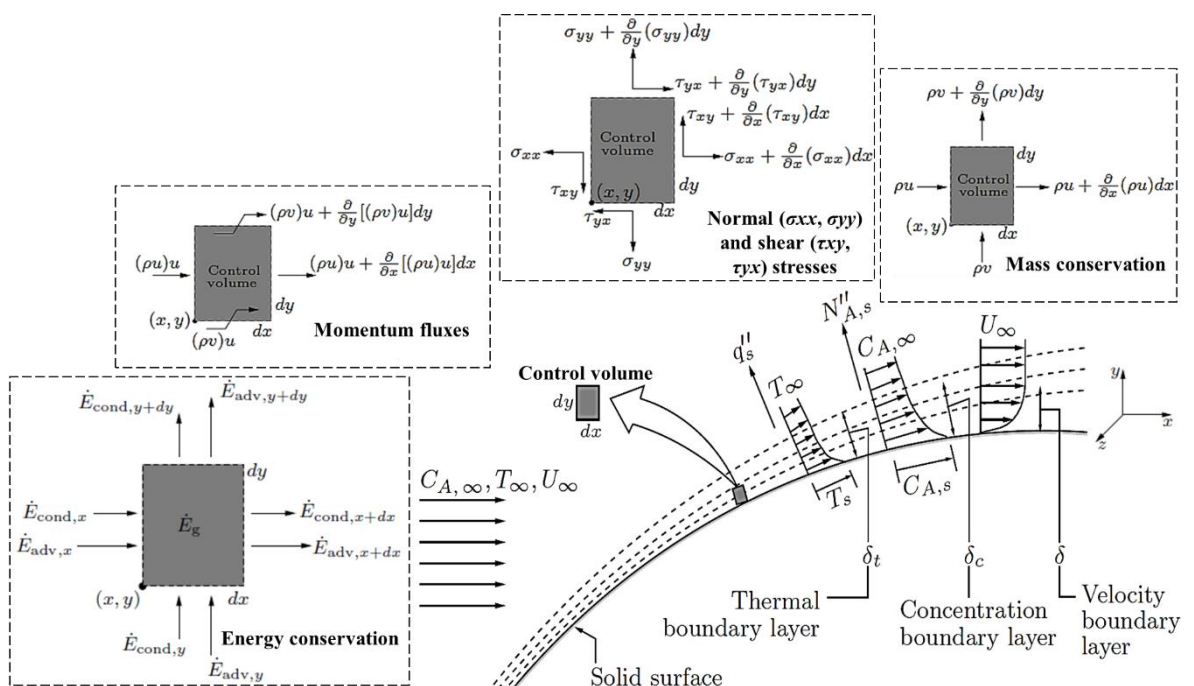


Figure 2.4. Development of velocity, thermal, and concentration boundary layers over a surface and differential control volume (dx.dy.1) analysis. Adaptation from [37].

Figure 2.4 shows the development of velocity, thermal, and concentration boundary layers over a solid surface when assuming a steady, two-dimensional flow with constant thermal conductivity. The mass conservation law or continuity equation applies to the velocity boundary layer and states that matter can neither be created nor destroyed. Thus, considering a differential control volume of length  $dx$ , height  $dy$ , depth unity and no mass generation or absorption inside, the mass flow into the control volume will be equal to the mass flow out of the control volume. This must be satisfied at every point in the velocity boundary layer, and it applies for a single species fluid, as well as for mixtures in which species diffusion and chemical reactions may be occurring [37]. A simplified version of the overall mass conservation requirement is:

$$\frac{\partial (\rho u)}{\partial x} + \frac{\partial (\rho v)}{\partial y} = 0 \quad (2.1)$$

Where

$u$  = velocity component in x-direction

$v$  = velocity component in y-direction

The second fundamental law that is valid for the velocity boundary layer is Newton's second law of motion or momentum conservation law. It states that the sum of all forces acting on the control volume must be equal to the net rate at which momentum leaves the control volume. There are two types of forces acting on the fluid in the boundary layer, body surfaces and surface forces. Gravitational, centrifugal, magnetic, and/or electric fields contribute to the total body force and are proportional to the volume. The surface forces result from the fluid's static pressure and viscous stress, which are proportional to the surface area.

At any location of the boundary layer, the viscous stress consists of two perpendicular components, normal stress  $\sigma_{ii}$  and shear stress  $\tau_{ij}$ . Each component has two subscripts, the first one is the orientation of the surface, and the second indicates the direction of the force component. Hence, the normal viscous stresses are tensile stresses, while the static pressure  $p$ , which originates from an external force acting on the control volume, is a compressive stress. Each of these stresses may change continuously along x- and y-directions. For this reason, Rathakrishnan used Taylor series expansion for the stresses and the net surface force, acting on the control volume along the x- and y-directions. A simplified equation for these steady and incompressible flows, considering Newton's second law (the change in momentum across the control volume is equal to the net force acting on the control volume and, the net force acting on the control volume is the sum of surfaces forces and body forces) and the continuity equation, are as follows:

$$\rho \left( u \frac{\partial u}{\partial x} + v \frac{\partial u}{\partial y} \right) = \frac{\partial}{\partial x} (\sigma_{xx}) + \frac{\partial \tau_{yx}}{\partial y} + X \quad (2.2)$$

$$\rho \left( u \frac{\partial v}{\partial x} + v \frac{\partial v}{\partial y} \right) = \frac{\partial \tau_{xy}}{\partial x} + \frac{\partial}{\partial y} (\sigma_{yy}) + Y \quad (2.3)$$

Where

$X$  = body force in the x-direction

$Y$  = body force in the y-direction

For the thermal boundary layer, the energy conservation principle accounts for the conservation of both mechanical and thermal energies. Rathakrishnan neglected the potential energy and combined the energy transport into the control volume via kinetic energy (advected by bulk motion), conduction, the work interaction involving body and surface forces and the energy generated within the control volume to express the energy conservation equation as follows [37]:

$$\begin{aligned} & - \frac{\partial}{\partial x} \left[ \rho u \left( e + \frac{V^2}{2} \right) \right] - \frac{\partial}{\partial y} \left[ \rho v \left( e + \frac{V^2}{2} \right) \right] + \frac{\partial}{\partial x} \left( k \frac{\partial T}{\partial x} \right) + \frac{\partial}{\partial y} \left( k \frac{\partial T}{\partial y} \right) + (Xu + Yv) - \frac{\partial}{\partial x} (pu) - \frac{\partial}{\partial y} (pv) + \\ & \frac{\partial}{\partial x} (\sigma_{xx}u + \tau_{xy}v) + \frac{\partial}{\partial y} (\tau_{yx}u + \sigma_{yy}v) + \dot{g} = 0 \end{aligned} \quad (2.4)$$

Where

$e$  = internal energy

$V^2/2$  = kinetic energy (advected)

$V^2 = u^2 + v^2$

$k$  = thermal conductivity (conduction)

$\dot{g}$  = the rate at which energy is generated per unit volume

Furthermore, the surface friction and the heat transfer rates strongly depend on the nature of the boundary layer. Therefore, it is essential to determine whether the boundary layer has a laminar or turbulent nature. The critical Reynolds number ( $Re_x$ ) is the value at which the flow transition from a laminar to a turbulent boundary layer. For external flows, it is known to vary from  $2 \times 10^5$  to  $3 \times 10^6$  depending on the surface roughness, the freestream's turbulence level, and the nature of the pressure variation along the surface [37].

$$Re_x = \frac{\rho_\infty U_\infty L}{\mu_l} \quad (2.5)$$

Where

$Re_x$  = critical Reynolds number

$\rho_\infty$  = freestream flow density

$U_\infty$  = freestream velocity of the flow

$\mu_l$  = viscosity of the fluid

$L$  = characteristic length (usually the distance from the leading edge) and can be substituted by diameter  $D$  when the analysis is on a pipe or high  $H$  when it is on a channel flow.

Additionally, from Figure 2.5, the outer edge of the velocity boundary layer is typically defined by  $u=0.99U_\infty$ ; thus, the boundary thickness is defined as  $\delta = \delta(x) = y_{(u=0.99U_\infty)}$  and by considering the volumetric flowrate, the displacement boundary thickness ( $\delta^*$ ) is defined as:

$$\delta^* = \int_0^\delta \left(1 - \frac{u}{U_\infty}\right) dy \tag{2.6}$$

While by considering the momentum flux, the momentum boundary thickness is defined as:

$$\theta = \int_0^\delta \frac{u}{U_\infty} \left(1 - \frac{u}{U_\infty}\right) dy \tag{2.7}$$

In laminar flow, there is no slip on the boundary; therefore, the velocity is zero, and the shear stress is defined as:

$$\tau = \mu \frac{\partial u}{\partial y} \tag{2.8}$$

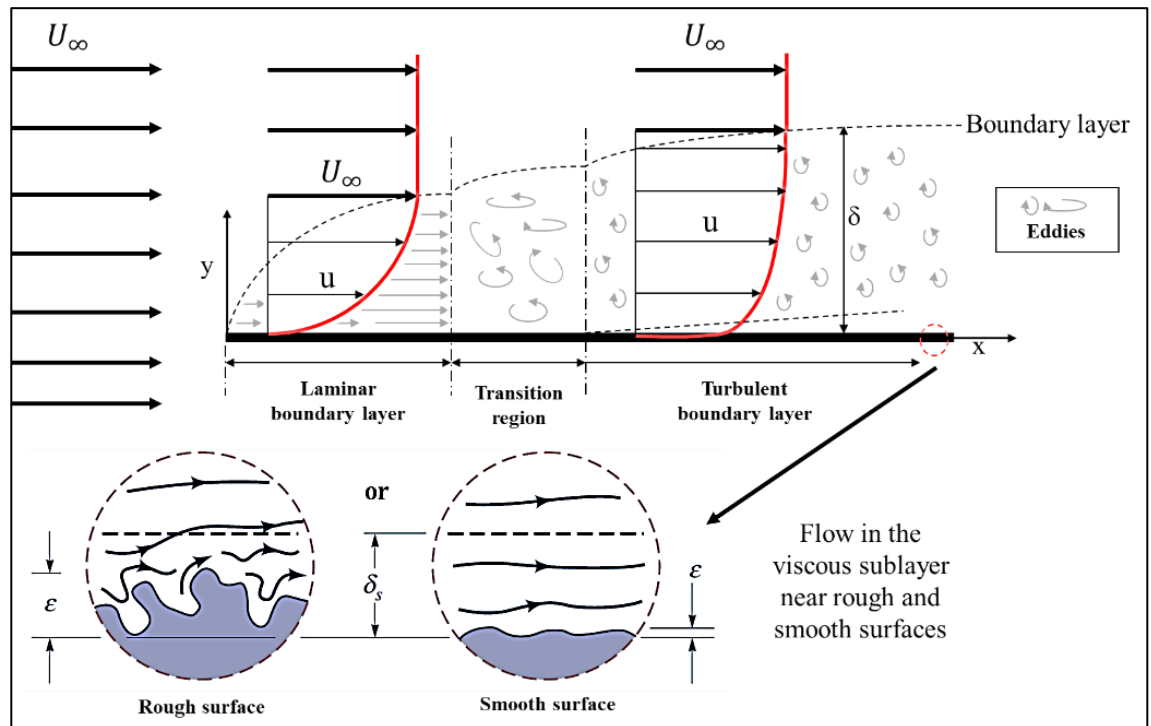


Figure 2.5. Transition from a laminar to a turbulent boundary layer and flow in viscous sublayer near rough and smooth surfaces. Adaptation from [41].

While in turbulent flow, the random motion of the fluid particles set the eddies up in the boundary layer, moving perpendicular to the surface and the mean flow direction, causing the fluid from the higher velocity areas to move into the slower velocity areas affecting the local velocity. This process is known as a momentum transfer phenomenon and can be represented as the shear stress acting on the fluid where the shear stress is greater in the turbulent flow than in the laminar flow:

$$\tau = \tau_{laminar} + \tau_{turbulent} \quad (2.9)$$

Where

$$\tau_{turbulent} = -\rho \overline{u'v'} \quad (2.10)$$

$u'$  = instantaneous velocity components that give rise to the eddies in the x-direction

$v'$  = instantaneous velocity components that give rise to the eddies in the y-direction

The turbulent shear stress, or Reynolds stress, can also be defined as:

$$\tau_{turbulent} = \varepsilon \frac{d\bar{u}}{dy} \quad (2.11)$$

Where

$\varepsilon$  = eddy viscosity

The eddy viscosity depends on the fluid and the flow conditions that change from one point to another, making difficult its use. Nevertheless, the German physicist Ludwig Prandtl proposed the Prandtl's Mixing Length Theory in 1904 to determine the values of the eddy viscosity. Prandtl selected two points within the turbulent boundary layer with a distance  $l$  between them, which is equivalent to the average size of the eddies or the mixing length and is dependent on the distance from the surface. Here  $u'$  is approximately equal to the difference in the mean velocities at the two points, and the positive fluctuation in the x-direction ( $u'$ ) causes a corresponding isotropic increase in the fluctuation in the y-direction ( $v'$ ). Therefore, the turbulent shear stress can be written as:

$$\tau_{turbulent} = \rho l^2 \left( \frac{d\bar{u}}{dy} \right)^2 \quad (2.12)$$

$\bar{u}$  = steady (mean) velocity component in the x-direction

Prandtl conceived the idea of the boundary layer as a thin region on the surface of a body in which viscous effects are significant and outside of which the fluid behaves essentially as if it were inviscid. Although the actual fluid viscosity is the same throughout, only the relative importance of the viscous effects (due to the velocity gradients) differs within or outside the boundary layer. This simplifies the analysis of large Reynolds number flows, thereby allowing a solution to external flow problems that are otherwise still unsolvable [41]. However, it was initially based on a constant of value  $\sim 0.4$ , which has now been proven to have different values that should be considered.

In 1908, Blasius solved the Navier-Stokes equations for steady 2D laminar, incompressible flows based on the simplifications introduced by Prandtl for a flow past a flat plate by using the following boundary conditions.

- The velocity at a large distance from the body is equal to the free stream velocity ( $u = U_\infty$  when  $y \rightarrow \infty$ )
- The velocity on a stationary surface is zero ( $u = v = 0$  when  $y = 0$ )

$$\frac{\partial u}{\partial x} + \frac{\partial v}{\partial y} = 0 \quad (2.13)$$

$$u \frac{\partial u}{\partial x} + v \frac{\partial u}{\partial y} = -\frac{1}{\rho} \frac{\partial p}{\partial x} + \nu \left[ \frac{\partial^2 u}{\partial x^2} + \frac{\partial^2 u}{\partial y^2} \right] \quad (2.14)$$

$$u \frac{\partial v}{\partial x} + v \frac{\partial v}{\partial y} = -\frac{1}{\rho} \frac{\partial p}{\partial y} + \nu \left[ \frac{\partial^2 v}{\partial x^2} + \frac{\partial^2 v}{\partial y^2} \right] \quad (2.15)$$

Because the boundary layers are very thin, the following approximations can be applied: the velocity component in the direction along the surface is much larger than the component of velocity normal to the surface (diffusion of momentum), and the velocity and temperature gradients are normal to the surface are much larger than the gradients along the surface the flow direction (diffusion of heat). Additionally, the normal stresses are negligible, and the conduction and the species diffusion rates in the y-direction are much larger than those in the x-direction [37]. Consequently, the governing equations can be simplified as follows:

Continuity equation:

$$\frac{\partial u}{\partial x} + \frac{\partial v}{\partial y} = 0 \quad (2.16)$$

x-momentum equation:

$$u \frac{\partial u}{\partial x} + v \frac{\partial u}{\partial y} = -\frac{1}{\rho} \frac{\partial p}{\partial x} + \nu \frac{\partial^2 u}{\partial y^2} \quad (2.17)$$

Where

$\nu$  = kinematic viscosity = momentum diffusivity =  $\mu / \rho$

y-momentum equation:

$$\frac{\partial p}{\partial y} = 0 \quad (2.18)$$

The static pressure in the freestream flow above the boundary layer does not vary through the boundary layer to the body's surface over which the boundary layer prevails. Thus, the static pressure  $p$  in the boundary layer depends only on  $x$  and is equal to the pressure in the freestream flow outside the boundary layer. The form of  $p(x)$ , which depends on the surface geometry, may then be obtained from a separate consideration of flow conditions in the freestream. Therefore, to simplify the energy equation, the pressure gradient should be treated as a known quantity, and  $\partial p / \partial x$  should be equal to  $dp/dx$ .

$$u \frac{\partial T}{\partial x} + v \frac{\partial T}{\partial y} = \alpha \frac{\partial^2 T}{\partial y^2} + \frac{\nu}{c_p} \left( \frac{\partial u}{\partial y} \right)^2 \quad (2.19)$$

Where

$\alpha = k / (\rho c_p)$  = thermal diffusivity

$c_p$  = specific heat capacity

These equations help identify key boundary layer similarity parameters and analogies between momentum and heat transfer. Rathakrishnan defined the following dimensionless variables as [37]:

Dimensionless length  $x$  (independent variable):

$$x^* = \frac{x}{L} \quad (2.20)$$

Dimensionless length  $y$  (independent variable):

$$y^* = \frac{y}{L} \quad (2.21)$$

Where

$L$  = characteristic length for the surface of interest

Dimensionless velocity component (dependent variable):

$$u^* = \frac{u}{u_\infty} \quad (2.22)$$

Dimensionless velocity component (dependent variable):

$$v^* = \frac{v}{U_\infty} \quad (2.23)$$

Where

$U_\infty$  = freestream flow velocity upstream of the surface.

Dimensionless temperature (dependent variable):

$$T_\theta = \frac{T - T_w}{T_\infty - T_w} \quad (2.24)$$

Where

$T_\infty$  = Temperature of the freestream flow

Dimensionless pressure (dependent variable):

$$p^* = \frac{p}{\frac{1}{2}\rho U_\infty^2} \quad (2.25)$$

Consequently, from the governing equations, the following dimensionless numbers are defined:

$$\text{Nusselt number} = Nu = \frac{hL}{k} \quad (2.26)$$

$$\text{Prandtl number} = Pr = \frac{\mu C_p}{k} = \frac{\nu}{\alpha} \quad (2.27)$$

Pr measures the relative effectiveness of momentum transport and energy transport by diffusion in the velocity (momentum) and thermal boundary layers, respectively. The energy and momentum transfers by diffusion are comparable for gases due to  $Pr \approx 1$ . For liquid metals,  $Pr \ll 1$ , so the energy diffusion rate greatly exceeds the momentum diffusion rate, while for oils, it is the opposite since  $Pr \gg 1$ . The value of Prandtl number Pr strongly influences the relative growth of the velocity and thermal boundary layers.

$$\text{Reynolds number} = Re = \frac{UL}{\nu} \quad (2.28)$$

Reynolds number is the ratio of inertia force to viscous force. For a differential control volume in a boundary layer, inertia forces are associated with the momentum flux of the fluid moving through the control volume.



$$\text{Stanton number} = St = \frac{h_x}{\rho C_p U_\infty} = \frac{Nu_x}{Re_x Pr} \quad (2.29)$$

St is a measure of the heat flux to the heat capacity of the fluid flow.

$$\text{Biot number} = Bi = \frac{hL}{k} \quad (2.30)$$

Bi, although similar in form to the Nusselt number, the k in Bi is the thermal conductivity of the solid.

$$\text{Eckert number} = Ec = \frac{U^2}{C_p \Delta T} \quad (2.31)$$

Ec provides a measure of the flow's kinetic energy relative to the enthalpy difference across the thermal boundary layer. It plays an essential role in high-speed flows for which viscous dissipation is substantial.

$$\text{Grashof number} = Gr = \frac{g\beta L^3 \Delta T}{\nu^2} \quad (2.32)$$

Where

$$\text{Volumetric thermal expansion coefficient} = \beta = -\frac{1}{\rho} \left( \frac{\partial \rho}{\partial T} \right)_p \quad (2.33)$$

Gr provides a measure of the ratio of buoyancy force to viscous force in the boundary layer. Its role in free convection is much the same as that of the Reynolds number in forced convection.

In order to relate momentum with heat transfer, two boundary layer scenarios can be analysed. In the first scenario, the viscous effects can be neglected since they are far smaller than the inertia effect when the region is very thin, and the Re number is very high. With this premise, the momentum boundary layer thickness ( $\delta$ ) and the thickness of the thermal boundary layer ( $\delta_t$ ) can be described and related in the following way [37]:

$$\frac{\delta}{L} \sim \frac{1}{\sqrt{Re_L}} \quad (2.34)$$

$$\frac{\delta_t}{L} \sim \frac{1}{(Re_L Pr)^{\frac{1}{2}}} \quad (2.35)$$

$$\frac{\delta_t}{\delta} = \frac{1}{(Pr)^{\frac{1}{2}}} = \sqrt{\frac{\alpha}{\nu}} \quad (2.36)$$

Additionally, The Reynolds analogy describes the following relation of Nu number and St number with skin friction coefficient ( $c_f$ ) for the boundary layer analysis when there is no pressure gradient and  $Pr = 1$ .

$$Nu_x = \frac{1}{2} Re_x c_f \quad (2.37)$$

As well:

$$\frac{\text{heat flux to wall}}{\text{convected heat flux}} = \frac{\text{momentum flux to wall}}{\text{convected momentum flux}}$$

On the other hand, the second scenario seeks an expression whereby the frictional resistance can be directly related to heat transfer. Here, the shear stress at the wall ( $\tau_w$ ) can be expressed in terms of a friction coefficient  $c_f$ :

$$\tau_w = c_f \frac{\rho U_\infty^2}{2} \quad (2.38)$$

This is the defining equation for the friction coefficient; additionally, the shear stress can also be calculated from the following relation [40]:

$$\tau_w = \mu \left( \frac{\partial u}{\partial y} \right)_{y=0} = \frac{3}{2} \frac{\mu U_\infty}{\delta} = \frac{3}{2} \frac{\mu U_\infty}{4.64} \left( \frac{U_\infty}{\nu x} \right)^{\frac{1}{2}} \quad (2.39)$$

Which leads to the exact solution of the boundary-layer equations yields:

$$\frac{c_{fx}}{2} = \frac{3}{2} \frac{\mu U_\infty}{4.64} \left( \frac{U_\infty}{\nu x} \right)^{\frac{1}{2}} \frac{1}{\rho U_\infty^2} = 0.323 Re_x^{-\frac{1}{2}} \quad (2.40)$$

Substituting this into the Stanton number:

$$St_x = \frac{Nu_x}{Re_x Pr} = \frac{h_x}{\rho c_P U_\infty} = 0.332 Pr^{-\frac{2}{3}} Re_x^{-\frac{1}{2}} \quad (2.41)$$

And regrouping into:

$$St_x Pr^{\frac{2}{3}} = 0.332 Re_x^{-\frac{1}{2}} = \frac{c_{fx}}{2} \quad (2.42)$$

The Reynolds-Colburn analogy is obtained, which expresses the relation between fluid friction and heat transfer for laminar flow on a flat plate when  $dp/dx \sim 0$  or turbulent flows without restriction on  $dp/dx$ .

This analogy is helpful to understand the physical processes in convection heat transfer processes and reinforce the notion that heat transfer and viscous-transport processes are related at both the microscopic and macroscopic levels [40]. In addition, the Blassius solution can relate the local (skin) friction coefficient,  $c_f$  (based on local shear stress).

$$c_f = \frac{\tau_w}{\rho U_\infty^2 / 2} \quad (2.43)$$

With Reynolds numbers:

$$c_f = \frac{0.664}{\sqrt{Re_x}} \quad (2.44)$$

And the friction drag coefficient,  $c_F$  (based on drag force)

$$c_F = \frac{D}{\rho U_\infty^2 bL / 2} \quad (2.45)$$

Where

$D$  = drag force

$b$  = width of the plate

With Reynolds numbers:

$$c_F = \frac{1.328}{\sqrt{Re_L}} \quad (2.46)$$

Due to the changes in the velocity and thermal boundary layers in the flow direction, the local friction and heat transfer coefficients vary along the surface of the plate. The local values of heat transfer and friction coefficients can be calculated to obtain the heat flux and drag force at a certain location. At the same time, their integral form can be used to determine the values for the entire surface area [37]. Then, the heat transfer rate  $\dot{Q}$  can be obtained as discussed in the condensation heat transfer section, and the drag or friction force  $D$  on the entire surface of the plate (wetted area), considering the momentum equation in the x-direction can be obtained as follows:

Drag force on plate ( $-D$ ) = momentum out – momentum in

$$-D = \rho_\infty b \int_0^h u^2 dy - \rho_\infty b U_\infty^2 h \quad (2.47)$$

Where

$h$  = height =  $\delta$  = boundary thickness

But the mass flowrate in must equal the mass flowrate out:

$$\rho_{\infty} b h U_{\infty} = \rho_{\infty} b \int_0^h u \, dy \quad (2.48)$$

Therefore:

$$D = \rho_{\infty} b \int_0^h u (U_{\infty} - u) \, dy = \rho_{\infty} b U_{\infty}^2 \int_0^h \frac{u}{U_{\infty}} \left(1 - \frac{u}{U_{\infty}}\right) \, dy \quad (2.49)$$

Or in terms of the friction coefficient (Holman, 2010):

$$D = \frac{1}{2} \rho_{\infty} U_{\infty}^2 A_s c_f \quad (2.50)$$

Where

$A_s$  = surface area

### 2.2.2 Nusselt's Theory

The filmwise condensation model for vapour on a vertical plate is shown in Figure 2.6. The following analysis of Nusselt's Theory is based on the work of several authors [37,38,40]. Considering this coordinate system, the assumptions made by Nusselt are as follow: a linear temperature distribution exists between the wall and vapour conditions. The vertical surface is kept at a uniform temperature ( $T_s$ ), the temperature of the condensate is  $T_{sat}$  at the interface and decreases gradually to  $T_s$  at the plate wall, the vapour temperature at the edge of the film is at the saturation temperature  $T_{sat}$  and the vapour temperature away from the liquid-vapour interface is  $T_v$ . For condensation to take place, the wall temperature must be less than the saturation temperature of the vapour ( $T_s < T_{sat}$ ). The flow of condensate takes place under gravity in the x-direction.

The film thickness  $\delta$  is seen to be zero at the top of the wall and increases with distance in the flow direction because of continued condensation at the liquid-vapour interface. The vapour's drag force on the condensate's motion is minimal; thus, the viscous shear of the vapour is negligible at  $y = \delta$ . The velocity of the condensate is zero at the wall because of the "no-slip" condition and reaches a maximum at the liquid-vapour interface. Fluid properties are constant, and heat transfer across the liquid film is by pure conduction. By Newton's second law, the force component acting on the volume element in the flow direction ( $x$ ) shown in Figure 2.6 can be written as:

$$\sum F_x = m a_x = 0 \quad (2.51)$$

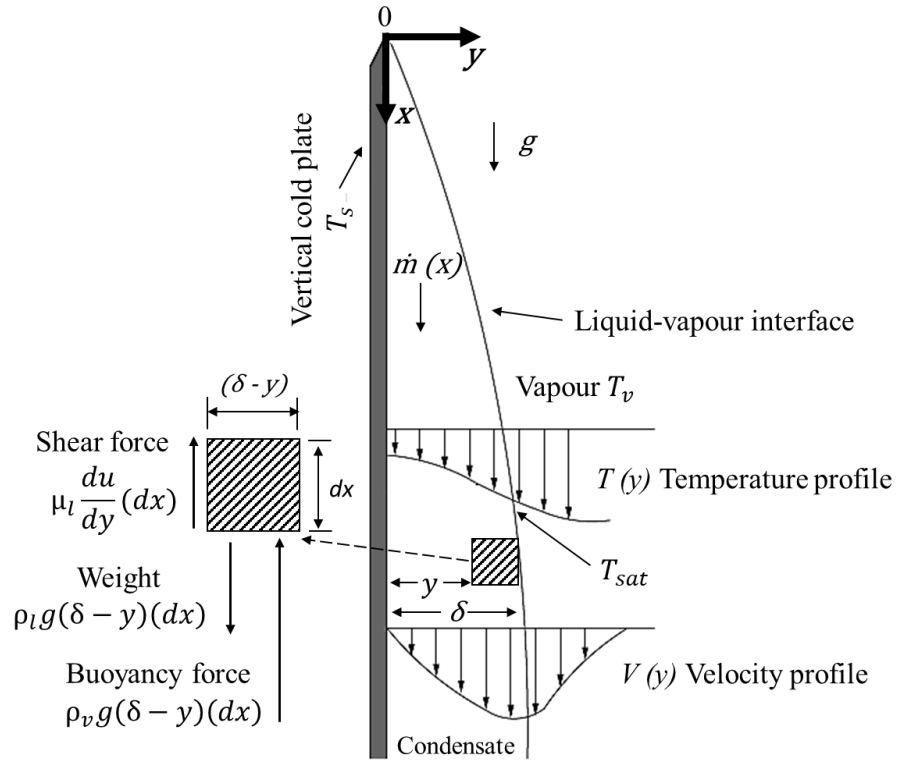


Figure 2.6. Filmwise condensation on a vertical plate. Adaptation from [37,38,40].

Since flow acceleration ( $a_x$ ) in the condensate layer is very small, it can be neglected. Therefore, the only force acting downward is the weight of the fluid element ( $m$ ) of thickness  $dx$  between  $y$  and  $\delta$ , and the forces acting upward are the viscous shear force at  $y$  and the buoyancy force due to the displaced vapour. Weight = Viscous shear force + Buoyancy force

$$\rho_l g (\delta - y) (dx) = \mu_l \frac{du}{dy} (dx) + \rho_v g (\delta - y) (dx) \quad (2.52)$$

Where

$\rho_l$  = density of the liquid

$g$  = gravitational acceleration

$\delta$  = film thickness

$\mu_l$  = viscosity of the liquid

$\rho_v$  = density of the vapour

$u$  = velocity

By reducing and integrating using the boundary condition  $u = 0$  at  $y = 0$ , the velocity gets defined as:

$$u = \frac{(\rho_l - \rho_v)g}{\mu_l} \left( \delta y - \frac{1}{2} y^2 \right) \quad (2.53)$$

The mass flow of condensate through any  $x$  position of the film is given by:

$$\dot{m}(x) = \int_0^\delta \rho_l \left[ \frac{(\rho_l - \rho_v)g}{\mu_l} \left( \delta y - \frac{1}{2} y^2 \right) \right] dy = \frac{\rho_l(\rho_l - \rho_v)g\delta^3}{3\mu_l} \quad (2.54)$$

This represents the rate of condensation of vapour over a vertical length  $dx$ . The heat transfer rate from the vapour to the plate through the liquid film equals the heat released by the vapour during condensation. Therefore, the heat transfer rate  $\dot{Q}$  becomes:

$$d\dot{Q} = d\dot{m} h_{fg} = k_l(dx) \frac{T_{sat} - T_s}{\delta} \quad (2.55)$$

Or

$$\frac{d\dot{m}}{dx} = \frac{k_l}{h_{fg}} \frac{T_{sat} - T_s}{\delta} \quad (2.56)$$

Where

$h_{fg}$  = latent heat of vaporisation/ condensation

$k_l$  = thermal conductivity of the liquid film

From the  $\frac{d\dot{m}}{dx}$  equations, the liquid film thickness at any location  $x$  can be determined:

$$\delta^3 d\delta = \frac{\mu_l k_l (T_{sat} - T_s)}{\rho_l (\rho_l - \rho_v) g h_{fg}} dx \quad (2.57)$$

Integrating from  $x = 0$  to  $x = x$ , the liquid film thickness at any location  $x$  is:

$$\delta(x) = \left[ \frac{4\mu_l k_l (T_{sat} - T_s) x}{\rho_l (\rho_l - \rho_v) g h_{fg}} \right]^{1/4} \quad (2.58)$$

The heat transfer rate from the vapour to the plate, at a location  $x$ , can be expressed as:

$$\dot{Q}_x = h_x (T_{sat} - T_s) = k_l \frac{T_{sat} - T_s}{\delta} \quad (2.59)$$

Thus, the heat transfer coefficient, at a location  $x$ , is defined as:

$$h_x = \frac{k_l}{\delta x} \quad (2.60)$$

So, the local convection heat transfer is expressed as:

$$h_x = \left[ \frac{\rho_l (\rho_l - \rho_v) g h_{fg} k_l^3}{4\mu_l x (T_{sat} - T_s)} \right]^{1/4} \quad (2.61)$$

Expressed in a dimensionless form in terms of the Nusselt number, this is:

$$Nu_x = \frac{hx}{k_l} = \left[ \frac{\rho_l(\rho_l - \rho_v)gh_{fg}x^3}{4\mu_l k(T_{sat} - \bar{T}_s)} \right]^{1/4} \quad (2.62)$$

The average value of the heat-transfer coefficient is obtained by integrating over the length of the plate (L):

$$\bar{h} = \frac{1}{L} \int_0^L h_x dx = \frac{4}{3} h_{x=L} \quad (2.63)$$

It is important to note that this expression will underestimate the heat transfer because it does not consider the effects of the nonlinear temperature profile in the condensate film and the cooling of the liquid down to an average temperature between  $T_{sat}$  and  $T_s$ . As a result, the actual heat transfer will be larger than the theoretical value. Both these effects can be accounted for by replacing  $h_{fg}$  with the modified latent heat  $h^*_{fg}$ .

$$h^*_{fg} = h_{fg} + 0.68c_{pl}(T_{sat} - T_s) \quad (2.64)$$

Where

$c_{pl}$  = specific heat capacity of the liquid at the average film temperature

Now, considering that superheated vapour enters the condenser at a temperature  $T_v$ , it must be first cooled to  $T_{sat}$  before it can condense, and the removed heat must also be transferred to the wall. The amount of heat released as a unit mass of superheated vapour when is cooled from  $T_v$  to  $T_{sat}$  is  $c_{pv}(T_v - T_{sat})$ , where  $c_{pv}$  is the specific heat of vapour at the average film temperature  $T_f = \frac{T_{sat} + T_s}{2}$ . The modified latent heat in this case becomes:

$$h^*_{fg} = h_{fg} + 0.68c_{pl}(T_{sat} - T_s) + c_{pv}(T_v - T_{sat}) \quad (2.65)$$

These laminar condensation equations match experimental data very well as long as the film remains smooth and well behaved. In practice, it has been found that waves will develop in the film for Reynolds numbers as low as 30 or 40. When this occurs, the experimental values of  $\bar{h}$  can be 20% higher, according to experiments conducted by McAdams [42]. Because this is such a common occurrence, a 20% increase should be included for design purposes. McAdams recommended the following equations for a vertical surface:

$$\bar{h} = 1.13 \left[ \frac{\rho_l(\rho_l - \rho_v)gh_{fg}k_l^3}{\mu_l(T_{sat} - T_s)L} \right]^{1/4} \quad (2.66)$$

### 2.2.3 Flow Regimes

When a plate on which condensation occurs is sufficiently large, or there is a sufficient amount of condensate flow, turbulence may appear in the condensate film. In the case of forced convection, heat transfer in condensation depends on the laminar or turbulent nature of the flow, as turbulence results in higher heat transfer rates. The criterion for determining whether the flow is laminar or turbulent is the Reynolds number, and for the condensate flow is defined as:

$$Re = \frac{D_h \rho_l \bar{V}_l}{\mu_l} = \frac{4A_c \rho_l \bar{V}_l}{P \mu_l} = \frac{4 \rho_l \bar{V}_l \delta}{\mu_l} \quad (2.67)$$

Where

$D_h = 4A_c/P = 4\delta$  = hydraulic diameter of the condensate flow

$A_c = P\delta$  = cross-sectional area of the condensate flow at the lowest part of the flow

$P$  = wetted perimeter of the condensate

$\delta$  = film thickness

$\rho_l$  = density of the liquid

$\mu_l$  = viscosity of the liquid

$\bar{V}_l$  = average velocity of the condensate at the lowest part of the flow

The heat transfer can be defined as:

$$\dot{Q} = hA(T_{sat} - T_s) = \dot{m}h^*_{fg} \quad (2.68)$$

Where

$h$  = heat transfer coefficient

$A$  = surface area on which the condensate occurs

$\dot{m} = \rho_l A \bar{V}_l$  = mass flow rate of the condensate at the lowest part

The mass flow becomes:

$$\dot{m} = \rho_l A \bar{V}_l = \frac{\dot{Q}}{h^*_{fg}} \quad (2.69)$$

Therefore

$$\bar{V}_l = \frac{\dot{Q}}{\rho_l A h^*_{fg}} = \frac{hA(T_{sat} - T_s)}{\rho_l A h^*_{fg}} \quad (2.70)$$

Substituting this into the Reynolds number equation:

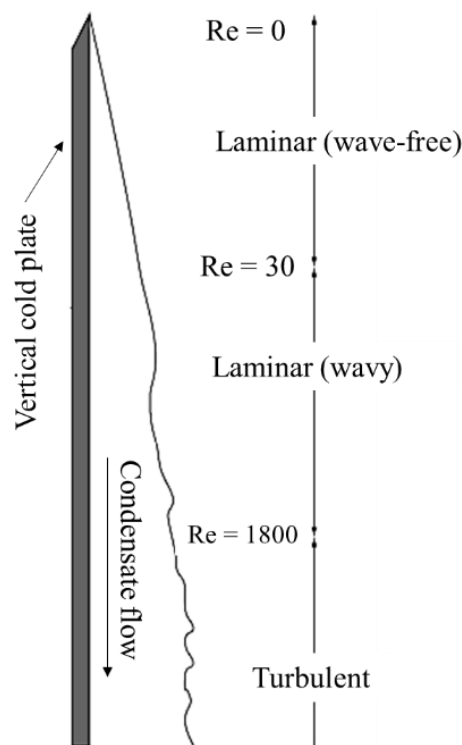
$$Re = \frac{4 \rho_l \delta hA(T_{sat} - T_s)}{\mu_l \rho_l A h^*_{fg}} = \frac{4 hA(T_{sat} - T_s) \delta}{\mu_l h^*_{fg} A} \quad (2.71)$$



Considering that  $\frac{\delta}{A} = \frac{1}{P}$

$$Re = \frac{4\dot{Q}_{condensation}}{P\mu_l h^*_{fg}} = \frac{4Ah(T_{sat}-T_s)}{P\mu_l h^*_{fg}} \quad (2.72)$$

The Reynolds number of the condensate flow increases in the flow direction. Because of this, the flow of liquid film exhibits different regimes, depending on the value of the Reynolds number. The outer surface of the liquid film will remain laminar and wave-free for  $Re \leq 30$ . For Reynolds number more than 30, waves appear on the free surface of the condensate, and the condensate flow becomes fully turbulent for Reynolds number about 1800 (Figure 2.7). The condensate flow is a mixture of laminar and turbulent flows in the Reynolds number range from 450 to 1800 [37].

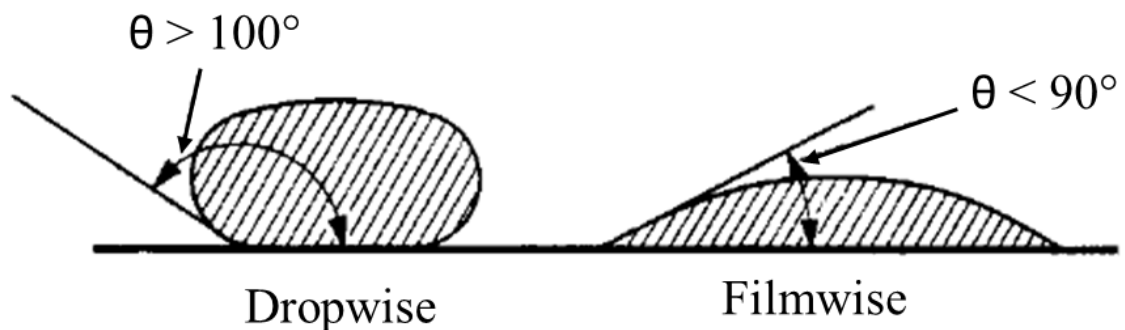


**Figure 2.7. Flow regimes for film condensation on a vertical plate. Adaptation from [37].**

Based on Nusselt's theory, flow condensation heat transfer correlations were developed for each regime. When Reynolds numbers are less than 30, the results are in agreement with experimental data, as long as properties of the liquid are evaluated at the film temperature ( $T_f$ ), and the  $h_{fg}$  and  $\rho_v$  are evaluated at  $T_{sat}$ . For Reynolds numbers between 30 and 1800, the interface at the liquid-vapour is wavy even though the flow in the liquid film is laminar. This flow is termed wavy laminar. Even though the waves at the liquid-vapour interface increase the heat transfer, they make it difficult to obtain analytical solutions for the heat transfer associated with the flow. Due to its wavy nature, the increase in heat transfer is usually about 20%, but it can exceed even 50% under certain conditions. The Reynolds number strongly influences the enhancement of heat transfer [43,44].

## 2.3 Types of Condensation

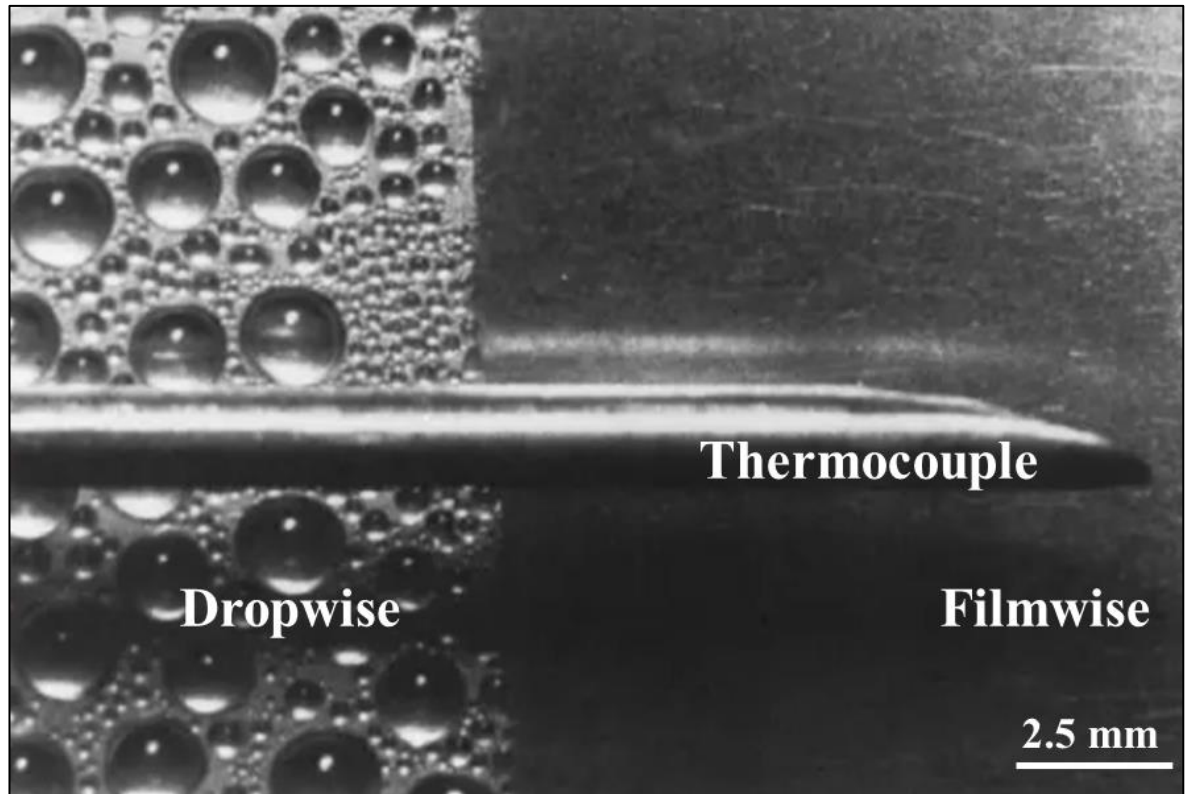
According to Ede [39], the study of heat transfer by condensation primarily focuses on the behaviour and effect of the liquid produced. This depends on the shape and size of the solid surface or nucleation sites; for example, condensate will drain more effectively from a horizontal tube than from the lower part of a tall vertical tube, which will be covered with a stream of liquid that has condensed higher up. The drainage rate also depends on the type of condensation, which is determined by the angle of contact between the condensate and the solid surface (Figure 2.8). If the angle ( $\theta$ ) is small, the liquid wets the surface and spreads out into a continuous layer or film. If the angle is more than  $100^\circ$ , the liquid does not spread out over the surface but draws together into small droplets. These types of condensation are known as "filmwise" and "dropwise", respectively [39].



**Figure 2.8. Dropwise condensation with a large droplet contact angle and filmwise condensation with a small droplet contact angle. Adaptation from [39].**

A clean and uncontaminated surface promotes filmwise condensation (FWC), in which the condensate wets the surface and forms a liquid film on the surface that slides down under the influence of gravity. The thickness of the liquid film increases in the flow direction as more vapour condenses on the film. The temperature gradient existing in the liquid film between the solid surface and the vapour serves as a resistance to heat transfer.

On the other hand, in dropwise condensation (DWC), a large portion of the area of the plate is directly exposed to the vapour; there is no film barrier to heat flow, leading to higher heat-transfer rates. In fact, heat transfer rates in dropwise condensation are nearly ten times higher than in filmwise condensation; for this reason, dropwise is preferred over filmwise condensation [37,38,40]. Figure 2.9 exemplifies steam dropwise condensation (left) and filmwise condensation (right) on a copper plate. The left side has a cupric oleate coating, while the plate's right side is clean copper where steam condenses as a continuous film. In this study by Professor J. W. Westwater (University of Illinois, Urbana), a 1.7 mm diameter thermocouple was used for temperature measurements. The final heat-transfer coefficient for the dropwise condensation was approximately seven times higher than for the filmwise condensation [40].



**Figure 2.9. Dropwise condensation and filmwise condensation on a copper plate. Photographs by Professor J. W. Westwater, University of Illinois, Urbana. Adaptation from [40].**

Nonetheless, dropwise condensation is difficult to maintain since most surfaces become wetted after exposure to a condensing vapour over an extended period of time. Numerous surface coatings and vapour additives have been used in attempts to maintain dropwise condensation for a more extended period of time, but they have not entirely succeeded [40]. Consequently, practical design methods are based on filmwise condensation. Initial studies on the heat transfer coefficient for filmwise condensation on a flat plate and a circular tube were conducted by Nusselt in 1916 [38].

### 2.3.1 Filmwise Condensation

The velocity relation developed for vertical plate (Nusselt's Theory) can also be used for laminar film condensation on the upper surfaces of plates that are inclined at an angle  $\theta \leq 60^\circ$  by replacing  $g$  in the equation by  $g \cos \theta$  [37].

$$\bar{h}_{inclined} = \bar{h}_{vertical} (\cos \theta)^{1/4} \quad (2.73)$$

Based on Nusselt's theory, Cengel [45] developed the average heat transfer coefficient for film condensation on the outer surface of a horizontal tube:

$$\bar{h}_{horizontal} = 0.729 \left[ \frac{\rho_l(\rho_l - \rho_v) g h_{fg}^* k_l^3}{D \mu_l (T_{sat} - T_s)} \right]^{1/4} \quad (2.74)$$

Where

$D$  = diameter of the tube

Thus, the correlation between the heat transfer for a vertical tube and horizontal tube can be defined as follows:

$$\frac{\bar{h}_{vertical}}{\bar{h}_{horizontal}} = 1.294 \left( \frac{D}{L} \right)^{1/4} \quad (2.75)$$

The analysis of condensation inside a horizontal tube (Figure 2.10) becomes difficult as it is influenced by the vapour velocity and the rate of liquid accumulation on the walls of the tube. For low vapour velocities, the following expression for condensation can be used to calculate the heat transfer coefficient [37,45].

$$\bar{h}_{internal} = 0.555 \left[ \frac{\rho_l(\rho_l - \rho_v) g k_l^3}{\mu_l (T_{sat} - T_s)} \left( h_{fg} + \frac{3}{8} c_{pl} (T_{sat} - T_s) \right) \right]^{1/4} \quad (2.76)$$

When

$$Re_{vapour} = \left( \frac{\rho_v V_v D}{\mu_v} \right)_{inlet} < 35,000 \quad (2.77)$$

Where

$\rho_v$  = density of the vapour

$V_v$  = velocity of the vapour

$D$  = inner diameter of the tube

$\mu_v$  = viscosity of the vapour

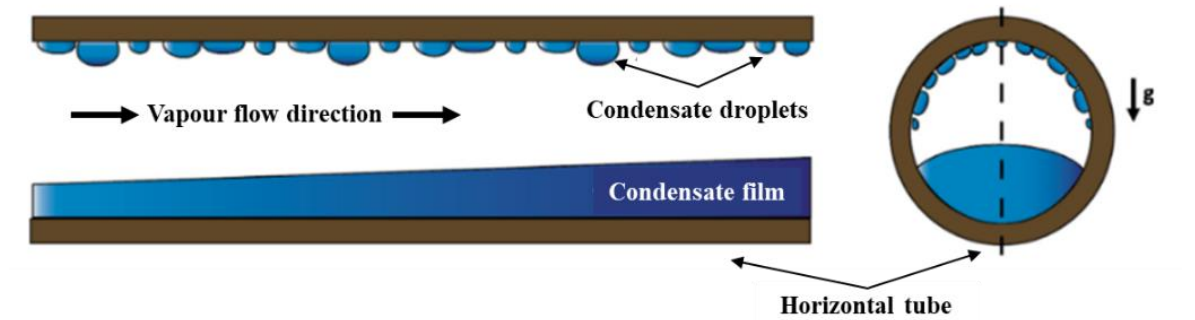


Figure 2.10. Condensate flow in a horizontal tube. Adaptation from [37,46].

More recently, Peng et al. [47] were able to compare theoretical and experimental results (Figure 2.11) by using the following equation for a circular condensing surface:

$$\bar{h}_{circular} = 0.83404 \left[ \frac{\rho_l(\rho_l - \rho_v)gh^*_{fg}k_l^3}{R\mu_l(T_{sat} - T_s)} \right]^{1/4} \quad (2.78)$$

Where

R = radius of the circular condensing surface

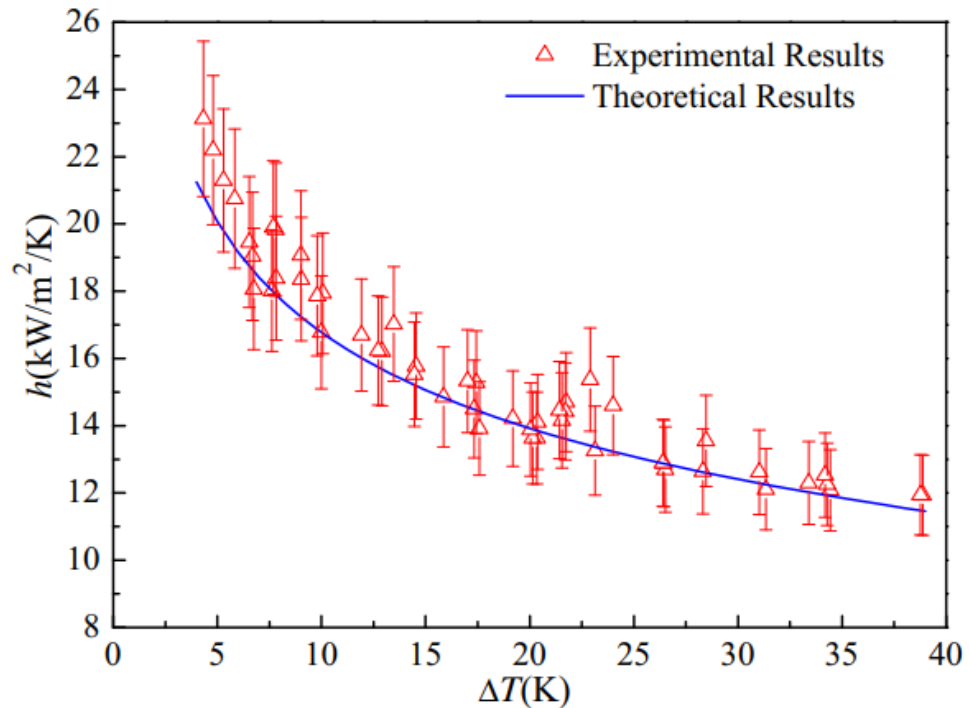


Figure 2.11. Comparison of experimental results and theoretical results of filmwise condensation heat transfer coefficients [47].

Additionally, Tokunaga & Tsuruta [48] used a Nusselt equation to process their data:

$$Nu_x = 0.45 \left[ 1.20 + \frac{Pr_L h_{fg}}{c_{p_l}(T_v - T_s)} \left( \frac{\rho_v \mu_v}{\rho_l \mu_l} \right)^{1/2} \right]^{1/4} (Re_x L)^{1/2} \quad (2.79)$$

Finally, the heat transfer coefficient significantly decreases in the presence of non-condensable gases. Even if they only represent 1% of the total volume, the coefficient can decrease between 30% and 50% and be much larger in dropwise condensation [38,39].

### 2.3.2 Dropwise Condensation

Dropwise condensation is one of the most effective heat transfer mechanisms; it is the process in which condensed vapour forms droplets of different diameters on the surface instead of a continuous liquid film. The droplets slide down when they reach a specific size, clearing the surface and exposing it to vapour, thus no liquid film, in this case, to resist heat transfer as in the case of film condensation. Because of this, the heat transfer coefficient achieved with dropwise condensation can be as high as ten times of what is associated with film condensation. However, sustaining the dropwise condensation for prolonged periods of time is not easy as it usually gets converted to a mix of dropwise/filmwise condensation or even entirely to film condensation within time, representing a challenge in designing a device for dropwise condensation [37,38]. For this reason, condensate droplets must be rapidly removed from the surface because the increasing droplet size acts as a thermal barrier. According to Miljkovic et al. [49], for traditional dropwise condensing surfaces, droplet removal typically relies on gravity, where droplet sizes must approach the capillary length ( $\approx 2.7$  mm for water) to overcome the contact line pinning force.

One of the most widely utilised systems that exhibit dropwise condensation is copper tubes carrying steam. However, when the condensing surface is made of poor thermal material, or when the thermal resistance on the other side of the surface is too large, the large heat transfer coefficient achievable with dropwise condensation is of no significance [37]. Consequently, Rathakrishnan [37] proposed a simple correlation for dropwise condensation of steam at a saturation temperature  $T_{sat}$  in the range from 22°C to 100°C:

$$\bar{h}_{dropwise} = 51,140 + 2,044 T_{sat} \quad (2.80)$$

Additionally, a simple correlation for heat flux ( $\text{kW/m}^2$ ) as a function of the absolute thermodynamic temperature (Kelvin) and the temperature difference between vapour and surface was developed using experimental data for vertical plates at various temperatures and pressures; it can also be used for DWC on horizontal tubes with maximum underestimation of 20% [50,51]:

$$q = (T_v - 273.15)^{0.8} * [5\Delta T + 0.3\Delta T^2] \quad (2.81)$$

### 2.3.3 Jumping-droplet Condensation

When two droplets coalesce ( $\sim 10 - 100 \mu\text{m}$ ), the released surface energy powers up the merged droplet to spontaneously self-propelled away from the condensing surface regardless of the gravity. This phenomenon, associated with condensation on superhydrophobic (low adhesion) surfaces, is known as droplet jumping. The superhydrophobic structured surface's role is to reduce the droplet adhesion to the surface by minimising the contact and breaking the symmetry of the coalesced droplet, resulting in the droplet accelerating and jumping out of the surface [49]. If superhydrophobic structured surfaces are appropriately designed, they can not only allow for easy droplet removal at micrometric length scales during condensation but also promise to enhance heat transfer performance and improve anti-dew and anti-icing surface properties [36,49,52].

According to Enright et al. [36], this phenomenon was first reported by Kollera and Grigull when experimenting with mercury dropwise condensation on rough steel surfaces. Miljkovic et al. [49] manufactured silanised copper oxide surfaces to promote jumping-droplet condensation, achieving 25% higher overall heat flux and 30% higher condensation heat transfer coefficient when compared to hydrophobic condensing surfaces at supersaturation. Figure 2.12 shows filmwise condensation on a smooth hydrophilic copper tube (a), dropwise condensation on a silane coated smooth copper tube (b), jumping-droplet superhydrophobic condensation on a nanostructured CuO tube and magnified view of the jumping phenomena (scale bar  $500 \mu\text{m}$ ) (c), and flooded condensation on a nanostructured CuO tube (d); for each case, the tube dimensions were with a chamber vapour pressure of  $2700 \pm 68 \text{ Pa}$  [49].

Another study showed a further enhancement of a heat transfer of 30% compared to classical dropwise condensation due to a larger population of micro-droplets that more efficiently transfer heat to the surface [52]. Additionally, a study on superhydrophobic surfaces provided a 30% higher heat transfer coefficient ( $92 \pm 12 \text{ kW/m}^2 \text{ K}$ ) when compared with dropwise condensation on the smooth Cu tube [53]. Figure 2.13 compares dropwise condensation and jumping-droplet condensation in terms of heat flux and temperature differential.

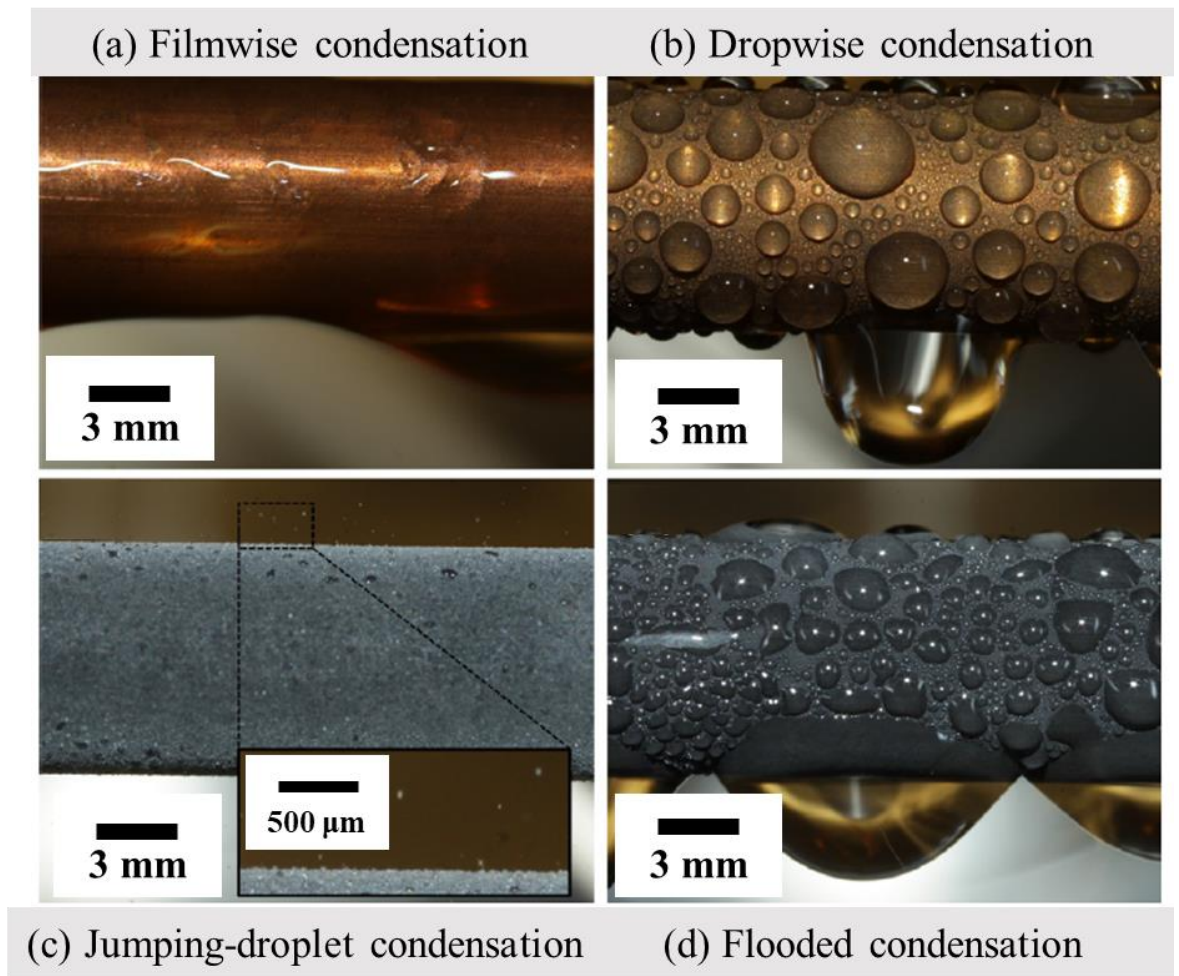


Figure 2.12. Experimental results from the study “Jumping-droplet-enhanced condensation on scalable superhydrophobic nanostructured surfaces” [49].

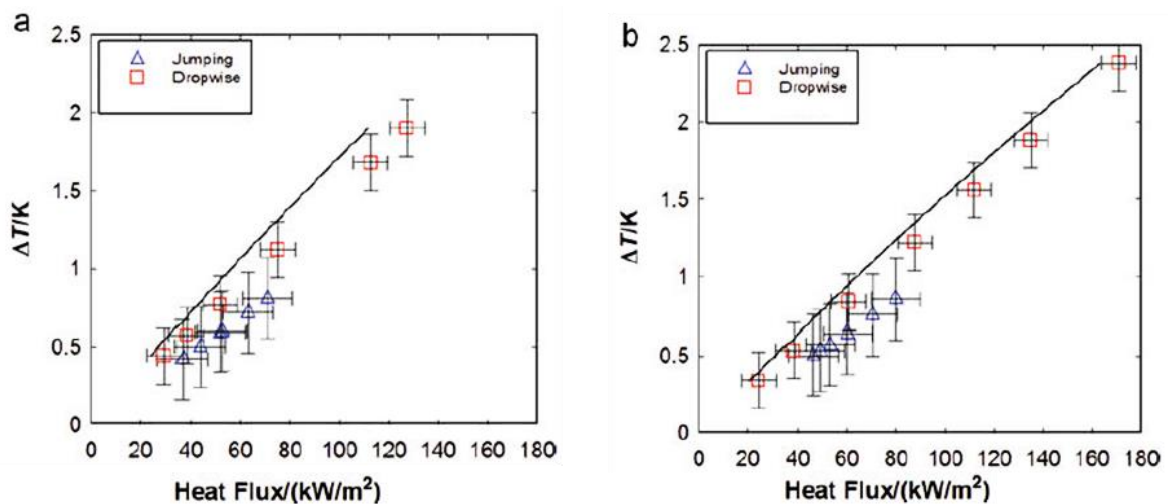
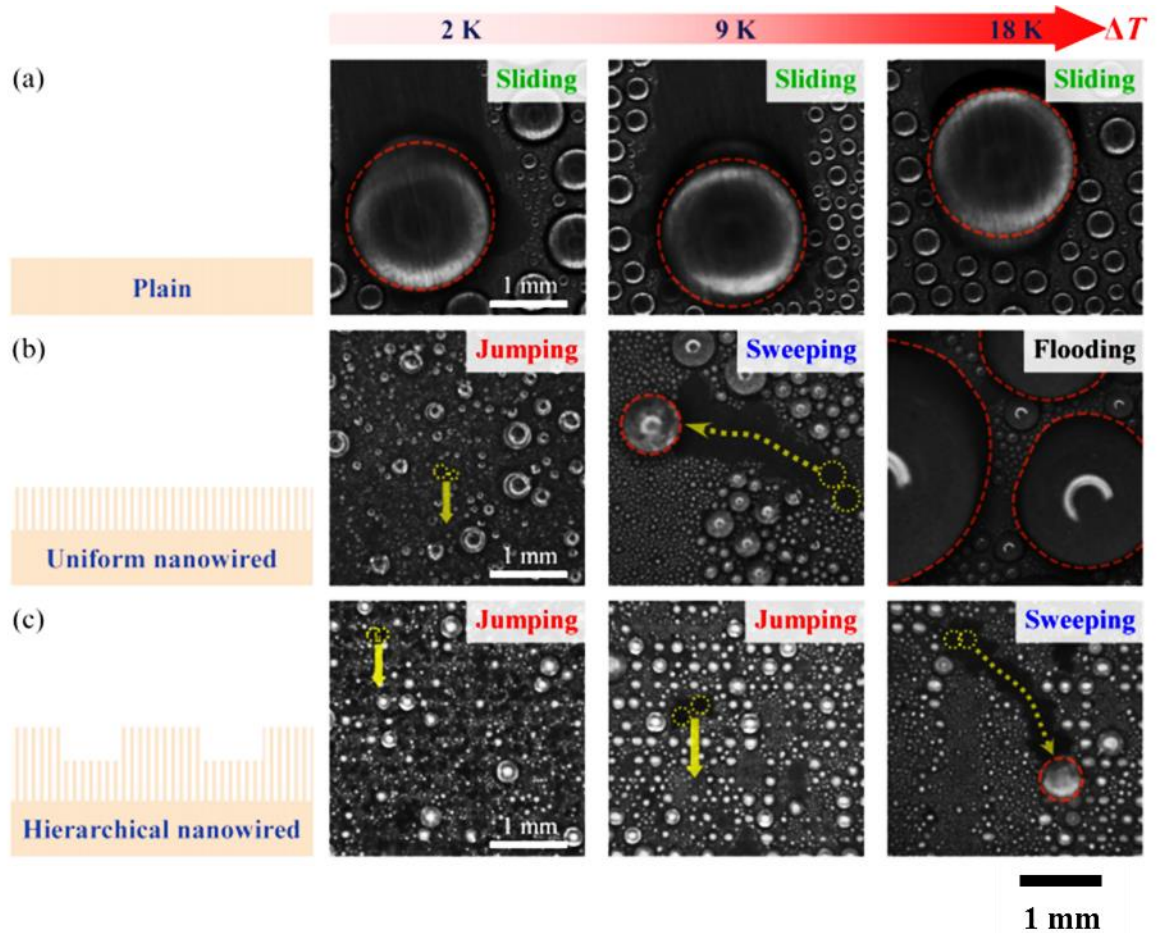


Figure 2.13. Heat flux during dropwise condensation and jumping droplet condensation on a tube sample for saturated vapour pressures  $P_v$  of (a) 2.2 kPa, (b) 2.7 kPa. Adaptation from [36].



Wen et al. [54] manufactured hierarchical superhydrophobic surfaces with copper micropatterned nanowire arrays by a standard photolithography and electroplating processes for the micro-elements and by surface using a two-step porous anodised aluminium oxide template-assisted to create the nanowires. Additionally, a self-assembled hydrophobic coating was implemented using the solution of n-octadecanethiol in ethanol to achieve superhydrophobicity (Figure 2.14).



**Figure 2.14.** Condensation modes and droplet behaviours on the three test surfaces [54].

The results showed a higher density of microdroplets, smaller departure radius of droplets, 133% wider range of surface subcooling, and 37% enhanced critical heat flux for jumping droplet condensation, compared to dropwise condensation on the uniform nano-wired superhydrophobic surface (Figure 2.15) [54].

Most importantly, the foundations for the design of an ideal structured surface as well as heat transfer experiments demonstrating the advantage of this jumping behaviour are lacking. Additionally, previous research pointed out that structured surfaces are relatively expensive to manufacture, requiring the use of a cleanroom environment that are not commonly used for arbitrarily shaped surfaces, representing a challenge in the eventual scale-up for large scale thermal applications [49].

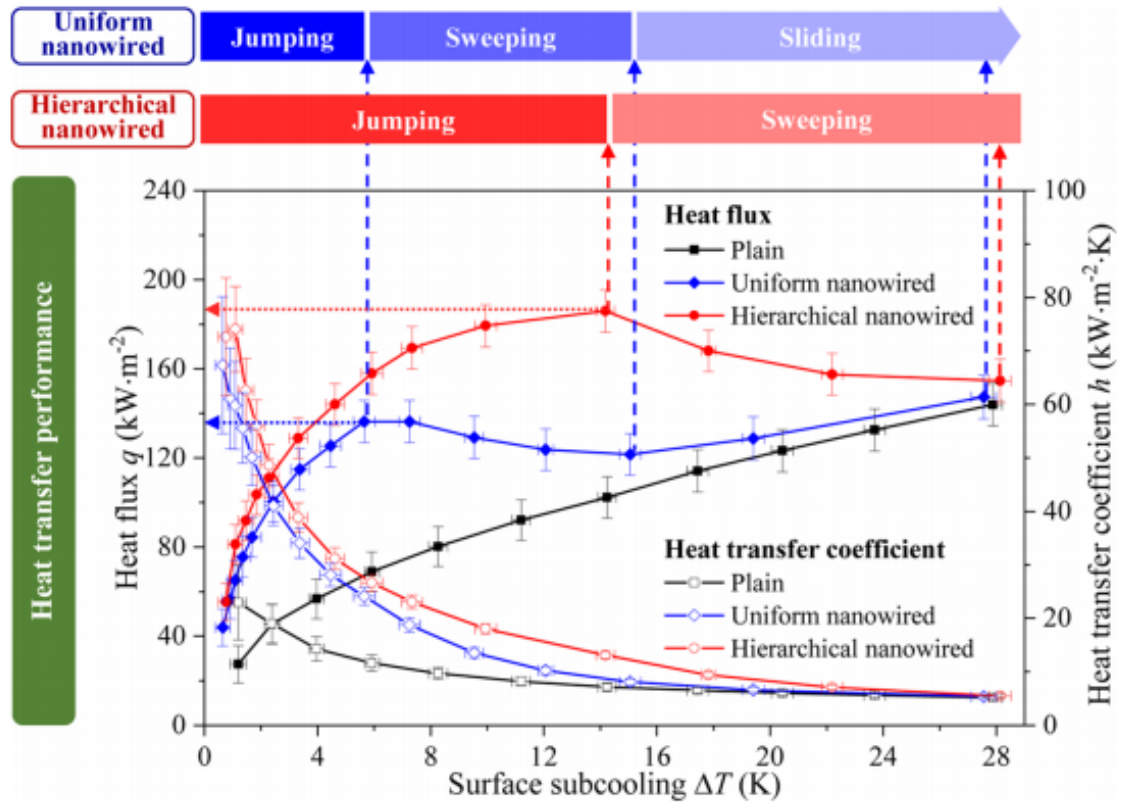
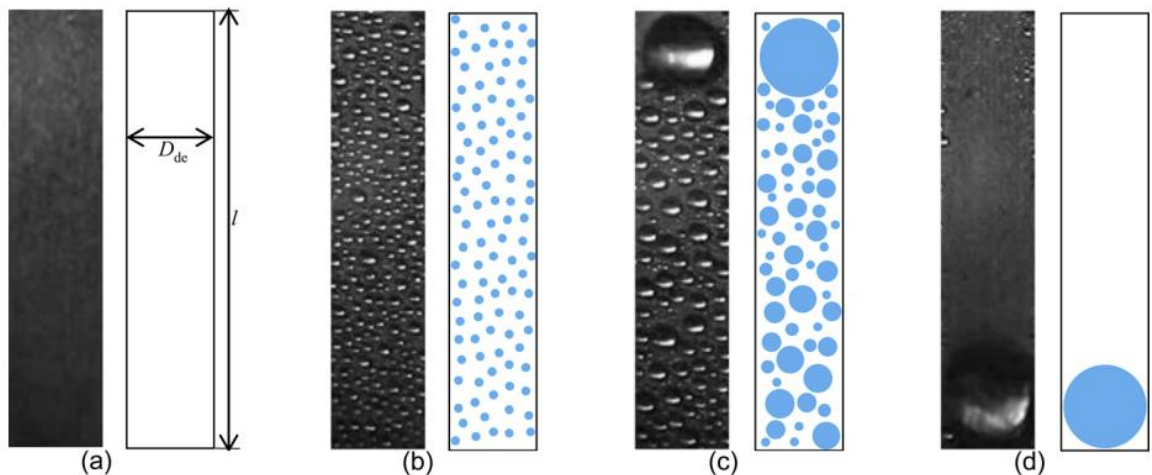


Figure 2.15. Condensation heat transfer performance. Heat flux and heat transfer coefficient as a function of surface subcooling [54].

## 2.4 Droplet Life Cycle

Condensation occurs at nucleation sites; the initial small droplets are mainly formed by direct deposition from the vapour phase onto the surface and grow due to continued condensation by absorbing water molecules. When the droplets become larger, and the distance between neighbouring droplets becomes closer, coalescence starts to be the dominating mechanism for droplet growth until the droplets reach a specific size and slide down, sweeping away other droplets in its path and leaving the condensing surface cleaned and exposed to the vapour to repeat the process [37,55]. This is known as the droplet life cycle and is based on three stages: nucleation, growth, and departure [56]. A complete life cycle covers about 75% to 80% of the surface from nucleation to the first removal of droplets [57]. Figure 2.16 shows the droplet life cycle stages (a) nucleation at the exposed surface (b) droplet growth by direct steam condensation (c) droplet growth by coalescences (d) droplet departure [58].



**Figure 2.16. Schematic the droplet life cycle stages (a) nucleation (b) growth by direct steam condensation (c) growth by coalescences (d) droplet departure [58].**

The droplet life cycle is an interesting phenomenon both in nature and in many technologies. By understanding the nucleation process and how the contact angle influences it, drop coalescence, and other effects, condensation rates can be predicted and optimised. At the same time, a rhythmic growth and departure of water droplets can be used for heat transfer enhancement by modifying the surface orientation and composition, vapour and surface temperatures, humidity, and vapour flow rate [59].

Mei et al. [57] simulated the processes of nucleation, growth, renucleation and departure of the droplets; the results showed that the apparent growth rate of droplets is strongly dependent on the number of initial droplets. Le Fevre and Rose [36] studied the heat transfer through a single droplet and the effective mean droplet size distribution to determine the dependence of surface heat flux on vapour–surface temperature difference ( $\Delta T$ ).

In the meanwhile, Enright [36] exposed the importance of the droplet surface curvature, condensate surface tension and surface supersaturation to determine the size of the smallest thermodynamically viable droplet and the number of activated nucleation sites because an increase in the nucleation site density causes the heat transfer coefficient to increase with increasing vapour–surface temperature difference.

Furthermore, Tanaka evaluated the local droplet size considering the two mechanisms of droplet growth: direct vapour accretion at the droplet surface and coalescence with neighbouring droplets to obtain predictions of the droplet size distribution for small non-coalescing droplets by using the population balance theory that is usually used to estimate the population of droplets of a given size [36]. To corroborate this, Anand et al. [60] stated in their research that the dynamics of coalescence between two neighbouring droplets at an interface during condensation is a complex function of their size, the growth rate of droplets, and attractive forces due to capillary interactions between them.

Leach et al. [59] found that coalescence profoundly affects the distribution of drop sizes. They obtained drop-size distributions after many generations of coalescence and nucleation from experiments and computer simulations of drop growth and coalescence performed under comparable conditions. The first peak at large radii in Figure 2.17 (left) is composed principally of survivors from the first generation of drops that nucleated at the beginning of the experiment and eventually increased in size. The second peak at smaller radii is composed of drops nucleated much later, and even though many of these smaller drops experienced many coalescence events, they never coalesced with a first-generation drop.

Figure 2.17 (right) shows the evolution of these drops average size, the mean radius of the small drop population grows very slowly after 2,000 seconds. The small drop population apparently approaches a steady state: drops lost to the large drop population by coalescence are replaced by new nucleation and growth. In contrast, the mean radius of the large drop population continues to grow throughout the experiment for at least 3,000 seconds. According to Leach et al. [59], this growth is partly driven by coalescence with other first-generation survivors.

Figure 2.18 shows Leach's experimental results on drop growth. Drop R is 50  $\mu\text{m}$  from the nearest large drop, drop S is 17  $\mu\text{m}$  and drop T is only 13  $\mu\text{m}$  from the nearest large drop. Drop R grew 20% faster than the drops closest to large drops. Leach found that adsorbed water diffusing between large and small drops has a higher probability of encountering the larger drop than the smaller drop, resulting in slower growth for the smaller drop. Basically, the large drops get larger at a faster rate. It was also found that the diffusive transport of adsorbed water limit is associated with the short average residence time for water molecules on the hydrophobic surface [59].

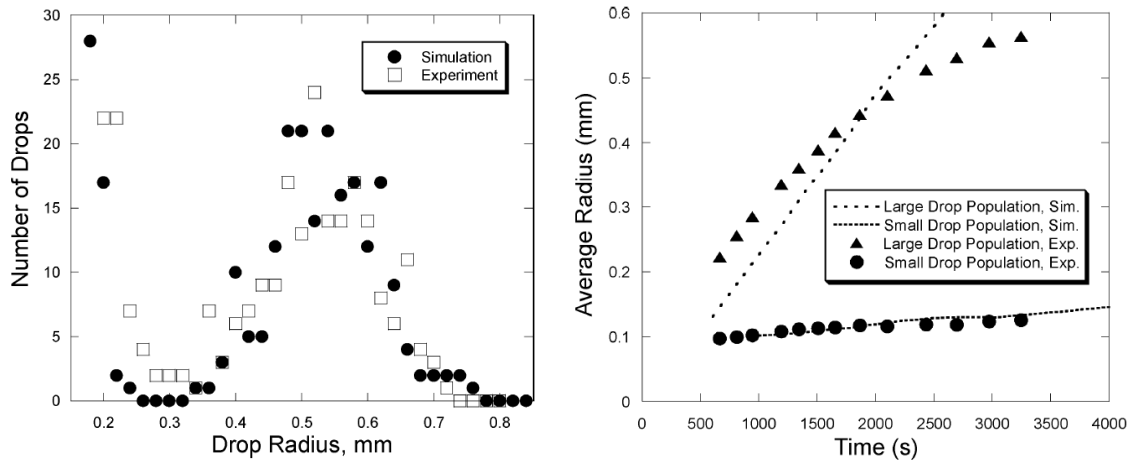


Figure 2.17. Drop-size distributions from experiments after 3000 seconds and simulations (left). Average drop sizes (right). Adaptation from [59].

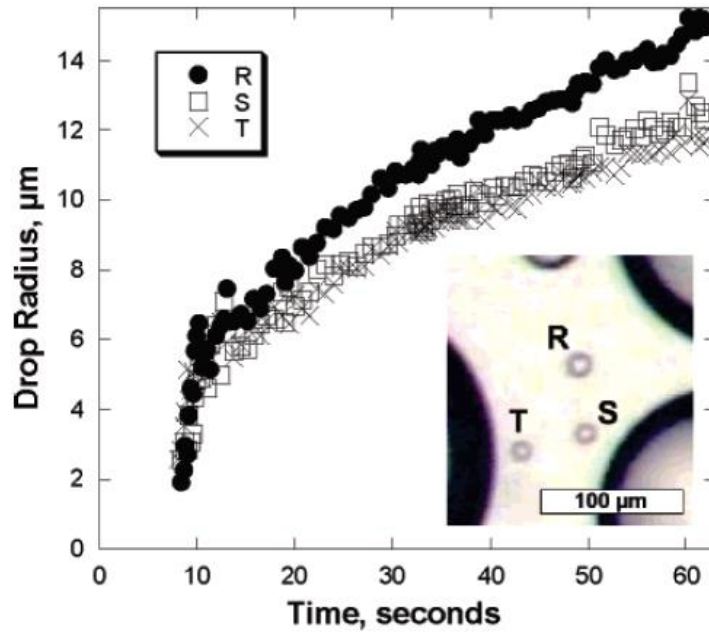


Figure 2.18. Leach's experiments on small drops growth (R, T, S) in terms of the vicinity with larger drops. Time  $t = 0$  corresponds to the coalescence event responsible for the nucleation of the three small drops. Adaptation from [59].

### 2.4.1 Surface Wettability

One of the key fundamental physical phenomena in liquid-solid contact systems is surface wetting, which refers to the interaction between the surface and the condensate. It is defined by the contact angles of the water droplet sitting on a surface and can be classified as ‘water-loving’ with contact angles between  $0^\circ$  and  $10^\circ$  for superhydrophilic surfaces, between  $10^\circ$  and  $90^\circ$  for hydrophilic surfaces, and as ‘water-fearing’ with contact angles between  $90^\circ$  and  $150^\circ$  for hydrophobic surfaces and superhydrophobic surfaces when the contact angle is greater than  $150^\circ$ . Most materials that are widely encountered in nature and engineering applications are neither completely wetting nor completely non-wetting, but through careful design, it is possible to alter their natural surface wettability to be more hydrophilic or hydrophobic [53,61].

In 1612, Galileo Galilei observed an ebony wood chip floating slightly below the surface of a water bath; this was the first observation of the wetting phenomenon; however, the concept of surface wettability or surface tension was not formally defined. It was until 1805, when the English physicist Thomas Young postulated a physical relationship between surface tension (surface free energy) and the static droplet-surface contact angle (CA), that wetting and contact angles became a scientific research topic [53]. The wettability of smooth and rough solids is governed by Young, Wenzel and Cassie–Baxter equations [62]. The Young equation results from the equilibrium of forces acting on the triple line (Figure 2.19) and is described as:

$$\gamma_{sv} = \gamma_{sl} + \gamma_{lv}\cos\theta \quad (2.82)$$

Where

$\gamma_{sv}$  = solid/vapour surface tension

$\gamma_{sl}$  = solid/liquid surface tension

$\gamma_{lv}$  = liquid/vapour surface tension

$\theta$  = static contact angle (CA)

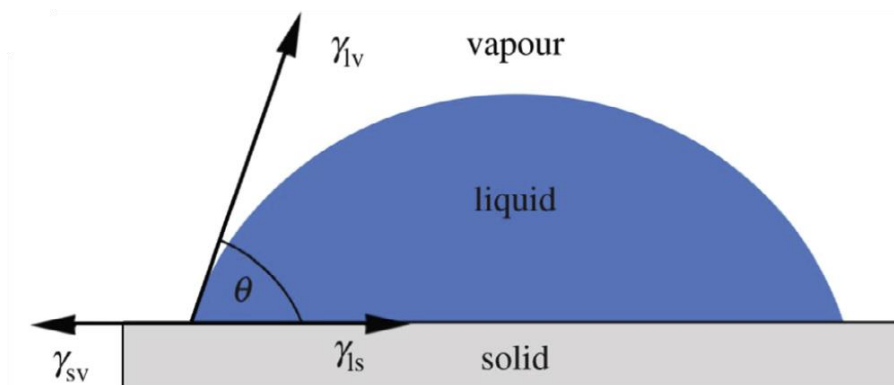


Figure 2.19. Schematic of Young's equation. Adaptation from [63]

The contact angle is the one that the liquid forms with the solid at their contact point, and it is determined by the attraction of the droplet molecules towards the surface (adsorption force) and the attraction of the droplet molecules towards one another (cohesive force), it measures and quantifies the amount of contact between the liquid and the solid. For example, a droplet will not wet a surface when the cohesive force is more dominant than the adhesive force, as with hydrophobic surfaces. The liquid/vapour surface tension depends on temperature and can be easily measured or found in the literature; however, the solid/vapour and solid/liquid surface tensions are not often readily known. Thus, measuring the static contact angle is a simple and popular method of determining the overall wettability of a material [53].

In 1936, Wenzel [64] proposed that roughness modification of metallic and non-metallic surfaces (from aluminium to glass) amplifies the wetting behaviour of the materials. Wenzel's experimental results showed that roughness makes a hydrophilic surface (wetting surface) more hydrophilic and a hydrophobic surface (non-wetting surface) more hydrophobic. Experimental studies demonstrated that the water contact angle decreases as the roughness factor increases, corroborating the Wenzel model [53]. The empirical relationship between the droplet static contact angle and the surface roughness factor was defined as:

$$\cos\theta^* = r \times \cos\theta \quad (2.83)$$

Where

$\theta^*$  = new apparent contact angle on the roughened surface

$\theta$  = contact angle on a smooth surface

$r$  = roughness = actual surface area / projected surface area

In 1944, Cassie and Baxter reported that in some cases, the Wenzel relation could not correctly predict the static contact angle of droplets on rough, porous surfaces [65]. As a result, they modified the Wenzel relation and introduced another formula that can be used to predict the new apparent contact angle on uniformly rough porous surfaces containing trapped air pockets:

$$\cos\theta^* = f_1 \cos\theta_1 + f_2 \cos\theta_2 \quad (2.84)$$

Where

$f_1$  = area in contact with droplet / projected surface area

$f_2$  = area in contact with air beneath the droplet / projected surface area

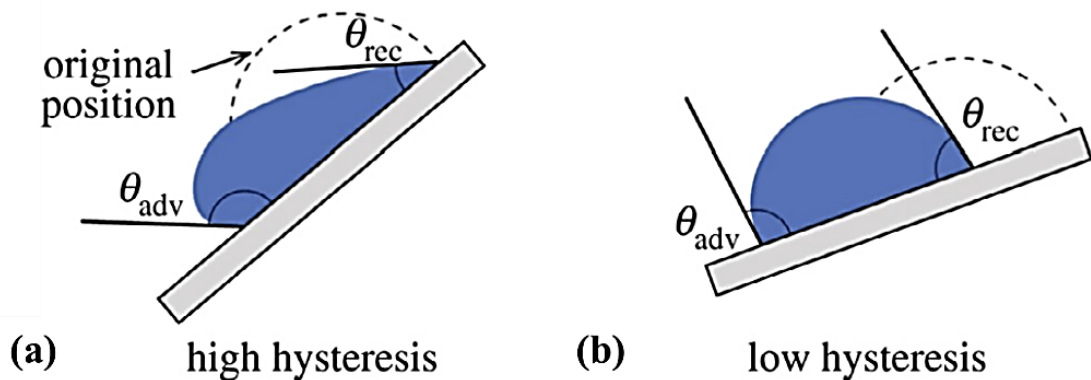
when  $f_2$  is equal to zero, the Cassie-Baxter equation reduces to the Wenzel relation

$\theta_1$  = contact angle of the smooth solid surface

$\theta_2$  = contact angle for air (i.e. 180°).

In 1950, Bikernian studied the wetting behaviour of grooved/ridged surfaces based on Wenzel's work [66]. It was found that roughness affects the wetting behaviour depending on (a) how much a surface is grooved/ridged and (b) the condition of the water droplet static contact angle on the original surface. Additionally, when the hysteresis is sufficiently small, a water droplet will spread spontaneously along the surface.

The contact angle hysteresis is the difference between the advancing and receding contact angle when the solid is set at an angle ( $\theta_{adv} - \theta_{rec}$ ) (Figure 2.20). The advancing and receding contact angles can be measured when a water droplet is injected onto the surface, and then the volume of the water droplet is increased or decreased until the maximum (or minimum) volume is achieved without a change in the droplet contact area.



**Figure 2.20.** (a) High contact angle hysteresis ( $\theta_{adv} - \theta_{rec}$ ), and (b) low contact angle hysteresis.

Adaptation from [63].

The contact angle hysteresis measures the intensity of the bond between the droplet and the surface; if it is low, the liquid tends to roll off the solid, and if it is high, the liquid tends to stick to the solid. A summary of his work on the behaviour of water droplets along grooved/ridged surfaces in terms of the hysteresis and the droplet contact angle is available in the literature [53].

As a consequence of the surface conditions, various wetting states can be observed when a water droplet rests on a textured surface (Figure 2.21). Previous studies reported that when hydrophilic textured surfaces are fully wetted, and the droplet has a partially spherical shape, the wetting state of the droplet is defined as the Wenzel state, also condensed droplets on the superhydrophobic surface with micro-rough architecture present Wenzel state. However, Liu et al. [67] indicated that as droplets continue to grow on a superhydrophobic surface, they transition to a Cassie-Baxter state, where droplets end up sitting on top of air-filled cavities with the ability to leave the surfaces at a small rolling angle. When a liquid film or precursor stretches out from the liquid droplet along the surface, the wetting state is called the hemi-wicking state (“sunny-side-up”).



In hydrophobic textured surfaces with micro-nano hierarchical roughness, commonly found in nature, the droplet is in the Cassie-Baxter state (a state often interchangeably with Cassie state). In some cases, droplets on hydrophobic textured surfaces have a Wenzel state or mixed state (where the Wenzel and Cassie states coexist) [61,67]. Lastly, the partially wetting state is when a droplet does not spread but instead forms a spherical cap resting on the substrate with a contact angle; this type of droplets, along with the Cassie state, are easier to remove than the droplets in a Wenzel state. [46].

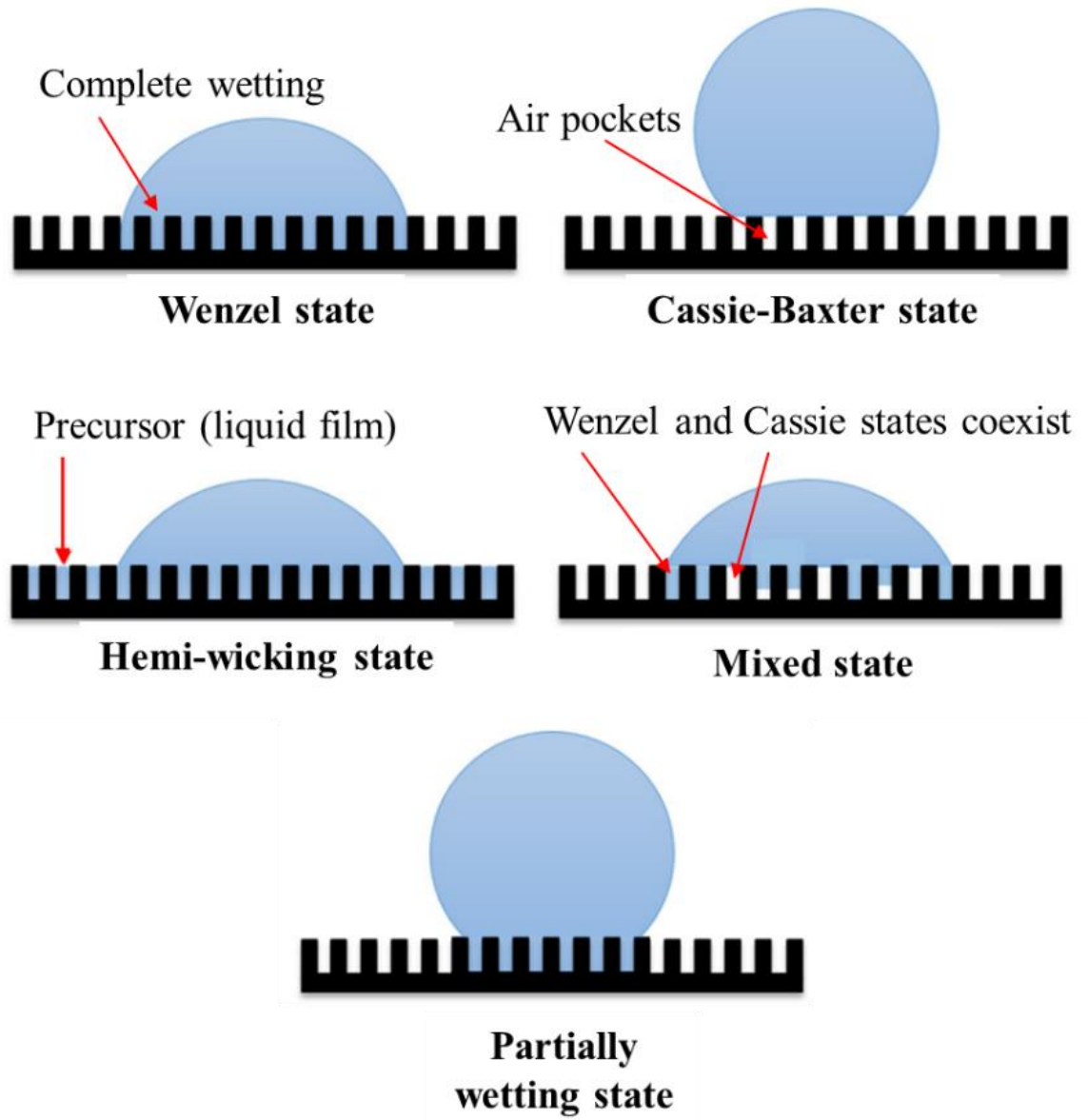


Figure 2.21. Different wetting states. Adaptation from [46,61,63].

## 2.5 Heat Transfer Enhancement Techniques

According to Enright et al. [36], understanding the mechanisms governing water condensation on surfaces is crucial for heat transfer processes. Water vapour preferentially condenses on solid surfaces rather than directly in the vapour because of the reduced activation energy of heterogeneous nucleation in comparison to homogeneous nucleation; as a result, the excess energy of the surface that controls the heterogeneous nucleation process also determines the wetting behaviour of the condensate, which has a significant impact on the overall heat and mass transfer performance.

Hence, heat transfer can be enhanced through "active" or "passive" techniques by modifying the surface properties. Active techniques require external power, such as electric or acoustic fields and surface vibration, while passive techniques employ unique surface geometries or fluid additives for enhancement [68]. The following techniques listing has been provided by Bergles et al. [69].

### Active techniques:

1. Mechanical aids
2. Surface vibration
3. Fluid vibration
4. Suction
5. Electrostatic fields
6. Injection
7. Jet impingement

### Passive techniques:

1. Coated surfaces
2. Rough surfaces
3. Extended surfaces
4. Displaced insert devices
5. Swirl flow devices
6. Coiled tubes
7. Surface tension devices
8. Additives for liquids
9. Additives for gases

For condensation heat transfer, only a few techniques from the listing can be functional due to the nature of this phase change process. The main obstacle for heat transfer is the condensate film that works as a barrier; its thickness is determined by the force that allows the condensate to drain. Therefore, any technique that promotes the film thickness reduction will provide heat transfer enhancement.

Water vapour condensing on high- or low-surface-energy surfaces forms a liquid film (FWC) or distinct droplets (DWC), respectively. To enhance filmwise condensation, a number of mechanical drainage forces, such as surface tension, suction, and centrifugal force, can be used to remove the accumulated condensate without increasing the surface contact area. Here the film condensation coefficient is inversely proportional to the condensate film thickness, which Gregoring first studied in 1954 and in 1971, Karkhu and Borovk incorporated extended surfaces as a passive technique for filmwise condensation because they reduce the thermal resistance by increasing the heat transfer coefficient and/or the surface area [68].

Alternatively, two passive techniques can be employed to promote dropwise condensation for higher heat transfer fluxes. The first one is by adding a promotional chemical into the vapour flow, which can be liquid droplets or solid particles, and the second one via surface wettability through chemical (coatings) or topographical (surface roughness) modification. Due to the unpredictable and complex nature of the flow source (meteorological phenomena) and the storage capabilities of the energy recovery device, adding chemical additives into the flow is an unpractical option for this research. Thus, coated and rough surfaces will be discussed in the following section.

### **2.5.1 Passive Techniques for Condensation Enhancement**

The development of innovative manufacturing techniques for surface structuring has allowed researchers to explore the optimisation of dropwise condensation and, in some cases, jumping-droplet condensation at micro-and nano-scales. This is particularly important because, since the discovery of the dropwise condensation process in the early 1930s by Schmidt et al. [70], a solution that simultaneously satisfies durability, cost, and performance requirements has yet to be found [36].

**Table 2.1. Dropwise condensation enhancement techniques. Adapted from [23]-[25], [38].**

Type	Technique	Description	Advantages	Disadvantages
Coated surfaces	Polymers	Non-wetting plastic coating such as Polytetrafluoroethylene (Teflon).	Promote DWC, excellent heat transfer with thin coatings.	Represent an additional thermal resistance that can be 60% as large as the resistance associated with film condensation.
	Self-assembled monolayers (SAMs)	~1-nm thick molecular film on condensing surfaces.	Low thermal resistance.	Robustness for long term stability and durability needs to be improved for industrial-based applications.
	Noble metals (NM)	Some examples are gold, platinum, silver, rhodium, or palladium.	NM are resistant to corrosion and oxidation in moist air.	Costly, requires a contaminant source to maintain DWC.
	Ion Implantation	Carbon, nitrogen and oxygen ions can be implanted on metals.	Acceptable heat transfer at low subcooling.	Expensive, flooding occurs at high subcooling, costly, scalability not demonstrated.
	Rare earth oxides (REOs)	Ceramic deposited on condensing surface.	Hydrophobic nature.	Thin coatings required due to low thermal conductivity. Lack of heat transfer data.
	Chemical additives	Chemical coating such as benzyl mercaptan, waxes or fatty acids (oleic, stearic, and ionic).	Promotes hydrophilic properties while reducing air pressure drop.	Expensive and difficult to maintain as their lifespan is short (up to 1,000 hours), requiring constant surface cleaning and re-promotion for further effectiveness.
	Lubricant-infused	Low energy structured surface infused with immiscible low energy liquid.	Low hysteresis, low contact angles, nucleation density control.	Effects of lubricant drainage still need to be studied.
Rough surfaces	Superhydrophobic surfaces	Surfaces demonstrate high contact angles and low adhesion due to structure enhanced hydrophobicity.	Promote droplet jumping to enhance heat transfer rates.	Increased thermal resistance of individual droplet growth, surface flooding at high supersaturations.
	Hierarchical surfaces	Surfaces consist of micro and/or nano-scale features.	Spontaneous droplet motion, increased condensing surface area.	Potential of multiple length scales not yet demonstrated, surface flooding at high supersaturations.
	Biphilic surfaces	Surfaces consist of hydrophobic and hydrophilic regions.	Provide spatial control of droplet nucleation.	Heat transfer data still are lacking.

## 2.6 Research on Condensation Heat Transfer Enhancement

In 2018, Edalatpour et al. [53] described how surface wettability could be achieved by modifying the surface chemical composition and/or geometric morphology (surface roughness) to bring operational benefit or advantage. The chemical composition is a natural material characteristic of the solid surface and is quantified based on the intrinsic contact angle, which is defined as the equilibrium contact angle of a water droplet on the ideal surface. Whilst, the geometric morphology is a mechanical characteristic of the solid surface and is quantified in terms of the roughness ratio (the ratio of the wetted area to the projected area) [61]. As a result, by creating a wettability pattern, it is possible to predetermine nucleation sites, as well as facilitate droplet motion and control of water droplet movement paths to spread out the condensate and facilitate drainage while reducing air pressure drop [53].

### 2.6.1 Coated Surfaces

Studies on coated surfaces obtained between 20 and 60% enhancement levels [36,68]. One example is the patent by Notaro that involved a coated surface geometry of 0.25 to 1.0 mm high metal particles covering 20 to 60% of the surface. Condensation occurred on the particle array and drained along the smooth base surface. For a given particle height, there is an optimum particle spacing. Correspondingly, experimental studies by Renken, Aboyoe and Mueller in 1993 and 1996, using coating thickness of 25 to 250  $\mu\text{m}$  and porosity of approximately 50%, showed that the thinnest coating provided the highest enhancement. According to Webb and Kim, on a porous coating, condensate drainage is assisted by capillary flow within the porous, resulting in the reduction of the condensate film thickness and thermal resistance [68]. Nonetheless, the promoters lose their effectiveness because of fouling, oxidation, and the removal of their coated layer from the surface over time [37,38].

### 2.6.2 Hydrophobic and Superhydrophobic Surfaces

Removing condensate from the surface can improve the surface heat-exchange coefficient by at least one order of magnitude when compared with flooded surfaces. Previous work on artificial hydrophobic and superhydrophobic surfaces has revealed that enhanced dropwise condensation occurs due to enhanced droplet shedding. To accomplish better mobility of coalescence-induced droplet jumping at length scales that relate gravity and surface tension below the capillary (Bond number  $< 1$ ) for condensate to drain, artificial surfaces require a suitable type of morphology or roughness material with low surface energy to enhance hydrophobicity for low adhesion to water in order to interact with liquids in a way that results in high contact angles and low contact angle hysteresis for condensate to drain [36,52,71,72].

In order to modify the surface wettability for the creation of superhydrophobic surfaces, Parin et al. [73] described two main phases in their research: (1) the etching phase, which creates the proper surface roughness, and the functionalisation step, where a hydrophobic layer is developed to decrease the surface free energy. Past studies combined roughness and low-surface-energy materials [36] to create superhydrophobic surfaces, while others combined roughness and a coating layer [73] [74] for DWC to enhance droplet shedding. In both procedures, the droplet contact angles exceeded  $150^\circ$ , and contact angle hysteresis approached  $0^\circ$  for the low-surface-energy materials and  $10^\circ$  for the coating layer. Enright mentioned that wetting interactions could be altered by using specific micro geometries on the surface to manipulate condensation behaviour so droplets can passively shed at microscopic length scales via droplet coalescence with better performance than coating layers [36].

Experimental studies carried out by Miljkovic et al. [49] achieved superhydrophobicity by applying a Sam-functionalised copper oxide-based nanostructured surface, obtaining 30% heat transfer enhancement. However, the increased supersaturation led to the flooding of the surface and degraded heat transfer performance by the end of the experiments.

### **2.6.3 Superhydrophobic Nanostructured Surfaces**

In 2015, Birbarah et al. [52] explored the idea of promoting jumping-droplet condensation through superhydrophobic nanostructured surfaces to achieve spontaneous droplet removal for a variety of applications, including self-cleaning, thermal diodes, anti-icing, anti-fogging, vapour chambers, electrostatic energy harvesting, and condensation heat transfer enhancement. However, heat transfer enhancement can be limited by droplet return to the surface due to (1) gravitational force, (2) entrainment in a bulk convective vapour flow occurring adjacent to the condensing surface due to buoyancy effects on vapour near the surface, and (3) entrainment in the local condensing vapour flow toward the surface due to the flow required for mass conservation of the condensing vapour. Birbarah et al. [52] proposed that the first two return mechanisms (gravity and bulk vapour flow) can be mitigated with a suitable geometric design of the macroscale condensing surface and vapour supply. Moreover, even though the third return mechanism (local vapour flow) is more difficult to eliminate due to the need to conserve mass of the condensing vapour flowing toward the surface, the understanding of structured surfaces will not only enhance heat transfer but also prevent progressive surface flooding and extend high-performance condensation operational time due to the reduction in large pinned droplets on the condensing surface.

### 2.6.4 Hierarchical Superhydrophobic Surfaces

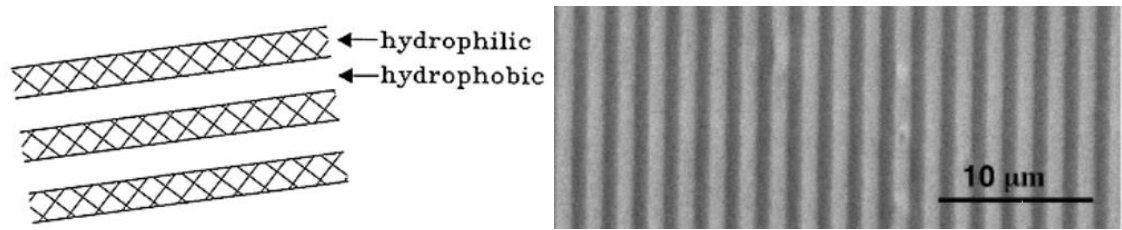
Several theoretical studies focused on the role of microscale topology during condensation have shown the importance of microscale features during coalescence events on hierarchical superhydrophobic surfaces for the merging of multiple droplets [36]. Enright and coworkers [36] identified that the surface architecture with various microscale topologies enables the transition of large droplets into the Cassie state (droplets do not penetrate the grooves on the microscale features leaving air gaps) and, at the same time, provides sufficient spacing in-between features to allow for mobile coalescence and departure. Boreyko and Chen were the first to report spontaneous droplet motion when using surfaces with superhydrophobic hierarchical nanoscale and microscale topologies during condensation [75]. However, some heat transfer experiments performed by Cheng on a hierarchically structured surface did not present any improvement due to flooding [36].

### 2.6.5 Hydrophilic Surfaces

In 2020, Zhang and Zhang [55] evaluated the condensation efficiency of hydrophobic surfaces (solution deposition of polysiloxane and propylamine polymer) with contact angles of  $108^\circ$ ,  $120^\circ$  and  $145^\circ$  through a droplet size distribution model. They found that high hydrophobicity leads to lower and slower droplet growth rates that result in a low droplet density. Self-removal of condensed droplets depends on the growth rate and the coalescing frequency of condensed droplets; faster growth and more frequent coalescence led to higher self-removal efficiency [72]. Additionally, nucleation on hydrophobic surfaces requires a higher degree of supersaturation than is required when condensing on hydrophilic surfaces, which promote rapid nucleation and growth of condensed water. Therefore, hydrophilic surfaces are a viable option that can alleviate many heat transfer issues caused by the lack of contact between droplets and solid material.

### 2.6.6 Biphilic Surfaces

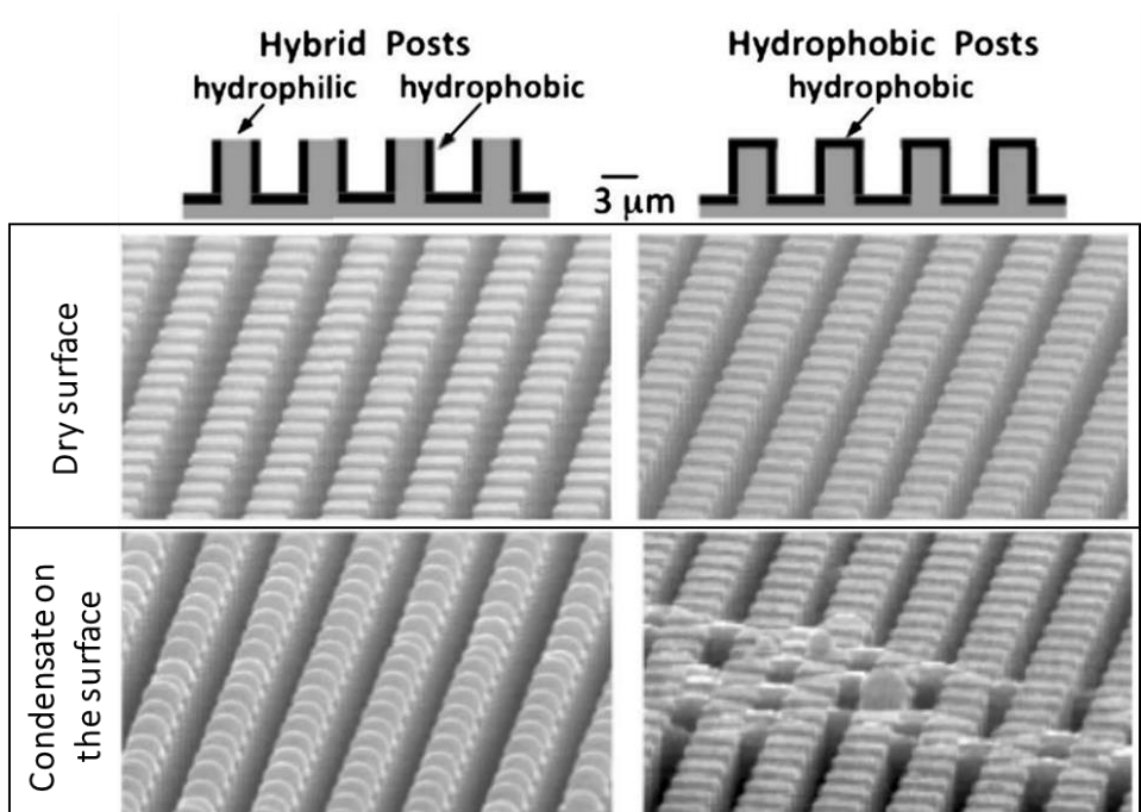
Departure on hydrophilic surfaces is more challenging to achieve. As a result, biphilic surfaces that contain a combination of hydrophilic and hydrophobic regions can reduce the energy barrier for vapour condensation while promoting droplet shedding to improve dropwise condensation [36]. The effects of biphilic surfaces on condensation heat transfer performance were first studied by Kumagai et al. [76]. They alternated stripes of hydrophobic and hydrophilic regions with dimensions at or above the capillary length scale; the results were bounded between the limits of complete DWC and FWC. The research teams of Drelich and Morita [77,78] studied the effects of using alternating hydrophobic and hydrophilic strips for wetting characterisation of hybrid surfaces with characteristic length scales below the capillary length (Figure 2.22). At the same time, Raj et al. [79] worked with hydrophobic/hydrophilic dots on dynamic droplet contact angles. Enright et al. [36] exposed the importance of understanding the roles of high-energy condensation sites and the need to minimise contact angle hysteresis to promote efficient droplet shedding.



**Figure 2.22.** Orientation of alternating hydrophilic and hydrophobic strips (left). SEM image of a micropatterned fluoroalkylsilane monolayer surface with hydrophilic/hydrophobic area (right).

Adaptation from [77,78].

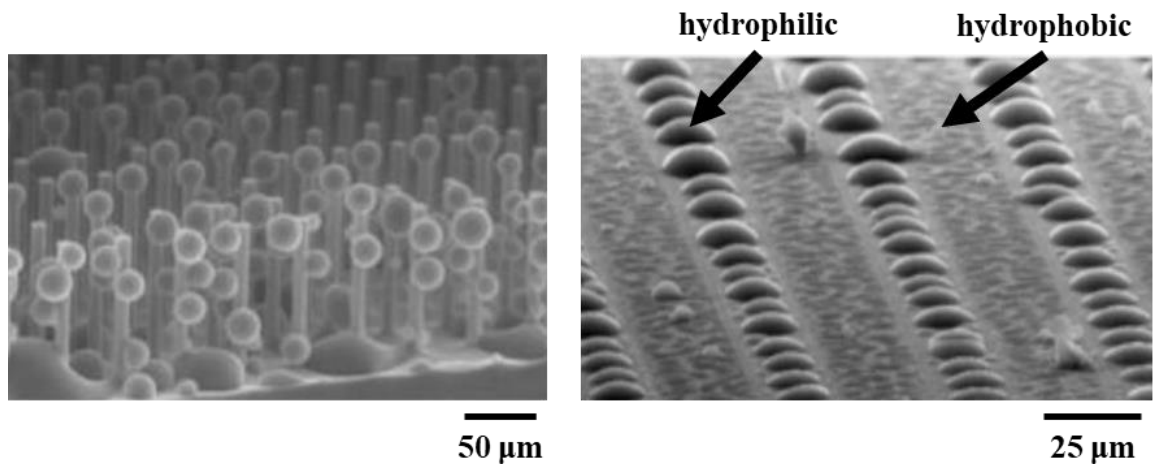
Varanasi et al. [80] investigated the use of hydrophobic–hydrophilic patterning in combination with structured roughness via a top-down lithography technique with the aim of spatially controlling heterogeneous nucleation while facilitating efficient droplet shedding (Figure 2.23).



**Figure 2.23.** Comparison of the condensation behaviour on a hybrid surface consisting of hydrophobic posts with hydrophilic tops (left) and a superhydrophobic surface consisting of hydrophobic posts (right). Adaptation from [80].

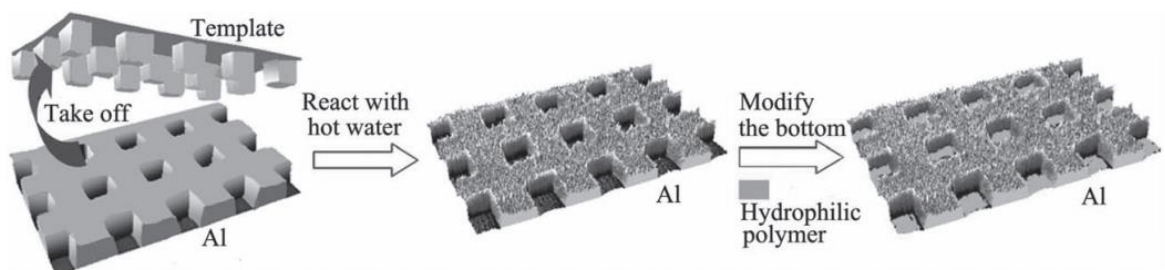
Experimental results showed that in contrast to the random nucleation behaviour of superhydrophobic surfaces, textured hydrophobic surfaces with hydrophilic tops promote nucleation and growth of Cassie-type droplets and can therefore exhibit superior droplet shedding properties under condensation (Figure 2.24).





**Figure 2.24.** Environmental scanning electron microscope (ESEM) images of condensation of water vapour on a superhydrophobic surface (left) and on a surface with alternating hydrophobic and hydrophilic segments (right). Adaptation from [80].

Through a bottom-up deposition process, Mishchenko et al. [81] were able to deposit hydrophilic polymers and particles on the tips of a range of superhydrophobic structures to induce precise spatial control over water condensation at the micrometre scale. Yao et al. [71] designed and manufactured a hybrid surface consisting of an array of hydrophobic and hydrophilic sites to study the effects of microscale surface features and chemistry on wettability; they found that using structured biphilic surfaces for condensation purposes results in a significant contact angle hysteresis effect due to the hydrophilic tips. A significant increase in condensate removal using a biphilic surface chemistry versus a uniformly hydrophobic surface chemistry was obtained when water condensation occurs on the hydrophilic region and surface tension–driven droplet jumping on the hydrophobic region for droplet removal [82]. Taking this into account and inspired by the peculiar hydrophilic/hydrophobic structures on a beetle's elytra, He et al. [72] developed a unique hierarchically structured superhydrophobic surface composed of micro-/nanoporous with hydrophilic polymer coatings at the base of the pores for efficiently controlling droplet self-removal (Figure 2.25).



**Figure 2.25.** Superhydrophobic Hierarchical Porous Alumina Surfaces' fabrication process integrates micro-contact printing and chemical bath deposition [72].

Other studies based on the Laplace pressure instability to gather droplets independent of coalescence-induced droplet growth mechanics [36] resulted in hemi-wicking droplets [83]; for example, Anderson et al. [82] studied a unique biphilic structured surface where the relative placement of the hydrophilic and hydrophobic regions on the surface was reversed compared to previous studies [71,80,81].

### 2.6.7 Wetting Gradient

Considering that the main obstacle of droplet motion is the contact angle hysteresis which pins the droplet edge to the surface, additional energy can be supplied to the droplet to overcome hysteresis and promote droplet motion through wetting gradient surfaces via mechanical vibration, electrical, chemical, thermal, electrochemical, topographical or photochemical methods [84]. In 2007, Zhang and Han studied different shape-gradient surfaces of wax and polyethylene for the hydrophobic area and mica for the hydrophilic area of millimetre size [85].

Lv and Hao [84] designed a wetting microstructured gradient surface (Figure 2.26), fabricated by standard photolithography and inductively coupled plasma (ICP) etching techniques, and self-assembled monolayer (SAM) of octadecyltrichlorosilane. They also obtained contact angles of  $105 \pm 1^\circ$ , and with the help of vibration, they found that the droplet always moved from the small-scale to the large-scale region to decrease its total surface energy [84].

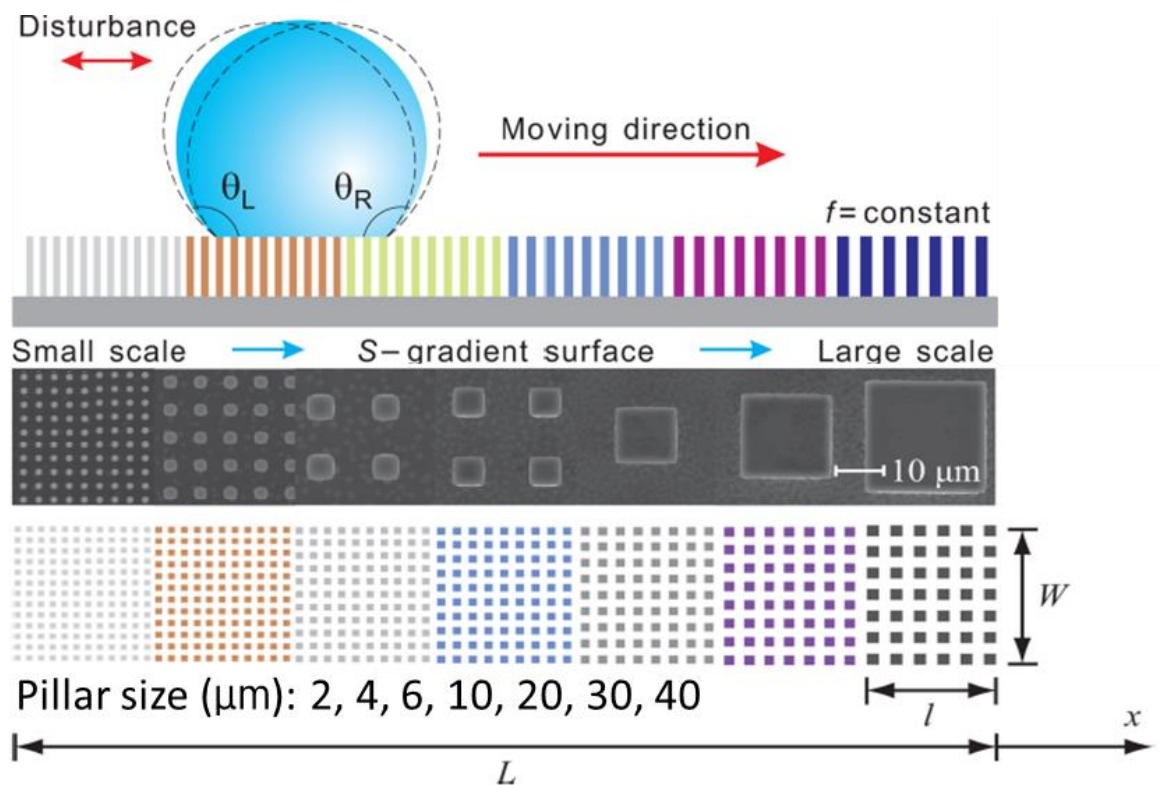


Figure 2.26. Wetting microstructured gradient surface for droplet motion. Adaptation from [84].

Similar experiments were performed by Shastry et al. [86], but they varied the size of the micropillars every 4 to 8 mm for the gradient effect; they stated that the air trapped between the droplet and the micropillars ensured a low solid-liquid contact area fraction and significantly reduced drag, allowing the droplets to move on the surface with a low amount of energy (Figure 2.27).

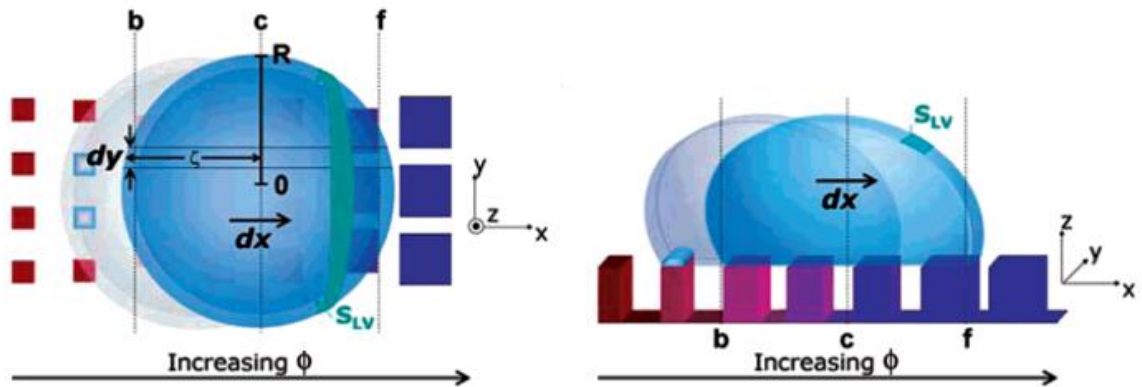


Figure 2.27. Shastry's diagram of a droplet slice of width  $dy$  shows moving a length  $dx$  down a contact angle gradient: (left) top view and (right) side view (the previous location of the droplet is shown in light grey). Adaptation from [86].

### 2.6.8 Hybrid Wetting Gradient

Sun et al. [87] employed a laser-etching method to fabricate a roughness gradient at millimetre scale from hydrophobic to hydrophilic structures on a chemical pre-treated silicon surface coated with fluoroalkylsilane, the microgrooves widths of the four groups, from left to right, are 200  $\mu\text{m}$ , 100  $\mu\text{m}$ , 50  $\mu\text{m}$  and 20  $\mu\text{m}$ , and the distances between them are 200  $\mu\text{m}$ , 100  $\mu\text{m}$ , 70  $\mu\text{m}$  and 40  $\mu\text{m}$  (Figure 2.28).

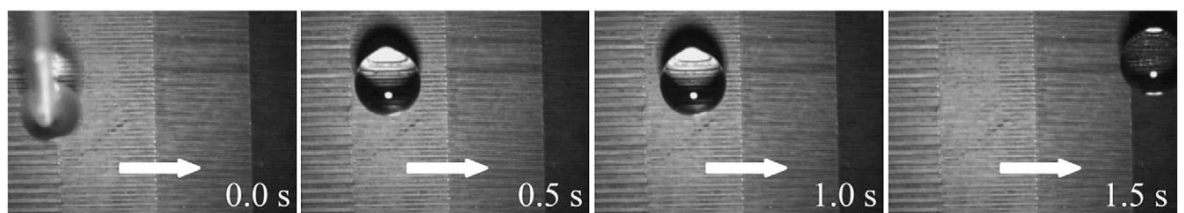


Figure 2.28. Sliding behaviour of a 10 mg water droplet on the roughness gradient surface reported by Sun et al. [85].

By developing a hybrid wettability gradient, Tokunaga and Tsuruta [48] were able to experimentally decrease flooding and increase heat transfer three times when compared to straight micro-patterns (Figure 2.29). This was achieved by adjusting the hydrophobic and hydrophilic micro-pattern widths, with the hydrophilic groove increasing towards the downstream direction to control the droplet size, while the wettability gradient enhanced the droplet drainage rate.

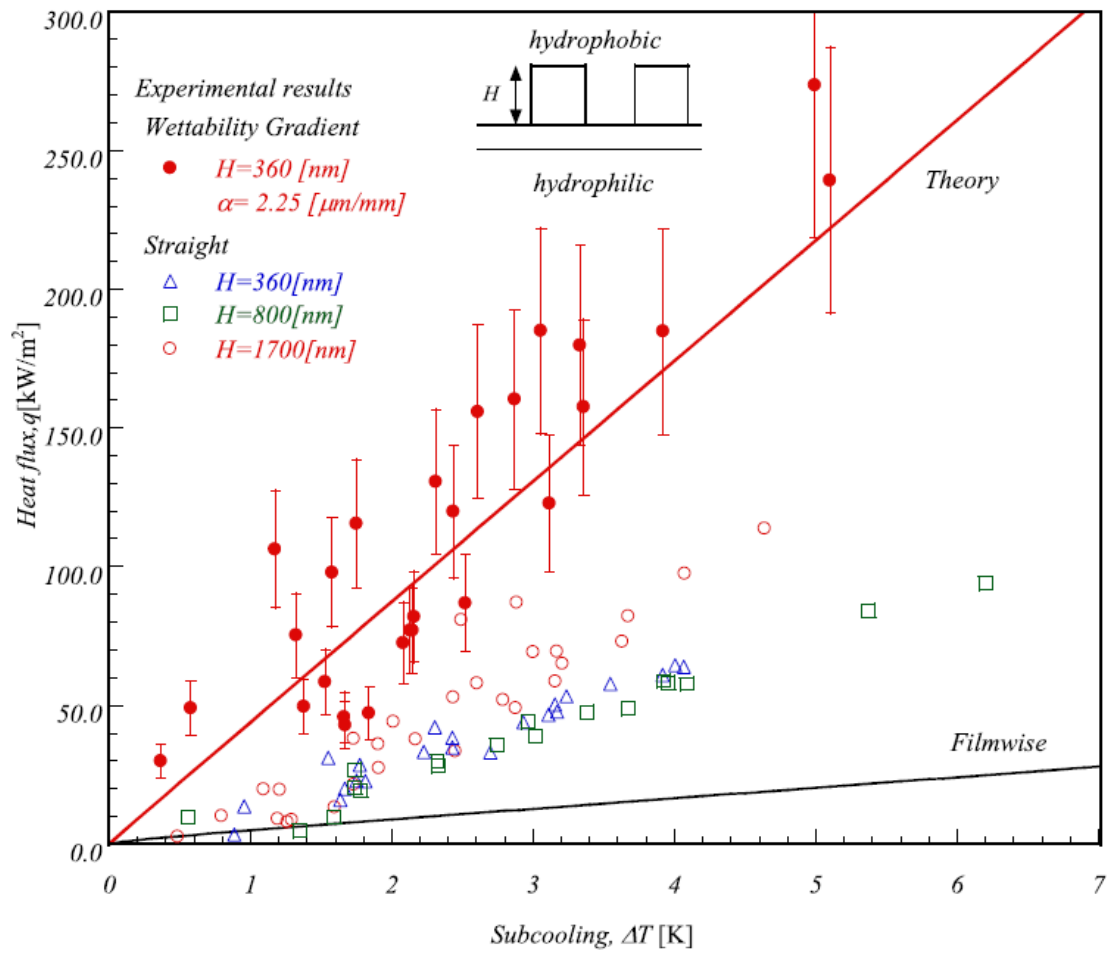


Figure 2.29. Comparison of condensation heat flux on straight patterns vs a wettability gradient.  
 Adaptation from [48].

An adaptation of current research on surface wettability modification results, collected by Edalatpour et al. [53] is presented in Appendix A.

## 2.7 Microstructured Surfaces: An Innovative Passive Technique

A passive condensation heat transfer enhancement technique is surface's wettability modification via chemical coatings (chemical modification) or surface structuring/texturing (topographical modification). By tailoring the wettability, surfaces can become more hydrophilic or more hydrophobic to improve condensate drainage, decrease condensate bridging, reduce air-side pressure drop, increase heat transfer coefficients, decrease drag, reduce water retention, delay frost formation, and/or control the movement of water in conventional energy systems.

### 2.7.1 Considerations for Design and Manufacturing

According to Motoki et al. [35], using a specific microstructured surface is expected to increase the heat transfer while reducing pressure losses and drag. The concept promotes the formation of micro-vortical tubes that, due to rotation, keep a continuous exchange of energy. Studies carried out by the same research team in Japan showed that tilted anticyclonic vortices induce the flow towards the wall to push low- (or high-) temperature fluids on the hot (or cold) wall, improving the wall heat flux. Motoki et al. [88] also found that optimised three-dimensional velocity fields achieve a much higher wall heat flux and much lower energy dissipation than those of plane couette turbulence. Furthermore, introducing an anticyclonic quasi-streamwise vortex in laminar wall-bounded shear flows has confirmed significant heat transfer enhancement compared to that of a cyclonic or purely streamwise vortex. Shear flow turbulence can significantly increase heat transfer compared to laminar flow, but it results in friction loss as a consequence of simultaneous promotion of momentum transfer [88]. This phenomenon can also reduce blow-off and flashback in combustion systems [19].

#### 2.7.1.1 Micro-geometry Design and Dimensions

Several considerations have to be taken into account for the microstructured surface geometry. Previous experiments by Bixler and Bhushan [89–91] have utilised a variety of riblet geometries, configurations, materials, fluids, and flow conditions for laminar and turbulent flow. Geometries include blade, sawtooth, scalloped, bullnose, butterfly wings, rice, and lotus leave geometries with continuous and segmented configurations in water, oil, and air. Important riblet parameters include spacing ( $s$ ), height ( $h$ ), and thickness ( $t$ ). Their results indicate that nature-inspired microstructured surfaces effectively reduce drag force in open and closed channel flow. These studies support the results shown by Motoki et al. [35,88] since they state that with appropriately sized riblets, vortices are lifted above the surface and presumably pinned at the riblet tips. Lifting reduces the total shear stress since vortices contact just the small riblet tips. Furthermore, Marschewski [92] found that microstructures with a herringbone-inspired shape passively enhance heat transfer in microchannels by efficiently triggering helicoidal fluid motion.

Other studies conducted by Fronk and Zada in 2016 [93] stipulate that microchannels offer very high heat transfer coefficients, but they also tend to result in large frictional pressure gradients, which are detrimental to the overall system efficiency. This represents a crucial cornerstone for the design of energy and combustion systems. Additionally, micro-geometries are more effective in turbulent versus laminar regimes [90], and in order to optimise their dimensions, simulating the interaction between the microstructured surfaces and turbulent flows would provide insight on the hydrodynamics performance that could potentially enhance heat transfer.

### 2.7.1.2 Wetting State

In addition to optimising the dimensions, the wetting state of the surface is an essential factor to be considered; single droplet heat transfer and drop distribution are highly affected by the contact angle [46]. Taking into account several studies [94–98] that concluded dropwise condensation is a spatial-temporal cyclic process with a consequence of time-dependent sub-processes occurring repeatedly. Zheng et al. [99] developed a guide (Figure 2.30) of the preferable wetting states for heat transfer enhancement based on the droplet life cycle stages, length and time scales. In this guide the red double arrow shows the droplet life cycle stages in which heat transfer is at its peak (preferable) while the undesirable area shows the stages that could represent a heat transfer barrier due to the amount of condensate on the surface. Thus, to achieve efficient dropwise condensation, the condensate must be removed from the surface so that it does not act as a thermal barrier [46].

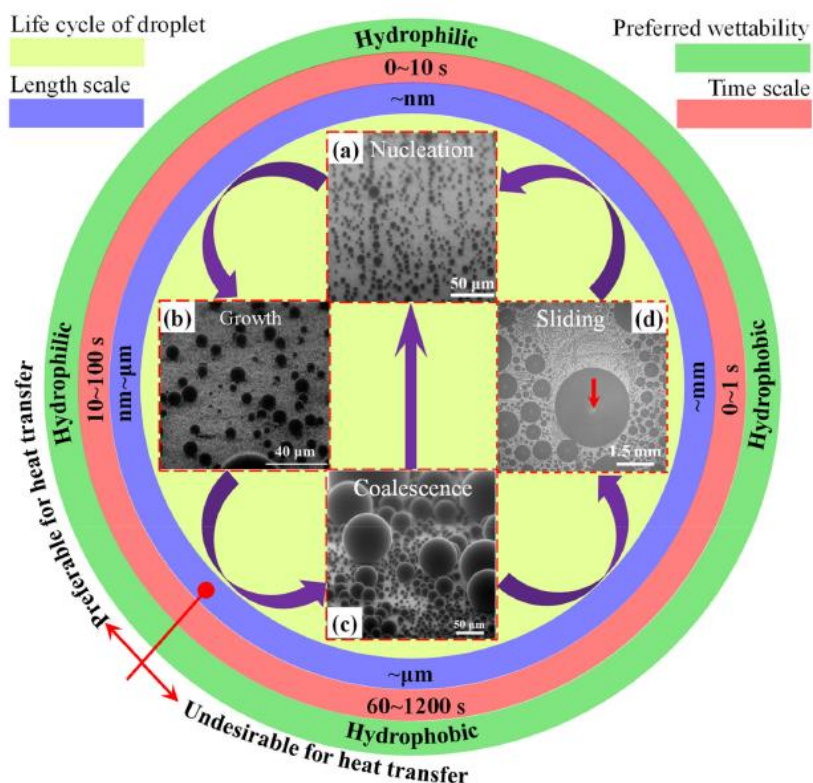
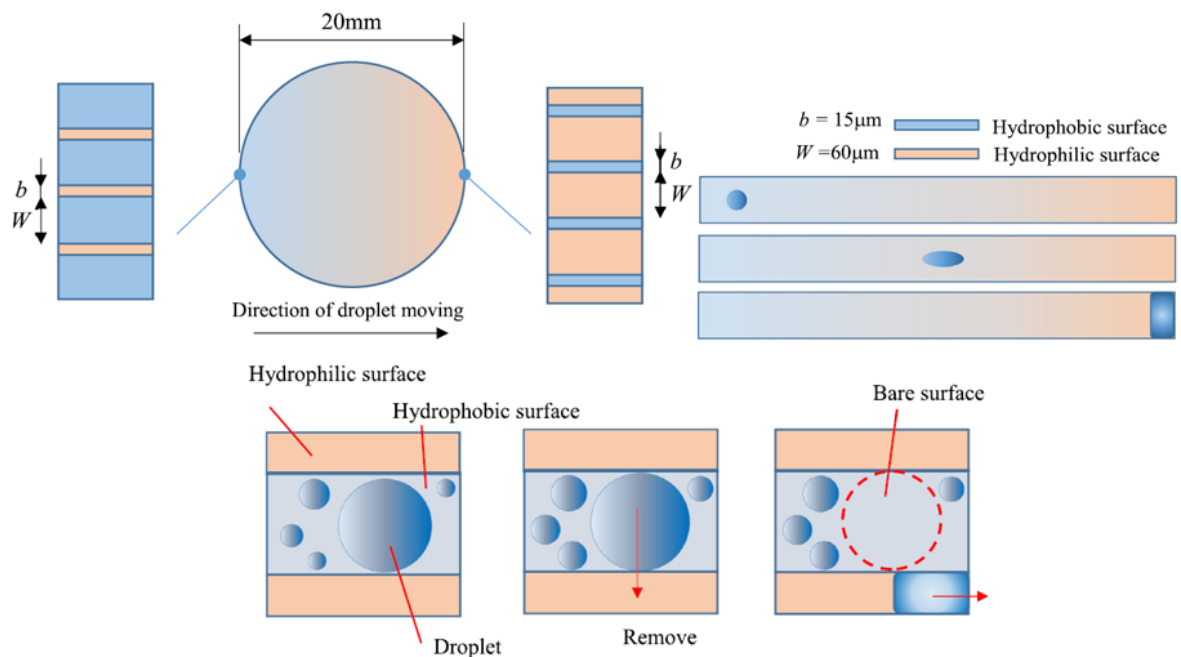


Figure 2.30. Preferable parameters for heat transfer based on the wetting state [99].

### 2.7.2 Biphilic Microstructured Surfaces

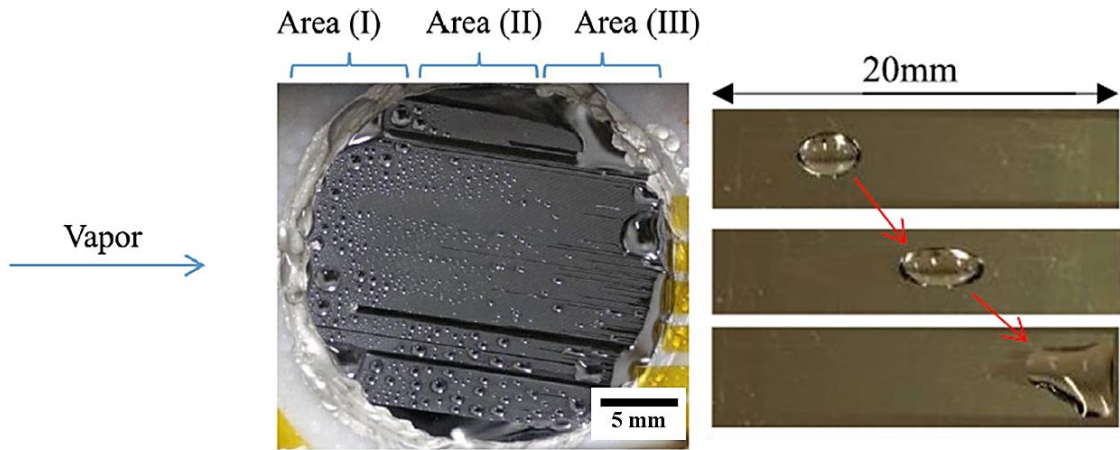
As mentioned before, Tokunaga and Tsuruta [48] achieved high heat flux values by using a biphilic surface with nano and microstructured surfaces (Figure 2.31). However, such patterns require a complex and expensive six-step process that needs chemical treatment. The biphilic pattern was made up of a 300-nm SiO<sub>2</sub> thin hydrophilic film (CA=35°) (created via oxidation on the silicon wafer) and a 360-nm CYTOP (Asahi Glass) hydrophobic layer (CA=100°).



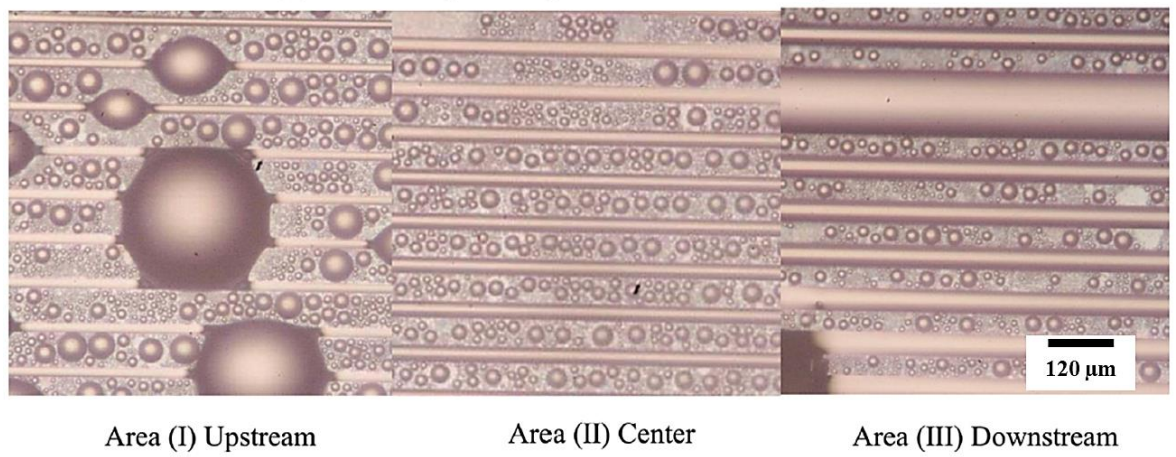
**Figure 2.31. Schematic image of a hybrid or biphilic condensing surface with wettability gradient.**

Adaptation from [48].

Albeit Tokunaga and Tsuruta's wettability gradient (Figure 2.32) enhanced the droplet drainage rate [48] when using modification at nanoscale, the high heat flux region increases the possibility of flooding due to the condensate; this could reduce the heat transfer coefficient by 40% [48,49]. Chemical treatments have been widely explored in both academia and industry since the 1950s [100]. Nonetheless, several limitations of chemical modification (such as inferior longevity and effectiveness, higher cost, and inability to translate lab-based strategies to larger scales [53]) foster the opportunity to explore the potential of topographical modification techniques via surface structuring/texturing.



(a) macroscopic images of the condensing surface



(b) microscopic images of each area

Figure 2.32. Condensation on a biphilic surface with wettability gradient. Adaptation from [48].



### 2.7.3 Microstructured Surfaces without Chemical Treatment

Topographical modification via surface structuring/texturing is a surface engineering method that does not require continuous maintenance or external additives and can be more enduring and robust than its chemical modification counterpart. Therefore, topographical modification can be considered a more reliable and cost-effective method for improving surface characteristics through passive mechanisms. Romano et al. [101] manufactured lotus-leaf-like surface structures via laser on a steel insert and on polypropylene replicas. Figure 2.33 shows the top view details and cross-section of the insert (a-b) and the tilted views and top views of the valley (1) and peak regions (2) of the polypropylene replicas (c-d).

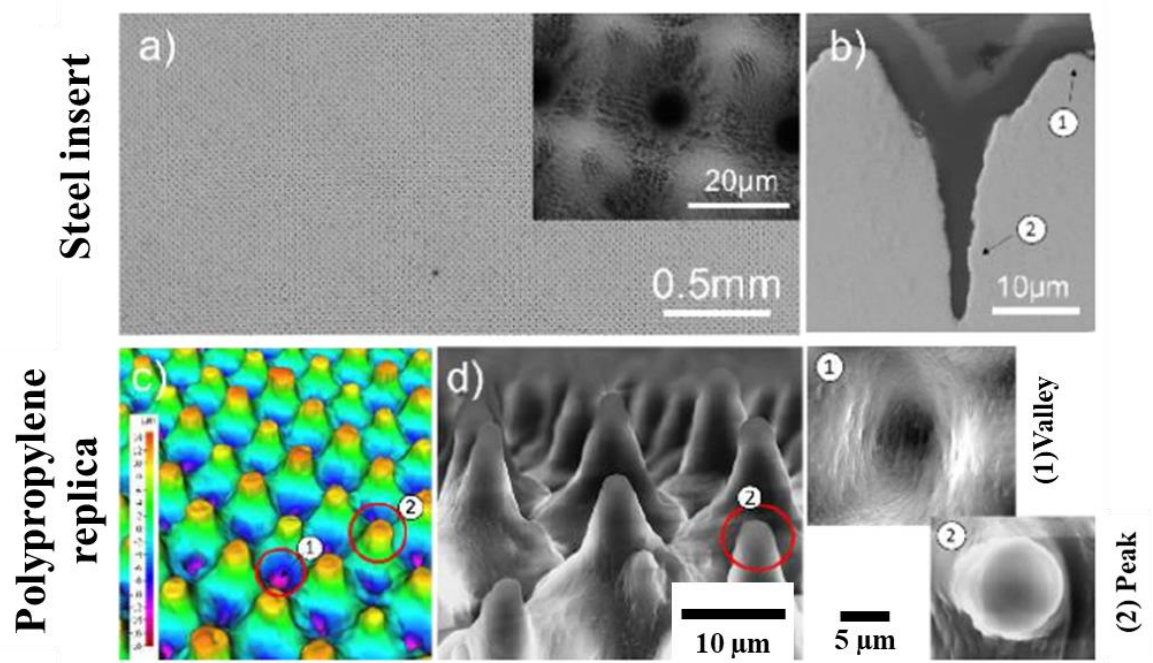


Figure 2.33. Lotus-leaf microstructured surface [101].

Rough surfaces may be either integral to the base surface or made by placing a roughness adjacent to the surface. Integral roughness is produced by machining or restructuring the surface. Rather than just increasing the heat transfer surface area, this technique intensifies mixing in the boundary layer near the surface, promoting artificial nucleation sites with a much higher performance than plain or smooth unstructured surfaces [68]. Furthermore, topographical modification at microscale has been shown to successfully reduce fouling, frictional pressure drop, and drag [19]. It also has the potential to enhance thermal harvesting, advanced electronics, biomedical devices, refrigeration systems, self-cleaning (building windows, medical equipment), wing de-icing (aerospace), windshields (automotive) and improve the permeability of membranes used in reverse osmosis, dehydration, and water purification systems [53].

#### 2.7.4 Summary and Identified Knowledge Gaps

Although one-wetting state microstructured surfaces have been successfully manufactured in the past without chemical treatment [101], the challenge is the manufacture of biphilic surfaces that can enhance each droplet life cycle stage without the use of chemicals. Therefore, microstructured surfaces created by topographical modification, rather than chemical modification; can assist in greater heat transfer during condensation by transferring energy from the large latent heat, associated with matter's phase change, to the surface of the device, instead of passing it to the drier air in energy systems, such as a heat exchanger. It is known in heat transfer that particle motions, such as vibration (wiggle about a fixed position), translation (move from one location to another), and rotation (revolve about an imaginary axis), give the particles kinetic energy, which can be related to momentum transfer [102].

After a comprehensive literature review on the use of microstructured surfaces as a passive technique for condensation heat transfer, it is inferred that they represent a viable passive mechanism method that should be evaluated to achieve the aim of the HPPE project. Microstructured surfaces can promote mixing within the boundary layer without significantly affecting the main flow. An innovative combination of micro-geometries can increase nucleation sites for droplet formation, growth and drainage rate to enhance heat transfer. Therefore, this study will first focus on designing, fabricating, and testing hydrophobic and hydrophilic structures/textures. This will be followed by designing, manufacturing, and testing a novel biphilic surface with a wettability gradient to enhance condensation heat transfer.

It is essential to mention that in addition to the thermal experiments for the heat transfer evaluation, isothermal experiments will be considered for the fluids dynamics (momentum transfer) evaluation. This is based on equipment availability and studies involving rough surfaces for up to 90% heat transfer enhancement [103]. Additionally, Medwell and Nicol used the heat-momentum analogy for roughness developed by Dipprey and Sabersky in 1963 to show that the benefits of rough surfaces are characterised by the roughness Reynolds number [104]. They introduced mixing in the condensate film via knurled roughness, and by increasing the roughness height, the thermal resistance of the viscous influenced region decreased while the film thickness ( $\delta$ ) remained constant. As a result, the enhancement produced by a given roughness size is directly related to the condensate film thickness.

## Chapter 3 : Methodology

The methodology followed in this doctoral research is described in this chapter. First, the research structure is presented and divided into four stages and three evaluation phases that are effectively embedded into each stage. The research stages are described in the first section of this chapter. Then the evaluation phases are listed and presented in more detail as follows: phase one is divided into three sections: design, manufacture, and characterisation; this is followed by phase two and then phase three, both containing experimental apparatus and design. Finally, the assessment criteria are explained at the end of the chapter.

### 3.1 Research Structure

Considering the previous work and the available resources at Cardiff University, this PhD research is divided into four research stages to compare different microgeometries parameters and into three evaluation phases (based on the design, manufacture and characterisation of the microstructured surfaces; fluids dynamics performance; and condensation heat transfer performance) to ultimately lead towards optimal surface textures designs, thus achieving the stated aim and objectives.

#### 3.1.1 Research Stages

This section gives a brief summary of the research stages. Figure 3.2 shows the procedure followed to name each workpiece, based on three distinct engineering parameters:

- a) Microstructure geometry (hydrophobic, hydrophilic and biphilic)
- b) Texturing technique
- c) Insert manufacturing technique

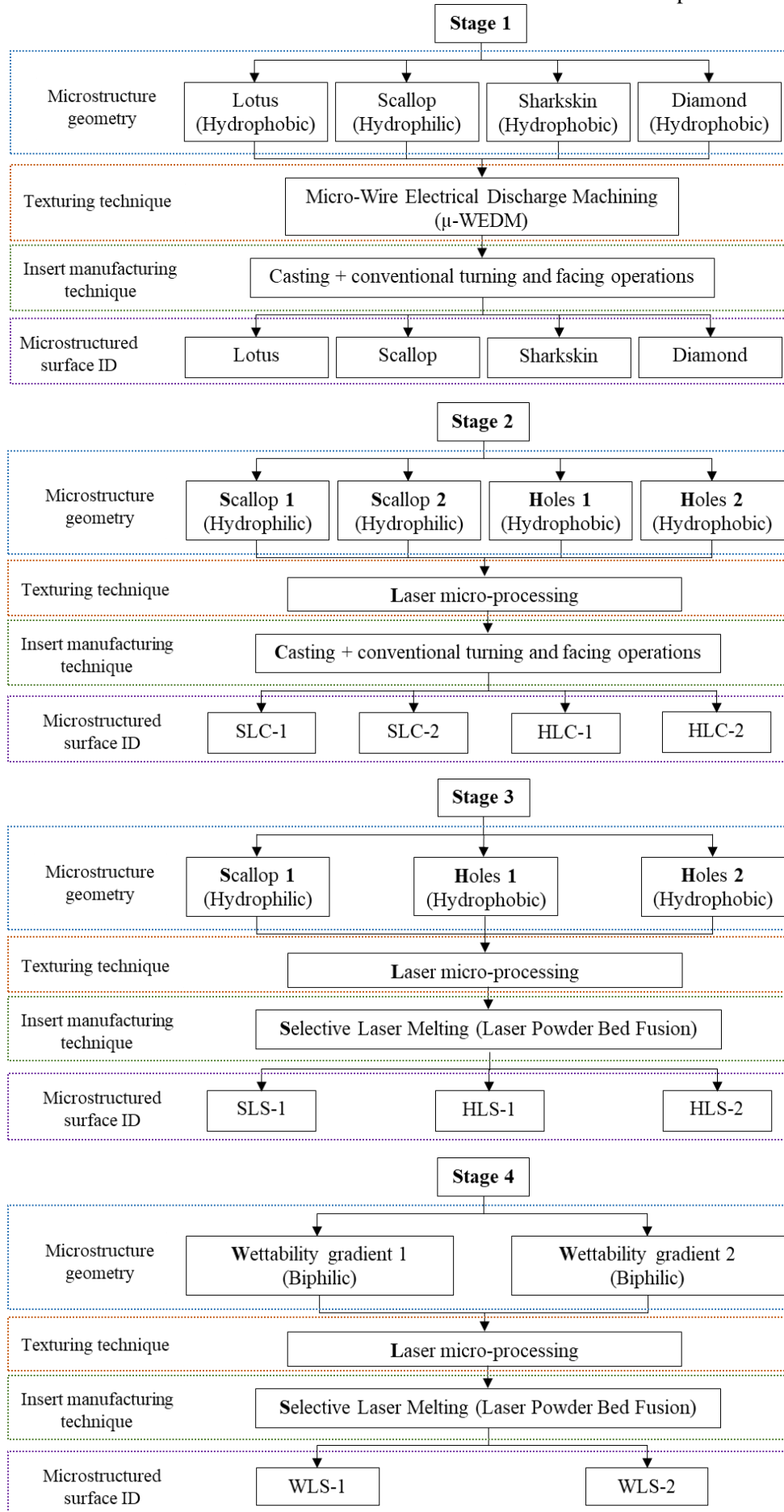
Unlike stage one, in which the name of the geometry was assigned directly to the name of the workpiece, the name or ID of the rest of the microstructured surfaces is given by three letters and a number. The first letter is related to the geometry, the second to the texturing technique and the third to the insert manufacturing technique, while the number is to differentiate if there is a variation in the dimensions of the same geometry. For example, in stage 2, "SLC-1" and "SLC-2", both workpieces have **scallop** geometries (hence the "S") which were created by **laser** (hence the "L") on inserts that were manufactured via **casting** (hence the "C"), the numbers 1 and 2 denote a difference or variation in the dimensions of the geometry.

The first stage is based on biomimetic engineering research previously done at the School of Engineering in Cardiff University. The microstructures were created by Micro-Wire Electrical Discharge Machining ( $\mu$ -WEDM) over inserts manufactured via casting and conventional turning and facing operations. In this PhD research, the resulting hydrophobic and hydrophilic microgeometries were further studied, and their performance was compared against an unstructured surface.

For the second stage, considering the three evaluation phases during the first research stage, the geometry with the best overall performance (hydrophilic scallop) plus a new geometry (hydrophobic holes) were selected, both with a second variation in order to compare the two wetting states. Laser micro-processing, a faster, cleaner and more flexible manufacturing technique, was selected over  $\mu$ WEDM as the texturing technique for this stage. The insert manufacturing technique was kept the same as the first stage.

For the third stage, the hydrophilic variation with the best overall performance and both hydrophobic geometries were manufactured by the same texturing technique. The insert manufacturing technique was changed for an additive layer manufacturing technique, laser powder bed fusion which has a much more stable production process and is a much faster technique than traditional metal casting [105]. This technique also allows for more design freedom, a high level of details and customisation for further research with more complex workpieces for the High Peak, Perishable Energies project.

Finally, for the fourth and last stage, a novel geometry was designed combining the hydrophilic and hydrophobic microstructures that achieved the best overall performance in previous stages. The aim is to create a biphilic wettability gradient. Two variants of this design were produced based on the two possible sequences of the manufacturing procedure used. For variant 1, the hydrophobic features were manufactured first, followed by the hydrophilic geometries. For variant 2, the hydrophilic features were manufactured first, followed by the hydrophobic features. The phases used in each research stage are described in more detail in the following sections.



**Figure 3.1. Research stages summary and ID procedure.**

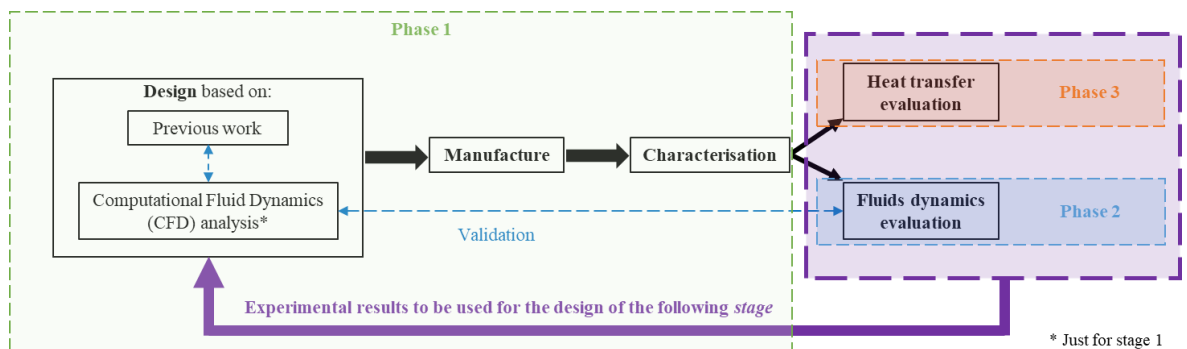
### 3.1.2 Evaluation Phases

All four research stages use three similar phases for designing, manufacturing, characterising, and evaluating the considered microstructured surfaces (Figure 3.1). The produced microstructured surfaces were compared against an unstructured surface during Phase 2 and Phase 3. The phases are:

Phase 1: Design, manufacture and characterisation

Phase 2: Fluids dynamics evaluation

Phase 3: Heat transfer evaluation



**Figure 3.2. Evaluation phases summary.**

Based on previous work (literature review), a microstructured surface design would ideally be optimised through CFD analysis to be then manufactured. Once the manufactured workpieces are ready, they would be characterised to compare the real dimensions with the design parameters. The heat transfer evaluation would help choose the design with the best performance to achieve this project's objectives, while the fluids dynamics evaluation would help validate the experimental and the numerical results. This was true for the first stage of the research; however, due to unforeseeable issues with the Hydro3D code used for the CFD analysis, the rest of the stages could not utilise it. Hence, the design of the subsequent research stages was based on the microstructures with the best performance in the fluids dynamics and heat transfer evaluation.

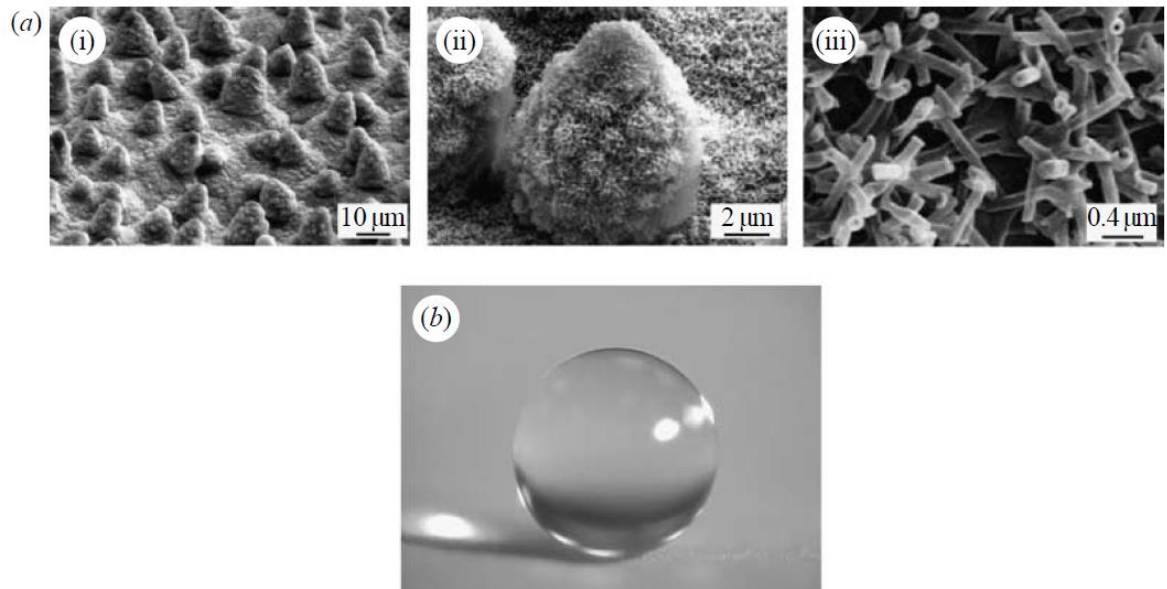
## 3.2 Phase 1: Design

The condensation phenomenon depends mainly on the surface characteristics [53]. On unstructured surfaces, it mainly depends on the nature of the fluid, the ambient conditions, the liquid-gas surface tension and surface energy, while on microstructured surfaces, their physical structure and the chemical heterogeneities also play a significant role [106]. Low hydrodynamic drag and self-cleaning properties can potentially enhance the performance of energy recovery systems by improving heat transfer during matter's phase change and controlling the boundary layer for drag reduction.

From macro to micro and nanoscale, the evolution and adaptation of species to the environment have inspired researchers to introduce bespoke and innovative solutions to complex engineering problems. The use of nature-inspired microstructures for energy applications is still under development [53]. However, by understanding the surface properties of natural species, biomimetic engineering can lead to the development of engineered materials with efficiently custom-made surface characteristics that can imitate physicochemical properties of plants and animals with prominent commercial and industrial interest in areas such as thermal engineering, fluid mechanics, transportation, electrical, electronics, construction, sportswear and biomedical sectors for energy recovery, reduced energy consumption, thermal and vehicle stabilisation, anti-fouling and surface self-cleaning.

### 3.2.1 Previous Work

The geometries design of the first stage was the result of previous work carried out in the school of engineering on biomimetic engineering [19]. The selection of the first geometries was based on the properties of lotus leaves (Figure 3.3) and shark skin (Figure 3.4) to improve the surface characteristics. The hydrophobicity of the lotus leaves facilitates self-cleaning and drag reduction, leading to easy drainage of water droplets while cleaning the surface to aid photosynthesis [107–109]. At the same time, the microscales or dermal denticles on shark skin promotes cleanliness and lower drag force that allows faster swimming capability of the shark species [90,110,111].



**Figure 3.3. (a) SEM images of lotus leaf, consisting of microstructures formed by papillose epidermal cells covered with three-dimensional epicuticular wax tubules on the surface (nanostructures). (b) Image of a water droplet sitting on a lotus leaf [109].**

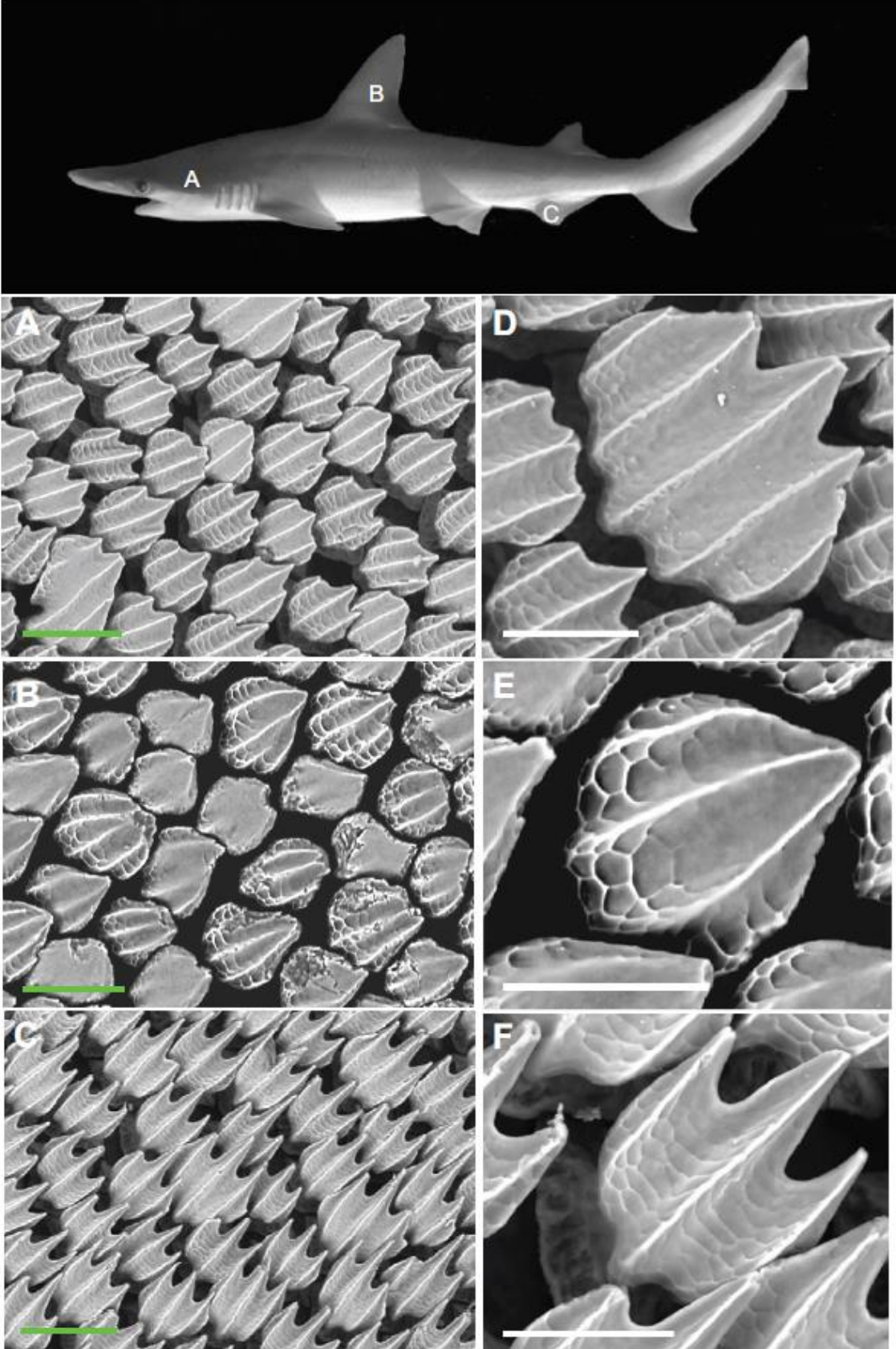
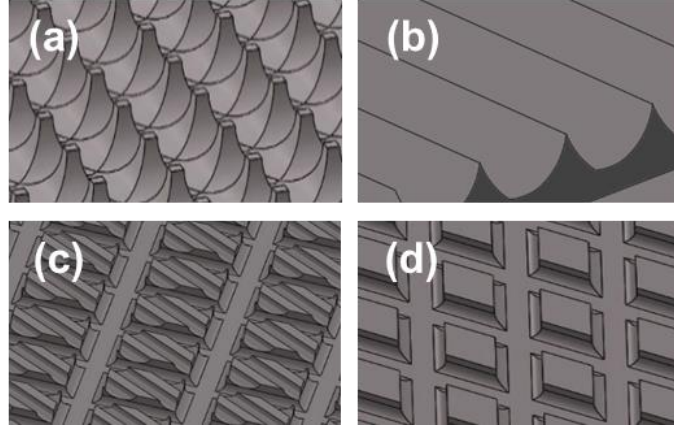


Figure 3.4. Environmental scanning electron microscope (ESEM) images of the bonnethead shark (*Sphyrna tiburo*) skin surface at different body locations. Green scale bars, 200  $\mu\text{m}$ ; white scale bars, 100  $\mu\text{m}$  [112].



Considering the complexity of these natural surface geometries and the limitations of the WEDM manufacturing technique, the closest achievable designs were selected based on the lotus leaves (Figure 3.5a) and the sharkskin (Figure 3.5c) and to extend the study, simpler designs such as diamond (Figure 3.5d) and scallop (Figure 3.5b) structures were also selected.



**Figure 3.5. Computer-aided drawing (CAD) for the microstructure geometries (a) Lotus, (b) Scallop, (c) Sharkskin and (d) Diamond [113].**

### 3.2.2 Computational Fluids Dynamics (CFD) Analysis

The biomimetic microstructured surfaces from stage one were previously analysed and optimised using an open-source code, Hydro3D, for their manufacture [19]. However, as mentioned in section 3.1, the design of stages 2 and 3 was based on the results of the respective previous stage (Chapter 4), while stage 4 information is available in Chapter 5. Regarding the design based on CFD analysis, the biggest challenge of modelling a turbulent flow over microstructured surfaces is the limitations of its computational cost at microscale. For this reason, the methodology used for the numerical analysis, or CFD analysis, was derived from previous research on the boundary layer of biomimetic microstructured surfaces at Cardiff University. A widely used open-source Large-Eddy Simulation (LES) based code for hydraulic engineering applications [114–116], Hydro3D, was modified and successfully validated to be used for microstructured surfaces analysis [19,113,117]. The code was developed to solve the following filtered Navier-Stokes equations on a cartesian block structure grid using the finite volume method for a turbulent, incompressible, three-dimensional flow field [118,119]:

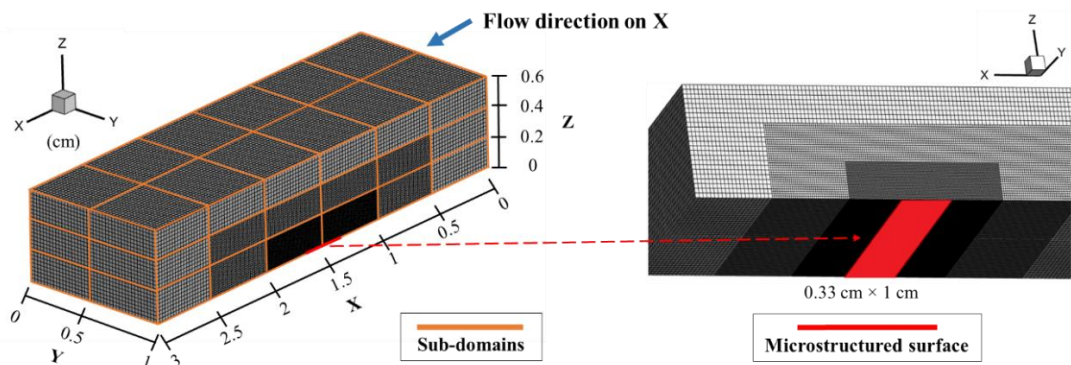
$$\frac{\partial u_i}{\partial x_i} = 0 \quad (3.1)$$

$$\frac{\partial u_i}{\partial t} + \frac{\partial(u_i u_j)}{\partial x_j} = -\frac{\partial p}{\partial x_i} + \frac{1}{Re} \frac{\partial^2 u_i}{\partial x_i \partial x_j} - \frac{\partial \tau_{ij}}{\partial x_j} \quad (3.2)$$

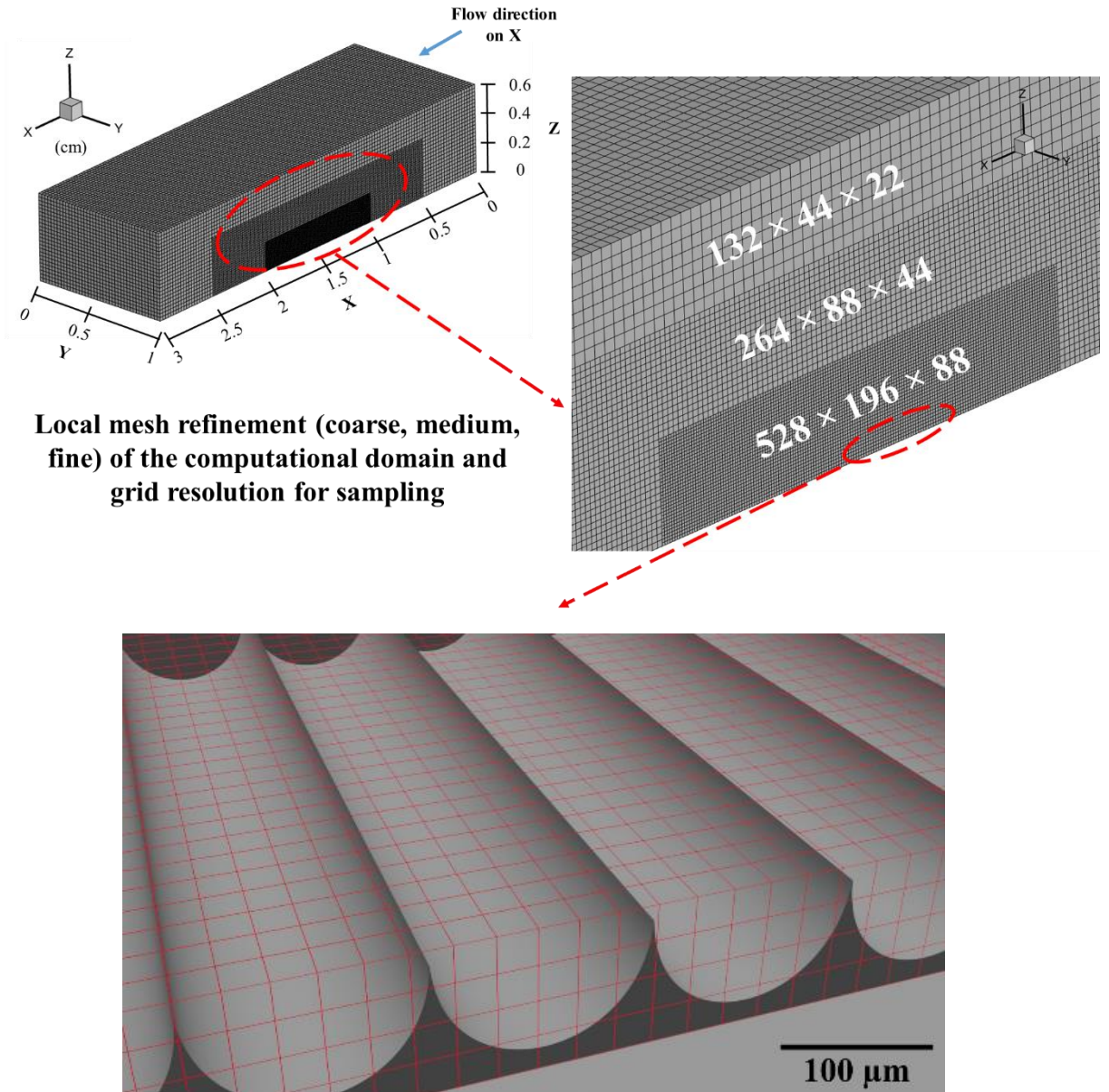
Where  $x_i$  and  $x_j$  are the spatial location vectors (i.e.  $x_i$  and  $x_j = x, y, z$  for  $i$  and  $j = 1, 2, 3$ );  $u_i, u_j$  ( $i, j = 1, 2, 3$ ) are the resolved velocity components in  $x$ -,  $y$ - and  $z$ - directions, respectively, normalised by the velocity  $U$ ; and  $p$  is the resolved pressure divided by the density.  $Re = UL/\nu$  is Reynolds number, where  $\nu$  is the kinematic viscosity, and  $L$  is the reference length scale.

This mathematical code for turbulence utilises the Immersed Boundary Method (IBM) to simplify problems relating to the grid around the object being modelled. Large-scale eddies are retained and directly solved by a transient solution in LES for incompressible flows. Meanwhile, the small eddies, which are smaller than the grid size, are removed and modelled using a turbulent Subgrid Scale (SGS) model such as Smagorinsky, Wall-adapting local eddy-viscosity (WALE) model and the One-Equation model. The WALE model was used to model the small-scale fluctuations to analyse the microstructured surfaces. Like most SGS models, it is based on an eddy viscosity assumption of modelling the subgrid tensor [120], here the subgrid viscosity dynamically works out with the square of the velocity gradient tensor rather than resolving through a strain rate like in a Smagorinsky-type model. This velocity tensor accounts for the effects of both strain and rotation rate of the smallest resolved turbulence fluctuations and recovers the proper near-wall scaling for the eddy viscosity without requiring a dynamic procedure. The model coefficient is proven to have a relatively constant value ( $C_w^2/C_s^2 \approx 10-12$ ) [120]. Additionally, the WALE model is invariant to any coordinate translation or rotation, and no test-filtering operation is needed [121]. This ensures the model's ability to calculate zero eddy viscosity in laminar shear flows automatically.

To tackle the challenge that microstructured surfaces present, through parallelised domain decomposition with Message Passing Interface (MPI), the computational meshed domain was divided into 36 smaller sub-domains (Figure 3.6), and by using Local Mesh Refinement (LMR), the mesh was refined by a 50% reduction in size between neighbouring levels from a coarse mesh for domains far from the microstructured surface to a finer mesh in domains at the vicinity of microgeometries, concentrating the computing effort on the most critical parts of the domain [19] (Figure 3.7).



**Figure 3.6. Computational meshed domain divided into 36 sub-domains and microstructured surface location.**



**Figure 3.7. Local Mesh Refinement (LMR) of the computational domain and grid resolution.**

The pre-set computational domain for microstructured surfaces analysis presents a fully developed turbulent flow inside a channel over a patch of microstructures on the lower wall aligned with the direction of the flow. The bottom boundary condition of the computational domain is no-slip, while the upper and lateral boundaries present slip conditions to eliminate the flow's wall effect over the duct's studied area [19]. In order to ensure a fully developed turbulent flow, a pre-set Synthetic-Eddy-Method (SEM) generates the inflow data as a velocity profile output file to be used as a pre-set velocity input for the next run. In order to compare and verify the code with the experimental phase of this project, the Reynolds number was set to 13,500, which is in the range of the experimental Reynolds numbers that can be obtained at the laboratory and the work performed by Al-fahham [19].

The ghost cell method was used to ensure the accuracy of the pressure and velocity values in the interface between the coarse and fine meshes (Figure 3.8). First, the values at the coarse computational grid cells are quadratically interpolated for pressure. Then, another quadratic interpolation is applied to calculate the fine ghost pressure. The edge-centre of the fine grids are calculated, and the arithmetic average of the fine-grid pressure is taken as the coarse grid pressure gradient to enforce the continuity of the gradient across the interface (Figure 3.8a). For velocity, the case is slightly more complicated since the calculation and interpolation should be done tangential to the local mesh refinement interface between fine and coarse grids (Figure 3.8b) and normal to the local mesh refinement interface between fine and coarse grids (Figure 3.8c) [119].

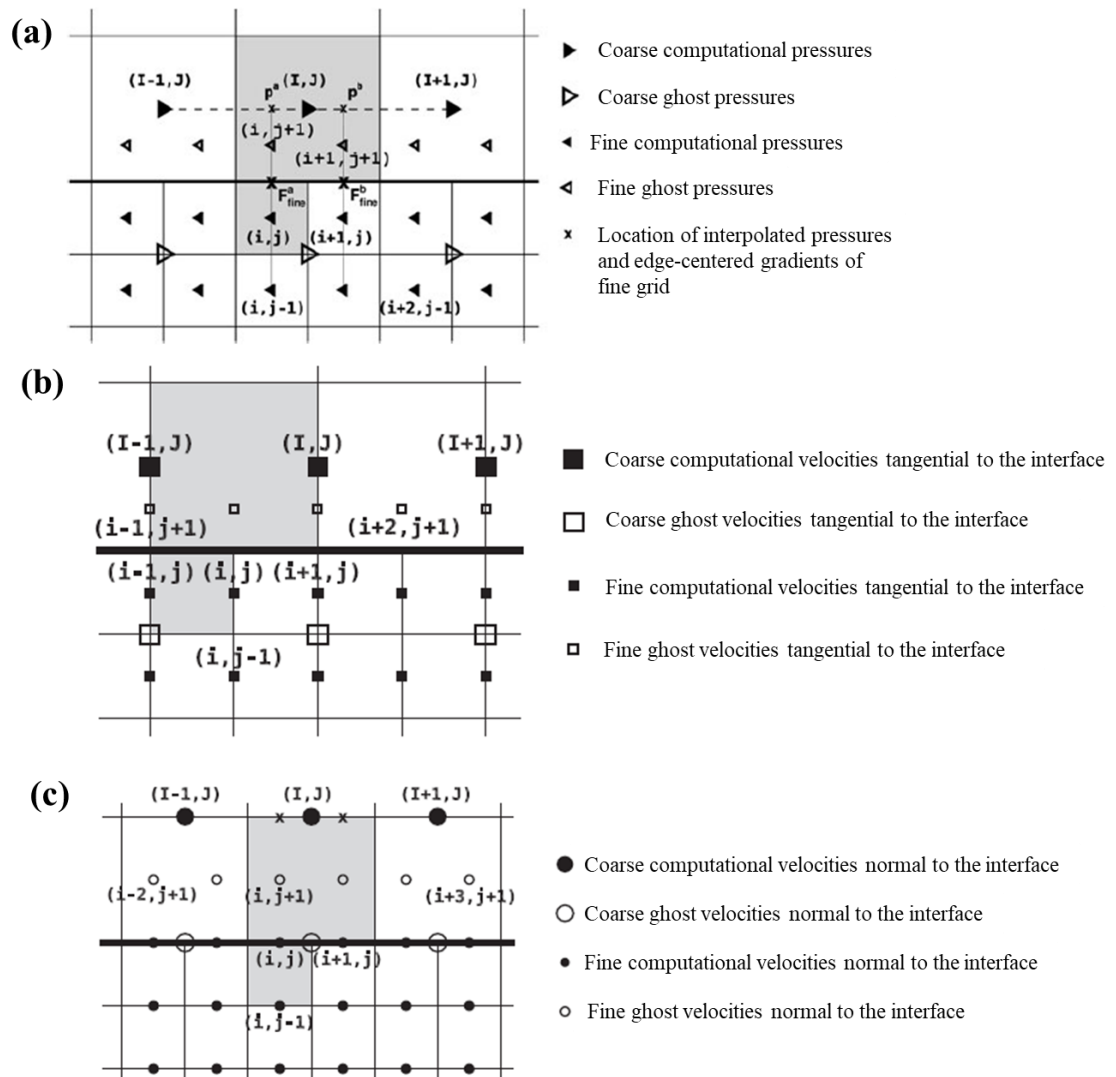
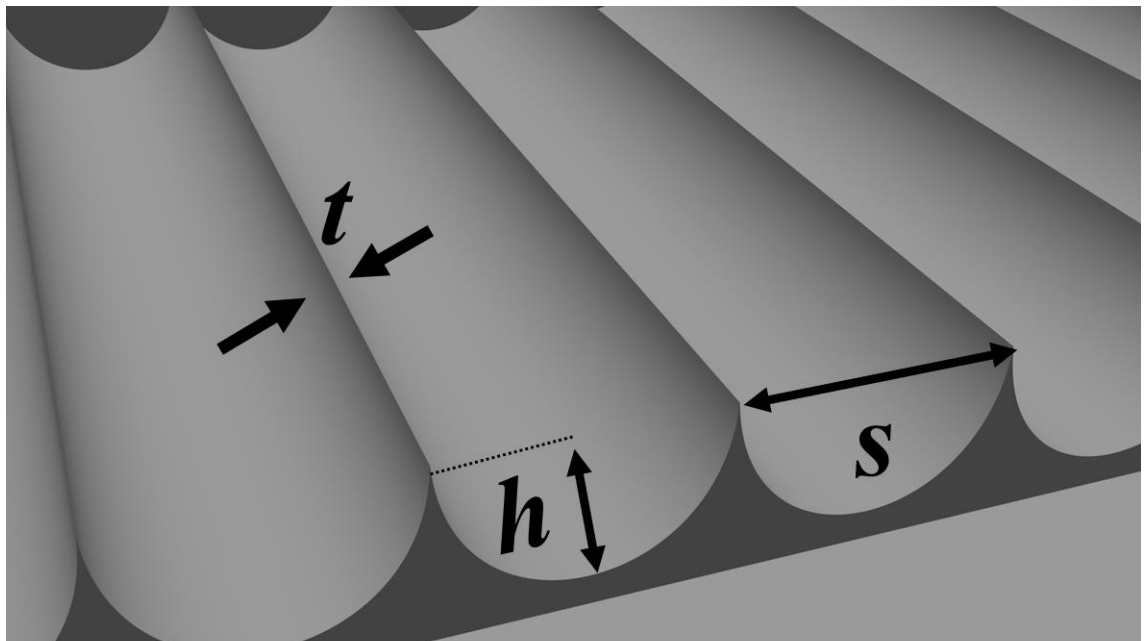


Figure 3.8. Ghost cell method (a) pressure locations, velocities (b) tangential (c) normal to the interface. Adaptation from [119].

The CFD set-up for this research was based on the validation of Hydro3D for microstructured surfaces to achieve the near-wall flow and save computational time. The microstructure geometries used to verify the Hydro3D code known as blade riblets were imposed in a small part of the computational domain to further study the flow before, over and behind the riblets [19,113,117]. The validation was based on drag reduction, the riblet height was kept constant for three models at  $h = 200 \mu\text{m}$  in order to have a non-dimensional height of  $\sim 10$  as studied by Martin and Bhushan [122] and the blade thickness was kept minimum at  $t = 12.5 \mu\text{m}$ , as the thickness plays a significant role in drag reduction. The space between riblets ( $s^+$ ) was also varied to be compared with the optimum  $s^+$  results reported by Bixler and Bhushan [89]. Figure 3.9 shows the riblet parameters for the Hydro3D validation, in which  $s$ ,  $h$ , and  $t$ , denote riblet space, riblet height, riblet thickness.



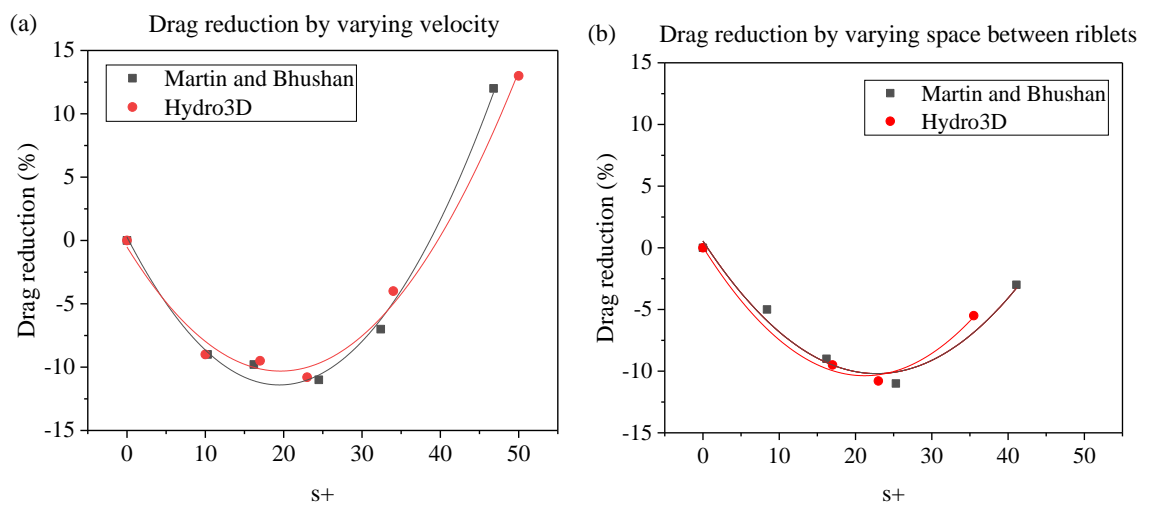
**Figure 3.9. Riblet parameters for the Hydro3D validation. Where  $s$ ,  $h$ , and  $t$ , denote riblet space, riblet height, riblet thickness.**

Therefore, the two approaches used by Al-fahham [19] for validation were: (1) Changing bulk velocity with constant  $h/s=0.5$ , which changed the shear velocity and  $s^+$ . The validation used values of  $s^+$  between 10-50 to cover what previous research has found to have the optimum drag reduction [123]. The second approach (2) was changing the space between blade riblets; three common ratios of  $h/s$  were chosen: 0.5, 0.8 and 1. Table 3.1 summarises the parameters used in each case for the code validation.

**Table 3.1. Cases tested numerically using Hydro3D for code validation. Adaptation from [19,113,117].**

Approach	Riblet space $s$ (mm)	Riblet height $h$ (mm)	Riblet thickness $t$ (mm)	Bulk velocity (m/s)	$h/s$ ratio	Dimensionless space ( $s^+$ )	Dimensionless height ( $h^+$ )	Dimensionless Thickness ( $t^+$ )
Varying bulk velocity	0.40	0.2	0.0125	5.0	-	10	5.0	0.30
	0.40	0.2	0.0125	3.0	-	17	8.5	0.48
	0.40	0.2	0.0125	2.0	-	23	11.5	0.65
	0.40	0.2	0.0125	1.5	-	34	17.0	0.87
	0.40	0.2	0.0125	1.0	-	50	25.0	1.15
Varying space	0.40	0.2	0.0125	-	0.5	17	8.5	0.48
	0.25	0.2	0.0125	-	0.8	23	8.5	0.48
	0.20	0.2	0.0125	-	1.0	34	8.5	0.48

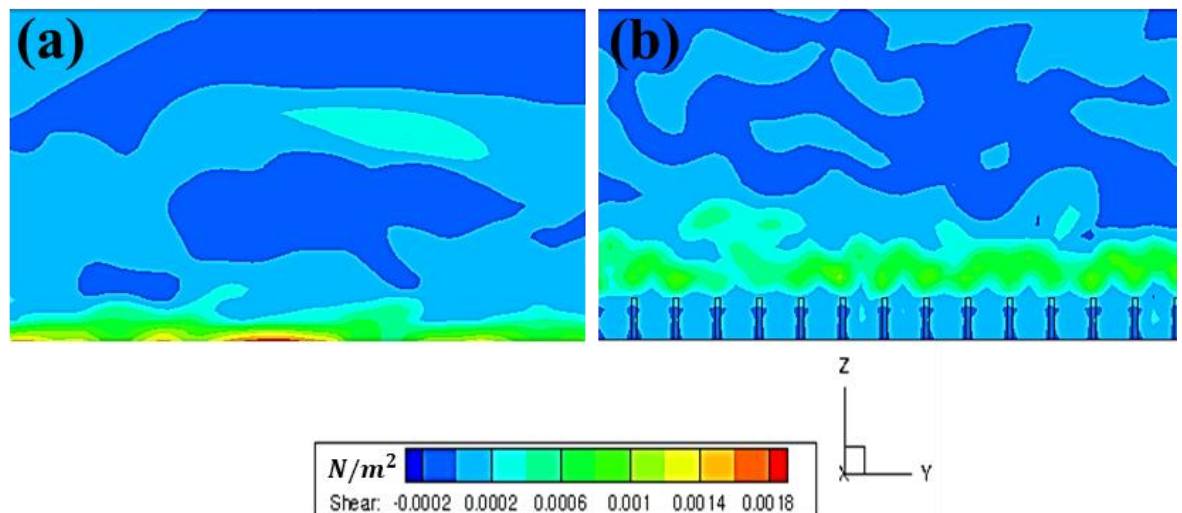
The drag reduction results were grouped in two sets of  $s^+$  values (Figure 3.10). In both approaches, the drag reduction increases after  $s^+ = 20$  due to eddies forming between the riblets and creating interference between the flow and the surface that reduces the friction and drag as a consequence. The first data set was obtained by varying the velocity, while the second set was recorded by varying the space between the riblets. The first set of results (Figure 3.10a) presented an acceptable agreement with the literature, showing that for the range of  $s^+$  between 0 and 45, the drag reduction followed the same tendency before diverging with high  $s^+$  ( $>45$ ). The second set of results (Figure 3.10b) also present proper alignment with the literature by exhibiting similar trends within a range of  $s^+$  between 0 and 30 before starting to diverge from Martin Bixler and Bushan's findings [89,122,123].



**Figure 3.10. Validation of the code through drag reduction as a function of  $s^+$ . (a) Approach 1: Varying velocity with  $h/s=0.5$ . (b) Approach 2: Varying space between riblets with constant height  $h$ . Adaptation from [19,113,117].**

The selection of the optimal microstructured surface can achieve a significant reduction in the drag by introducing the required flow disturbances into the boundary layer. Thus, boundary layer control can inhibit the drag-generating mechanisms. In terms of drag reduction, the shear stress at the wall plays a significant role in the transition from laminar to turbulent conditions, and its integration with the area is directly proportional to the drag force [124]. The planar geometry of the wall, in this case micro-geometries, have an influence on the turbulent boundary layer. They create flow perturbations that influence coherent structures in the flow, such as high-speed streaks and quasi-streamwise vortices, which achieve a significant skin-friction-drag reduction [125]. Additionally, the longitudinal and transversal protrusion heights in the boundary layer influence the wall shear stress which is a function of the viscosity and the velocity gradient at the wall. The effect of microstructures on the shear stress near the wall against an unstructured surface is shown in Figure 3.11. The shear stress in the microstructured surface was between 44.5% and 89% less than the generated in the unstructured surface because the riblets maintain the vorticities over the riblet tips, leading to the reduction of velocity fluctuations near the wall and thus decreasing the surface area attached to the high-velocity fluctuations, which in turn reduces the wall shear stress.

A user manual for microstructured surfaces simulations using Hydro3D in the Hawk supercomputer is available in Appendix B.



**Figure 3.11.** Shear stress ( $N/m^2$ ) near the wall for (a) unstructured surface (b) microstructured surface (blade geometry of height = 200  $\mu m$  and width = 280  $\mu m$ ). Adaptation from [19,113,117].

### 3.3 Phase 1: Manufacture of the Microstructured Surfaces

The microstructures were designed to be manufactured on the top surface of grade 316L stainless steel inserts (Figure 3.12). The height of the inserts was 25 mm, while the bottom 10 mm had a diameter of 28 mm and the top 15 mm had a diameter of 25 mm. The insert design is based on the manufacturing restrictions and the required characteristics of the experimental equipment (Section 3.5.1).

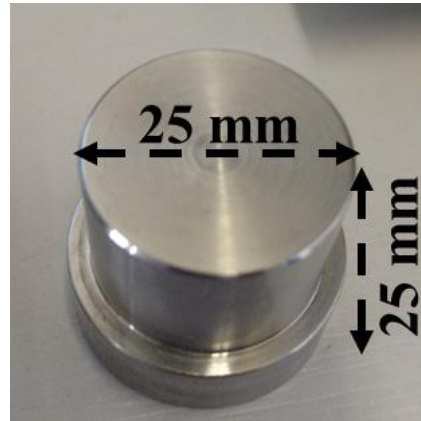


Figure 3.12. Grade 316L stainless steel insert manufactured via casting (Unstructured surface).

Hence, the manufacture is divided into two main categories, the *insert manufacturing techniques*, which are the techniques used to create the body of the surfaces on which the microgeometries were created and the *texturing techniques*, which are the techniques used to create the microgeometries on the top surfaces. The selection of the techniques was down to the availability of the equipment in the school of engineering.

#### 3.3.1 Insert Manufacturing Techniques

##### 3.3.1.1 Casting

Prior to the fabrication of the microstructures for stages one and two, grade 316L stainless steel inserts were manufactured via casting, followed by conventional turning (axial movement along the side of the workpiece) to remove material to form the bottom step and facing operations (radial movement along the end of the workpiece) to remove a thin layer of material to provide a smooth flat surface with a final roughness of 2  $\mu\text{m}$ .



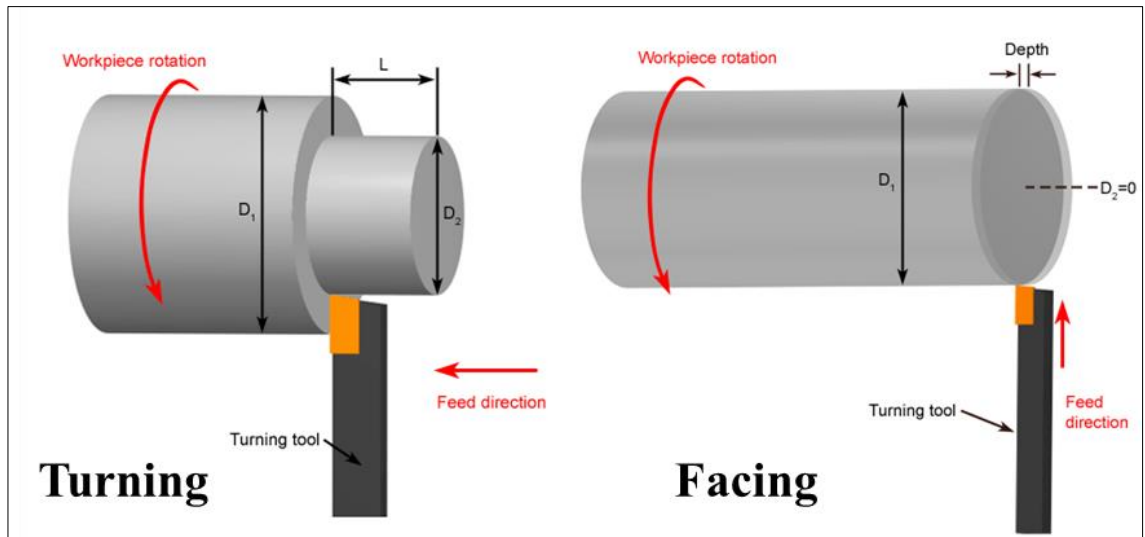


Figure 3.13. Conventional turning and facing operations © CustomPartNet. Adaptation from [126].

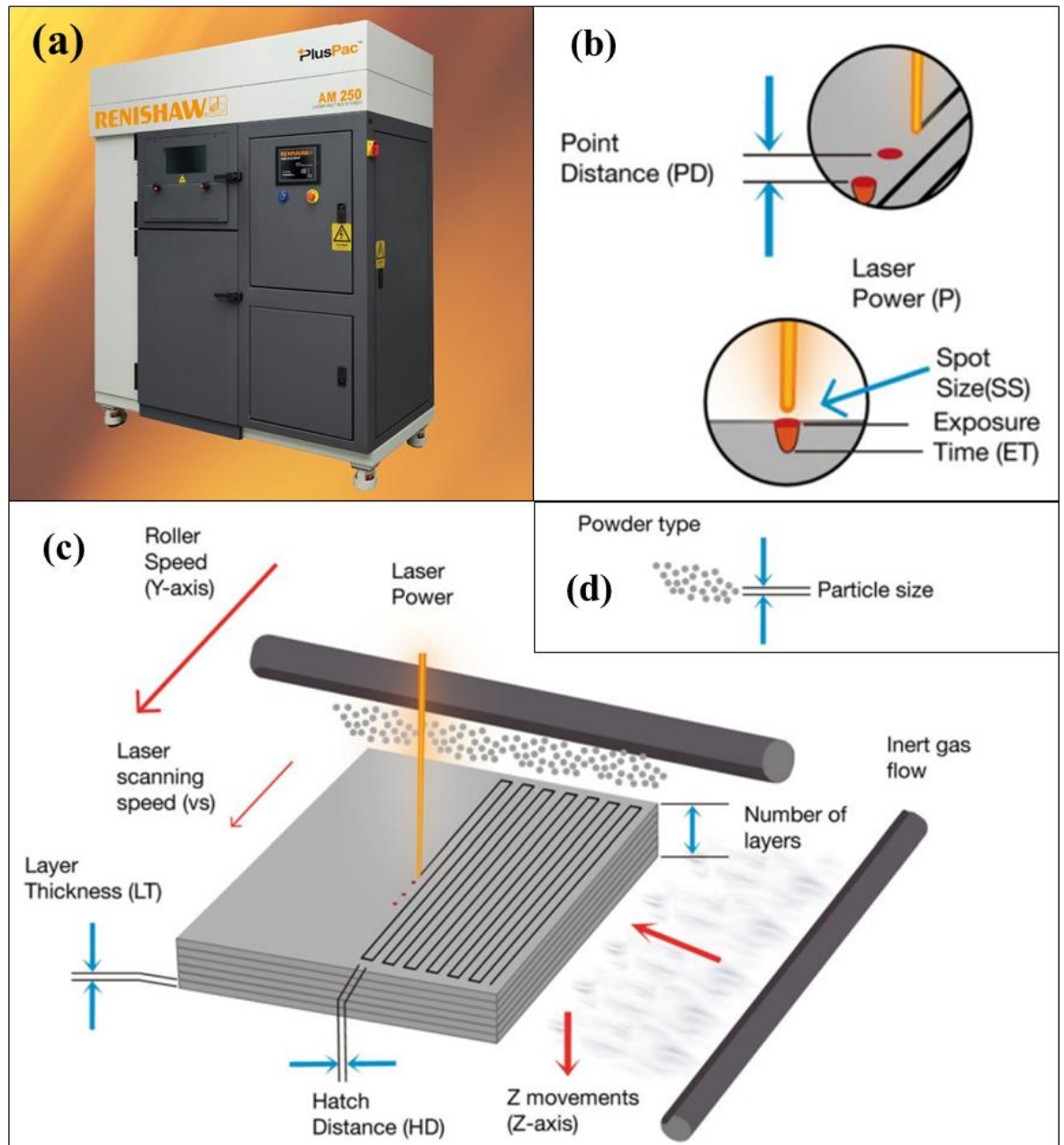
### 3.3.1.2 Laser Powder Bed Fusion

For stages 3 and 4, inserts were produced by Laser Powder Bed Fusion. This additive manufacturing process utilised SS316L powders of  $\sim 15\text{--}45\ \mu\text{m}$  average particle size, a 200 W laser power, with a beam spot size of  $56\ \mu\text{m}$  (Gaussian profile) and layer thickness of  $50\ \mu\text{m}$ . The point distance between two consecutive laser beam spots was  $60\ \mu\text{m}$  with a laser exposure time of  $80\ \mu\text{s}$ , while the hatch distance was set at  $110\ \mu\text{s}$ . This produced a relatively rough and uneven surface, as shown in Figure 3.14. Consequently, the top faces were treated with a nanosecond fibre laser ( $1064\ \text{nm}$  wavelength) to reduce surface asperities for the texturing technique used in stages three and four.



Figure 3.14. Perspective and top view of the stainless steel inserts.

Renishaw AM250's additive manufacturing, metal 3D printing, technology is a digitally driven process that uses a high-powered ytterbium fibre laser to fuse fine metallic powders into 3D objects direct from 3D CAD data (Figure 3.15). The metallic powder is distributed evenly across the build plate in layer thicknesses ranging from 20 to 100 microns forming the 2D cross-section. The layer of powder is then fused using the laser in a tightly controlled atmosphere. The process is repeated, building up the workpiece layer by layer [127].



**Figure 3.15.** (a) Renishaw AM250 machine (b) Laser parameters (c) AM process parameters (d) Powder material specifications. Adaptation from [127,128].

### 3.3.2 Texturing Techniques

#### 3.3.2.1 Micro-Wire Electrical Discharge Machining ( $\mu$ -WEDM)

The selected microstructure geometries for stage one were produced on the planar top faces of the stainless-steel inserts via micro-wire electrical discharge machining ( $\mu$ -WEDM) with a 100  $\mu\text{m}$  in diameter wire. Figure 3.16 presents the working principles of  $\mu$ -WEDM (AGIE Excellent) [129]; from a wire supply wheel (1) a wire (2) is fed via wire guide coils (3) and control units (4). The control units are usually made of diamond in order to resist abrasion. The thread is finally collected by a wire take-up wheel (5) or cut into smaller pieces when consumed. The wire acts as a cathode and the workpiece as an anode. Therefore, when the wire is placed close to the workpiece, a spark discharge occurs, which causes material from both the workpiece and the wire to be removed. The discharge is supported by a dielectric supply (6), which helps to cool the process and dispose of decompressed material. The spark gap (7) causes the machined contour to be slightly larger than the diameter of the wire (8); the width of this cut is known as Kerf (9).

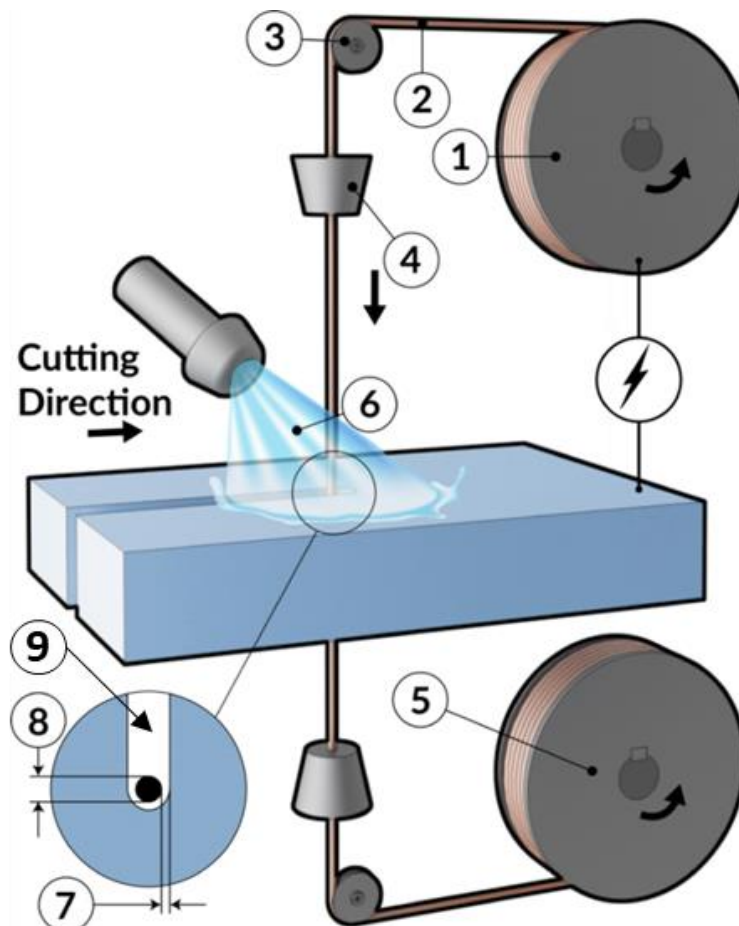


Figure 3.16. Representation of micro-wire electrical discharge machining ( $\mu$ -WEDM). Adaptation from [129].

The contour is controlled by the workpiece movements in the horizontal plane; due to this restriction, the microgeometries are limited to 2½D features. However, additional degrees of freedom can be achieved when the workpiece is rotated at specific angles for multiple cuts to produce 3D features. As mentioned before, the main geometries to be manufactured were Lotus and Sharkskin for their biomimetic surface properties; the first geometry needed two cuts while the second needed three cuts. Considering the manufacturing restrictions, the simpler geometries based on lotus and sharkskin, scallop and diamond, just needed one and two cuts, respectively.

### 3.3.2.2 Laser Texturing

Laser micro-processing, a faster, cleaner and more flexible manufacturing technique (Figure 3.17), was selected for the following stages to produce different geometries on the different types of inserts. The DMG-Lasertec 40 apparatus was utilised (Figure 3.18). The microgeometries were generated on the planar top faces of both types of inserts using the same laser source but with different laser energies (0.066 and 0.25 mJ), frequencies (10 and 80 kHz), beam scanning speeds (400, 600, 700 and 1000 mm/s) and set distances between the unidirectional textured grooves/laser tracks (25 and 60 µm). A pulse width of 65 ns and a Gaussian beam profile with a focal spot size of 32 µm were used in all workpieces.

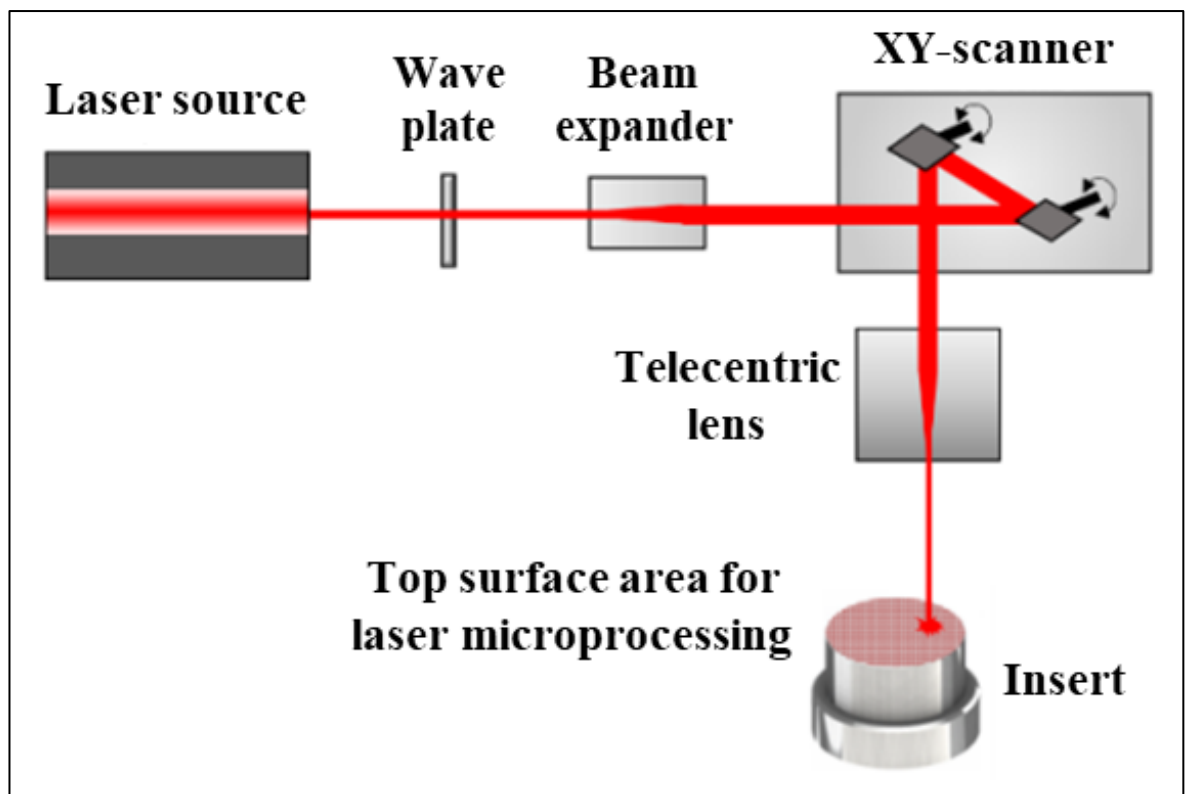


Figure 3.17. Laser micro-processing diagram. Adaptation from [101].

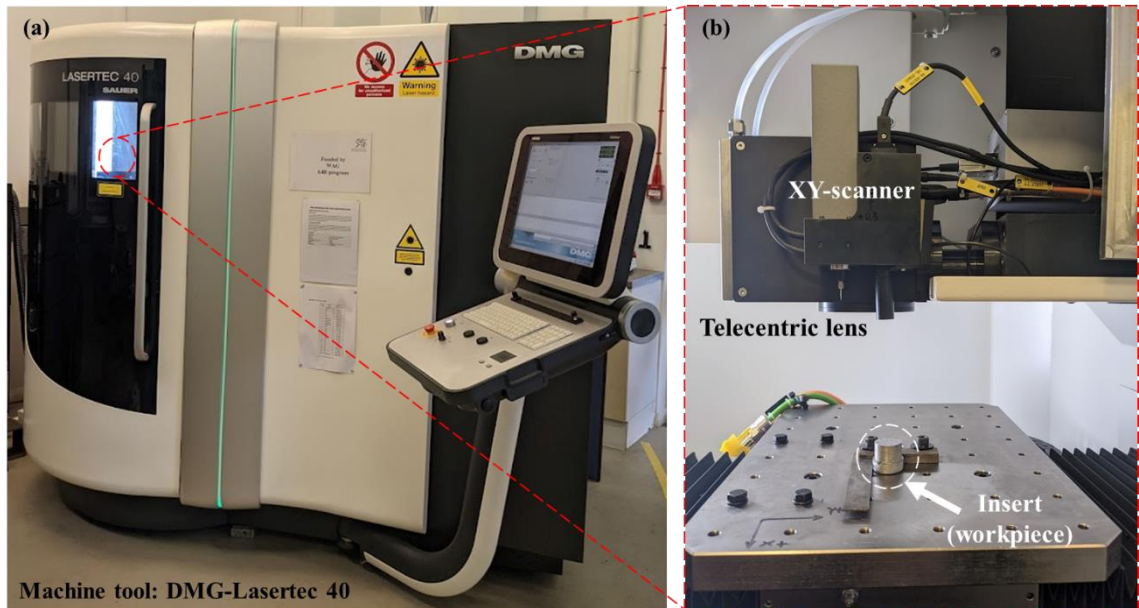


Figure 3.18. DMG-Lasertec 40. (a) Exterior view and (b) interior view.

### 3.3.3 Cleaning Procedure

Prior to the characterisation and experimental phase, the inserts were cleaned in an ultrasonic bath using 20 ml of acetone in a 50 ml beaker for 5 minutes (cleaning time) at ambient temperature and a frequency of 40 kHz. In addition, before every test, compressed air was used to eliminate any residues on the surface.

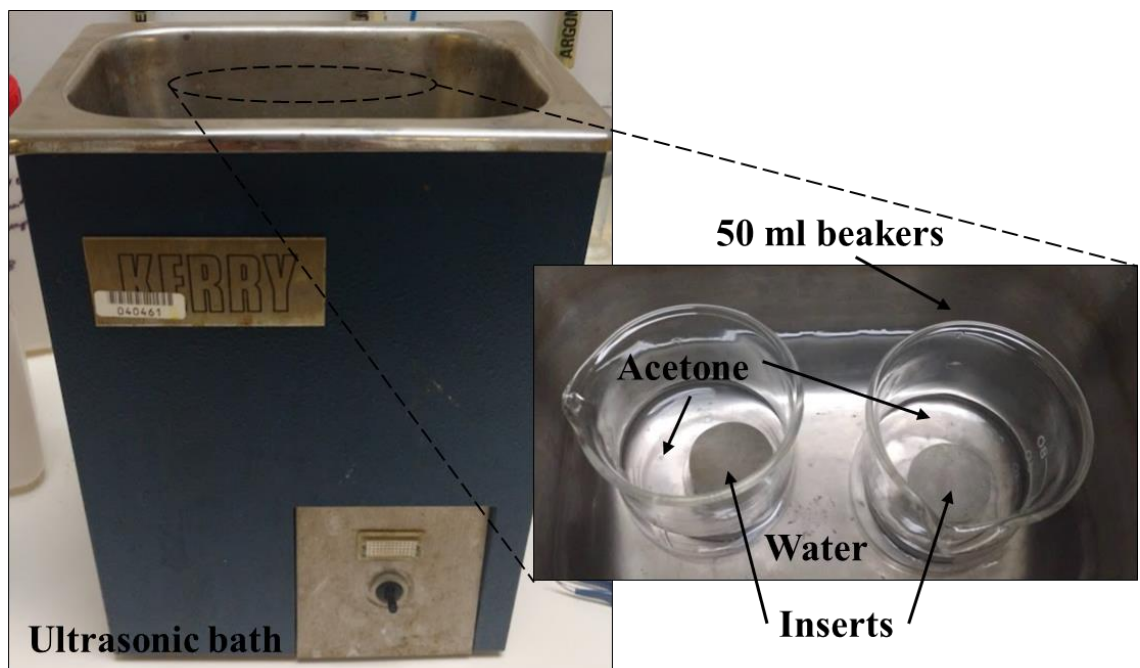


Figure 3.19. Cleaning apparatus.

### 3.4 Phase 1: Characterisation of the Microstructured Surfaces

#### 3.4.1 Area Scanning (3D Optical Profiler)

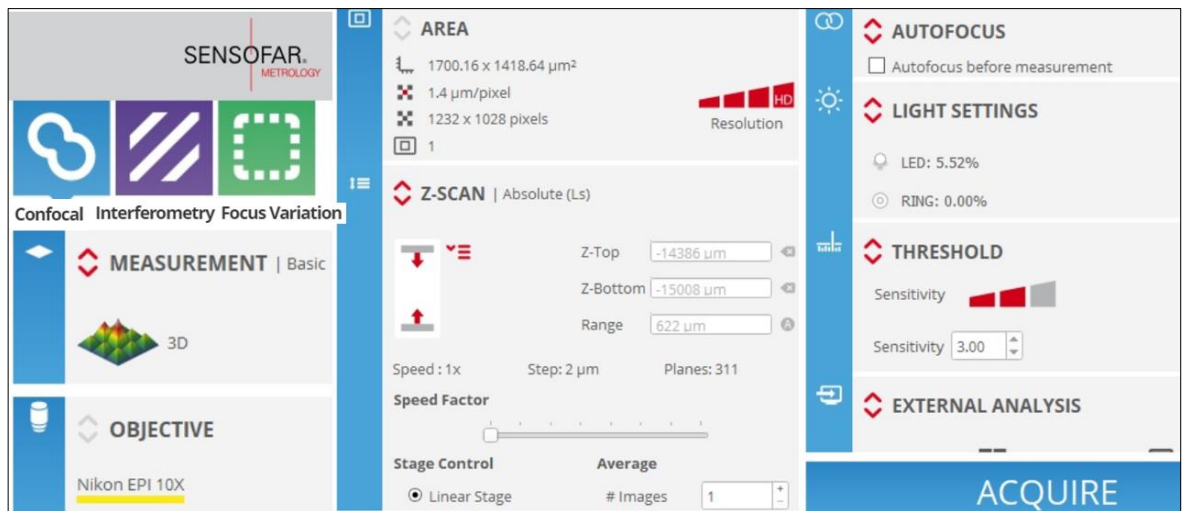
Sensofar is an optical profilometer that combines important optical measuring modes; the Smart model has one white light source that can provide the following measurement modes in the same sensor head: confocal microscopy, white light interferometry, focus variation, continuous confocal and confocal. The Smart is ideal for obtaining a fast, non-invasive assessment of a 3D micro and nano-geometry of technical surfaces, including surface resolution down to 0.1 nm, surface roughness, textures and structuring, and thin-film thickness measurements; depending on the application, it can be combined with a single LED light source (red, green, blue or white). One final advantage is the absence of moving parts, apart from a high-resolution motorised nosepiece for interchangeable objectives, which might complicate measurement repeatability [130].



Figure 3.20. Sensofar Smart equipment [131].

##### 3.4.1.1 Software Set-up

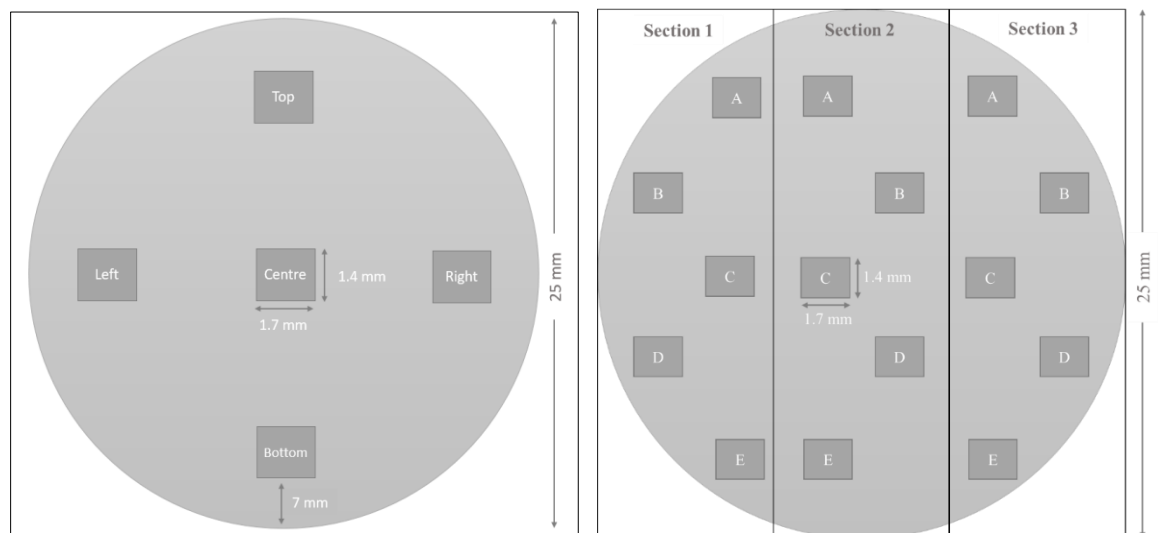
Sensofar works with an intuitive 3D interface software, SensoSCAN 6, which includes customisable tool features and powerful analysis algorithms that can be accessed using the Software Development Kit (SDK) to easily take measurements, display and analyse data [132,133]. Figure 3.21 shows the selected set-up for the inserts' scans. After acquiring the data for every scan, the option "Restore" from the "Data Analysis" (toolbox on the right side of the screen) was selected in order to fill the gaps for a better measurement result.



**Figure 3.21. SensoSCAN set-up.**

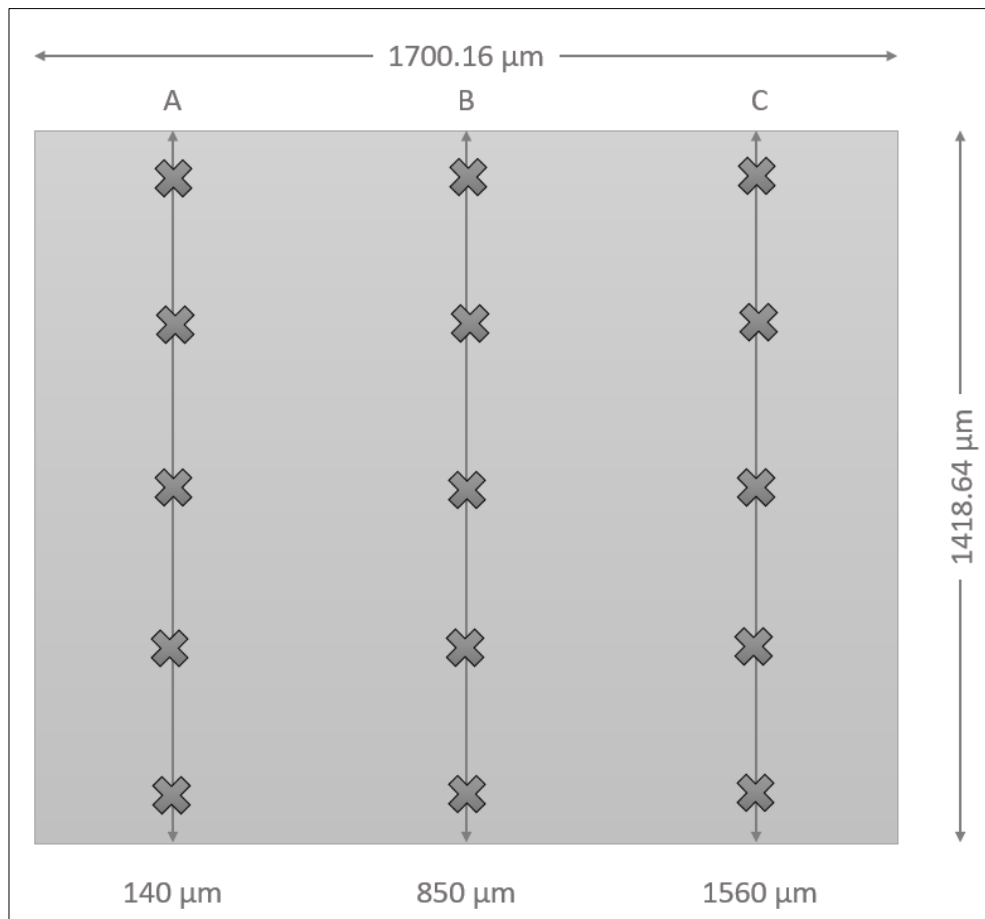
### 3.4.1.2 Sample Collection

For stages 1, 2 and 3, five 1.7 mm x 1.4 mm areas were scanned in each of the 25 mm inserts (Figure 3.22, left). While for stage 4, five areas of the exact dimensions were scanned in each of the three sections of both biphilic wettability gradient inserts (Figure 3.22, right). For the first three stages, the areas were identified as left, centre, right, top and bottom. For stage four, the areas were identified as A, B, C, D, and E.



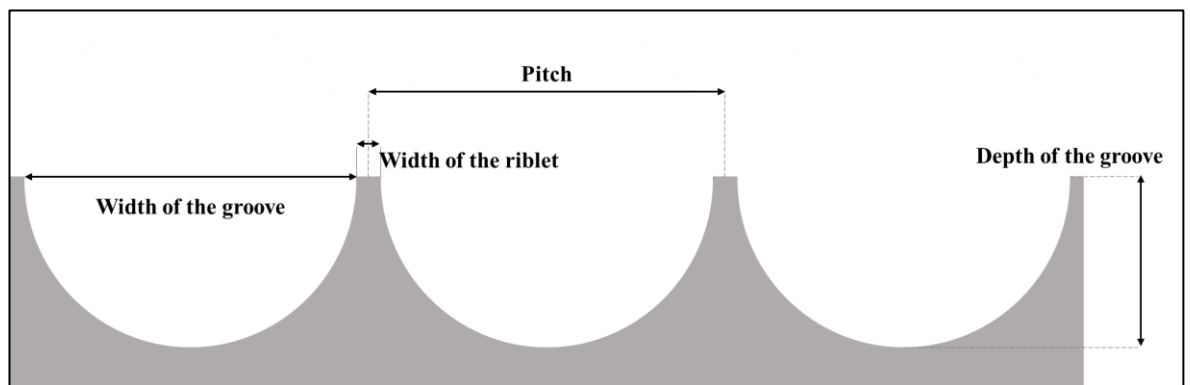
**Figure 3.22. Representation of the insert's top view with the scanned areas (left) for stages 1, 2 and 3; (right) for stage 4.**

Each scanned area was then divided into three sections: A, B and C, from where five measurement points were chosen (Figure 3.23).



**Figure 3.23. Representation of the measurement points in the scanned area.**

At each point, four different groove characteristics were measured for geometries based on riblet shape, as shown in Figure 3.24. Width of the groove, width of the riblet, pitch and depth of the groove. A total of 75 measurements were taken for each characteristic and sample. On the other hand, for the hydrophobic features, the diameter of the holes and the distance between them were measured (Figure 3.25).



**Figure 3.24. Groove characteristics.**



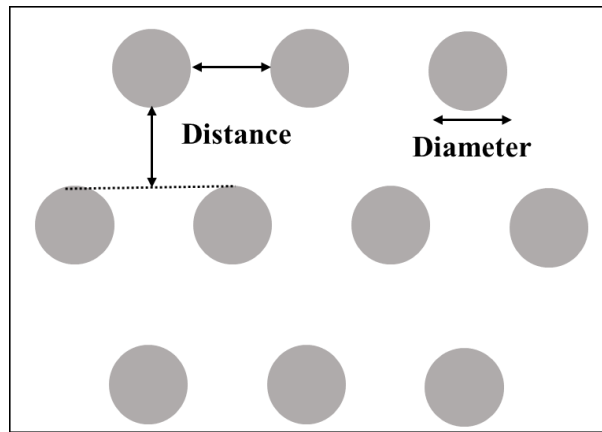


Figure 3.25. Representation of the characteristics of the hydrophobic features (holes).

### 3.4.2 Characterisation Data and CFD Link Program

The characterisation data generated by the 3D optical profiler can be processed to be used in the Hydro3D code to optimise the design of a specific microstructure. Sensofar generates a point cloud file of over 1.3 million points representing the scanned geometry of  $0.17 \text{ cm} \times 0.14 \text{ cm}$ ; however, Hydro3D can only handle geometries up to 100,000 points due to the required computational time they represent. In addition to the point cloud reduction, it is necessary to modify the coordinates of each point in order to locate them inside the desired computational sub-domain. For these reasons, a C# application was developed. A technical guide to process characterisation data into Hydro3D input files is presented in Appendix C.

First, based on the ghost cell method, the sample points are located every  $10 \mu\text{m}$  in the x-direction, every  $25 \mu\text{m}$  in the y-direction and every  $23 \mu\text{m}$  in the z-direction. The microstructured surface area in the computational domain should cover  $0.5 \text{ cm} \times 1 \text{ cm}$  in the finer mesh, which starts at  $x = 1.25$ ,  $y = 0$  and  $z = 0$  (Figure 3.26).

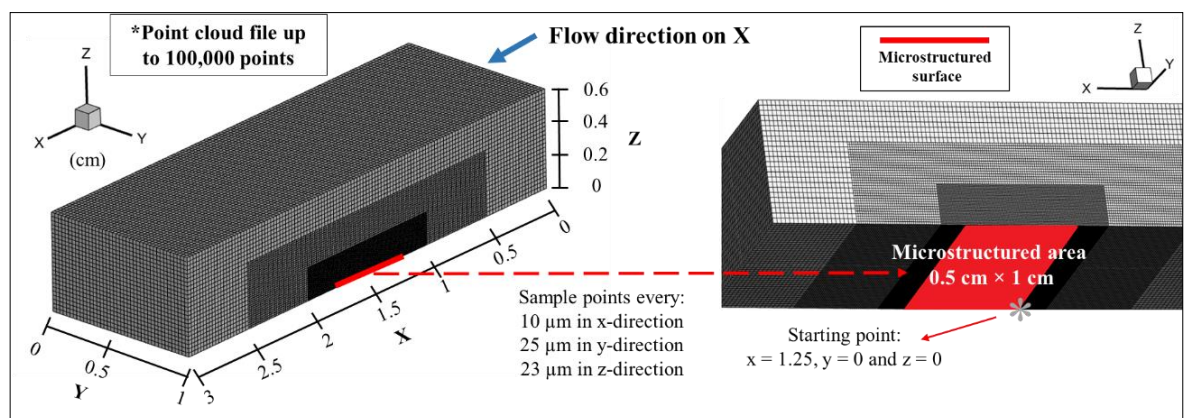


Figure 3.26. Hydro3D point cloud requirements.

The Sensofar output file covers a smaller area but contains ten times the number of points; additionally, the units are in  $\mu\text{m}$  while Hydro3D requires centimetres. The Sensofar point cloud characteristics are shown in Figure 3.27.

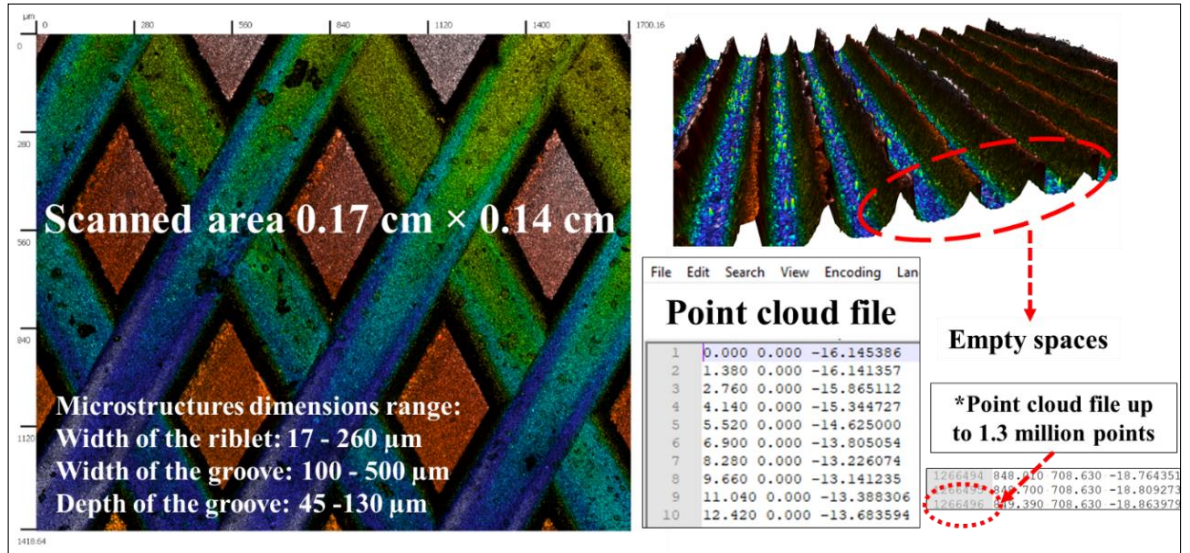


Figure 3.27. Sensofar point cloud characteristics.

In order to meet the Hydro3D requirements, the Sensofar point cloud file is processed as shown in Figure 3.28 by the C# application. After the file is generated, the number of points can be reduced by using the 'spatial' mode of CloudCompare, in which the space between the points can be set between  $5 \mu\text{m}$  and  $10 \mu\text{m}$  to meet the Hydro3D requirements for the ghost cell method without affecting the scanned geometry.

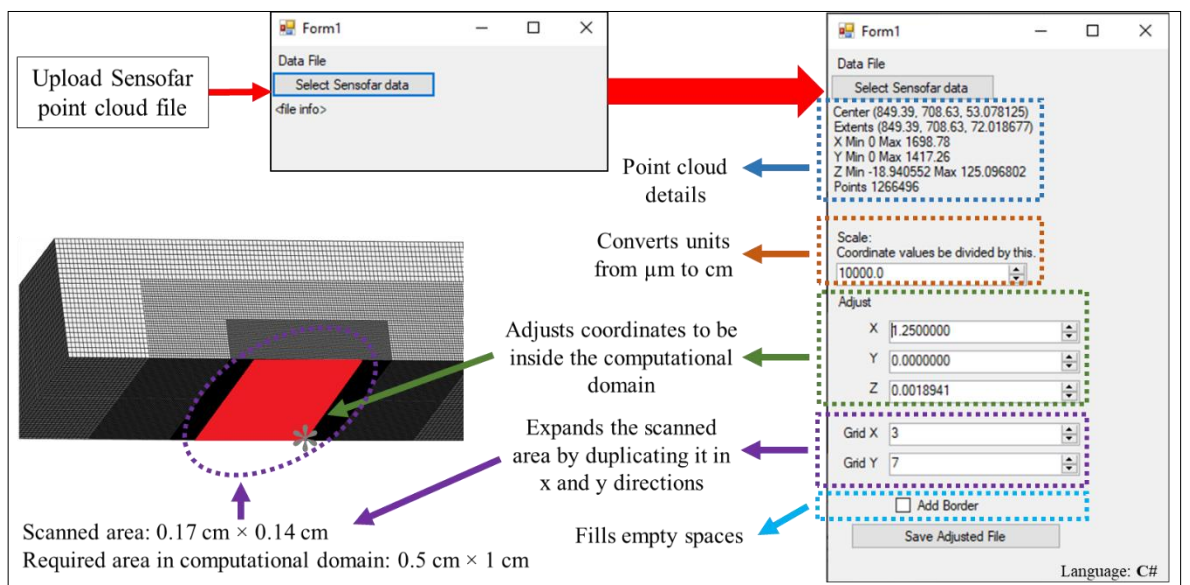
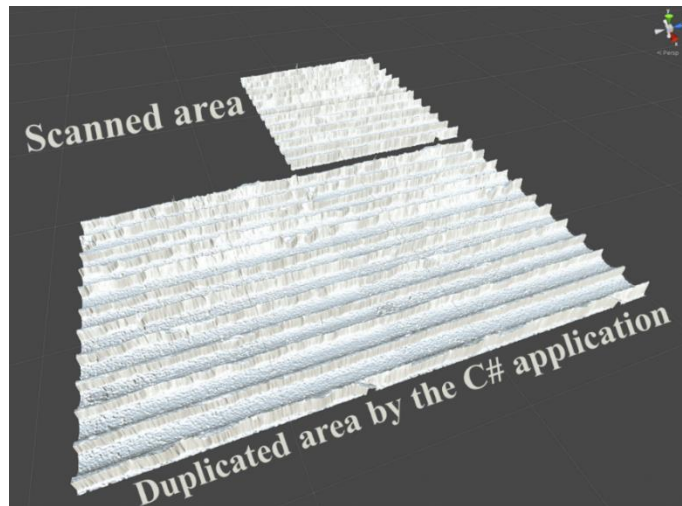
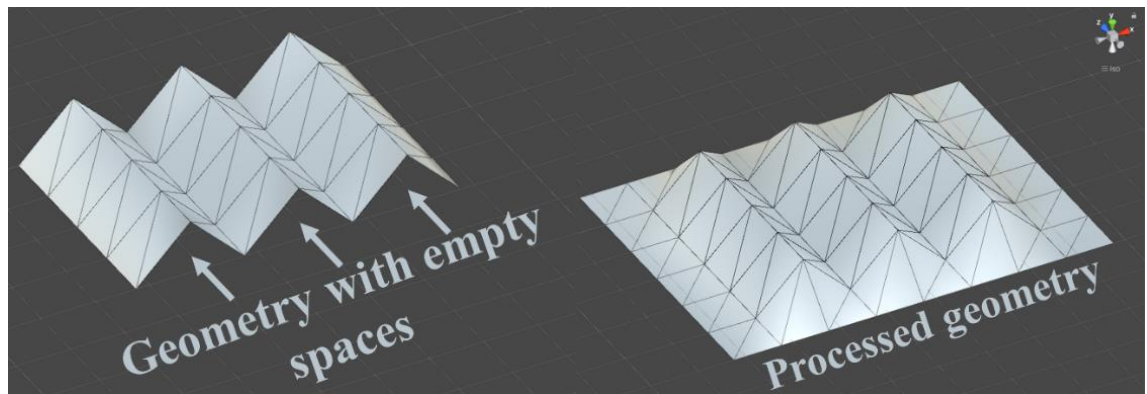


Figure 3.28. C# application for Sensofar point cloud file processing.

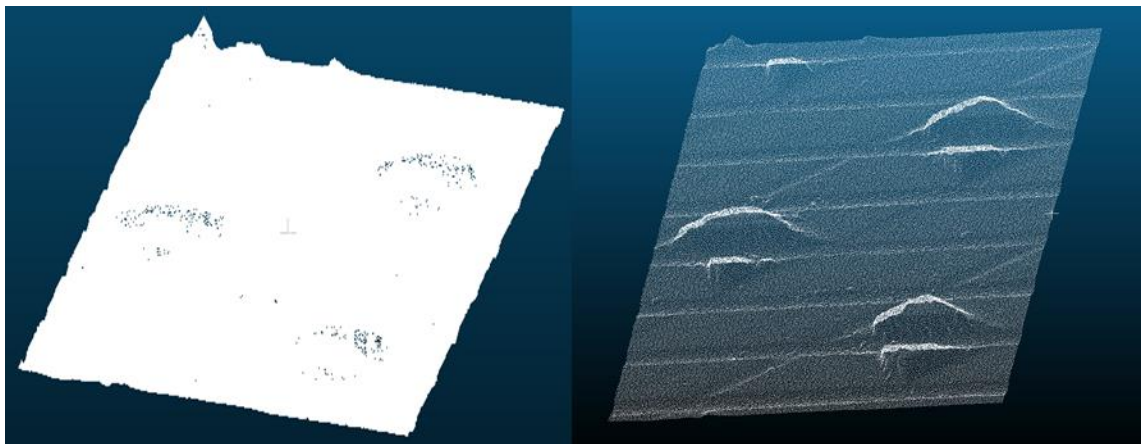
Figure 3.29 shows a scanned area and the result after being duplicated to meet the CFD requirements, while Figure 3.30 shows a geometry before and after filling the empty spaces. Figure 3.31 shows two point clouds; on the left, the original scanned of 1.26 million points, and on the right, the resulting set of data points after reduction.



**Figure 3.29.** Point cloud before and after are duplication.



**Figure 3.30.** Point cloud before and after processing the empty spaces.



**Figure 3.31.** Point cloud before and after points reduction.

### 3.4.3 High-Resolution Surface Analysis

The scanning electron microscope (SEM) produces a largely magnified image by using electrons instead of light to form an image. As shown in Figure 3.32 [134], an electron gun produces a beam of electrons at the top of the microscope; it follows a vertical path through the microscope, which is held within a vacuum. The beam travels through electromagnetic fields and lenses, focusing the beam on the sample. Once the beam hits the sample, electrons and X-rays are ejected from the sample. Detectors collect these X-rays, backscattered electrons, and secondary electrons and convert them into a signal that is sent to a screen similar to a television screen. This produces the final image. Because the metallic workpieces are conductive, they did not require preparation for the SEM. Images of 50X, 100X, 200X, 500X, 1000X, 2000X magnification were taken depending on the targeted features of the microstructured surfaces.

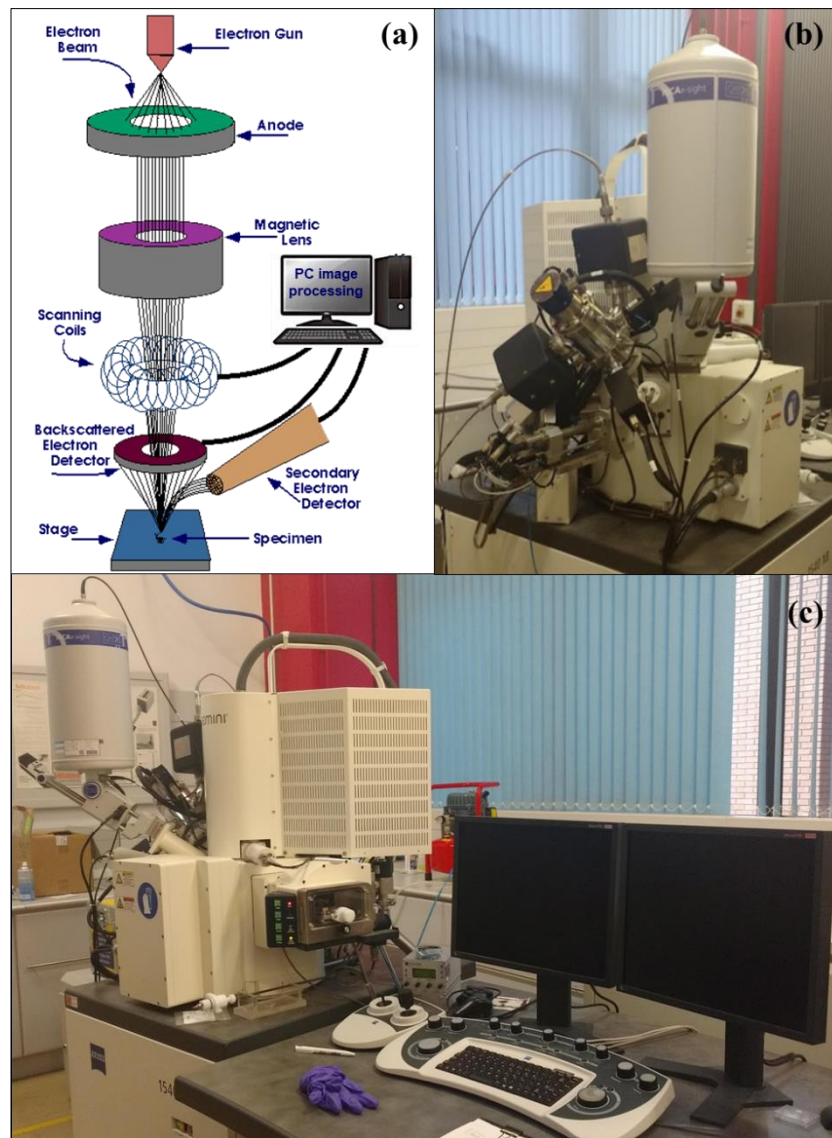


Figure 3.32. Scanning Electron Microscope (a) diagram [134], (b) back view, and (c) front view.

### 3.4.4 Wettability Characterisation

Surface wettability can be characterised by the static apparent contact angle  $\theta_s$  formed by the intersection of the liquid-solid and the liquid-gas interfaces of a sessile droplet resting on a surface, it not only depends on the droplet properties but also on a wide range of parameters, including the surface roughness or the surface microstructure. The interface where liquid, solid, and gas coexist is called the contact line [135]. The experimental approach uses a shadowgraph configuration (Figure 3.33) with a High Dynamic Range (HDR) mode imaging and image analysis to obtain the contact angle between a water droplet and the different microstructured surfaces. For this study, single water droplets of 0.05 ml were generated by a 3.0 ml pipette and allowed to travel vertically downwards towards the different microstructured surfaces. The distance between the pipette and the microstructured surfaces was 10 mm. Droplet contact angles were recorded by a Google Pixel 4a camera (12.2 MP dual-pixel, 1.4  $\mu\text{m}$  pixel width, Optical + electronic image stabilisation,  $f/1.7$  aperture and  $77^\circ$  field of view) coupled with a 4K High-Definition 100 mm Macro lens and back-illuminated by a diffuser-LED array in a traditional shadowgraph configuration inside of a shooting tent (Figure 3.33). The resolution for the contact angle experiments was set to  $4032 \times 3024$  (12.19 MP), and a High Dynamic Range (HDR) mode was used to take multiple shots at different exposures to create sharper and more defined images.

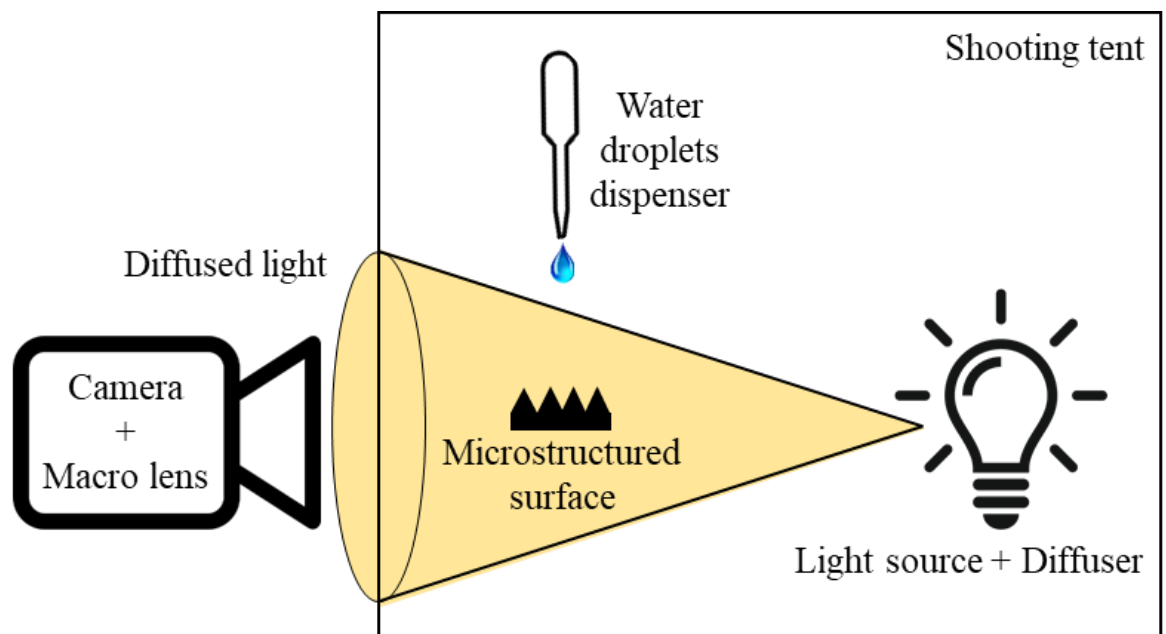
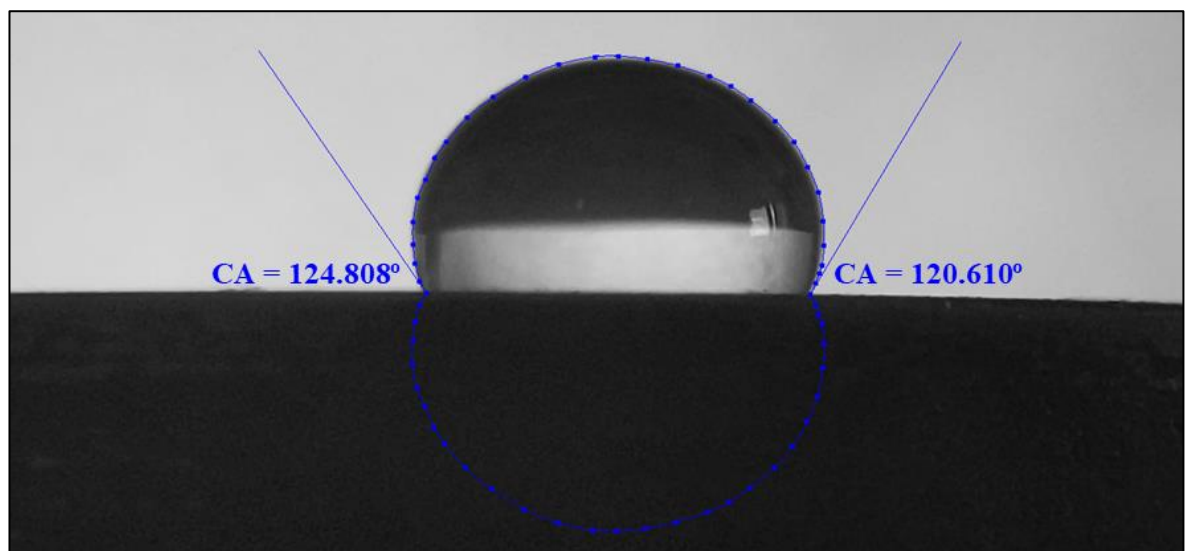


Figure 3.33. Shadowgraph configuration diagram.

High contact angled surfaces are known as hydrophobic ( $90^\circ - 150^\circ$ ) or super-hydrophobic ( $>150^\circ$ ) surfaces; they present a low degree of wetting, which indicates low solid surface energy or chemical affinity. On the other hand, surfaces with a low contact angle are known as hydrophilic ( $10^\circ - 90^\circ$ ) or super-hydrophilic ( $0^\circ - 10^\circ$ ) surfaces; their high solid surface energy or chemical affinity shows a high or sometimes complete degree of wetting. It is important to mention that the biphilic microstructured surface (stage 4) presented a fast drainage effect; as soon as the droplets pass through section 2 and section 3, the departure stage of the droplet is faster than expected, and it cannot be captured in pictures. Hence slow-motion 1/4x videos were filmed to then export frames to analyse the wettability behaviour based on static contact angle. The contact angles of the biphilic wettability gradient surface (Section 2 and 3) were obtained at 250 milliseconds; after this, the contact angles decreased to  $0^\circ$ , presenting a complete wetting state that helped with the departure of the droplets.

The image analysis was performed by ImageJ, a public domain Java image processing program. Two different plug-ins were used and manually corroborated using a virtual protractor. The first plug-in, 'DropSnake' (Figure 3.34), is based on B-spline snakes (active contours) to shape the drop [136]. Figure 3.35 shows the second plug-in, 'LBADSA' (Low-Bond Axisymmetric Drop Shape Analysis), which is based on the fitting of the Young-Laplace equation to the image data [137,138]. The wettability experiments were repeated twenty times for each microstructured surface and corroborated by using a virtual protractor technique to calculate contact angles (Figure 3.36).



**Figure 3.34. DropSnake technique for contact angles (CA) analysis.**

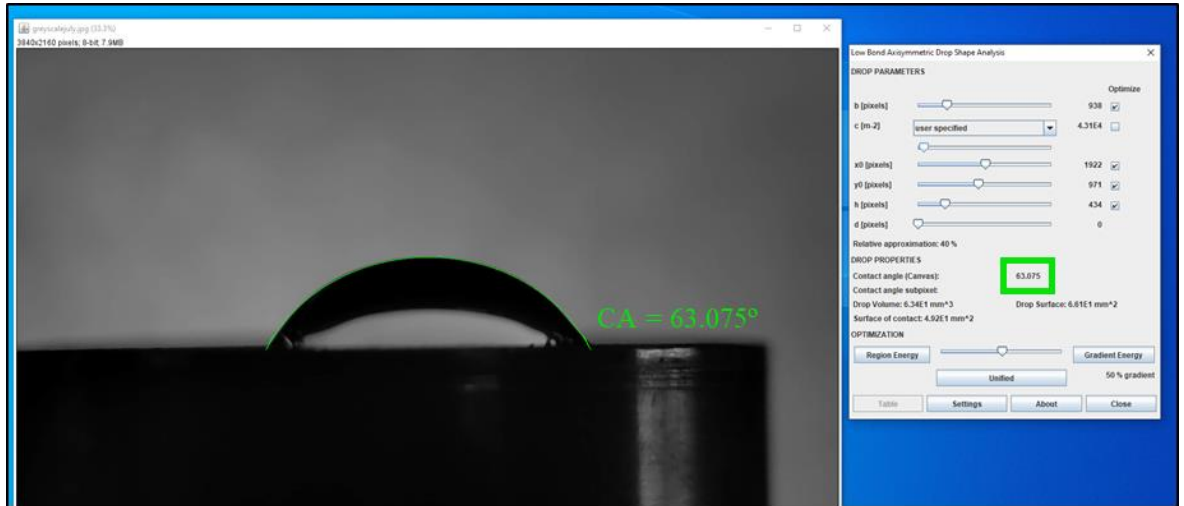


Figure 3.35. Low-Bond Axisymmetric Drop Shape Analysis (LBADSA) for contact angles (CA).

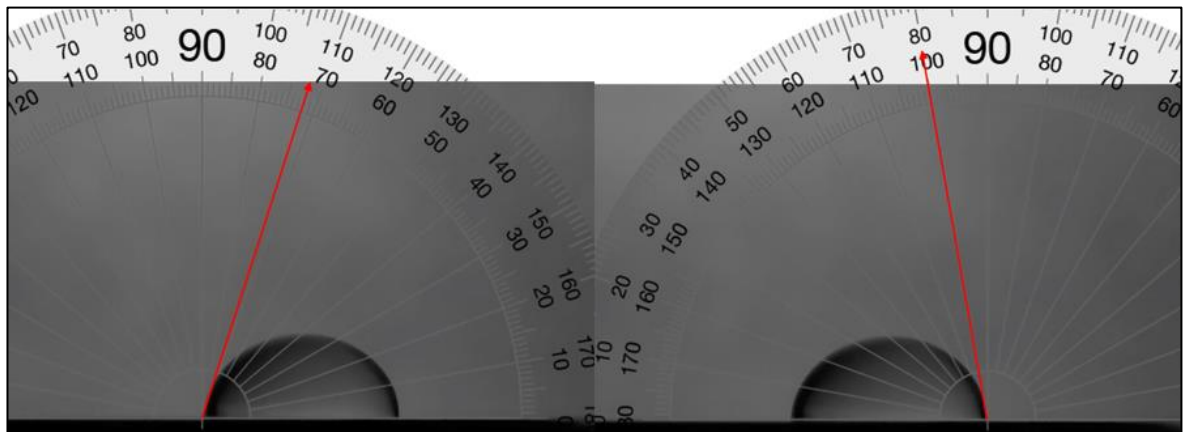
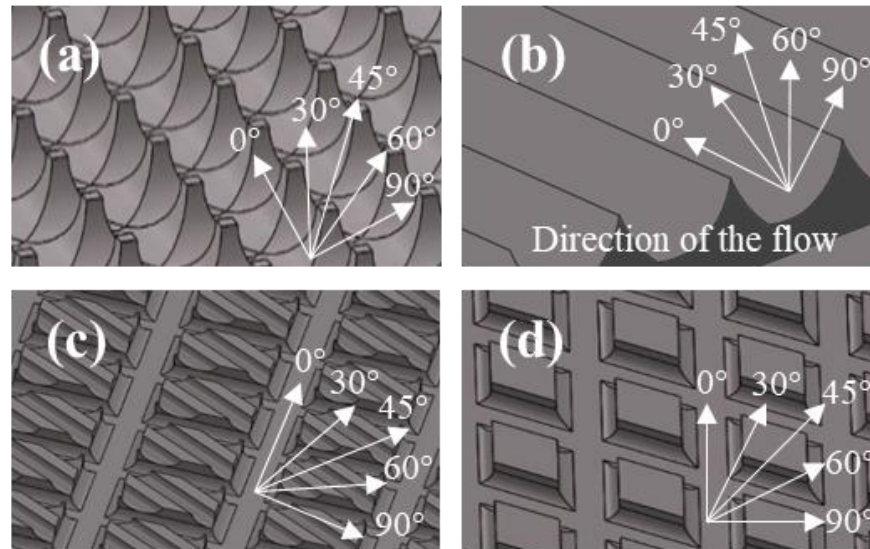


Figure 3.36. Virtual protractor technique used to calculate contact angles (CA).

### 3.5 Phase 2: Fluids Dynamics Evaluation (Momentum Transfer)

Boundary layer control and drag reduction are the main parameters of the numerical-experimental validation for designing microstructured surfaces. The boundary layer thickness and the drag force were obtained through the velocity profiles of the microstructured surfaces. Additionally, the performance of the microstructured surface geometries at different angles of action (i.e.  $0^\circ$ ,  $30^\circ$ ,  $45^\circ$ ,  $60^\circ$  and  $90^\circ$ ) against the airflow direction (Figure 3.37) was analysed in order to optimise the design.



**Figure 3.37.** Angles of action against the flow direction (a) Lotus, (b) Scallop, (c) Sharkskin and (d) Diamond. Adaptation from [113].

#### 3.5.1 Experimental Apparatus

The air duct test rig was specially designed to test the 25 mm inserts with microstructured surfaces under isothermal diffusion turbulent flow in a cost-effective way. The duct rig was composed of a centrifugal fan, two rotameters, a support disc for the inserts, a unislide and a hotwire anemometer (Figure 3.38). The maximum delivered flow by the pipe system is 3000 L/min; the delivery pipe has two air rotameters that can measure up to 2000 L/min. The fan is driven by a 7.5 kW, 3 phase motor, and the intake of the centrifugal fan is provided with an air filter to ensure that the delivered air is free from any particle that could damage the hotwire probe. The test section contains an entry hole on the top of the duct for the stainless-steel disc support. The diameter and thickness of the support disc are 76 mm and 10 mm, respectively, while a collar of 82 mm diameter and 4 mm thickness aids in fixing the support into the hole on the duct. The support disc has a 25 mm hole for placing the microstructured insert specimens and a 4.5 mm hole for positioning the hotwire probe. The 25 mm insert has a guide of angles marked on the top together with a collar that allows it to freely rotate on the disc support (Figure 3.38b).



The bottom face of the 25 mm insert is ensured to be aligned with the bottom face of the support disc and the inner surface of the top part of the duct to test the microstructured surface effectively. The unislide, supplied by LG Motion, holds the hotwire probe and helps move it precisely. The movement of the hotwire probe is 1 mm in the vertical direction for each complete turn of the leadscrew. The total vertical distance that could be covered is 16 cm, with a minimum achievable distance of  $10 \mu\text{m} \pm 2 \mu\text{m}$ . The selection of the hotwire anemometer was based on the 'Hot-wire and Hot-film Probe Selection Guide' by Dantec Dynamics. The hotwire system used in this study consists of a 55P11 probe, MiniCTA 54T42 and StreamWare Basic software. The 55P11 Probe is designed to measure one-dimensional velocities up to 100 m/s in air flows.

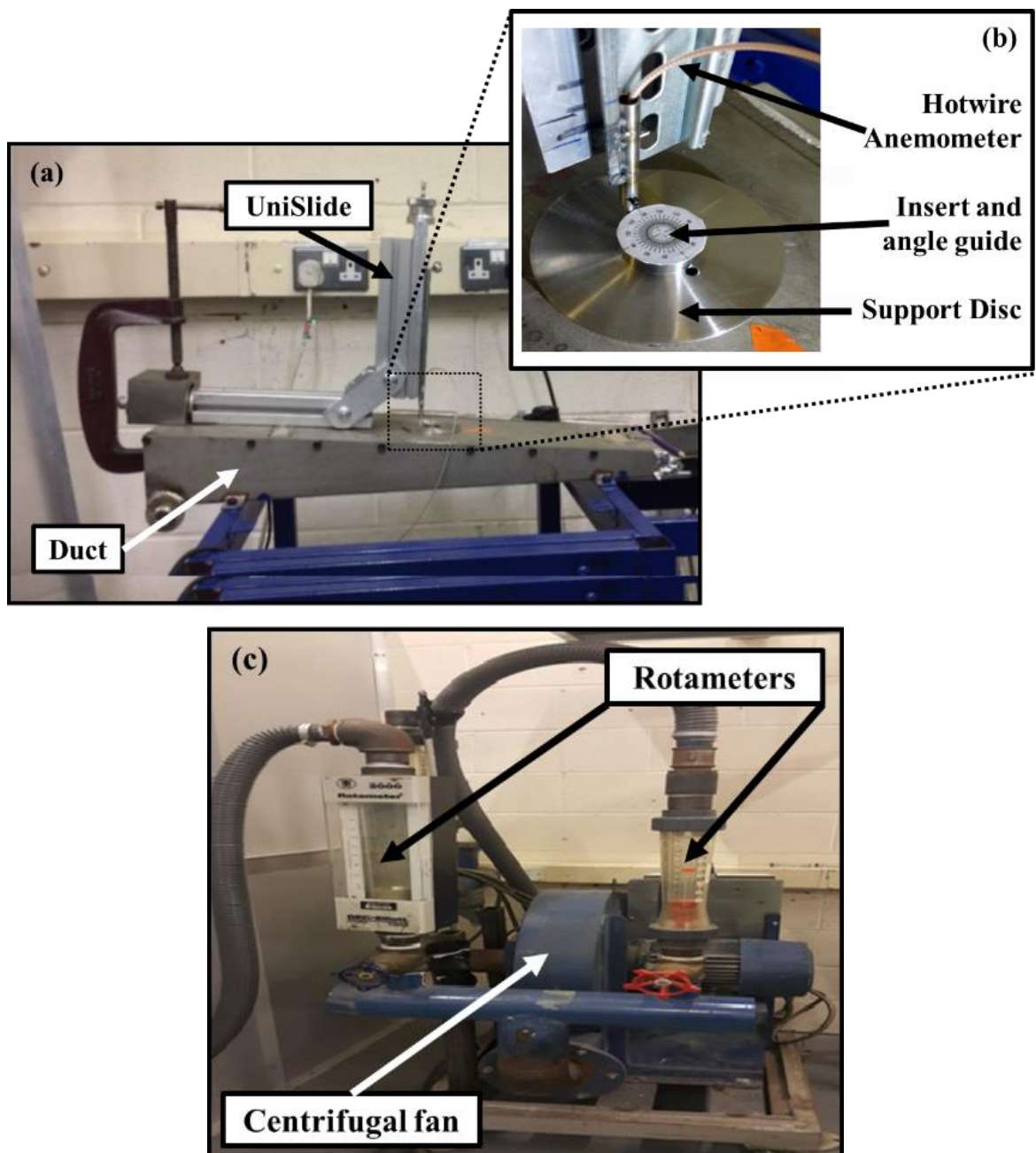


Figure 3.38. Air Duct Test Rig.

### 3.5.2 Experimental Design

The experiments were conducted in the air duct test rig (shown in Figure 3.38) with turbulent flow under isothermal and atmospheric conditions using a hotwire anemometer to measure velocities in the boundary layer. Each set of experiments took seven hours and was carried out four times on different days to corroborate repeatability. Three velocity measurements were undertaken for each geometry, angle, and position from the wall in the vertical direction to obtain the velocity profiles in the boundary layer. The test equipment is subject to certain risk and errors. In order to reduce the uncertainty for the velocity values, a calibration was performed for every experimental run. The uncertainty of the calibration was within 5% and the experimental data was fitted with a 4th order polynomial function.

The duct had an internal height of 20 mm (20,000  $\mu\text{m}$ ) at the test area. Therefore, considering that the boundary layer thickness is defined as the distance between the wall and the point where the velocity reaches 99% of the free stream velocity and assuming that the free stream velocity is approximately located at 10 mm (10,000  $\mu\text{m}$ ) from the wall, velocity measurements were taken at every 100  $\mu\text{m}$  from the wall until the distance reached 1,000  $\mu\text{m}$ . Further measurements were taken every 1,000  $\mu\text{m}$  until the distance reached 13,000  $\mu\text{m}$  from the wall to ensure that the velocity profiles included the entire boundary layer. Based on previous studies that showed damage to the hotwire probe when working at less than 125  $\mu\text{m}$  from the wall [19], this study did not consider velocities at less than 100  $\mu\text{m}$  from the wall to avoid damage to the experimental apparatus.

In order to provide a fully developed turbulent flow, ten experiments were performed to find the most reliable flow rate delivered by the system. Furthermore, to validate and compare results with the numerical simulations conducted in the present study as well as with that reported in the literature [139], the Reynolds number was considered to be between 8000 and 13,500. As a result, a flow rate of 1000 L/min was selected. The hotwire calibration system for this study was previously validated by using a Laser Doppler Anemometry (LDA) at the same conditions with 10  $\mu\text{m}$  seeding particles [19]. Thus, for every experimental run, a set of velocities were measured at different flow rates (0, 250, 350, 450, 550, 650, 750, 850, 950, 1000, 1050, 1150, 1250 L/min) using an AF210 anemometer to develop a calibration curve for the hotwire anemometer system.

The outer edge of the velocity boundary is typically defined by  $u=0.99U_\infty$ ; thus, the boundary layer thickness ( $\delta$ ) is defined as:

$$\delta = \delta(x) = y(u=0.99U_\infty) \quad (3.3)$$

Where  $U_\infty$  is the free stream velocity, and  $y_{(u=0.99U_\infty)}$  is the distance from the surface at which the velocity equals 99% of the  $U_\infty$ .

The Drag force ( $D$ ) was calculated as follows:

$$D = \rho_\infty b \int_0^{hy} u(U_\infty - u) dy = \rho_\infty b U_\infty^2 \int_0^{hy} \frac{u}{U_\infty} \left(1 - \frac{u}{U_\infty}\right) dy \quad (3.4)$$

Where  $hy$  is the height and  $b$  width of the plate.

### 3.5.3 Swirl Flow Rig Set-up

An additional experiment for boundary layer control and drag reduction was carried out using a swirl of eight blades; each blade had microstructures on the top surface (scallop). The purpose of this experiment was to evaluate repeatability when using laser melting machine and laser texturing techniques in a more complex workpiece. It has been envisaged that the HPPE unit (confidential) will employ swirling flows to enhance the residence time of the fluid. Therefore, an initial evaluation of this geometry was preliminarily characterised. It is emphasised that this part of the project was in addition to the development of new surfaces, and further research will be needed on the use of the new geometries for their implementation in swirling systems. The main measuring equipment and experimental design remained the same as the previous experiment, but instead of using the air duct test rig, a burner set-up was utilised to run air through the swirler.

For this experiment, the selected hotwire probe can achieve the necessary frequency response in kHz with a typical accuracy of  $\pm 0.5\%$  at velocities from a few cm/s to 100 m/s with high turbulence levels, which is usually encountered in swirling flow systems [19,140,141]. In order to ensure that the velocity profiles include the entire boundary layer, velocity measurements were taken up to 20,000  $\mu\text{m}$  from the top surface of the blade. The measurement point of each blade can be seen in Figure 3.39; they are located between the centre of the workpiece and the mark at the edge. As described in section 3.5.2, this experiment did not consider velocities at less than 100  $\mu\text{m}$  from the wall to avoid damage to the hotwire probe [19].

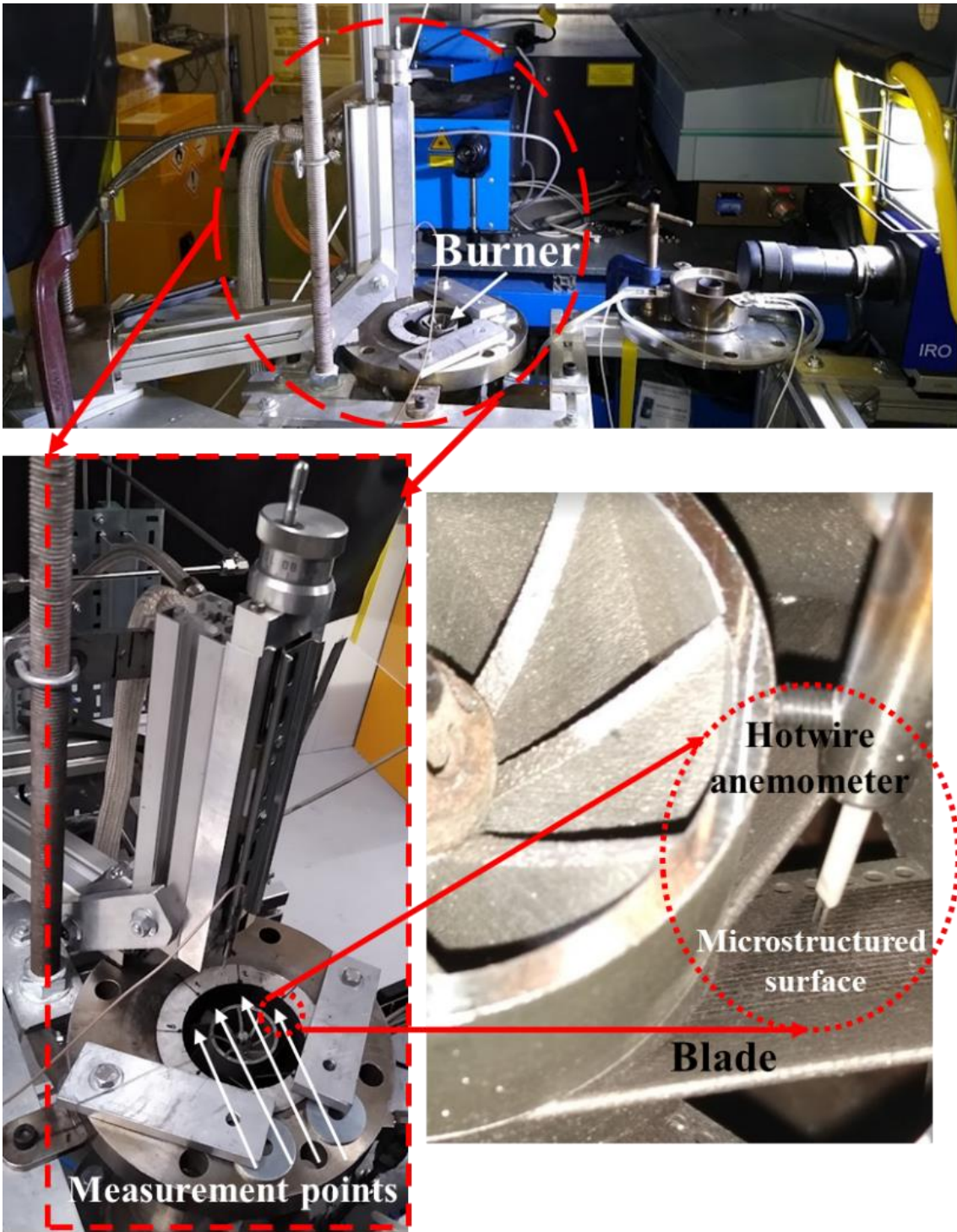


Figure 3.39. Experimental set-up for the swirl evaluation from different views.

### 3.6 Phase 3: Heat Transfer Evaluation

The objective of the condensation heat transfer experiments is to evaluate the effectiveness of the microstructured surface geometries to facilitate nucleation, growth and condensate drainage in order to enhance heat transfer through the increase of surface temperature differential ( $\Delta T_s$ ). Research in this area has been successfully undertaken using different surface modification techniques to increase heat transfer and detachment of droplets whilst delaying surface flooding [106]. Surface condensation can take place through two mechanisms: Dropwise Condensation (DWC) and Filmwise Condensation (FWC). Numerical and experimental studies demonstrated heat transfer enhancement when grooved surfaces are used to decrease liquid film thickness. In addition, Orejon et al. [106] demonstrated notable heat transfer performance with simultaneous DWC/FWC by varying the microstructured surfaces' design parameters despite the fact that FWC offered an order of magnitude lower heat transfer coefficients than DWC due to the thickness of the liquid film covering the solid surface [142].

#### 3.6.1 Experimental Apparatus

The experimental apparatus was designed to test the four microstructured inserts with respect to an unstructured insert. The apparatus consists of the condensation chamber, data acquisition/control system, and humidifier system (Figure 3.40).

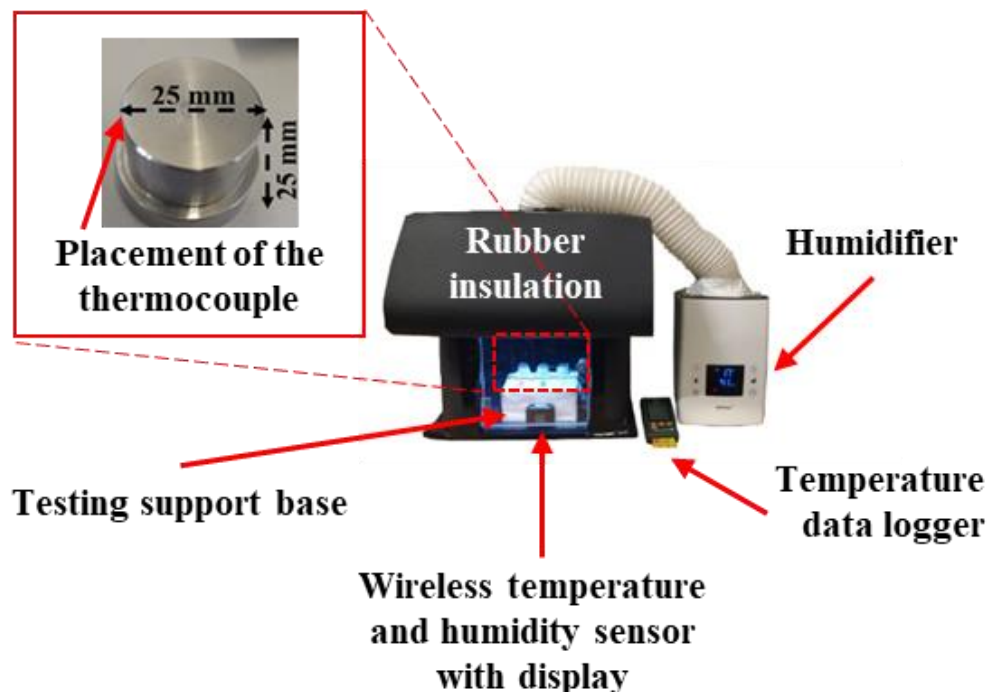


Figure 3.40. Experimental apparatus for the condensation heat transfer experiments. Adaptation from [143].

The condensation chamber consisted of a 400 mm × 400 mm × 500 mm Perspex chamber with a visualisation window of 250 mm × 300 mm; a 100 mm diameter opening at the top for the entry of humid air from the humidifier; a 20 mm × 20 mm opening on the bottom sidewall to connect the inserts with the data acquisition system and another similar opening at the bottom of the back wall to drain the condensate out of the chamber. The chamber was insulated with a 13 mm thick nitrile rubber sheet to reduce heat loss and surface condensation. There was an insulated testing support base of 180 mm × 130 mm inside the chamber for three inserts to be placed on, with a 20 mm separation space between them. Each insert had a 0.9 m long bead wire subminiature type-K thermocouple probe attached near the microstructured surface (Fig. 7). The thermocouples were connected to a 3-Channel LCD temperature data logger, with an accuracy of  $\pm (0.5\% + 0.5^\circ\text{C})$  from  $-100^\circ\text{C}$  to  $+1300^\circ\text{C}$ , which was part of the data acquisition/control system outside the chamber. The data acquisition/control system also consisted of a wireless temperature and humidity sensor with a display inside the chamber with a temperature accuracy of  $\pm 0.5^\circ\text{C}$  from  $0^\circ\text{C}$  to  $+40^\circ\text{C}$  and a humidity accuracy of  $\pm 2\%$  typical from 20% to 80% and  $\pm 5\%$  maximum from 0% to 100%. The displayed data was used to control the temperature inside the chamber using a fan that blew air through nichrome wire coils before starting the humidifier to increase the humidity in the chamber. A temperature, humidity and dew point data logger with an LCD screen was used to acquire and record the conditions inside the condensation chamber with a temperature accuracy of  $\pm 0.55^\circ\text{C}$ , typically from  $5^\circ\text{C}$  to  $60^\circ\text{C}$  and a humidity accuracy of  $\pm 2.25\%$  from 20% to 80% and  $\pm 3\%$  maximum from 0% to 100% at temperatures up to  $60^\circ\text{C}$ . Finally, the humidifier contained an ultrasonic water vaporiser, a temperature and %RH sensor and an air humidity control that delivered flows between 250 and 400 mL/hr.

### 3.6.2 Experimental Design

For the thermal experiments, the following arguments were taken into consideration: (1) The rate of heat transfer ( $\dot{Q}$ ) is directly proportional to the surface temperature differential ( $\Delta T_s$ ). Hence  $\Delta T_s$  was chosen as the main parameter in this study to analyse the effects of the microstructured surface geometries during condensation. (2) The humid flow velocity entering the condensation chamber is low (0.15 m/s); thus, the interfacial shear between the liquid and the vapour is negligible [142]. (3) Taking into account the application of the microstructured surfaces in energy recovery systems where the condensation phenomenon occurs under humid environments, the temperature and relative humidity in the condensation chamber were set up to  $301.57\text{ K} \pm 0.5\%$  and  $96 \pm 3\% \text{ RH}$  and  $1.02\text{ bar} \pm 0.5\%$  according to the statistical analysis and collection of data by The National Oceanic and Atmospheric Administration (NOAA) [144].

The inserts were insulated with waterproof, insulating tape, leaving the top surface open for testing. The thermocouples for the temperature measurement were placed inside the insulating area, right at the edge between the top and side faces. Each set of experiments was carried out for a period of 8 minutes under stable conditions. Temperature and %RH measurements inside the chamber were recorded every 10 seconds, whereas the inserts' surface temperatures were measured every 20 seconds. The experiment is subject to certain risk and errors resulting from the laboratory room conditions and equipment maintenance. In order to reduce the uncertainty for the temperature values, a reference workpiece was used in every experimental run to compare and analyse the data.

With the recorded data, two differential temperatures were calculated; the inserts' surface temperature differential ( $\Delta T_s$ ), which is the difference between the final temperature of the insert and its temperature at the beginning of the experiment, and the surface subcooling temperature differential ( $\Delta T$ ) which is defined as the temperature difference between the humid air and the surface temperature. Consequently, the specific heat absorbed by the inserts ( $Q$ ) in Joules, the rate of heat transfer ( $\dot{Q}$ ) in Watts, heat flux ( $q$ ) in  $W/m^2$  and heat transfer coefficients ( $h$ ) in  $W/m^2K$  were calculated as follows:

$$Q = m * Cp * \Delta T_s \quad (3.5)$$

$$\dot{Q} = Q * t \quad (3.6)$$

$$q = \dot{Q}/A_s \quad (3.7)$$

$$h = q/\Delta T \quad (3.8)$$

Where  $m$  is the mass of the insert in kg,  $Cp$  is the specific heat capacity of the 316L stainless steel in  $J/kgK$ ,  $t$  is the time of the experiment in seconds, and  $A_s$  is the surface area in  $m^2$ .

### 3.7 Experimental Uncertainty Analysis

Experimental uncertainty analysis is the study and evaluation of uncertainty in an experiment to prove its accuracy. It is required for analysing the errors from the obtained results of an experiment. Errors and uncertainties occur naturally due to the selection of instruments, condition of the instrument and laboratory, calibration of equipment, and environmental conditions. They can also be associated to human limitations of the experimenter for manual observation and measurement of readings [145].

A number of measures were implemented for repeatability purposes and to reduce uncertainties and errors. Number of tests, readings, conditions, parameters, variables, use of experimental references for comparison and experimenter training were considered and are described in Chapter 3, while the uncertainties and errors are included in the results of Chapter 4, Chapter 5 and Appendix D.

The equations used for the statistical analysis to measure the experimental uncertainty and errors are based on the guidelines of the United Kingdom Accreditation Service:

Average or Arithmetic Mean ( $A$ ) is the sum of all the numbers (elements) in a list divided by the number of elements in that list [146].

$$A = \frac{1}{n} * \sum_{i=1}^n x_i \quad (3.9)$$

$A$  = average or arithmetic mean

$n$  = the number of elements in the list

$x_i$  = the value of each element in the list

Standard Deviation ( $\sigma$ ) is a measure of how spread out or dispersed the data in a set are relative to the set's mean [147].

$$\sigma = \sqrt{\frac{\sum_{i=1}^n (x_i - A)^2}{n}} \quad (3.10)$$

$\sigma$  = standard deviation

$A$  = average or arithmetic mean

$n$  = the number of elements in the list (sample size)

$x_i$  = the value of each element in the list



Standard Error of the Mean (*SEM*) or standard deviation of the mean is a method used to estimate the standard deviation of a sampling distribution, also known as uncertainty [148].

$$SEM = \frac{\sigma}{\sqrt{n}} \quad (3.11)$$

*SEM* = standard error of the mean

$\sigma$  = standard deviation

*n* = the number of elements in the list (sample size)

Margin of Error (*MOE*) is a statistical expression used for the measurement of random deviations from the results. It is the amount of error that can occur in real scenarios instead of achieving the direct statistical results from samples. A lower margin of error indicates a high confidence level and vice versa [149].

$$MOE = z_{\gamma} \times \sqrt{\frac{\sigma^2}{n}} \quad (3.12)$$

*MOE* = margin of error

$\sigma$  = standard deviation

*n* = the number of elements in the list (sample size)

$z_{\gamma}$  = quantile or z-score

$\gamma$  = confidence level

### 3.8 Assessment Criteria

Once all the phases have been evaluated, an assessment criteria table will be available at the end of each stage; an example is available in Table 3.2. The component related to the heat transfer enhancement phase has the highest value due to the aim of this research on energy recovery systems.

Depending on the performance of each of the workpieces, points will be assigned as follows:

- For the workpiece with the best performance = (Available points for the phase / # of workpieces) × # of workpieces.
- For the workpiece with the second-best performance = (Available points for the phase / # of workpieces) × (# of workpieces – 1).
- For the workpiece in third place = (Available points for the phase / # of workpieces) × (# of workpieces – 2).
- For the workpiece in fourth place = (Available points for the phase / # of workpieces) × (# of workpieces – 3).

**Table 3.2. Assessment criteria example.**

Example - Assessment criteria		Workpiece				Obtained points based on performance
Component	Value	Best performance	2nd best	3rd best	4th	
CFD analysis (Best performance / Drag reduction)	20	20	15	10	5	
Manufacture and characterisation (Smallest percentage difference between design and manufactured)	20	20	15	10	5	
Experimental boundary layer control and drag reduction	20	20	15	10	5	
Experimental heat transfer enhancement	40	40	30	20	10	
<b>Total points</b>	100	100	75	50	25	

## Chapter 4 : Performance Evaluation Results of Hydrophobic and Hydrophilic Microstructured Surfaces (Stages 1, 2 and 3)

This chapter presents the results of each evaluation phase for stages 1, 2 and 3. This intends to describe how each of these stages contributed to the novel biphilic wettability gradient approach used for condensation heat transfer enhancement via microstructured surfaces, presented in stage 4 (Chapter 5). Additionally, the swirl flow experimental results are presented at the end of the chapter.

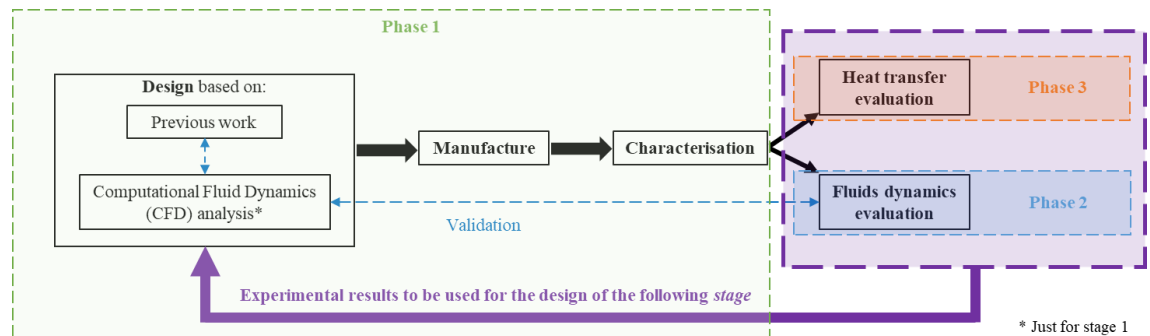


Figure 4.1. Evaluation phases summary.

Initially, the microstructured surface designs, based on previous work, were meant to be optimised through CFD analysis to be then manufactured and characterised. The obtained characterisation data would then be fed to the CFD code to optimise the following stages using actual dimensions obtainable from the manufacturing phase. However, the CFD optimisation could not be performed due to unforeseeable issues with the Hydro3D code used for the CFD analysis after stage one. More specifically, the Hydro3D code for microstructured surfaces analysis was not able to run due to the supercomputer upgrade from Raven to Hawk [150]; the code was specifically written to work under Raven conditions and requirements. Several attempts to adapt the code to Hawk were made; however, the software engineering, coding skills, Hydro3D software documentation and technical support were limited to successfully performing this task. Other CFD software was considered, but their capability to simulate turbulent flow over microstructured surfaces was not appropriate for this study since the software did not differentiate the different micro-geometries, in addition to time restrictions and access to software licenses.

Consequently, the designs of the subsequent research stages were only based on the microstructures that achieved the best performance in the fluids dynamics and heat transfer evaluation, along with information collected in the literature review. Also, during phase one, the manufactured workpieces were characterised for each stage to assess their wetting behaviour and compare the real produced dimensions with the designed dimensions. The experimental evaluations (phases two and three) results supported the design and optimisation of the following stage.

## 4.1 Stage 1: Microstructured Surfaces Produced via $\mu$ -WEDM on Cast Specimens

The first stage was based on biomimetic engineering research previously done at the School of Engineering in Cardiff University. Hydrophobic and hydrophilic microgeometries were compared against an unstructured surface. The microstructures were created by Micro-Wire Electrical Discharge Machining ( $\mu$ -WEDM) over inserts manufactured via casting and conventional turning and facing operations.

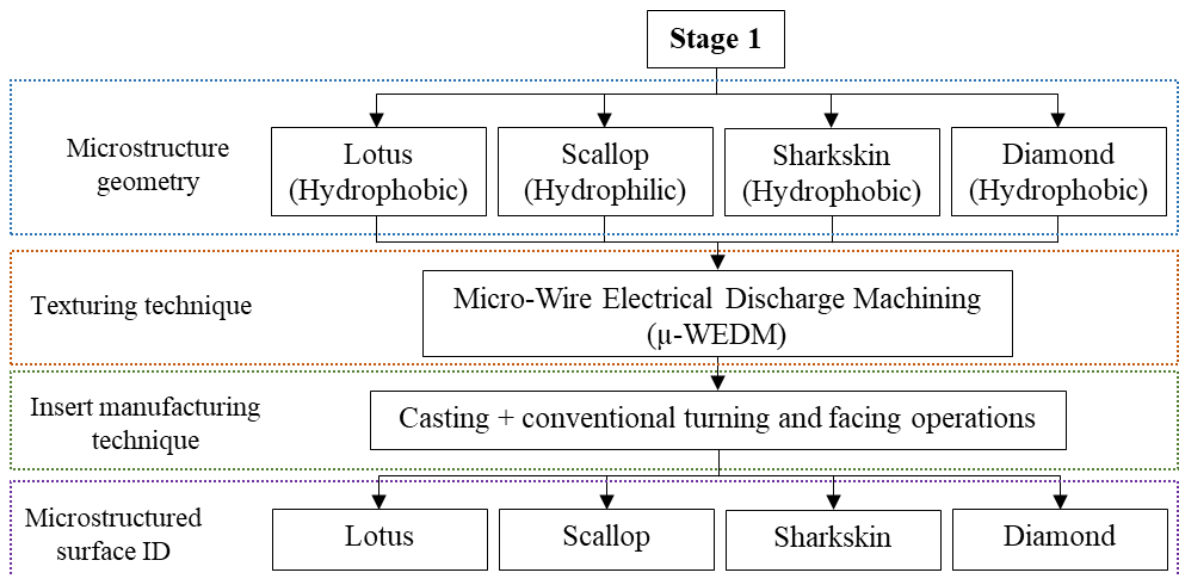


Figure 4.2. Summary of the microstructured surfaces in Stage 1.

### 4.1.1 Phase 1: Design, Manufacture and Characterisation

#### 4.1.1.1 Design

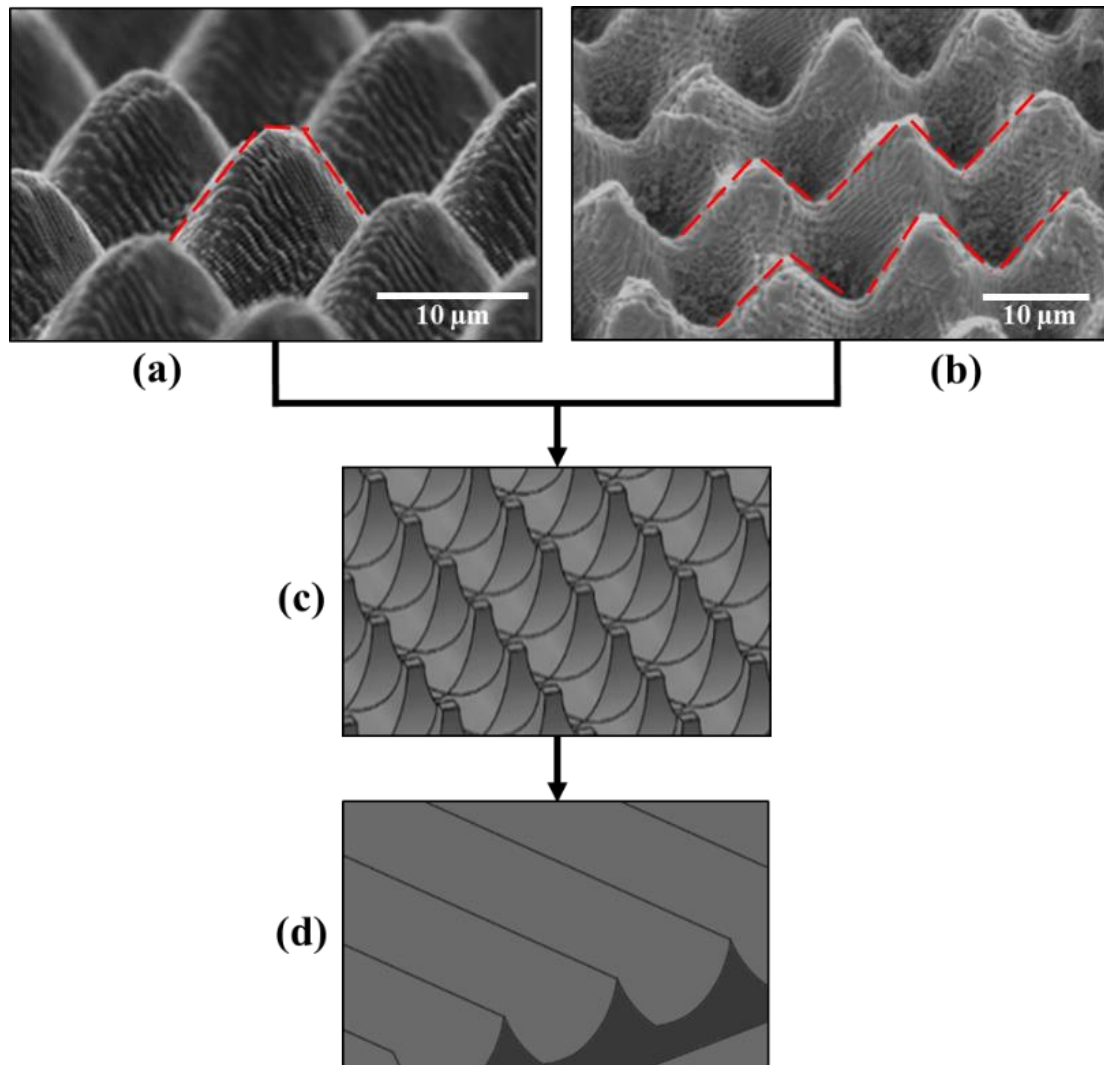
##### 4.1.1.1.1 Previous Work

The selection of the first geometries was based on the wetting properties of lotus leaves, the hydrodynamic advantages of shark skin, and the manufacturing limitations. As mentioned in the previous chapter, these geometries are the outcome of previous work carried out in the school of engineering on biomimetic engineering [19]; the optimisation of the geometries resulted in the nominal dimensions shown in Table 4.1.

**Table 4.1. Nominal dimensions of the micro-geometries (Stage 1).**

Geometry	Lotus	Scallop	Sharkskin	Diamond
Width of grooves ( $\mu\text{m}$ )	130	100	520	280
Depth of grooves ( $\mu\text{m}$ )	65	75	130	130
Width of riblets ( $\mu\text{m}$ )	25	25	260	260

Figure 4.3 shows the pyramidal configuration of the lotus leaf (a, b) [151,152] with the resulting geometry design for this investigation “Lotus” (c) and a simplified version “Scallop” (d). Figure 4.4 shows the sharkskin configuration, the red arrows in (a) illustrate the multiple cuts in a riblet while (b) identify the simpler outer shape of the riblet [112], (c) represents the resulting geometry design for this investigation “Sharkskin” and a simplified version “Diamond” (d).



**Figure 4.3. (a-b) SEM images of the lotus’ pyramidal configuration, adaptation from [151,152]. (c) Lotus and (d) Scallop Computer-aided designs (CAD) [113,143].**

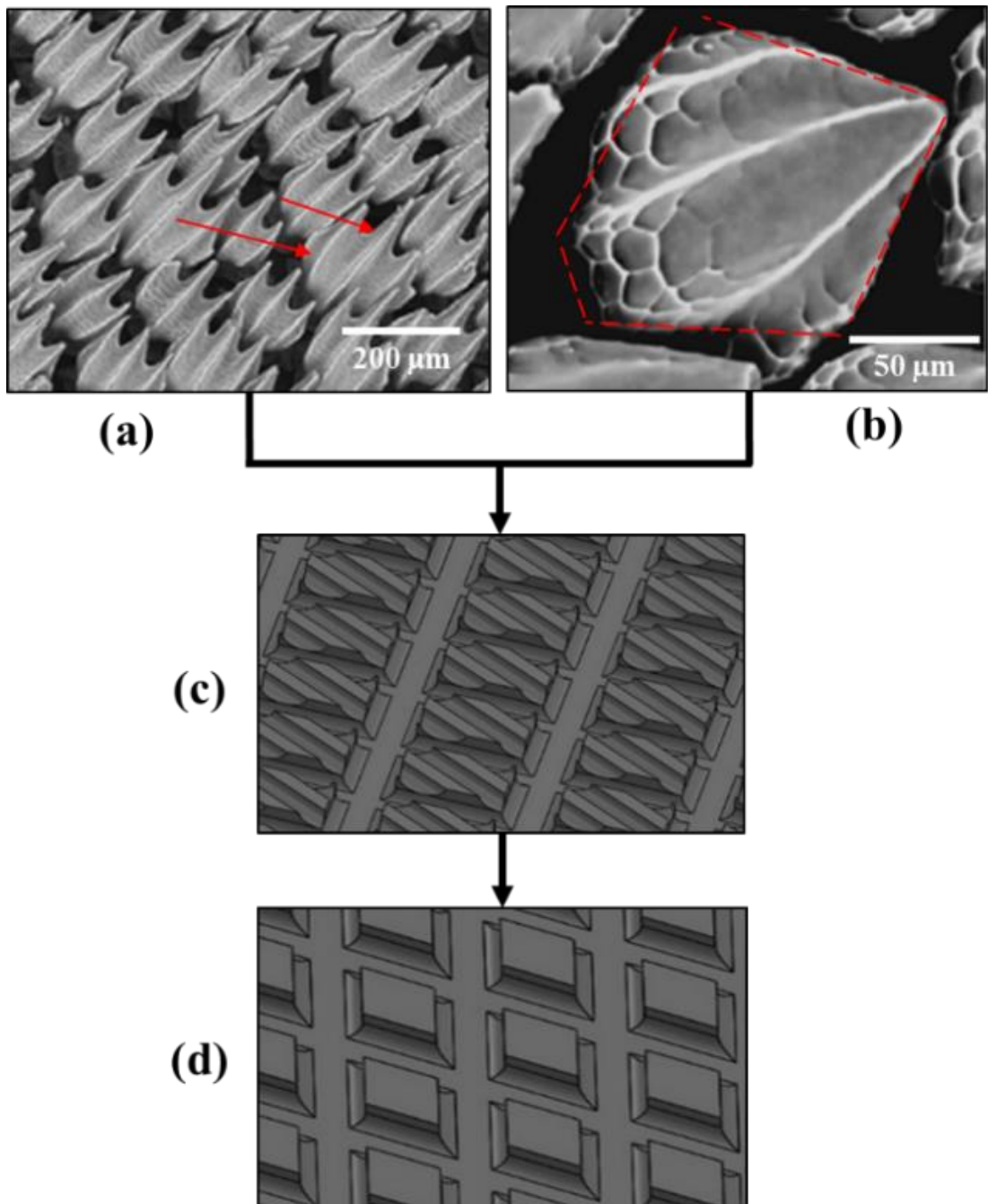
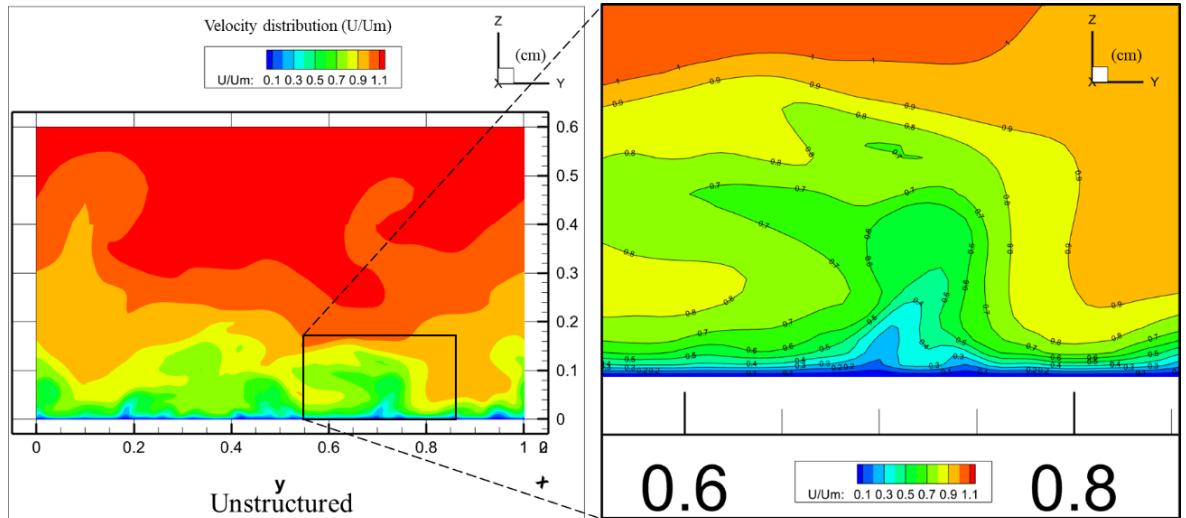


Figure 4.4. (a-b) ESEM images of the shark skin surface configuration, adaptation from [112]. (c) Sharkskin and (d) Diamond Computer-aided designs (CAD) [113,140].

#### 4.1.1.1.2 Computational Fluids Dynamics (CFD) Results

As mentioned in the previous chapter, the drag force is directly proportional to the integration of the shear stress with the area [124]. The wall shear stress is a function of the viscosity and the velocity gradient at the wall, this plays a significant role in the transition from laminar to turbulent conditions; for this reason, frames were extracted at 15 mm from the inlet in the x-direction in order to analyse the effect of the microstructured surfaces near the wall under turbulent conditions ( $Re = 13,500$ ).



**Figure 4.5. Velocity distribution near the wall of an unstructured surface.**

Figure 4.5 shows the velocity distribution ( $U/U_m$ ) in the unstructured surface, where  $U$  is the local velocity in the x-direction and  $U_m$  is the bulk velocity at the inlet. Even when there are no microstructures on the surface, velocity fluctuations related to the structure of the flow can be observed as a ‘finger’-like structure in the turbulent boundary layer near the wall (Figure 4.5, right hand side graph), the fine grid resolution in this area is  $528 \times 196 \times 88$  as seen in Figure 3.7. Laskari [153], studied velocity fluctuations as the result of the evolution of the freestream boundary and the temporal organisation of the velocities; while Hutchins and Marusic [154] emphasize the Reynolds shear stress contribution and relation to Townsend's (1976) theory of active and inactive motions. They observed how the *large-scale wall-parallel motions associated with the streamwise velocity bring amplification or excitation of small-scale  $u$ ,  $v$  and  $w$  fluctuations, in a manner that will produce increased (small-scale) Reynolds stress fluctuations beneath them* [154], creating such fluctuations in the velocity distribution near the wall.

Figure 4.6 shows the velocity distribution ( $U/U_m$ ) in the channel with microstructures on the bottom surface. The unstructured surface graph shows higher velocities than its counterparts in Figure 4.6. As a consequence, the absence of microstructured surfaces promotes higher Reynolds numbers, this significant increase of momentum near the wall allows the boundary layer to withstand a larger unfavourable pressure (positive pressure gradient) that results in higher wall shear stress and drag force [155][19].

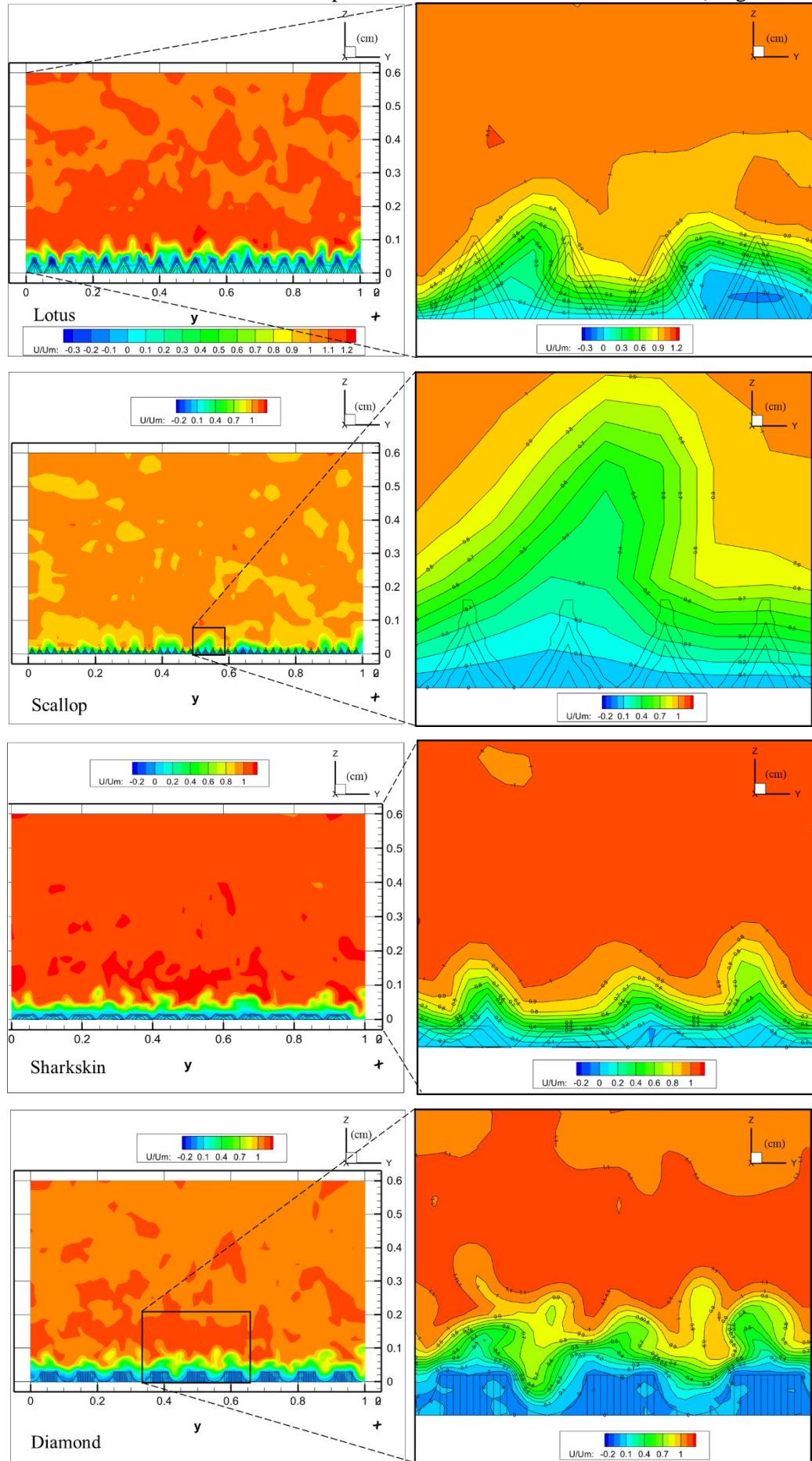


Figure 4.6. Velocity distribution near the wall of the microstructured surfaces from stage 1.



From these results, the boundary layer thickness can be found at  $U/U_m = 0.99$ , for the unstructured surface is 2.3mm, 0.83 mm for Lotus, 0.58 mm for Scallop, 0.60 mm for Sharkskin and 0.77 mm for Diamond. After this point, the effect of the wall drastically decreased, and the velocity reached the mainstream velocity value or bulk velocity. The designed microstructured surfaces, Lotus, Scallop, Sharkskin and Diamond, provided a boundary layer thickness reduction of 64.45%, 75.22%, 74.24% and 66.79%, respectively, when compared against the unstructured surface.

When comparing the microstructured surfaces against the unstructured surface, it is possible to see how the different micro-geometries or riblets influence the dynamics in the boundary layer. The velocity distributions at the bottom inside the valleys show low velocities (values up to 10% of the mainstream velocity) and high velocities over the riblets (values over 10% of the mainstream velocity for the Scallop and Diamond micro-geometries and up to 80% of the mainstream velocity for the Lotus and Sharkskin micro-geometries). When the high velocities move up towards the main flow stream, the velocity gradient decreases near the wall and increases towards the main flow stream. Furthermore, the micro-geometries create micro-channels that decrease turbulence. The reduction in turbulence is the result of the restriction in lateral and normal velocity. Although the velocity at the entrance of the channels has high fluctuation, the flow slows down inside the channel [19]. These phenomena cause a similar trend in momentum and skin friction values near the wall. Thus, the shear stress located in the mainstream close to the riblet tips is higher than the one in the valleys.

The vorticity behaviour on microstructured surfaces is shown in Figure 4.7, while Figure 4.8 shows the vorticity behaviour on an unstructured surface. Vortices are generated in the lateral and normal direction of the flow; the lateral vorticities in the free stream increases the ejection of the vortices in the normal direction. From the flow velocity in the z-direction data and the vorticity behaviour on an unstructured surface, a large vortex (2 mm in diameter) located higher up in the domain (approximately at 1 mm from the wall) causes the normal velocity to rise while increasing the shear stress. The creation of normal velocity regions causes more momentum transfer and higher Turbulence Kinetic Energy (TKE) due to the mix of high and low velocities. Moreover, the vortex diameter is related to the Reynold number and the strength of the turbulence at the point where the vorticity is generated. However, the vorticity behaviour images of the different microstructured surfaces show that smaller vortices (between 0.5 mm and 1 mm in diameter) are generated closer to the wall over the riblets; this phenomenon slows down the flow velocity when microstructures are present by blocking the flow entering the valleys between the riblets.

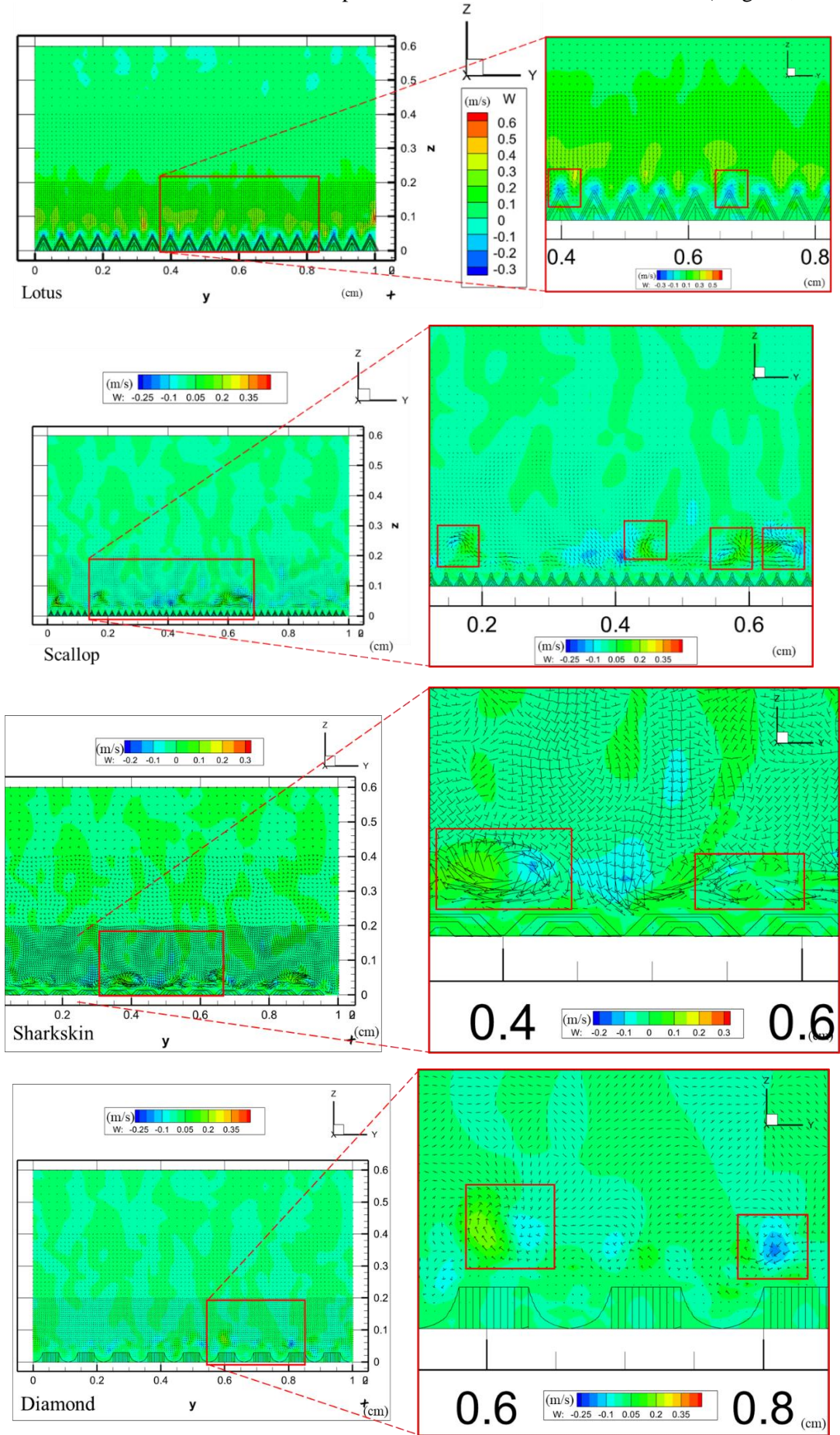


Figure 4.7. Flow velocity in the z-direction and vorticity behaviour on different microstructured surfaces.

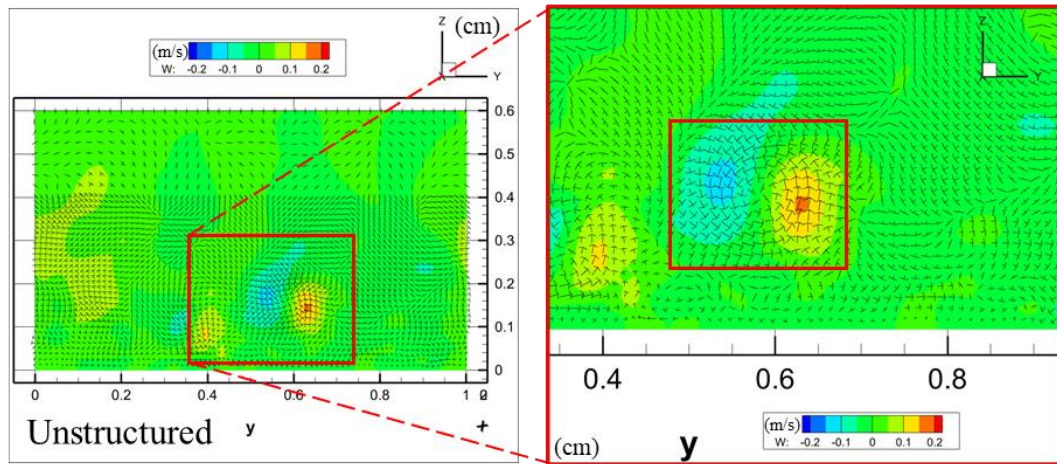


Figure 4.8. Flow velocity in the z-direction and vorticity behaviour on an unstructured surface.

Turbulence Kinetic Energy (TKE) is the mean kinetic energy per unit mass associated with eddies in turbulent flow; it represents the measure of the intensity of turbulence. Physically, the turbulence kinetic energy is characterised by measured root-mean-square (RMS) velocity fluctuations [156]. Therefore, when the mean velocity increases, the turbulence kinetic increases as a consequence. Figure 4.9 shows the TKE over an unstructured surface, Figure 4.10 shows the TKE over the Lotus and Scallop microstructured surfaces and Figure 4.11 the TKE over the Sharkskin and Diamond microstructured surfaces.

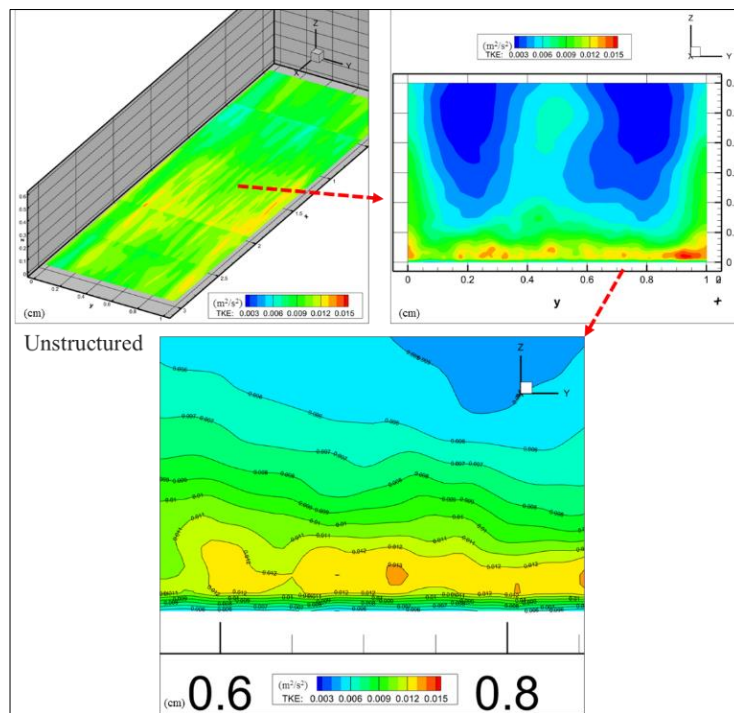


Figure 4.9. Turbulence kinetic energy (TKE) near the wall of an unstructured surface.

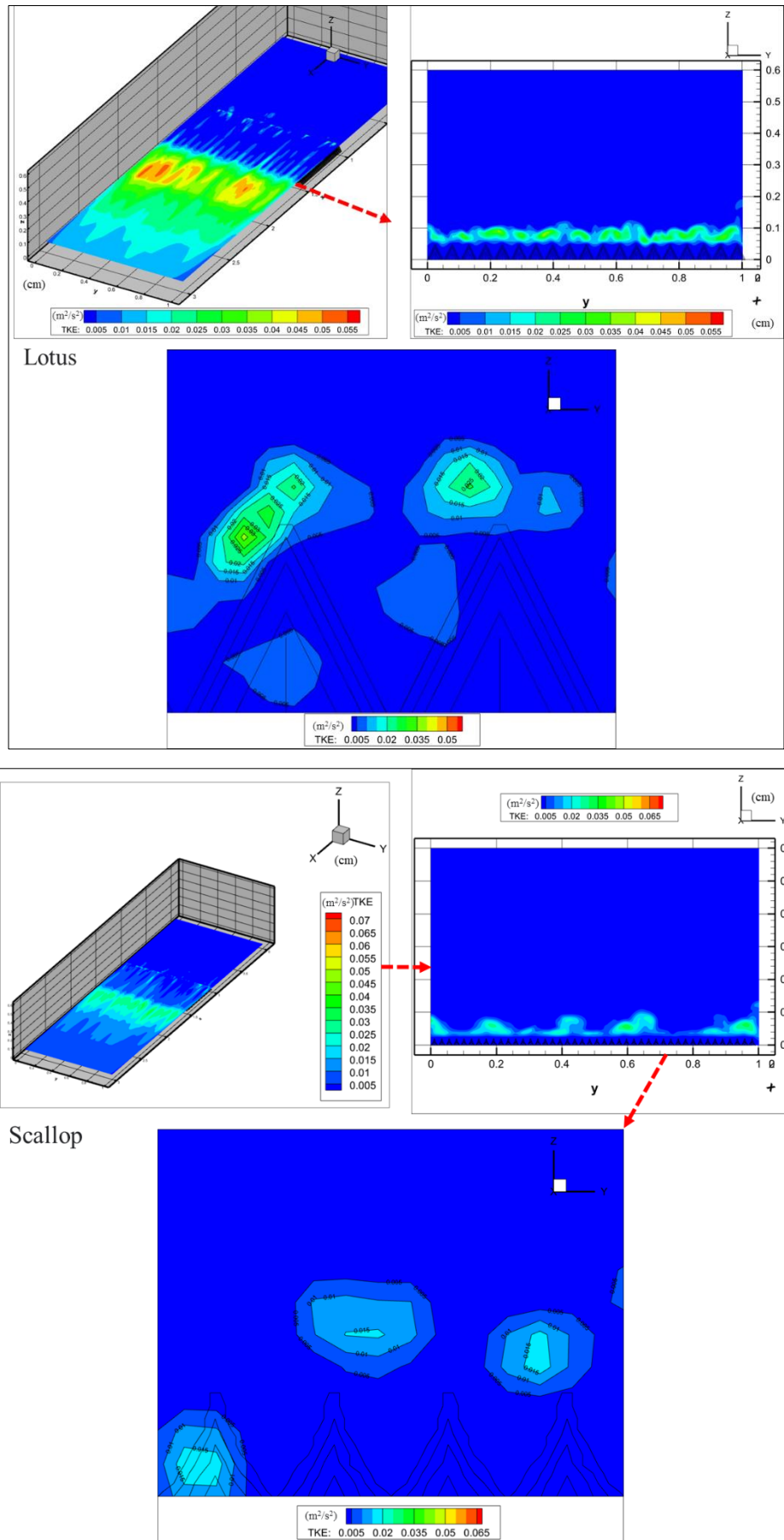


Figure 4.10. Turbulence kinetic energy (TKE) near the wall of the Lotus and Scallop microstructured surfaces.

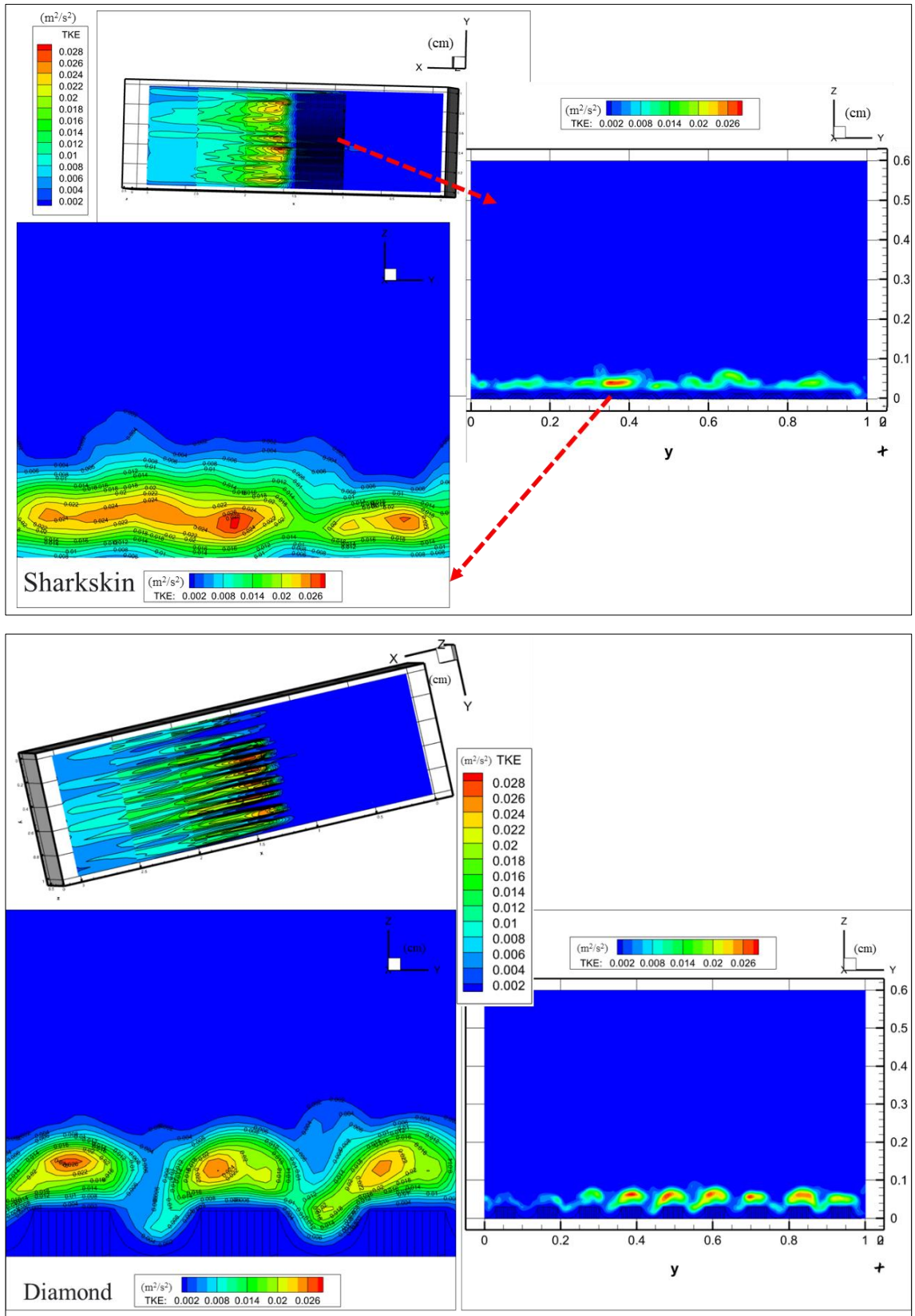


Figure 4.11. Turbulence kinetic energy (TKE) near the wall of the Sharkskin and Diamond microstructured surfaces.

Due to the reduction in the lateral and normal velocities the microstructured surfaces caused, the TKE on microstructured surfaces is lower when compared to the unstructured surface at the same distance from the wall in the z-direction. The numerical results showed a reduction between 28.57% and 71.13% of Turbulence Kinetic Energy when microstructured surfaces are present. Regarding the TKE behaviour near the microgeometries, the upper areas around the riblets present larger values of TKE than the TKE values at the bottom of the valleys between the microgeometries. TKE values over the Lotus micro-geometry go from 0.005 J/kg ( $\text{m}^2/\text{s}^2$ ) at base or the bottom of the valley to 0.03 J/kg ( $\text{m}^2/\text{s}^2$ ) at the top of the riblet, for Scallop TKE values go from 0.005 J/kg ( $\text{m}^2/\text{s}^2$ ) to 0.015 J/kg ( $\text{m}^2/\text{s}^2$ ) and for the Sharkskin and Diamond microgeometries the TKE values go from 0.002 J/kg ( $\text{m}^2/\text{s}^2$ ) to 0.026 J/kg ( $\text{m}^2/\text{s}^2$ ). The increase in TKE in front of the riblets in the upper area can be attributed to the riblet thickness at the base. According to Al-fahham (2017), the flow is forced to stagnate and change its direction, which generates high TKE spots, while the mixing of the flow that leaves the valleys at low velocities increases the TKE behind the riblet. Additionally, the separation of the flow that was attached to the riblet tip surface also increased the TKE behind the riblets [19].

Figure 4.12 shows the shear stress on an unstructured surface; higher and more variable values are observable near the wall due to the selected Local Mesh Refinement (LMR) of the computational domain and grid resolution (Chapter 3). The effect of the microstructured surfaces on the shear stress near the wall is shown in Figure 4.13 for the Lotus and Scallop microstructured surfaces and Figure 4.14 for the Sharkskin and Diamond microstructured surfaces.

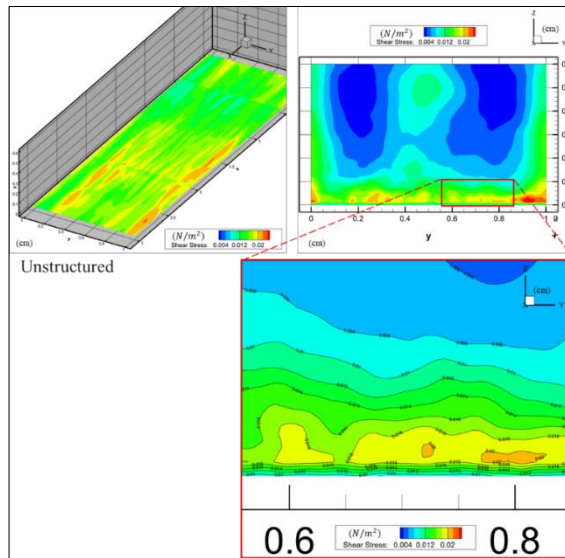


Figure 4.12. Shear stress ( $\text{N}/\text{m}^2$ ) near the wall of an unstructured surface.

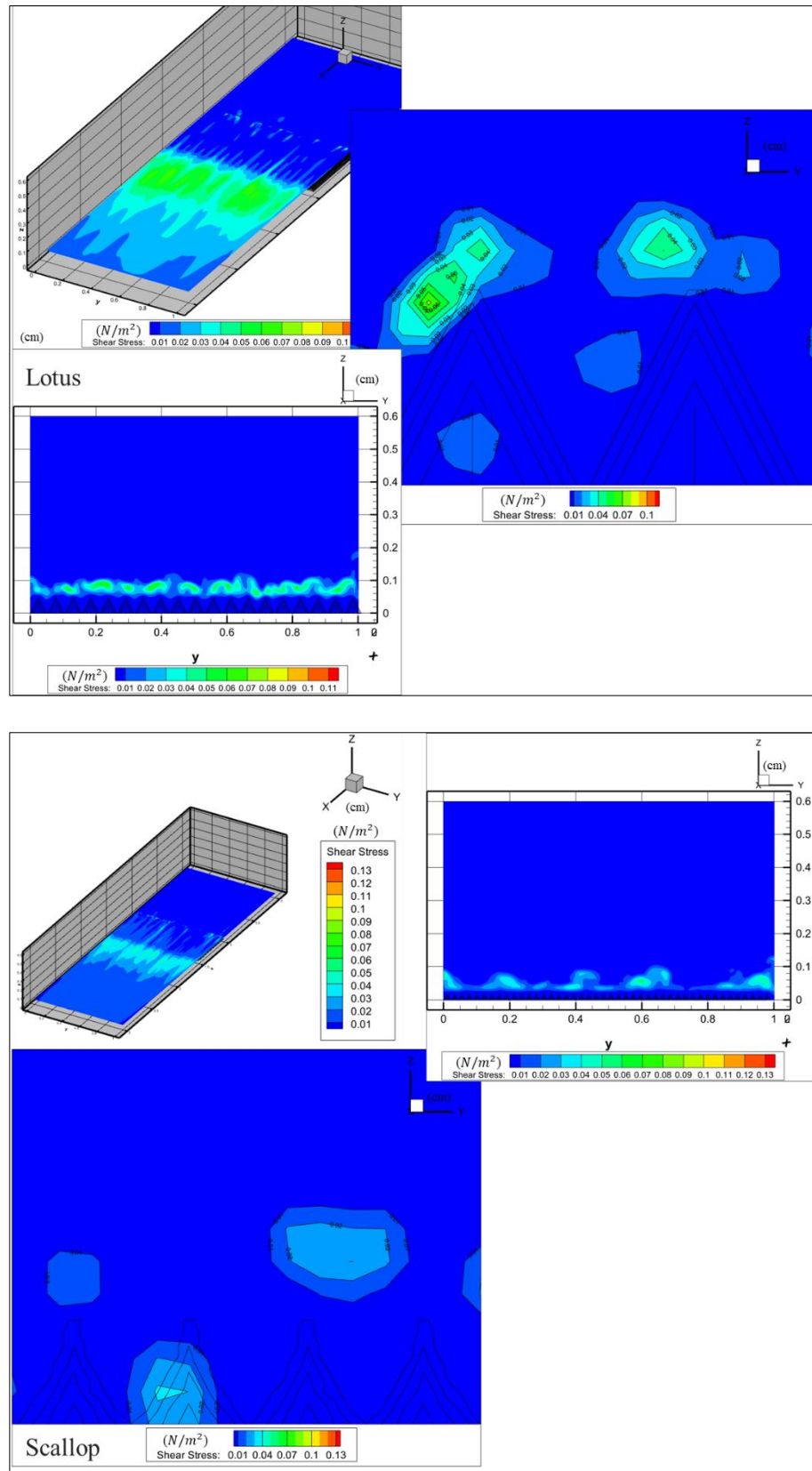


Figure 4.13. Shear stress ( $N/m^2$ ) near the wall of the Lotus and Scallop microstructured surfaces.

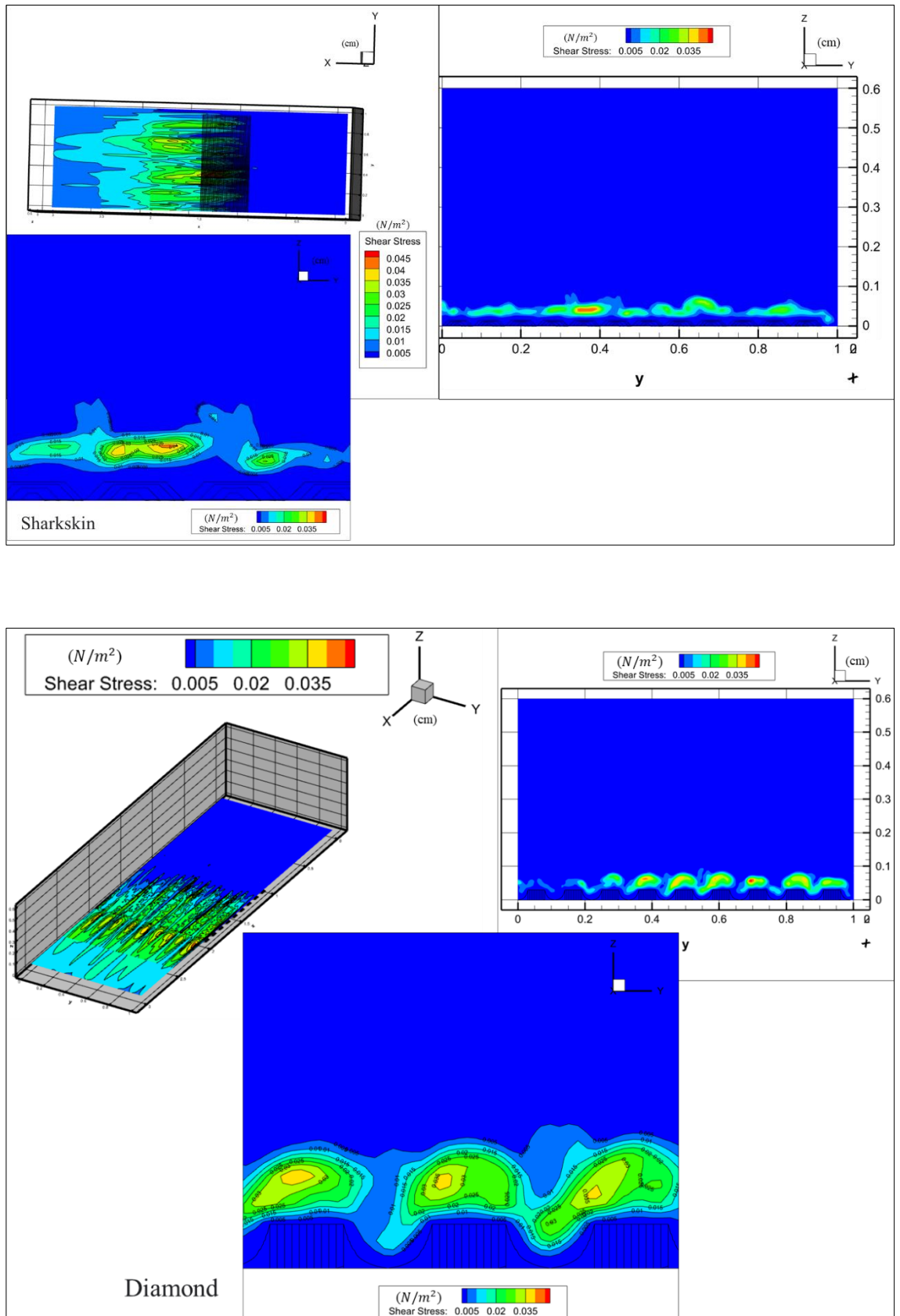


Figure 4.14. Shear stress ( $N/m^2$ ) near the wall of the Lotus and Scallop microstructured surfaces.



The lowest values of shear stress in the domain are found where the microstructured surfaces are located. As an outcome of the velocity gradient and TKE reduction, the shear stress surrounding the micro-geometries and in the valleys between the riblets is less than the one above the microstructured surface. However, the shear stress at the riblet tip can decrease as a result of the velocity components and TKE reduction. Similar to the turbulence kinetic energy (TKE) trends, the shear stress exhibits low values when compared against the unstructured surface at the same position over the micro-geometries, moderate values in front of the riblets and high values behind the riblets (mainly skin shear stress). High values are caused by high mixing rates between high and low-velocity flows. The low values are associated with the low velocities and low velocity fluctuating in the valleys. In consequence, although microstructured surfaces present a larger wetted area, the maximum shear stress values (i.e.  $0.13 \text{ N/m}^2$  against  $0.026 \text{ N/m}^2$ ) are between 16.67% and 61.54% smaller than the ones in the unstructured surface. This is caused by the location of the shear stress near the wall of the microstructured surfaces, appearing in three positions, at the valleys between the riblets and at the sidewalls and tips of the riblets. The velocity gradient at the riblet and the sidewall is too low, and only at the tip of the riblet, the velocity gradient is high due to the riblets maintaining the vorticities over the riblet tips, which leads to the reduction of velocity fluctuations near the wall [19]. Therefore, the reduction of the surface area attached to the high-velocity fluctuations and wall shear stress results in up to a 12% reduction of the drag force.

Figure 4.15 presents a comparison of relative drag reduction between numerical results, experimental results, and previous studies. The numerical drag reduction results are comparable to the experimental results of this study; they follow the same tendency with a difference between 3% and 16% for the Scallop, Sharkskin and Diamond microgeometries; however, experimental values for the Lotus microgeometry double the numerical values, this can be attributable to the experimental equipment performance and the variation in dimensions between the design and the manufactured micro-geometries. In addition, when comparing against the literature [19], the Lotus's results present 26% difference, Scallop 38%, Sharkskin 93% and Diamond 24%. These differences are attributable to the location of the microstructures in the domains and undocumented parameters used for the simulations of the preceding works, such as the Synthetic-Eddy-Method parameters that generate the inflow data.

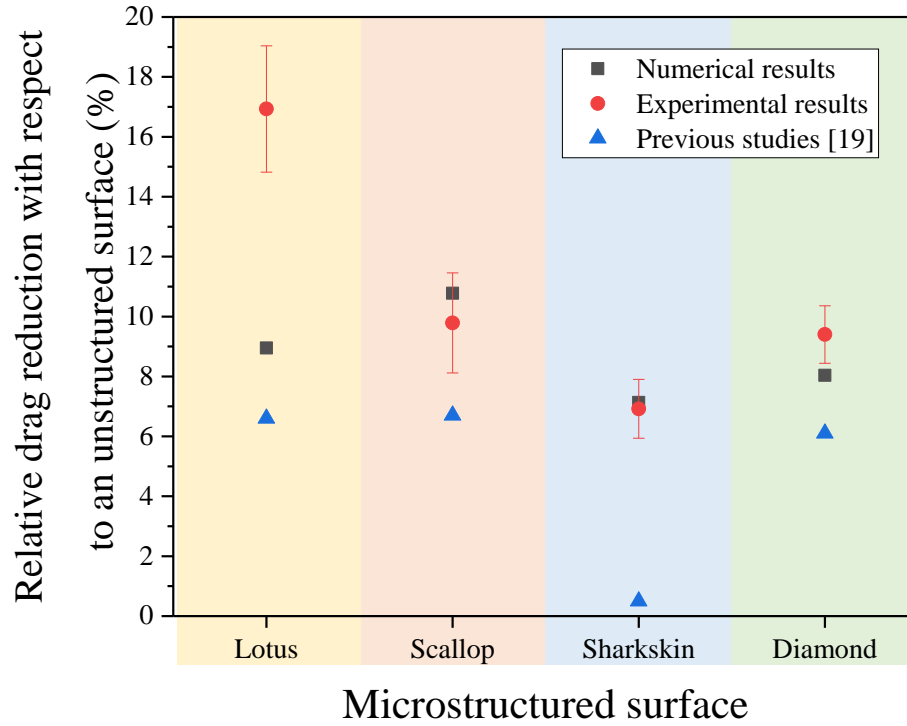


Figure 4.15. Comparison of relative drag reduction between numerical results, experimental results and previous studies [19].

#### 4.1.1.2 Manufacture and Characterisation of the Microstructured Surfaces

The microstructure characterisation results obtained from the 3D optical profilometer (Sensofar), together with the percentage deviations from the nominal dimensions, are shown in Table 4.2. Considering the scanned data, the manufacturing technique for creating microstructures presented a percentage difference between 0.58% and 45.22%. The simplified geometries, Scallop and Diamond, achieved four-time higher roughness than their original counterpart, the Lotus and Sharkskin geometries, respectively. Images of the top view of the final manufactured workpiece and Sensofar scans are presented in Figure 4.16 against the corresponding computer-aided designed (CAD) geometries.

**Table 4.2. Characterisation data of the microstructured surfaces and percentage difference with respect to the nominal dimensions.**

Geometry	Parameter	Width of grooves	Depth of grooves	Width of riblets	Surface area $A_s$ ( $m^2$ )	Projected surface area $A_s$ ( $m^2$ )	Roughness $R_a$ ( $\mu m$ )
<b>Unstructured</b>		-			0.00049	0.00049	2
<b>Lotus</b>	Nominal dimension ( $\mu m$ )	130	65	25	0.00058	0.00049	5.32
	Measured dimension ( $\mu m$ )	126.21	54.79	16.66			
	Percentage difference (%)	2.92	15.71	33.36			
<b>Scallop</b>	Nominal dimension ( $\mu m$ )	100	75	25	0.00107	0.00049	20.17
	Measured dimension ( $\mu m$ )	101.56	75.63	26.53			
	Percentage difference (%)	1.56	0.84	6.12			
<b>Sharkskin</b>	Nominal dimension ( $\mu m$ )	520	130	260	0.00057	0.00049	9.72
	Measured dimension ( $\mu m$ )	448.08	71.22	323.71			
	Percentage difference (%)	13.83	45.22	24.50			
<b>Diamond</b>	Nominal dimension ( $\mu m$ )	280	130	260	0.00070	0.00049	41.65
	Measured dimension ( $\mu m$ )	278.39	121.71	251.70			
	Percentage difference (%)	0.58	6.38	3.19			

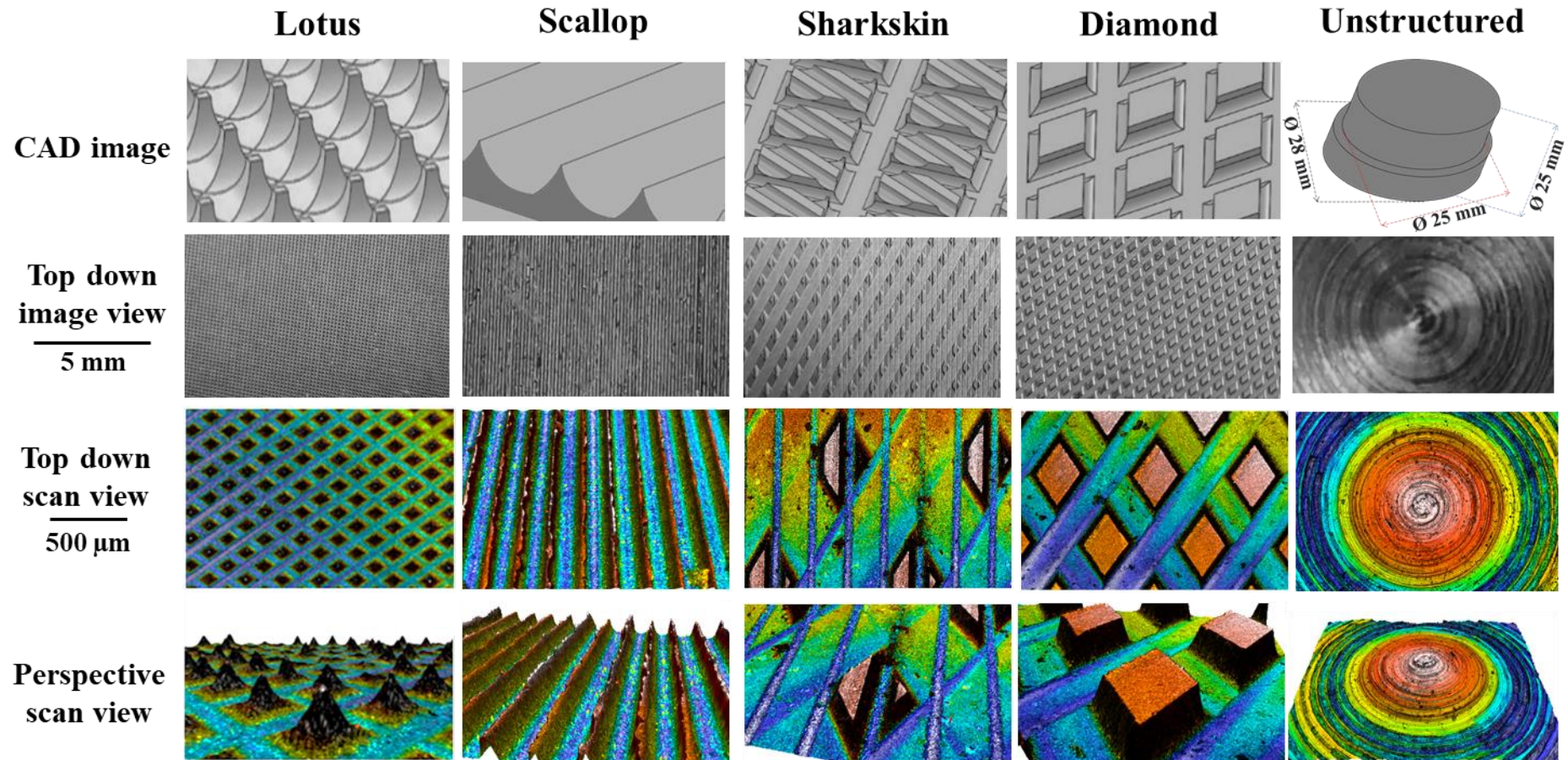
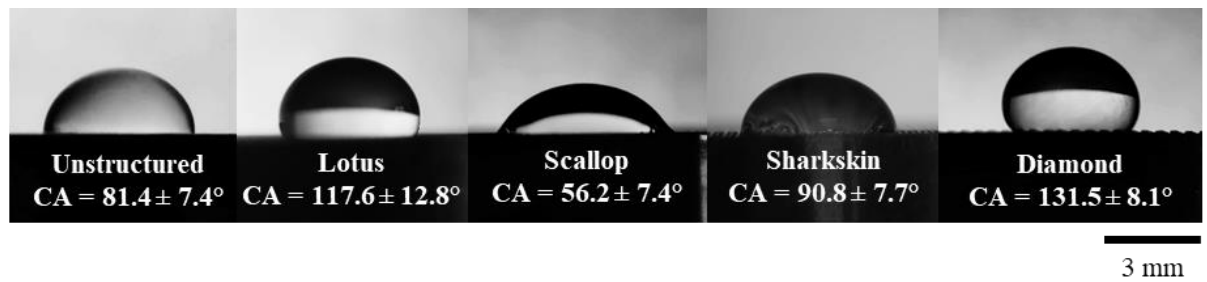


Figure 4.16. CAD designs, manufactured workpieces top view images and 3D scans (Sensofar) of the Lotus, Scallop, Sharkskin, Diamond and unstructured surfaces [113,140].

The microstructure wettability characterisation results (contact angles), together with the margin of errors and the standard error, are shown in Table 4.3. Additionally, images of the contact angle between the water droplets and the different geometries are presented in Figure 4.17.

**Table 4.3. Wettability characterisation data for the microstructured surfaces of stage 1, margin and standard errors.**

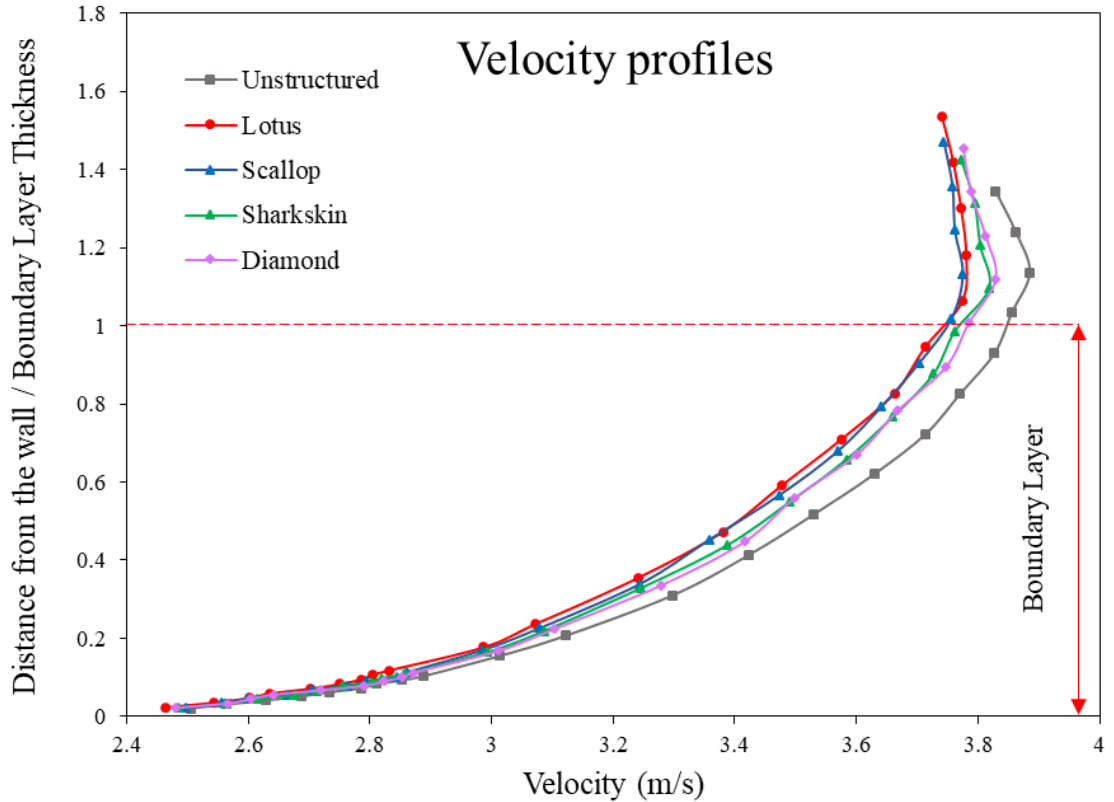
Geometry	Contact Angle (°)	Margin of error ( $\pm$ )	Standard Error	Wetting State
Unstructured	81.41	7.38	2.66	Hydrophilic
Lotus	117.60	12.80	4.61	Hydrophobic
Scallop	56.20	7.37	2.65	Hydrophilic
Sharkskin	90.80	7.70	2.77	Hydrophobic
Diamond	131.47	8.12	2.92	Hydrophobic



**Figure 4.17. Contact angles between water droplets and the unstructured and microstructured surfaces of stage 1.**

### 4.1.2 Phase 2: Fluids Dynamics Evaluation Results (Momentum Transfer)

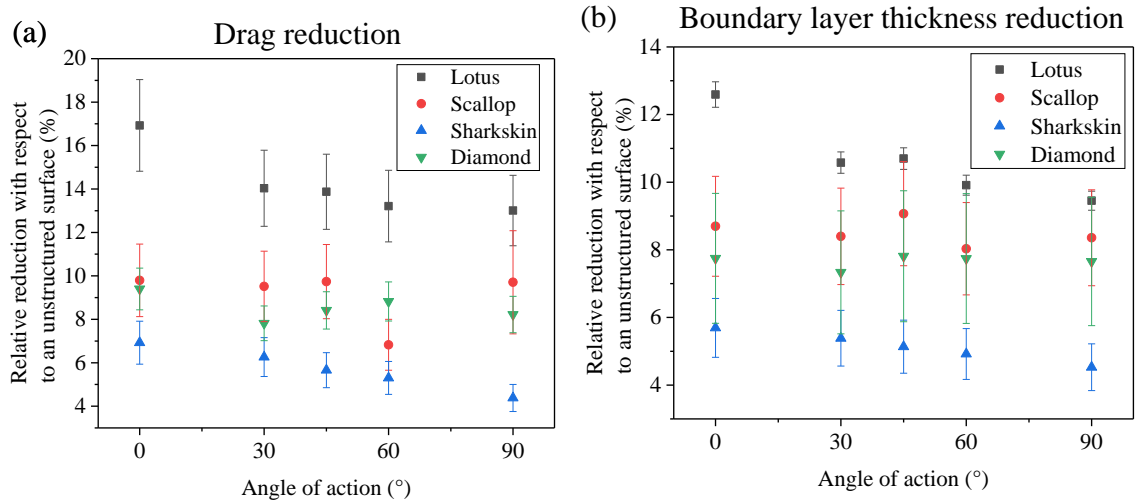
As a result of the velocity experiments for boundary layer control and drag reduction, a velocity profile for each microstructured surface and the unstructured surface was developed on stage 1 (Figure 4.18).



**Figure 4.18. Velocity profiles of the stage 1 microstructured surfaces and unstructured surface.**

Figure 4.19 comprises the experimental boundary layer thickness reduction and drag reduction of each microstructured surface at different angles of action (i.e.  $0^\circ$ ,  $30^\circ$ ,  $45^\circ$ ,  $60^\circ$  and  $90^\circ$ ) with respect to the unstructured surface of stage one. More detailed results are available in Appendix D.

The angle of action's effect had a minor impact on the drag reduction when compared to the geometry's contribution. For Lotus, there was a difference of 1% only between the angles of action associated with the highest and lowest drag reduction. For the Scallop structure, this difference was 2.9%, while that for the Sharkskin and Diamond geometries were 2.5% and 1.6%, respectively (Figure 4.19a). Additionally, the differences between the highest and lowest boundary layer thickness reduction with respect to the angles of action for each geometry were as follows: 3% for Lotus, 1% for Scallop, 0.5% for Diamond and 1% for Sharkskin structure (Figure 4.19b).

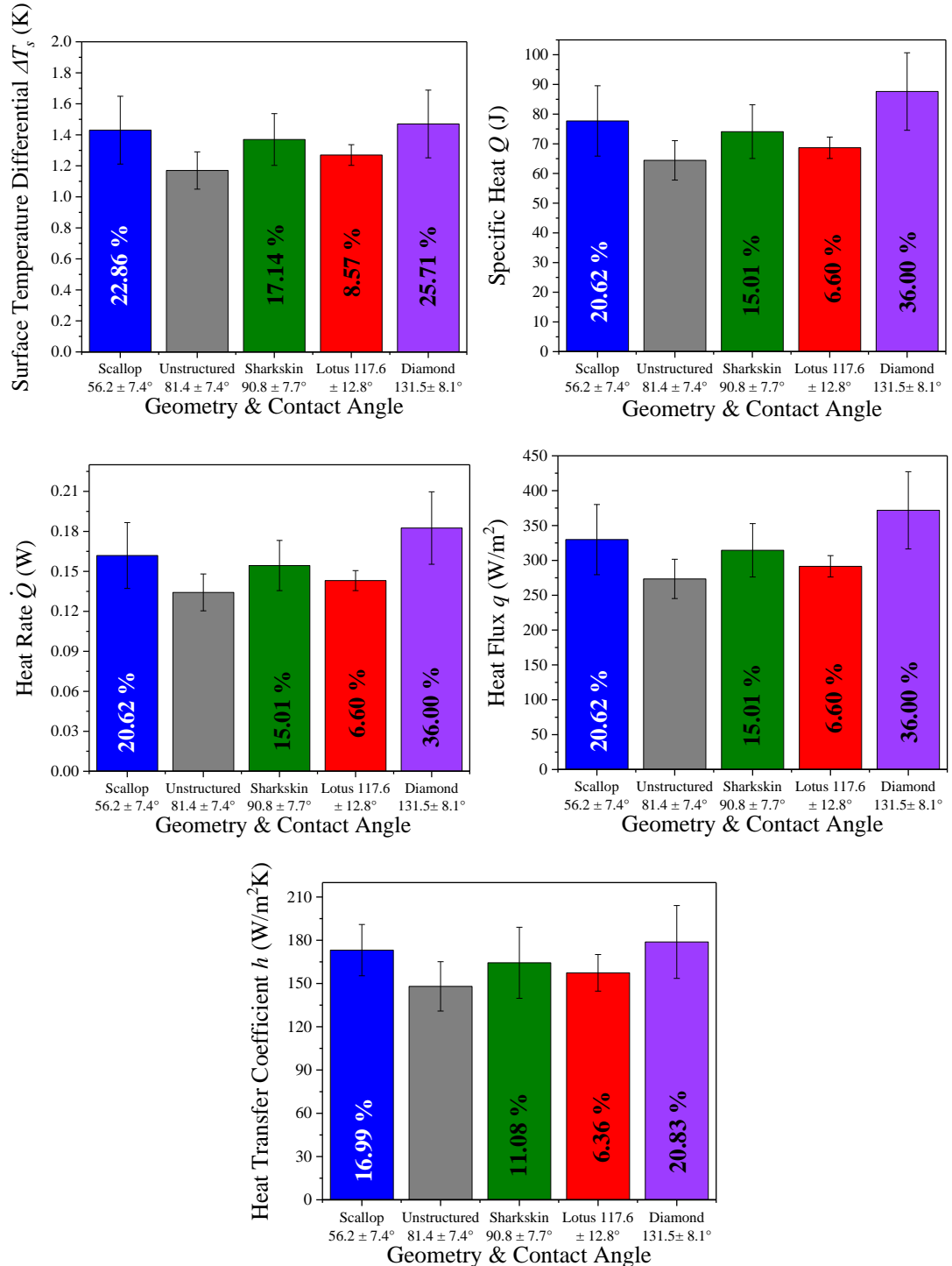


**Figure 4.19. (a) Experimental Drag Reduction, (b) Experimental Boundary Layer Thickness Reduction.**

The experimental results exhibit similar trends of the numerical drag reduction when using microstructured surfaces; however, the experimental average drag reduction (10.75%) was almost twice the values predicted by the numerical models (7%) when compared against an unstructured surface. This experimental result is comparable to the 9.9% drag reduction obtained by Bechert [157]. Figure 4.19a shows the effects of the microstructure geometry and the angle of action on drag reduction. The geometry with the highest drag reduction effect in comparison to an unstructured surface was Lotus (16.9%), followed by Scallop (9.8%), Diamond (9.4%) and finally Sharkskin (6.9%), with standard errors of the mean of 0.12, 1.67, 0.96 and 0.99, respectively. In each of the geometries, the maximum drag reduction was observed at the 0° angle of action. However, the angle of action's effect had a minor impact on the drag reduction when compared to the geometry's contribution. For Lotus, there was a difference of 1% only between the angles of action associated with the highest and lowest drag reduction. For the Scallop structure, this difference was 2.9%, while that for the Sharkskin and Diamond geometries were 2.5% and 1.6%, respectively.

### 4.1.3 Phase 3: Heat Transfer Evaluation

Figure 4.20 presents the results of the condensation experiments after eight minutes in the condensation chamber. This includes surface temperature differential ( $\Delta T_s$ ), specific heat absorbed by the insert ( $Q$ ), heat rate ( $\dot{Q}$ ), heat flux ( $q$ ), heat transfer coefficient ( $h$ ) results with a percentage of improvement with respect to an unstructured surface.

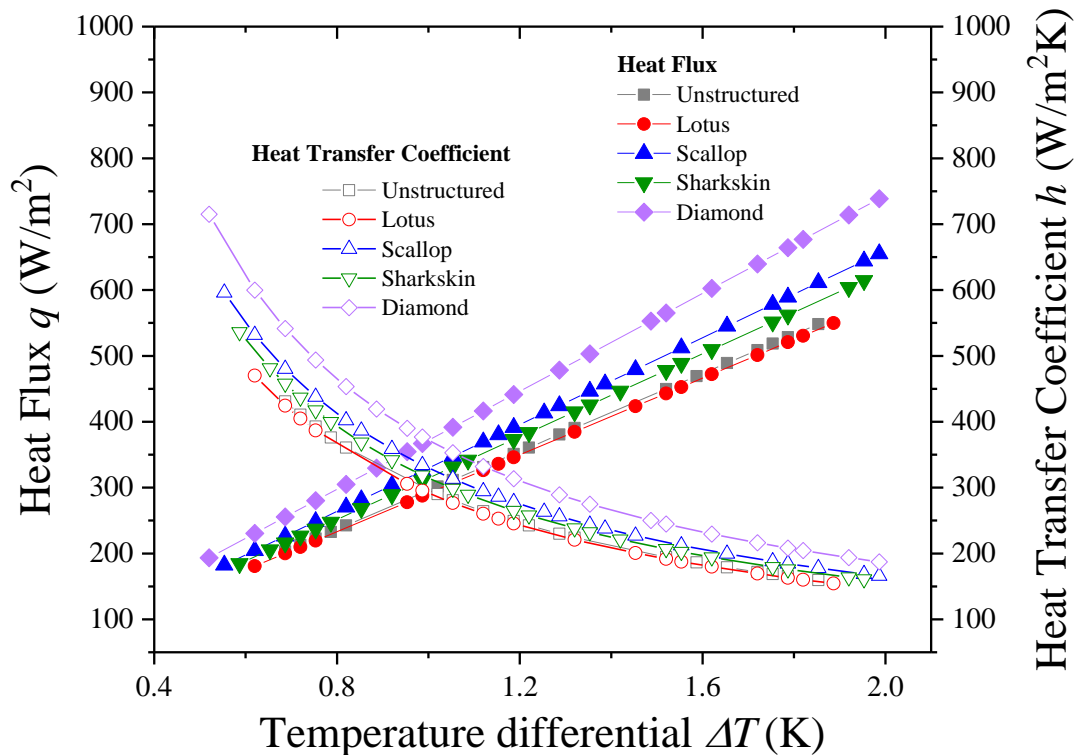


**Figure 4.20.** Surface temperature differential ( $\Delta T_s$ ), specific heat absorbed by the insert ( $Q$ ), heat rate ( $\dot{Q}$ ), heat flux ( $q$ ) and heat transfer coefficient ( $h$ ) results with percentages of improvement with respect to an unstructured surface (Stage 1).



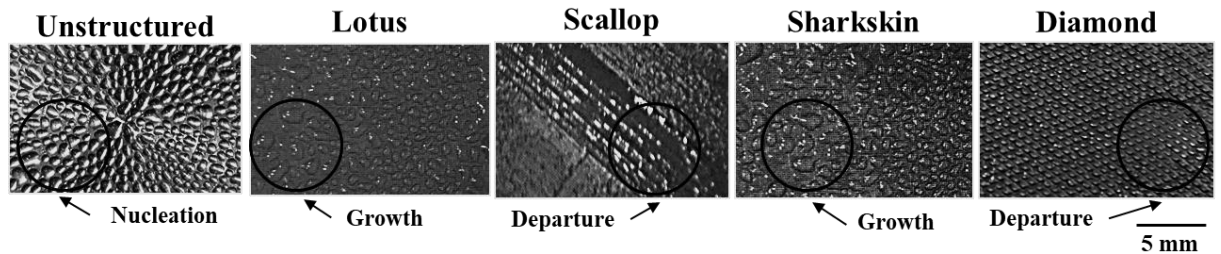
The surface temperature differentials ( $\Delta T_s$ ) in the Lotus, Scallop, Sharkskin and Diamond structured surfaces were higher by 8.57%, 22.86%, 17.14% and 25.71%, respectively, than the unstructured surface. Thus, the highest  $\Delta T_s$  was observed with the Diamond geometry. Previous work by Chatterjee et al. [56] also reported a 25% improvement in the heat transfer, while Qi et al. [142] found that grooved surfaces can enhance heat transfer by 50% when compared with smooth surfaces. Additionally, when considering the larger superficial area ( $A_s$ ) that the microstructures represent, the specific heat ( $Q$ ), heat rate ( $\dot{Q}$ ), and heat flux ( $q$ ) are 6.6% - 36% greater than that of the unstructured insert, while the heat transfer coefficient ( $h$ ) is between 6.36% and 20.83%. The closer the contact angle is to the superhydrophilic or the superhydrophobic wetting state, the better the heat transfer enhancement results.

Figure 4.21 displays the condensation heat transfer performance based on heat flux ( $q$ ) and heat transfer coefficient ( $h$ ) as a function of the surface subcooling temperature differential ( $\Delta T$ ). The results are comparable with the work carried out by Wen et al. [54]. The obtained coefficients (in the range of 150 to 800 W/m<sup>2</sup>K) follow a similar trend reported by Ghosh et al. [158] and Mahapatra et al. [159] in which condensation heat transfer coefficients were in the ranges of 30-90 W/m<sup>2</sup>K, and 30-120 W/m<sup>2</sup>K, on patterned aluminium surfaces with chemical coatings. This infers that microstructured surfaces without chemical coating can promote higher heat transfer coefficients than unstructured and chemically treated surfaces.



**Figure 4.21.** Condensation heat transfer performance. Heat flux ( $q$ ) and heat transfer coefficient ( $h$ ) as a function of the surface subcooling temperature differential ( $\Delta T$ ).

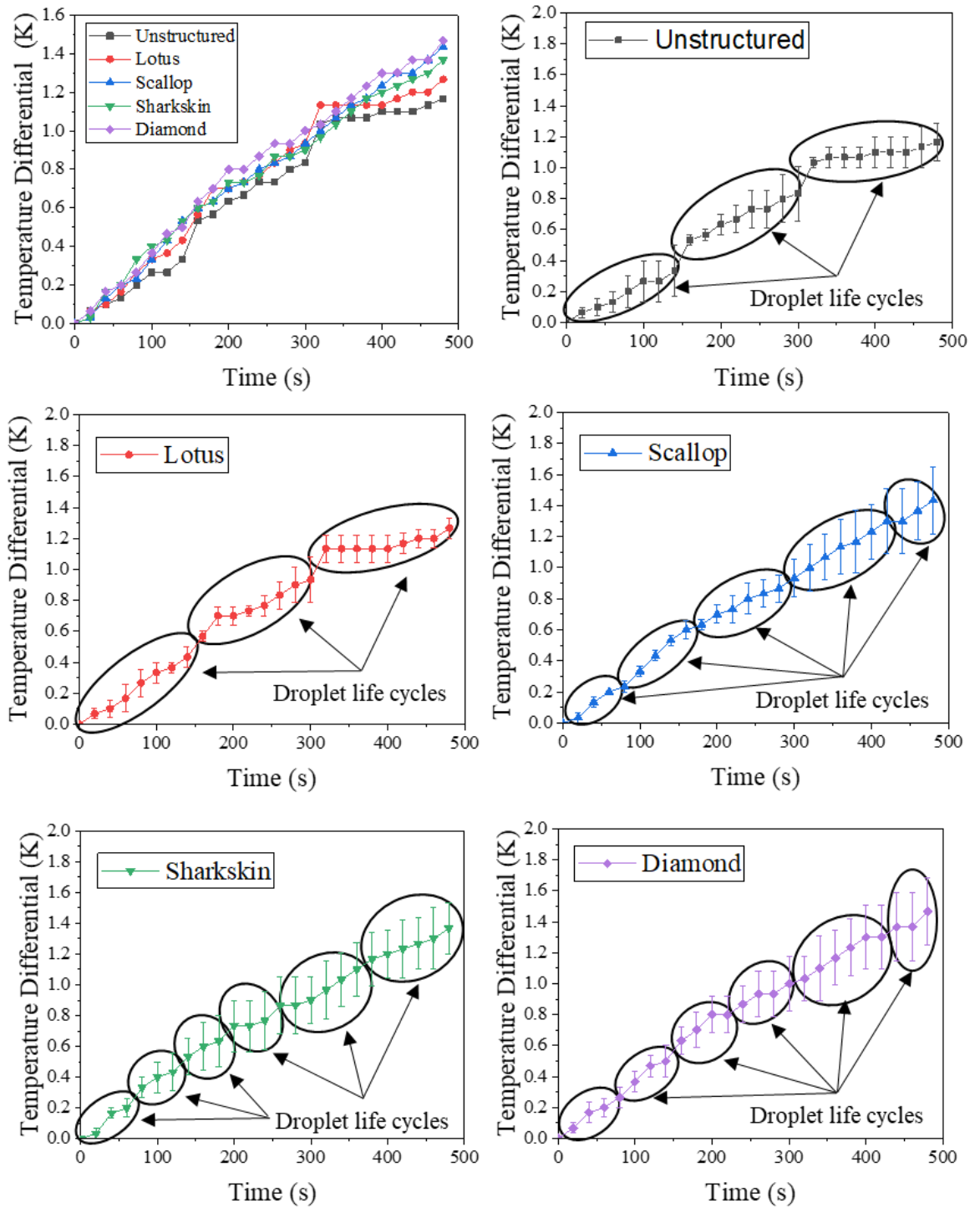
Images of the condensate after 8 minutes on each workpiece are shown in Figure 4.22, in which different stages of the droplet life cycle can be visualised on the microstructured surfaces. An inversely proportional relationship between the droplet size and the  $\Delta T_s$  was observed during the experiments, which is consistent with the studies conducted by Chatterjee et al. [160], Peng et al. [47,161] and Xu et al. [162] on dropwise condensation heat transfer. Additionally, this observation is in agreement with the results reported by Chatterjee et al. [56] and Wen et al. [54], in which a higher temperature differential presented a lower droplet density and size. Furthermore, three stages of droplet life were observed in this study: nucleation, growth, and departure. The droplets on the unstructured surface reached to the first stage of the life cycle after 8 mins of condensation, while those on the Lotus and Sharkskin structured surfaces signalled the second stage, whereas the droplets on the Diamond and Scallop surfaces were already in the final stage of their life.



**Figure 4.22.** Formation of condensates on the unstructured and microstructured surfaces of stage 1.

A qualitative analysis of the number of droplet life cycles is shown in Figure 4.23; the analysis is based on the temperature change trend over time of the microstructured surfaces and the condensate state during the experiment. In the droplet life cycle, a more significant interaction between the humid air and the microstructured surface is observed during the nucleation stage, leading to a greater change in the temperature. These variations in the differential temperature help identify the cycles. This innovative method has the potential to provide essential information on condensation when there is no visualisation equipment, such as environmental scanning electron microscope (ESEM), or when the wet mode is not available for condensation in this type of equipment. In order to validate this method, recreating the experiments in the ESEM to compare the results has been proposed. However, due to COVID-19 laboratory restrictions and the absence of equipment availability in wet mode, it was not possible to perform the validation of the proposed method.

Although the droplets on the unstructured surface were evenly distributed, the droplet life cycle was longer on this insert compared to the other structured surfaces. From Figure 4.23, only three droplet life cycles are observed for the unstructured surface and the Lotus structure. In contrast, the Scallop structure exhibits five, while the Sharkskin and the Diamond structured surfaces display six droplet life cycles, approximately.



**Figure 4.23. Surface temperature differential ( $\Delta T_s$ ) vs time, showing droplet life cycles.**

According to Anand et al. [60], the removal of the condensates from the surface results in a considerable increase in heat transfer. Grooten and Geld [163] also detailed that a higher frequency of droplet removal reduces the probability of droplets sticking onto the condensation surface. These could, in part, explain the higher  $\Delta T_s$  observed for the microstructured surfaces in the present study.

While comparing among the various microstructures, the Diamond and Scallop structures exhibit the highest  $\Delta T_s$  (Figure 4.20), possibly due to the geometry configuration that places them closest to the superhydrophilic (CA = 56.20°) and superhydrophobic (CA = 131.50°) wetting states with respect to the other structures (Table 4.2 and 4.3), thereby rendering a higher condensation rate as well as a greater drainage rate.

Additionally, by analysing the changes in the surface temperature trends, higher temperature change is observed at the nucleation stage, whereas more stable temperature change is noted during growth. The droplet life cycle duration is approximately 80 to 150 seconds (Figure 4.23). According to Zheng et al. [99], the stages of growth and coalescence can take up to 100 and 1,200 seconds each, giving as a result droplet life cycle times from 70 seconds to 1,311 seconds (21.85 minutes). Chatterjee et al. [56] reported droplet life cycles between 9 and 12 seconds by visualising the condensates on copper patterned surfaces at different flows using a digital camera; whereas He et al. [164] reported cycles between 421.1 and 487.4 seconds for aluminium micro-/nano surfaces with chemical coating by using optical microscopy visualisation. By corroborating the temperature change trend, the quantification of droplet life cycles could optimise the performance of each stage for condensation heat transfer enhancement.

#### 4.1.4 Assessment Summary

In order to select the best-microstructured surface of stage one to be used in stage two, the following components have been considered with a total weight of 100 points:

1. Phase 1: Overall performance in the Computational Fluids Dynamics (CFD) results (20 points).
2. Phase 1: Smallest percentage difference between the designed and the manufactured workpieces, considering manufacture performance and characterisation data (20 points).
3. Phase 2: Overall performance in experimental boundary layer control and drag reduction results (20 points).
4. Phase 3: Overall performance in condensation heat transfer results (40 points).

Table 4.4 shows a summary of the evaluation carried out in stage one. Even though the Diamond micro-geometry achieved the best performance in the heat transfer component, the Scallop was confirmed to be the easiest geometry to be manufactured while achieving the best CFD performance. This opens up the opportunity for further research in which the design-CFD-manufacture-characterisation loop can be optimised. Additionally, the Scallop micro-geometry achieved the second-best performance in all the different experiments, which means that it could not only work in heat transfer enhancement for this project, but it could also be used in other areas such as combustion, water harvesting, desalination, electronic thermal management, petrochemical refining, power plants and heating, ventilation, and air conditioning [46]. Hence, expanding the scope of this investigation.

**Table 4.4. Assessment summary of stage one.**

Stage 1 - Assessment criteria		Obtained points based on performance			
Component	Value	Lotus	Scallop	Sharkskin	Diamond
CFD analysis (Best performance / Drag reduction)	20	15	20	5	10
Manufacture and characterisation (Smallest percentage difference between design and manufactured)	20	10	20	5	15
Experimental Boundary Layer control and Drag reduction	20	20	15	5	10
Experimental heat transfer enhancement	40	10	30	20	40
<b>Total points</b>	<b>100</b>	55	<b>85</b>	35	75

## 4.2 Stage 2: Microstructured Surfaces Produced via Laser Micro-Processing on Cast Specimens

For the second stage, since the geometry with the best performance from the first stage is hydrophilic, an additional hydrophobic geometry was also selected. Two workpieces with variations in dimensions were considered for each wetting state. The texturing technique was changed to laser micro-processing, while the insert manufacturing technique was kept the same as the first stage.

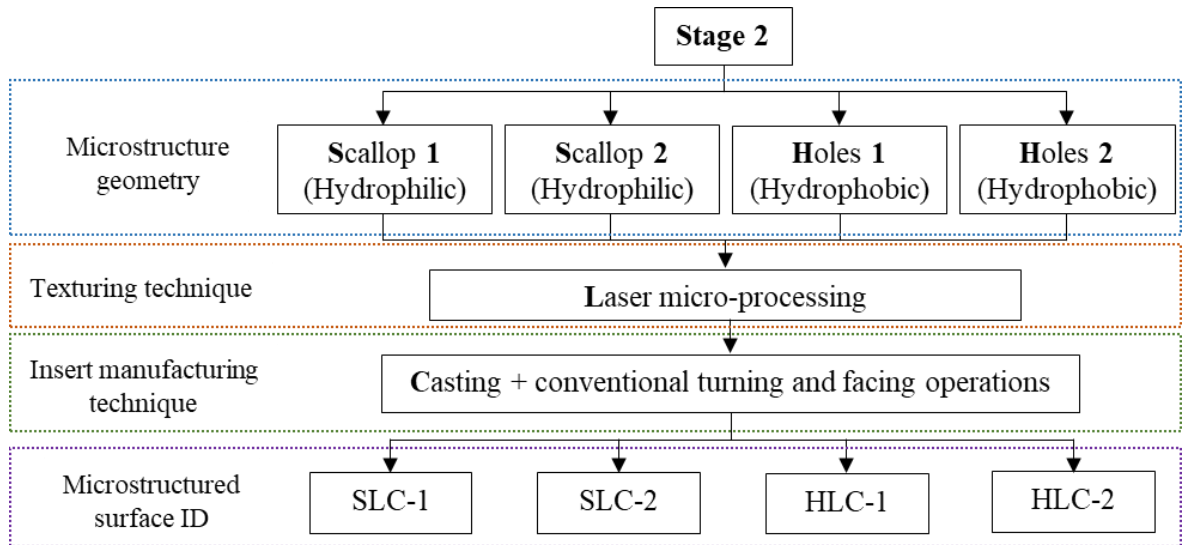


Figure 4.24. Summary of the microstructured surfaces in Stage 2.

### 4.2.1 Phase 1: Design, Manufacture and Characterisation

#### 4.2.1.1 Design

Due to the previously discussed issues with the Hydro3D code used for the CFD analysis of stage one, the design of stage two was only based on the microstructure with the best performance from stage one, the scallop geometry. Due to the hydrophilic behaviour of the scallop microstructured surface, an additional hydrophobic microstructured surface was selected in order to compare both wettability behaviours when laser micro-processing is used for topography modification on casting-manufactured inserts.

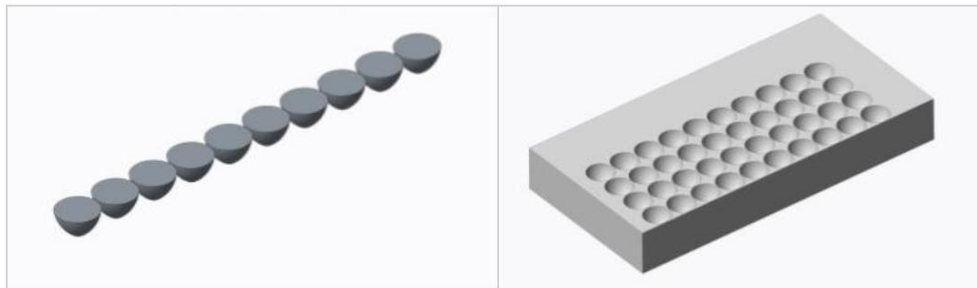
##### 4.2.1.1.1 Previous Work

As mentioned before, these geometries are the outcome of previous work carried out in the school of engineering on biomimetic engineering [19,165] and the results from stage one. The optimisation of the scallop geometry variations, considering the laser capabilities, resulted in the nominal dimensions shown in Table 4.5.

**Table 4.5. Nominal dimensions of the micro-geometries based on Scallop (Stage 2).**

Geometry	Scallop (Stage 1)	SLC-1	SLC-2
Width of grooves ( $\mu\text{m}$ )	100	65	60
Depth of grooves ( $\mu\text{m}$ )	75	225	185
Width of riblets ( $\mu\text{m}$ )	25	45	50
Pitch ( $\mu\text{m}$ )	125	110	110

The hydrophobic workpieces, known as “holes”, are based on surface texturing research carried out in the school of engineering at Cardiff University [165]. The hydrophobic holes are created by a sequence of laser pulses, as shown in Figure 4.25. For the workpieces, HLC-1 and HLC-2, the dimensions are the result of the chosen parameters mentioned in Chapter 3; hence, the characterisation data is shown in the following section.

**Figure 4.25. Schematic of hydrophobic holes manufactured by laser pulses [165].**

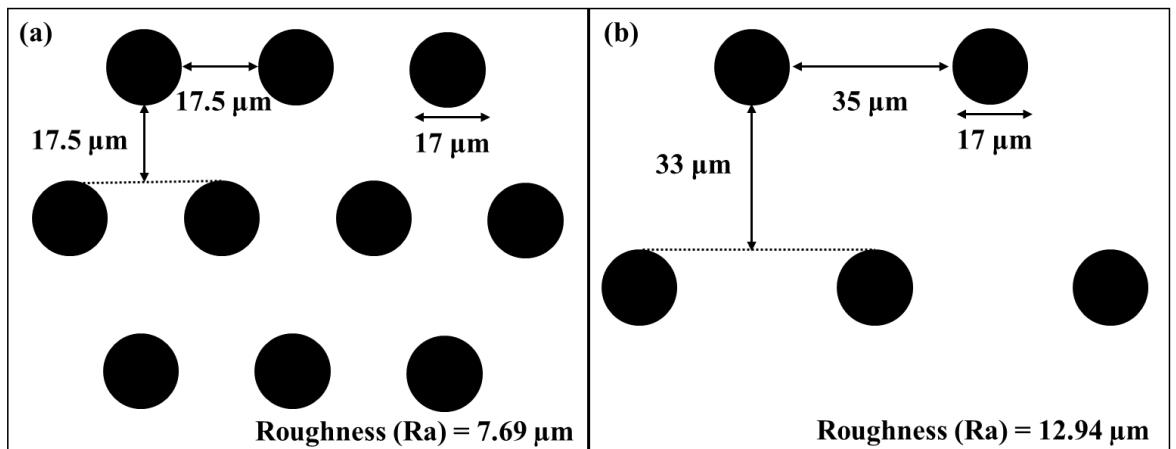
#### 4.2.1.2 Manufacture and Characterisation of the Microstructured Surfaces

The scallop-based microstructures characterisation results obtained from the 3D optical profilometer (Sensofar), together with the percentage deviations from the nominal dimensions, are shown in Table 4.6. However, due to the surface irregularities presented on the hydrophobic surfaces (Figure 4.6, perspective scan view), the scanning electron microscope (SEM) was employed to obtain the visual representations of the specimens and dimensions (Figure 4.26). Images of the final manufactured workpiece, Sensofar scans and SEM images are presented in Figure 4.27.

Considering the scanned data, the manufacturing technique for the creation of microstructures presented a percentage difference between 0.38% and 6.12%, which means that the creation of micro-geometries via laser provides a better outcome than Micro-Wire Electrical Discharge by reducing the percentage difference between the designed and manufactured workpiece up to 86.40%. The hydrophilic microstructures, based on the scallop geometry, achieved up to eight-time higher roughness than the hydrophobic microstructured surfaces (holes).

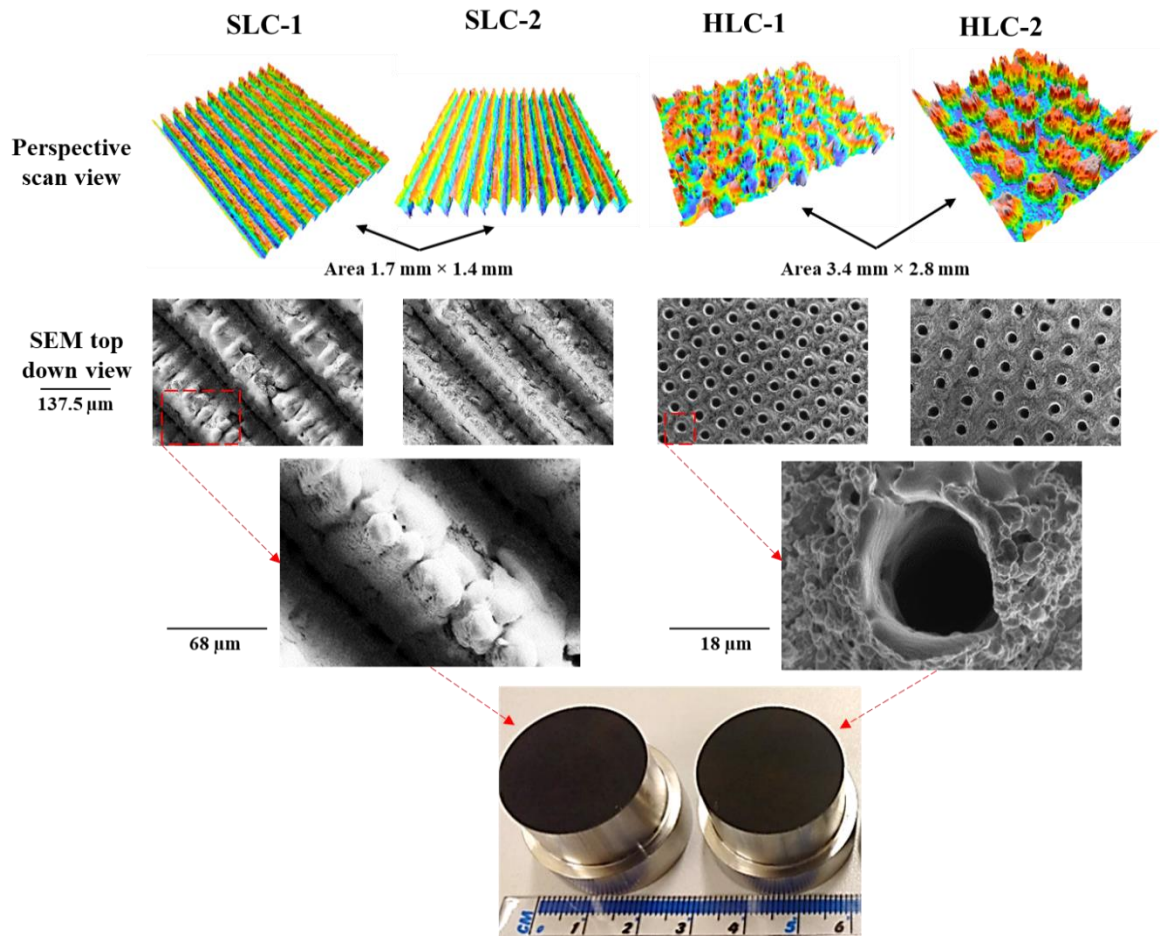
**Table 4.6. Characterisation data of the unstructured surface, scallop (stage 1 for comparison), SCL-1, SCL-2 and percentage difference with respect to the nominal dimensions.**

Geometry	Parameter	Width of grooves	Depth of grooves	Width of riblets	Pitch	Surface area $A_s$ ( $m^2$ )	Projected surface area $A_s$ ( $m^2$ )	Roughness $S_a$ ( $\mu m$ )
Unstructured	-					0.00049	0.00049	2
Scallop (Stage 1)	Nominal dimension ( $\mu m$ )	100	75	25	125	0.00107	0.00049	20.17
	Measured dimension ( $\mu m$ )	101.56	75.63	26.53	128.09			
	Percentage difference (%)	1.56	0.84	6.12	2.47			
SLC-1	Nominal dimension ( $\mu m$ )	65	225	45	110	0.00246	0.00049	63.16
	Measured dimension ( $\mu m$ )	65.36	223.80	46.08	111.44			
	Percentage difference (%)	0.55	0.53	2.4	1.31			
SLC-2	Nominal dimension ( $\mu m$ )	60	185	50	110	0.00216	0.00049	47.31
	Measured dimension ( $\mu m$ )	60.97	185.71	48.49	109.46			
	Percentage difference (%)	1.62	0.38	3.02	0.49			



**Figure 4.26. Characterisation data of (a) HLC-1 and (b) HLC-2.**





**Figure 4.27.** Manufactured workpieces images, 3D scans (Sensofar) and SEM images of the SLC-1, SLC-2, HLC-1 and HLC-2 [166].

The microstructure wettability characterisation results (contact angles), together with the margin of errors and the standard error, are shown in Table 4.7. Additionally, images of the contact angle between the water droplets and the different geometries are presented in Figure 4.28. Unlike the Scallop from the previous stage, both scallop variations on stage two achieved higher contact angles, thus diminishing the hydrophilic behaviour.

**Table 4.7.** Wettability characterisation data for the microstructured surfaces of stage 2, margin and standard errors.

Geometry	Contact Angle (°)	Margin of error (±)	Standard Error	Wetting State
Unstructured	81.41	7.38	2.66	Hydrophilic
SLC-1	70.50	10.74	3.87	Hydrophilic
SLC-2	71.18	14.55	5.24	Hydrophilic
HLC-1	127.13	5.18	1.87	Hydrophobic
HLC-2	122.78	8.95	3.22	Hydrophobic

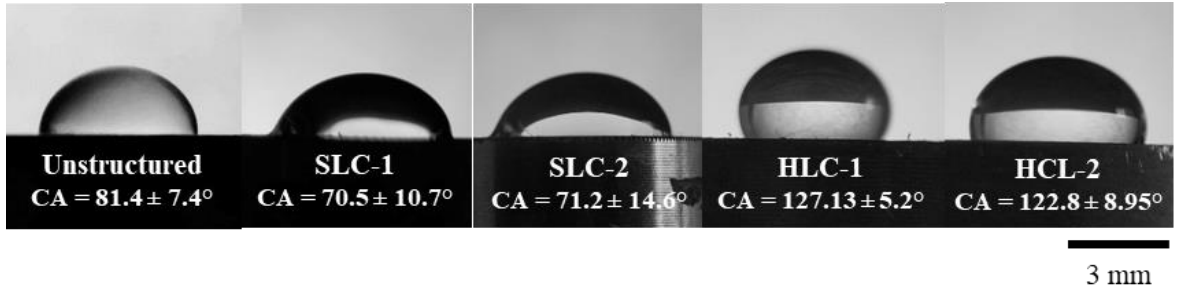


Figure 4.28. Contact angles between water droplets and the unstructured and microstructured surfaces of stage 2.

### 4.2.2 Phase 2: Fluids Dynamics Evaluation Results (Momentum Transfer)

As a result of the velocity experiments for boundary layer control and drag reduction, a velocity profile for each microstructured surface and the unstructured surface was developed on stage two. Due to the minor effect the angle of action had in the previous stage, the experimental data for stage two was collected at what would be equivalent to  $0^\circ$ . As seen in Figure 4.29, higher velocities in the boundary layer provide a higher drag force.

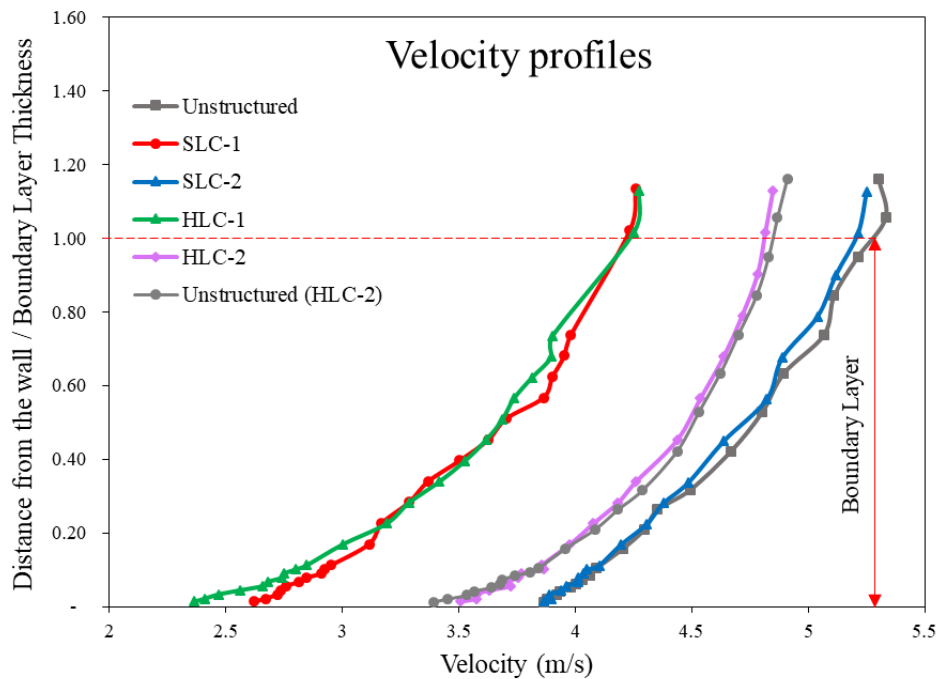
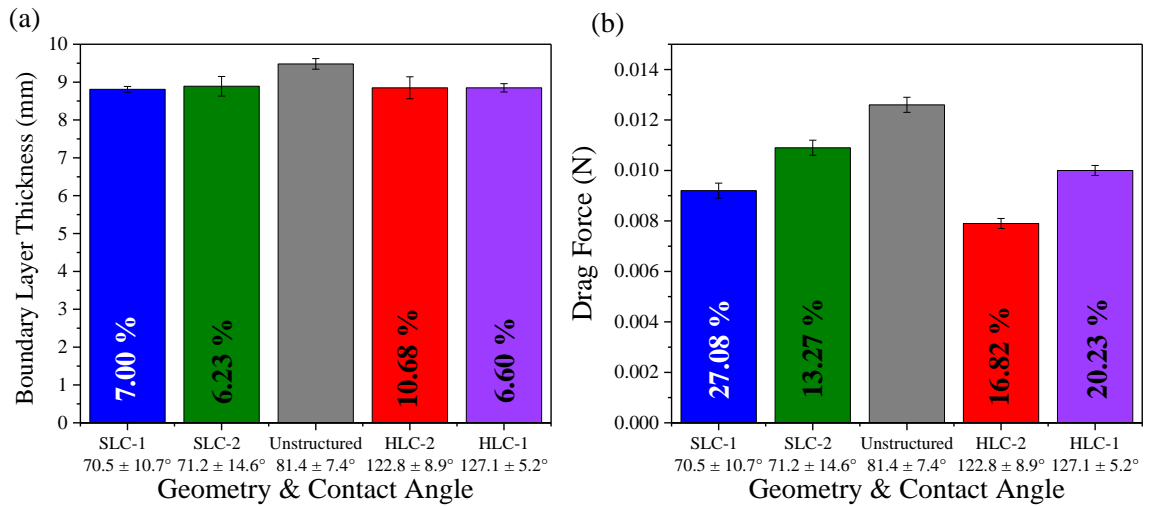


Figure 4.29. Velocity profiles of stage 2 microstructured surfaces and unstructured surface.

Figure 4.30 comprises the experimental boundary layer thickness (mm), boundary layer thickness reduction (%), drag force (N) and drag reduction (%) of each microstructured surface and the unstructured surface of stage two. More detailed results are available in Appendix D, in which a second set of the unstructured surface’s results were used to compare the HCL-2 performance.

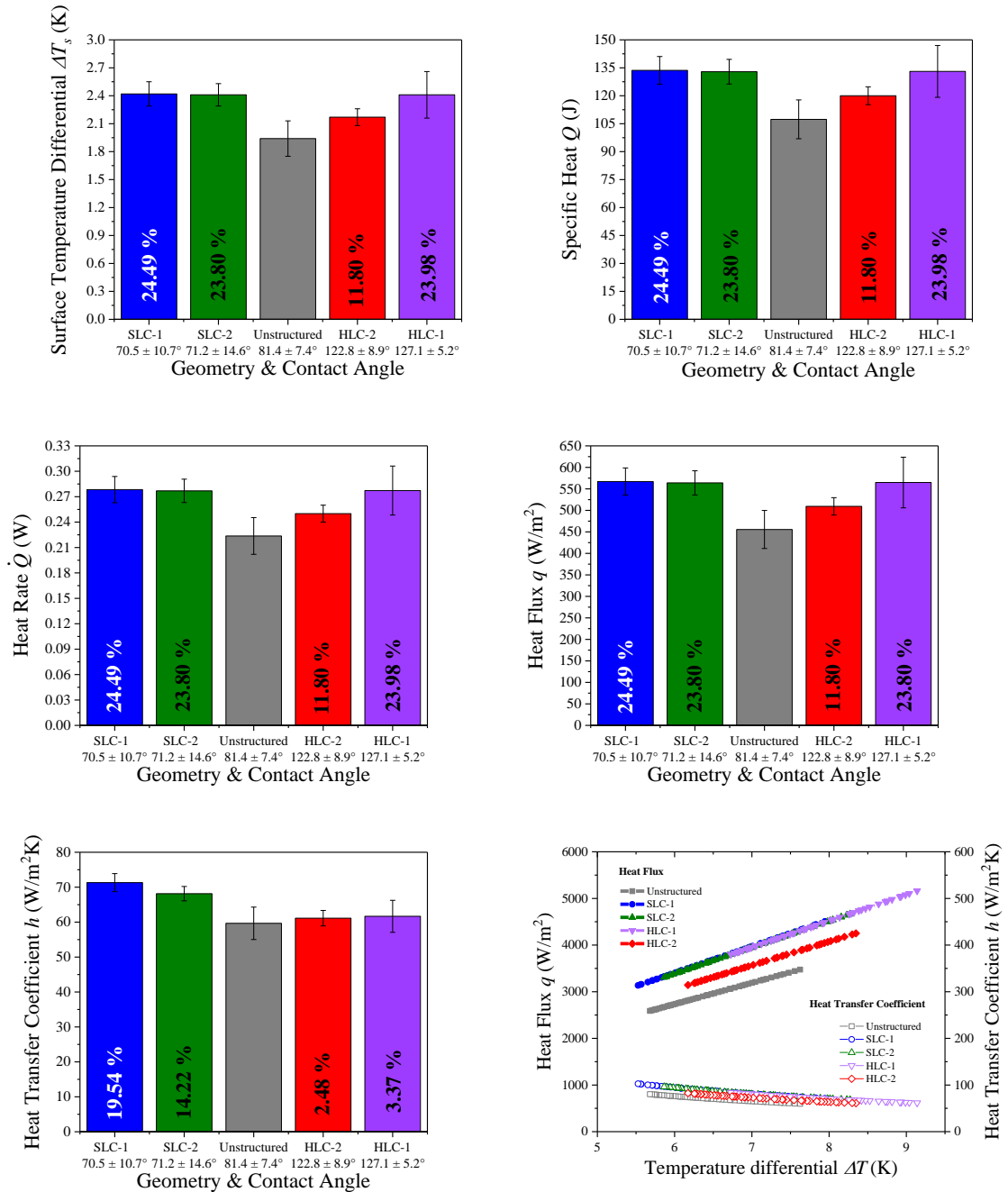


**Figure 4.30. (a) Experimental boundary layer thickness (mm), boundary layer thickness reduction (%). (b) Drag force (N) and drag reduction (%) with respect to an unstructured surface (Stage 2).**

The smaller velocities profiles presented in SLC-1 and HLC-1 resulted in a 27.08% and 20.23% decrease in drag force and up to 7% on boundary layer thickness reduction. When comparing against the Scallop microstructured surface from stage one, SLC-1 from stage two tripled the amount of drag reduction. In contrast, there was no significant change in boundary layer thickness reduction when compared against stage one results.

### 4.2.3 Phase 3: Heat Transfer Evaluation

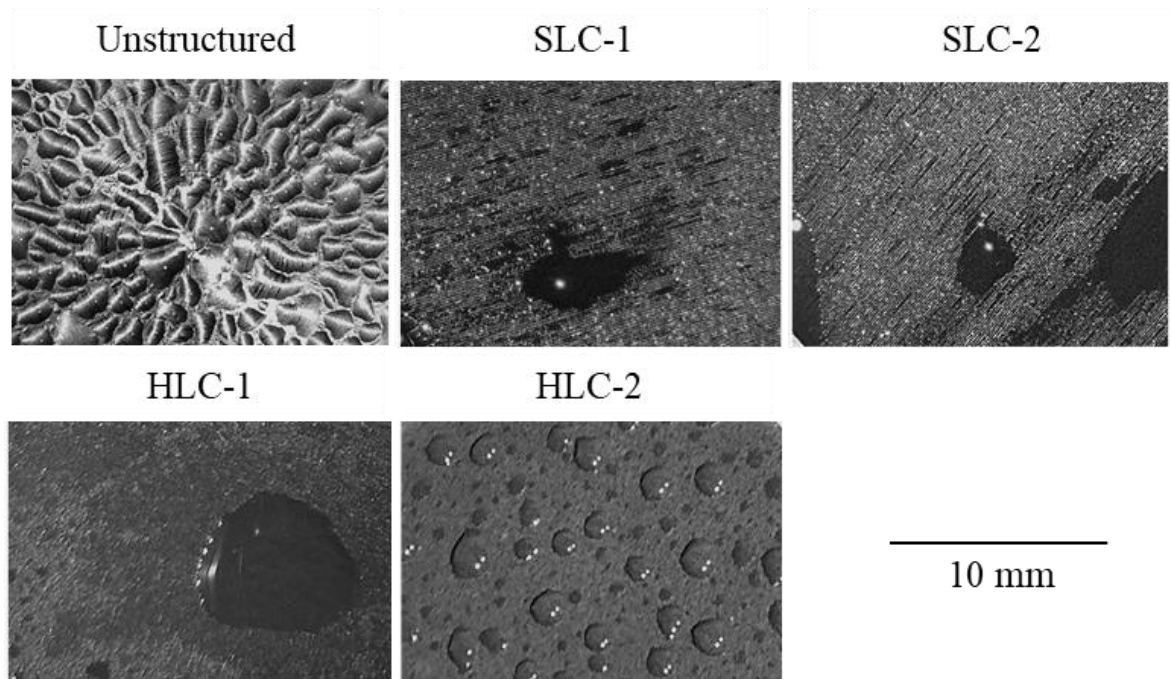
Figure 4.31 presents the results of the condensation experiments after eight minutes in the condensation chamber. This includes surface temperature differential ( $\Delta T_s$ ), specific heat absorbed by the insert ( $Q$ ), heat rate ( $\dot{Q}$ ), heat flux ( $q$ ), heat transfer coefficient ( $h$ ) results with percentage of improvement with respect to an unstructured surface, and Heat flux ( $q$ ) and heat transfer coefficient ( $h$ ) as a function of the surface subcooling temperature differential ( $\Delta T$ ).



**Figure 4.31. Stage 2 condensation heat transfer performance. Surface temperature differential ( $\Delta T_s$ ), specific heat absorbed by the insert ( $Q$ ), heat rate ( $\dot{Q}$ ), heat flux ( $q$ ), heat transfer coefficient ( $h$ ) results with percentage of improvement with respect to an unstructured surface, and Heat flux ( $q$ ) and heat transfer coefficient ( $h$ ) as a function of the surface subcooling temperature differential ( $\Delta T$ ).**

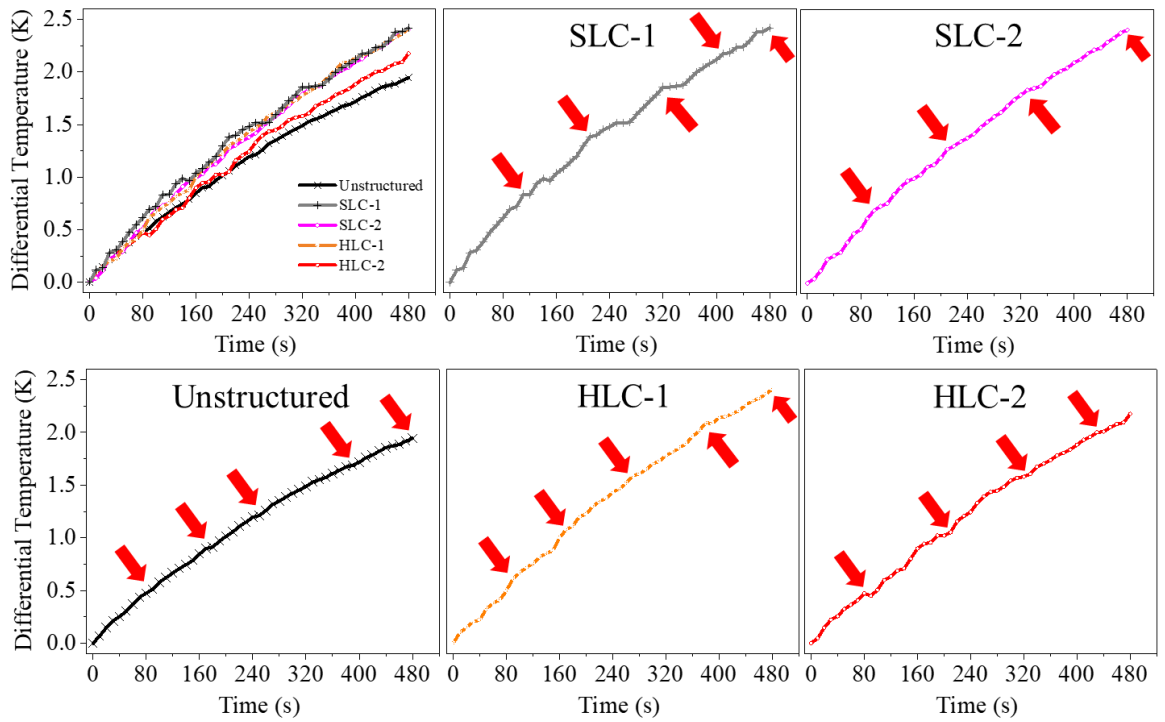
Similarly to stage one, the closer the contact angle is to the superhydrophilic or the superhydrophobic state, the better the heat transfer enhancement results. In stage one, a hydrophilic scallop surface with a contact angle of  $56.2^\circ \pm 7.4^\circ$  achieved surface temperature differentials ( $\Delta T_s$ ), specific ( $Q$ ), heat rate ( $\dot{Q}$ ), and heat flux ( $q$ ) enhancement of up to 22.86% while SLC-1 with a contact angle of  $70.5^\circ \pm 10.7^\circ$  achieved 24.49% enhancement. On the hydrophobic side, contact angles between  $117.6^\circ \pm 12.8^\circ$  and  $131.5^\circ \pm 8.1^\circ$  from stage one showed between 6.6% and 36% enhancement while contact angles between  $122.8^\circ \pm 8.9^\circ$  and  $127.1^\circ \pm 5.2^\circ$  from stage two presented between 11.80% and 23.80% enhancement.

Images of the condensate after 8 minutes on each workpiece are shown Figure 4.32, in which different stages of the droplet life cycle can be visualised. As mentioned in stage one, an inversely proportional relationship between the droplet size and the  $\Delta T_s$  was observed, this explains the higher  $\Delta T_s$  observed for the scallop specimens in this stage since they presented smaller droplet size. Additionally, a higher frequency of condensate removal reduces the likelihood of droplets sticking onto the surface which significantly increases the interaction between the humid air and the surface, thus promotes the enhancement of heat transfer [60,163].



**Figure 4.32.** Formation of condensates on the unstructured and microstructured surfaces of stage 2.

The qualitative analysis on the number of droplet life cycles is shown in Figure 4.33. During the 8-minute experiments, the unstructured surface, SLC-1, and HLC-1 exhibited 5 droplet life cycles while SLC-2 and HLC-2 displayed ~4.5 cycles with times between 96 and 106.7 seconds per cycle. These results remain in the same range as stage one and previous studies [99]. The analysis is based on the temperature change trend over time of the microstructured surfaces and the condensate state during the experiment. In the droplet life cycle, a more significant interaction between the humid air and the microstructured surface is observed during the nucleation stage, leading to a greater change in the temperature. These variations in the differential temperature help identify the cycles.



**Figure 4.33. Surface temperature differential ( $\Delta T_s$ ) vs. time, showing droplet life cycles (Stage 2).**

#### 4.2.4 Assessment Summary

In order to select the best microstructured surface of stage one to be used in stage two, the following components have been considered with a total weight of 100 points:

1. Phase 1: Smallest percentage difference between designed and manufactured workpieces, considering manufacture performance and characterisation data (20 points).
2. Phase 2: Overall performance in experimental boundary layer control and drag reduction results (30 points).
3. Phase 3: Overall performance in condensation heat transfer results (50 points).

Table 4.8 shows a summary of the evaluation carried out in stage two. The hydrophilic scallop variant SLC-1 achieved the best performance in each component, while the hydrophobic variant HLC-1 presented the second-best overall performance.

Stage 2 - Assessment criteria		Obtained points based on performance			
Component	Value	SLC-1	SLC-2	HCL-1	HCL-2
<b>Manufacture and characterisation (Smallest percentage difference between design and manufactured)</b>	<b>20</b>	<b>20</b>	15	10	10
<b>Experimental Boundary Layer control and Drag reduction</b>	<b>30</b>	<b>30</b>	7.5	15	22.5
<b>Experimental heat transfer enhancement</b>	<b>50</b>	<b>50</b>	25	37.5	12.5
<b>Total points</b>	<b>100</b>	<b>100</b>	47.5	<b>62.5</b>	45

Table 4.8. Assessment summary of stage two.

### 4.3 Stage 3: Microstructured Surfaces Produced via Laser Micro-Processing on Selective Laser Melted Specimens

For the third stage, the hydrophilic scallop variant with the best performance (SLC-1), and both hydrophobic geometries were chosen to corroborate repeatability and expand the knowledge on the available manufacturing resources for further research on heat transfer enhancement when using more complex workpieces than the current inserts. Therefore, the three workpieces for stage three were manufactured by the same texturing technique used in stage two, laser micro-processing. In contrast, the insert manufacturing technique was changed from casting and conventional turning and facing operations to an additive layer manufacturing technique, laser powder bed fusion.

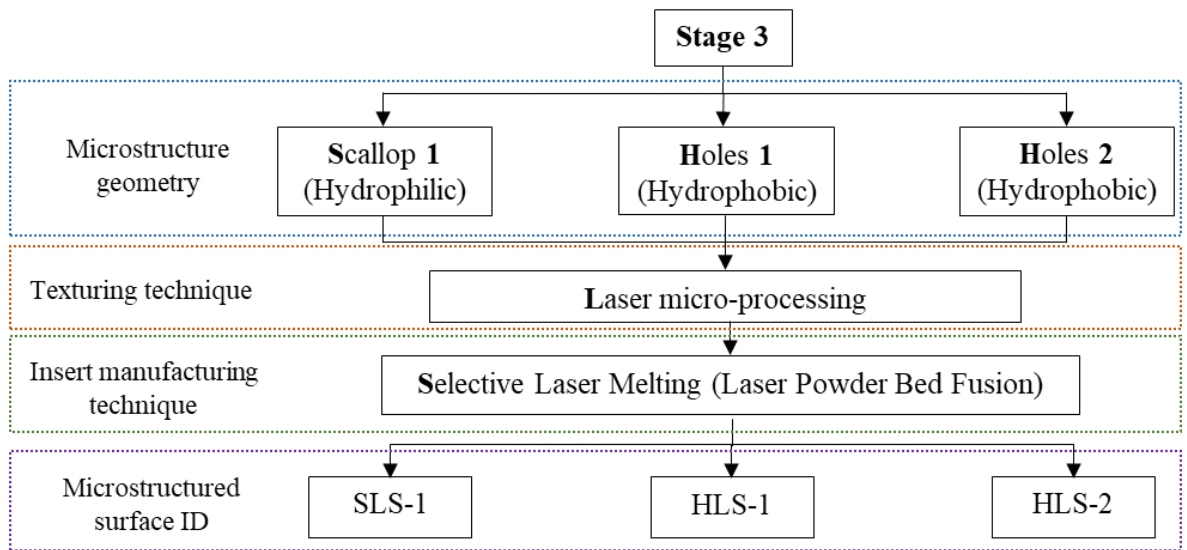


Figure 4.34. Summary of the microstructured surfaces in Stage 3.

#### 4.3.1 Phase 1: Design, Manufacture and Characterisation

##### 4.3.1.1 Design

The design of the stage three microstructured surfaces was based on the microstructures from stage two. One scallop microstructured surface workpiece and two hydrophobic microstructured surface variations were created by laser micro-processing on inserts manufactured by selective laser melting.

##### 4.3.1.1.1 Previous Work

These geometries are the outcome of previous work carried out in the school of engineering on biomimetic engineering [19][165] and the results from stage two. The optimisation of the scallop geometry, considering the laser capabilities, resulted in the nominal dimensions shown in Table 4.9.



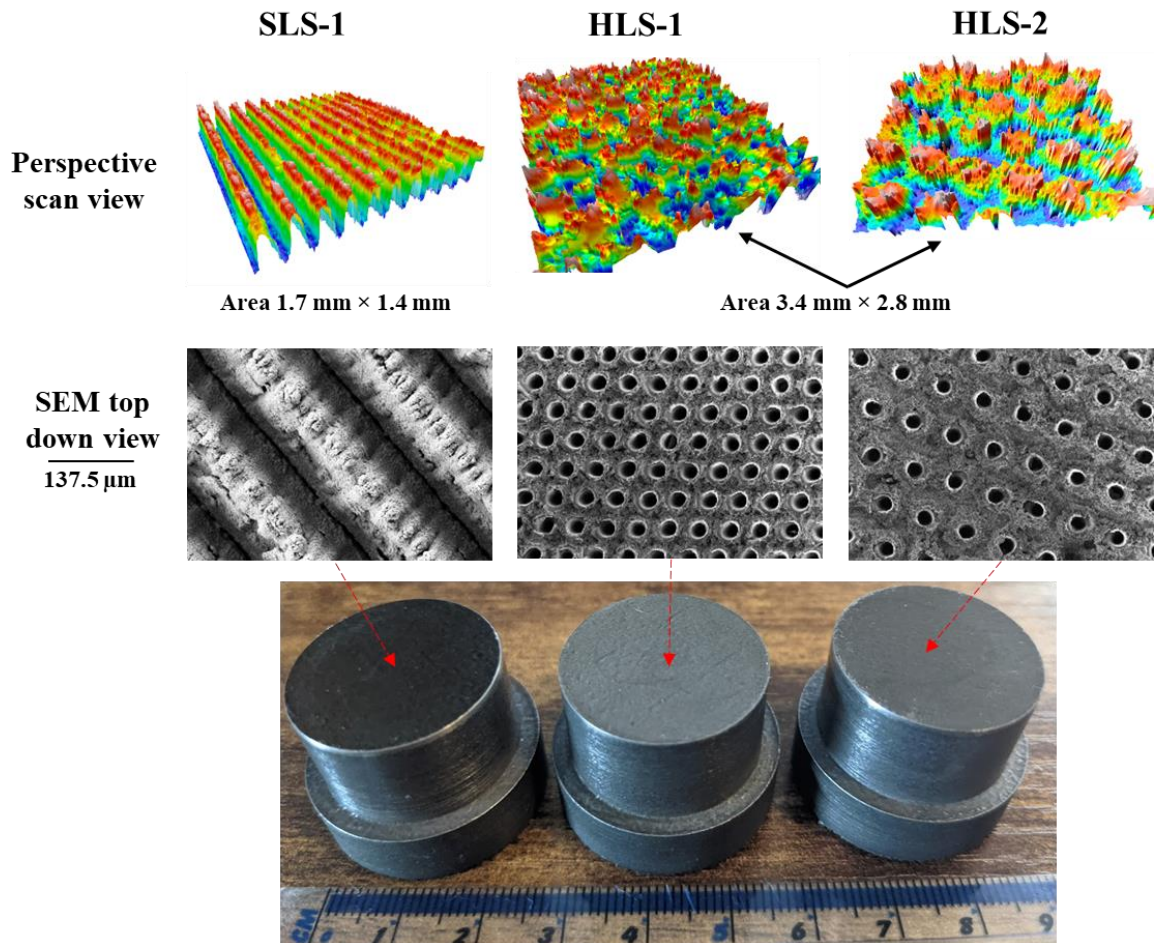
**Table 4.9. Nominal dimensions of the micro-geometry based on Scallop (Stage 3). \* For comparison purposes.**

Geometry	SLC-1*	SLS-1
Width of grooves ( $\mu\text{m}$ )	65	65
Depth of grooves ( $\mu\text{m}$ )	225	225
Width of riblets ( $\mu\text{m}$ )	45	60
Pitch ( $\mu\text{m}$ )	110	125

Regarding the hydrophobic workpieces, the creation of the “holes” followed the same procedure used for the two variations in the second stage; therefore, the characterisation data is shown in the following section.

#### 4.3.1.2 Manufacture and Characterisation of the Microstructured Surfaces

Images of the final manufactured workpiece, Sensofar scans and SEM images are presented in Figure 4.35.



**Figure 4.35. Manufactured workpieces images, 3D scans (Sensofar) and SEM images of the SLS-1, HLS-1 and HLC-S [166].**

The scallop-based microstructures characterisation results obtained from the 3D optical profilometer (Sensofar), together with the percentage deviations from the nominal dimensions, are shown in Table 4.10. However, due to the complex geometry presented on the hydrophobic surfaces, the scanning electron microscope (SEM) was employed to obtain the visual representations of the specimens and dimensions (Figure 4.36). Considering the scanned data, the hydrophilic microstructure, based on the scallop geometry, achieved up to nine-time higher roughness than the hydrophobic microstructured surfaces (holes).

**Table 4.10. Characterisation data of the unstructured surface, scallop, SLC-1, SLS-1 and percentage difference with respect to the nominal dimensions. \* For comparison purposes.**

Geometry	Parameter	Width of Grooves	Depth of Grooves	Width of Riblets	Pitch	Surface Area $A_s$ (m <sup>2</sup> )	Projected Surface Area $A_s$ (m <sup>2</sup> )	Roughness $S_a$ (μm)
<b>Unstructured*</b>		-				0.00049	0.00049	2
<b>Scallop* (Stage 1)</b>	<b>Nominal dimension (μm)</b>	100	75	25	125	0.00107	0.00049	20.17
	<b>Measured dimension (μm)</b>	101.56	75.63	26.53	128.09			
	<b>Percentage difference (%)</b>	1.56	0.84	6.12	2.47			
<b>SLC-1* (Stage 2)</b>	<b>Nominal dimension (μm)</b>	65	225	45	110	0.00246	0.00049	63.16
	<b>Measured dimension (μm)</b>	65.36	223.80	46.08	111.44			
	<b>Percentage difference (%)</b>	0.55	0.53	2.4	1.31			
<b>SLS-1 (Stage 3)</b>	<b>Nominal dimension (μm)</b>	65	225	60	125	0.00226	0.00049	78.64
	<b>Measured dimension (μm)</b>	68.33	224.68	60.53	128.86			
	<b>Percentage difference (%)</b>	5.12	0.14	0.88	3.09			

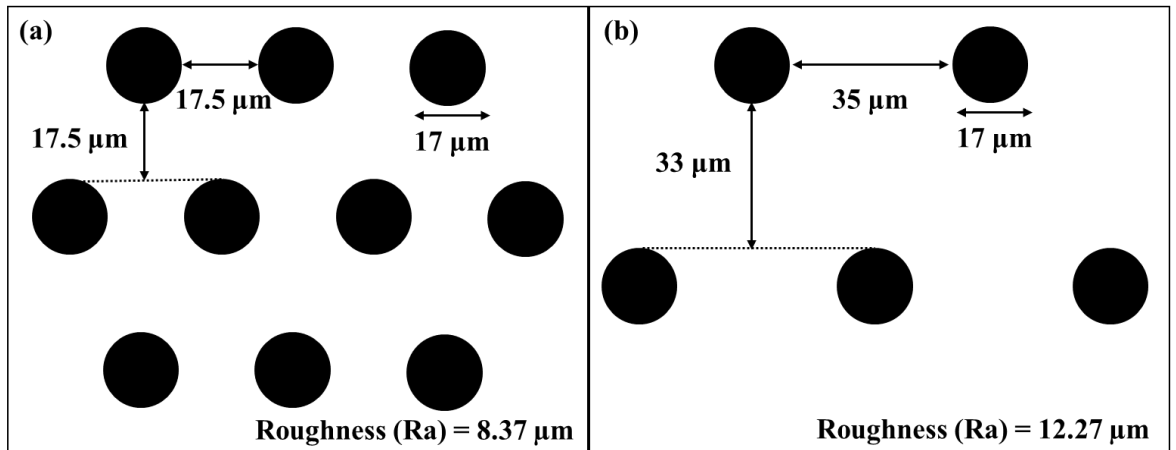


Figure 4.36. Characterisation data of (a) HLS-1 and (b) HLS-2.

The microstructure wettability characterisation results (contact angles), together with the margin of errors and the standard error, are shown in Table 4.11. The three additive layer manufactured workpieces achieved higher contact angles than their counterparts from stage two; however, the percentage difference was not significant.

Table 4.11. Wettability characterisation data for the microstructured surfaces of stage 3, margin and standard errors.

Geometry	Contact Angle (°)	Margin of error (±)	Standard Error	Wetting State
Unstructured	81.41	7.38	2.66	Hydrophilic
SLS-1	73.17	9.44	3.40	Hydrophilic
HLS-1	128.79	8.55	3.08	Hydrophobic
HLS-2	124.00	5.23	1.88	Hydrophobic

Additionally, images of the contact angle between the water droplets and the different geometries are presented in Figure 4.37. The difference in contact angle between SLC-1 from stage two and SLS-1 from stage three is 3.65%, i.e. it increased from  $70.50^\circ \pm 10.74^\circ$  to  $73.17^\circ \pm 9.44^\circ$ . The difference in contact angle between HLC-1 from stage two and HLS-1 from stage three is 1.3%, increasing from  $123.13^\circ \pm 5.18^\circ$  to  $128.79^\circ \pm 8.55^\circ$ . The difference in contact angle between HLC-2 from stage two and HLS-2 from stage three is 0.99%, increasing from  $122.78^\circ \pm 8.95^\circ$  to  $124^\circ \pm 5.23^\circ$ .

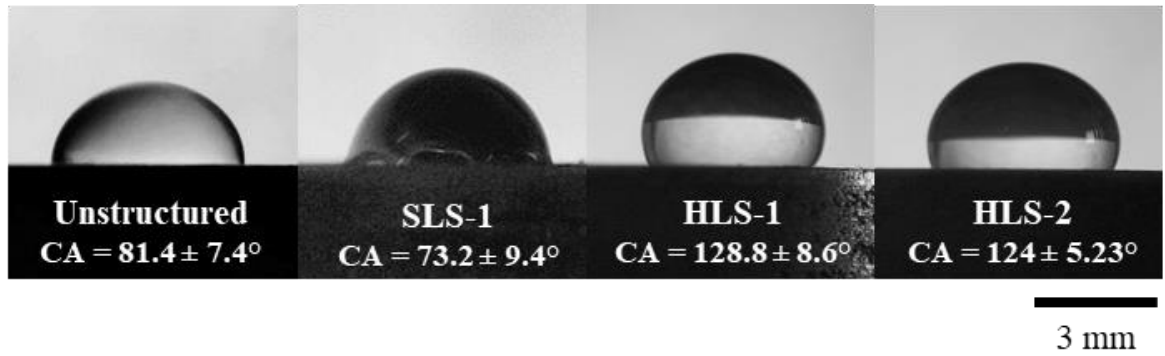


Figure 4.37. Contact angles between water droplets and the unstructured and microstructured surfaces of stage 3.

### 4.3.2 Phase 2: Fluids Dynamics Evaluation Results (Momentum Transfer)

As a result of the velocity experiments for boundary layer control and drag reduction, Figure 4.38 presents the velocity profile of each microstructured surface and the unstructured surface on stage three.

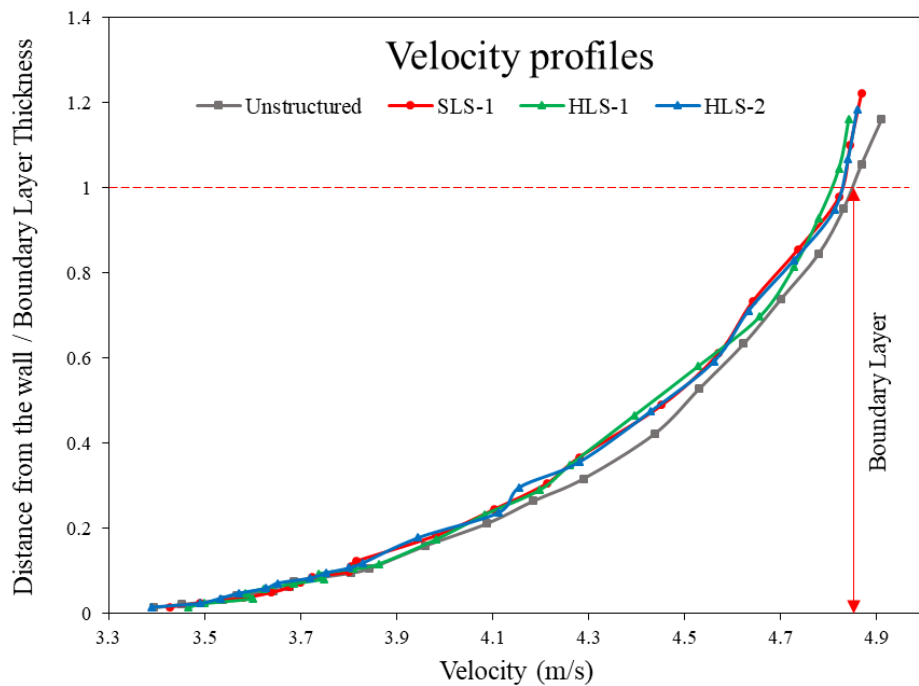
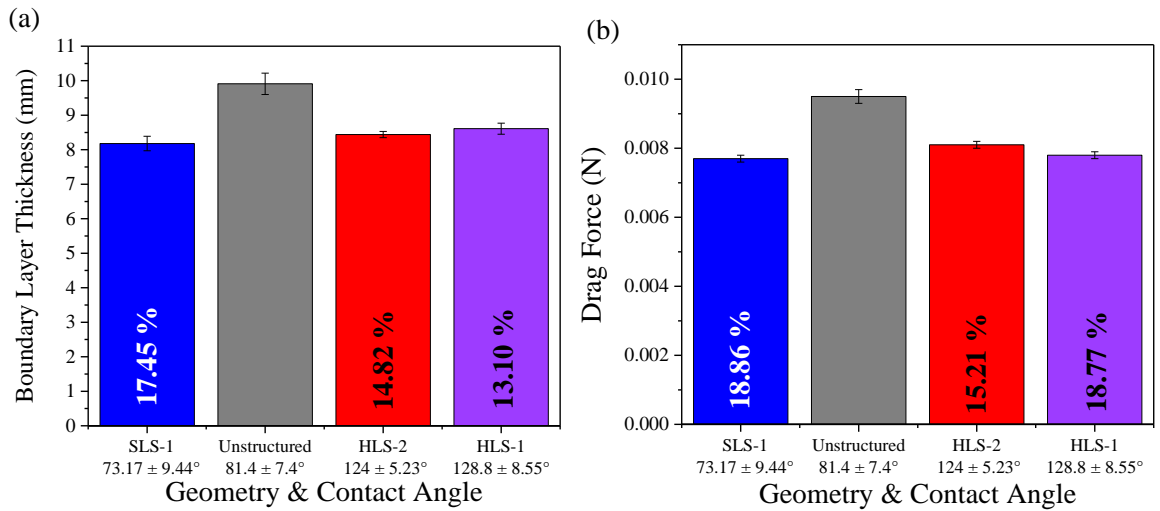


Figure 4.38. Velocity profiles of the stage three microstructured surfaces and unstructured surface.

Due to the minor effect the angle of action had in stage one, the experimental data for stage three was collected at what would be equivalent to  $0^\circ$ . Figure 4.39 comprises the experimental boundary layer thickness (mm), boundary layer thickness reduction (%), drag force (N) and drag reduction (%) of each microstructured surface and the unstructured surface of stage three. More detailed results are available in Appendix D.

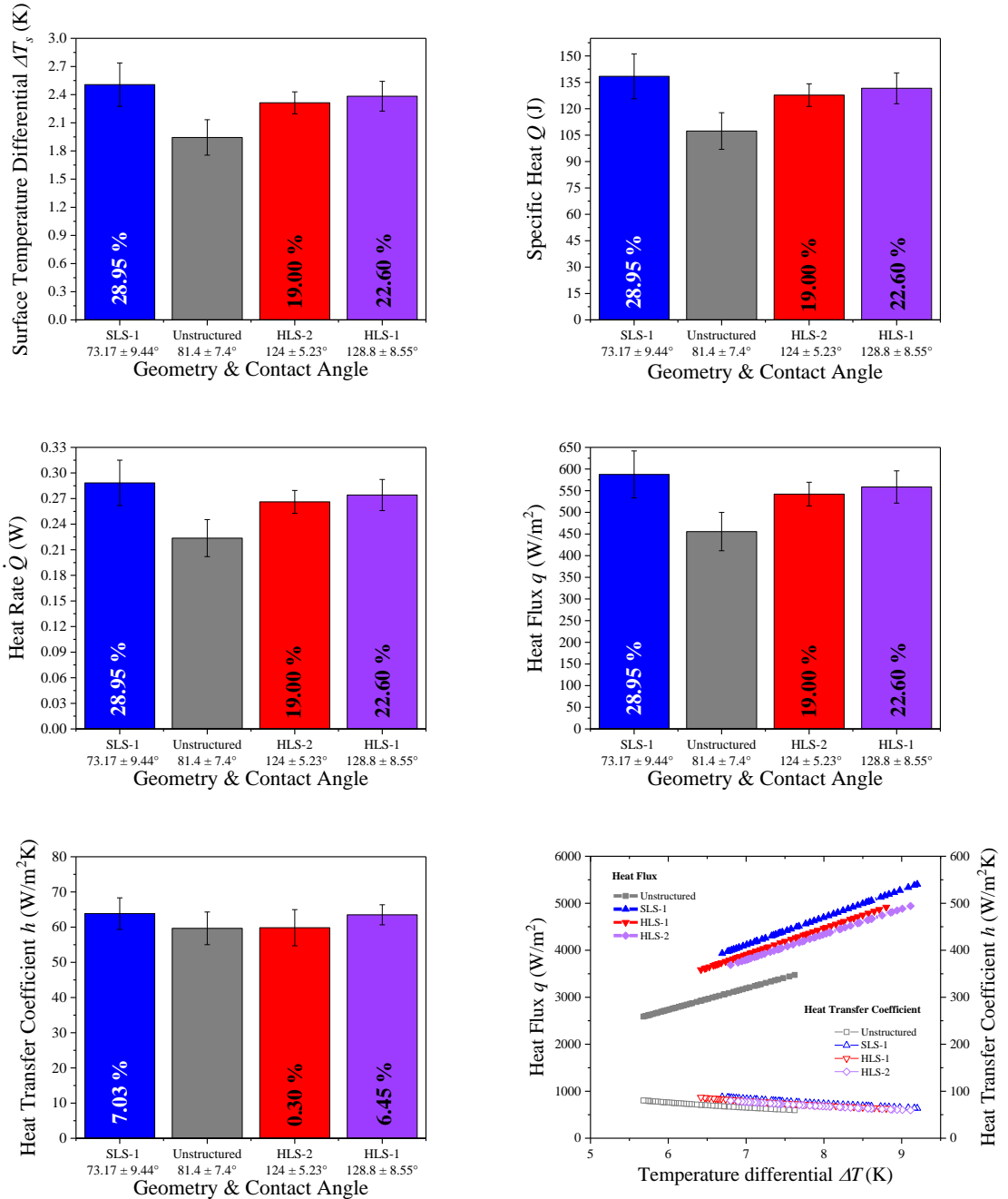


**Figure 4.39. (a) Experimental boundary layer thickness (mm), boundary layer thickness reduction (%). (b) Drag force (N) and drag reduction (%) with respect to an unstructured surface (Stage 3).**

When compared against stage two, stage three workpieces achieved higher boundary layer thickness reduction; on the contrary, stage two workpieces achieved higher drag reduction. In overall, the hydrophilic scallop SLS-1 microstructured surface presented the best performance in stage three, followed by the hydrophobic HLS-1 microstructured surface; following the same trend that was observed in stage two.

### 4.3.3 Phase 3: Heat Transfer Evaluation

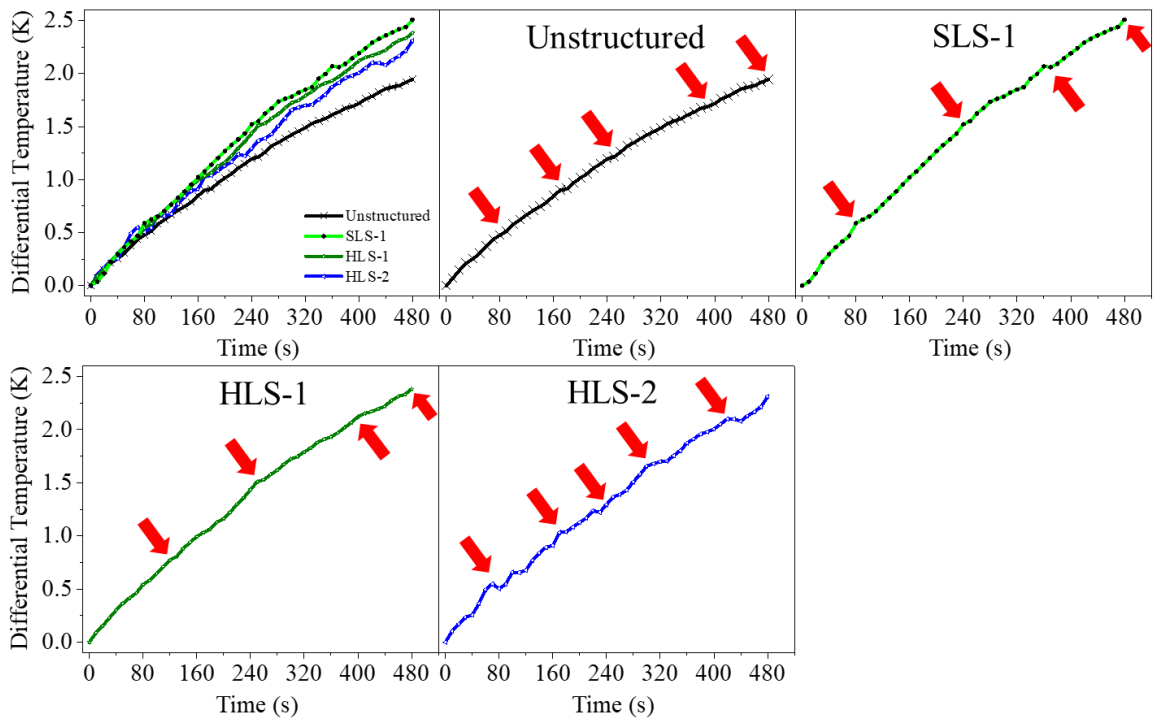
Figure 4.40 presents the results of the condensation experiments after 8 minutes in the condensation chamber. This includes surface temperature differential ( $\Delta T_s$ ), specific heat absorbed by the insert ( $Q$ ), heat rate ( $\dot{Q}$ ), heat flux ( $q$ ), heat transfer coefficient ( $h$ ) results with a percentage of improvement with respect to an unstructured surface, and Heat flux ( $q$ ) and heat transfer coefficient ( $h$ ) as a function of the surface subcooling temperature differential ( $\Delta T$ ).



**Figure 4.40. Stage 3 condensation heat transfer performance. Surface temperature differential ( $\Delta T_s$ ), specific heat absorbed by the insert ( $Q$ ), heat rate ( $\dot{Q}$ ), heat flux ( $q$ ), heat transfer coefficient ( $h$ ) results with percentage of improvement with respect to an unstructured surface, and Heat flux ( $q$ ) and heat transfer coefficient ( $h$ ) as a function of the surface subcooling temperature differential ( $\Delta T$ ).**

Following the same trend as stages one and two, the workpieces with the lowest and the highest contact angles achieved the best heat transfer results. In overall, the hydrophilic microstructured structure from stage three presented better results than its counterpart in stage two. SLS-1 achieved up to 28.95% enhancement on stage three, while SLC-1 achieved 24.49% on stage two. On the hydrophobic side, the 23.98% and 11.80% enhancement provided by HLC-1 and HLC-2 in stage two, changed to 22.60% and 19% enhancement provided by HLS-1 and HLS-2, respectively.

From the qualitative analysis on the number of droplet life cycles in Figure 4.41, SLS-1 appears to be between the fourth and fifth droplet life cycle, while HLS-1 displays ~3.5 cycles, HLS-2 ~5.5 cycles and the unstructured ~5 cycles. Stage three workpieces presented times between 87.27 and 137.14 seconds per cycle; these results are within the reported times by Zheng et al. [99]. Droplet drainage appears to be more efficient in SLS-1 than its counterpart SLC-1. HLS-1 appears to be halfway through the cycle while its counterpart in stage two, HLC-1, was at the end. HLS-2 presents a larger droplet size and density than its counterpart HLC-2 in stage two. The analysis is based on the temperature change trend over time of the microstructured surfaces and the condensate state during the experiment.



**Figure 4.41.** Surface temperature differential ( $\Delta T_s$ ) vs time, showing droplet life cycles (Stage 3).

Images of the condensate after 8 minutes on each workpiece are shown in Figure 4.42. In SLS-1, droplets have been drained, while in HLS-1 and HLS-2, droplet growth and coalescence can be observed.

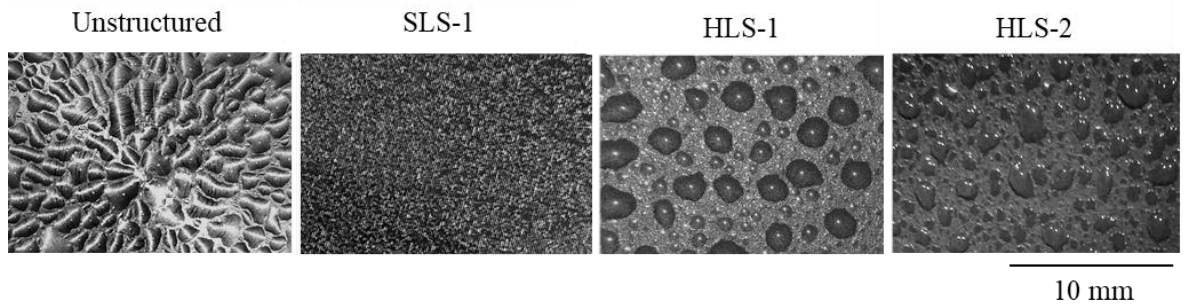


Figure 4.42. Formation of condensates on the unstructured and microstructured surfaces of stage 3.

#### 4.3.4 Assessment Summary

In order to select the best-microstructured surface of stage one to be used in stage three, the following components have been considered with a total weight of 100 points:

1. Phase 1: Smallest percentage difference between designed and manufactured workpieces, considering manufacture performance and characterisation data (20 points).
2. Phase 2: Overall performance in experimental boundary layer control and drag reduction results (30 points).
3. Phase 3: Overall performance in condensation heat transfer results (50 points).

Table 4.12 shows a summary of the evaluation carried out in stage three. Similar to stage two, the hydrophilic scallop variant SLS-1 achieved the best performance in each component, while the hydrophobic variant HLS-1 presented the second-best overall performance.

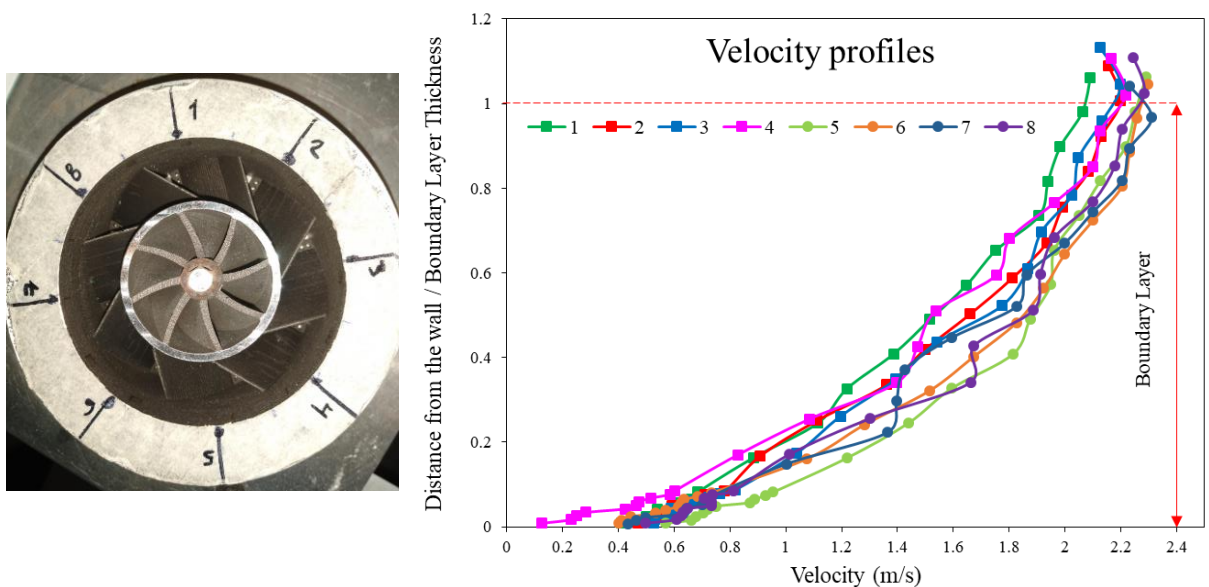
Table 4.12. Assessment summary of stage three.

Stage 3 - Assessment criteria		Obtained points based on performance		
Component	Value	SLS-1	HLS-1	HLS-2
Manufacture and characterisation (Smallest percentage difference between design and manufactured)	20	20	13.33	13.33
Experimental Boundary Layer control and Drag reduction	30	30	20.00	10.00
Experimental heat transfer enhancement	50	50	33.33	16.67
<b>Total points</b>	<b>100</b>	<b>100</b>	<b>66.67</b>	40.00



## 4.4 Swirl Flow Experimental Results

As mentioned in stage three, by changing the insert's manufacturing technique from casting and conventional turning and facing operations to additive layer manufacturing (selective laser melting), more complex workpieces, such as a swirler, can be tested to analyse the effect of the microstructured surfaces on the flow. The swirler is composed of eight blades with hydrophilic scallop microstructures on each of the top surfaces to evaluate the repeatability that microstructured surfaces on complex specimens can provide (Figure 4.43a). Considering the facilities and equipment available at the school, velocity experiments were carried out to evaluate boundary layer thickness and drag reduction. Figure 4.43b presents the velocity profile of each blade.



**Figure 4.43. (a) Tested swirler. (b) Velocity profile of each blade in the swirl flow experiment the stage.**

Considering the swirler as a whole, repeatability and reproducibility in additive layer manufacturing is an area of underdeveloped research [167]. Thus, this evaluation is based on the boundary layer thickness and the drag force that each blade provides. Figure 4.44 shows the boundary layer thickness and the drag force results. Standard deviation, standard deviation of the mean, margin of error, coefficient of variation and more detailed results are available in Appendix D. The results show up to 17% difference in boundary layer thickness and up to 28% difference in drag force with acceptable coefficients of variation of 5.01 and 10.37, respectively.

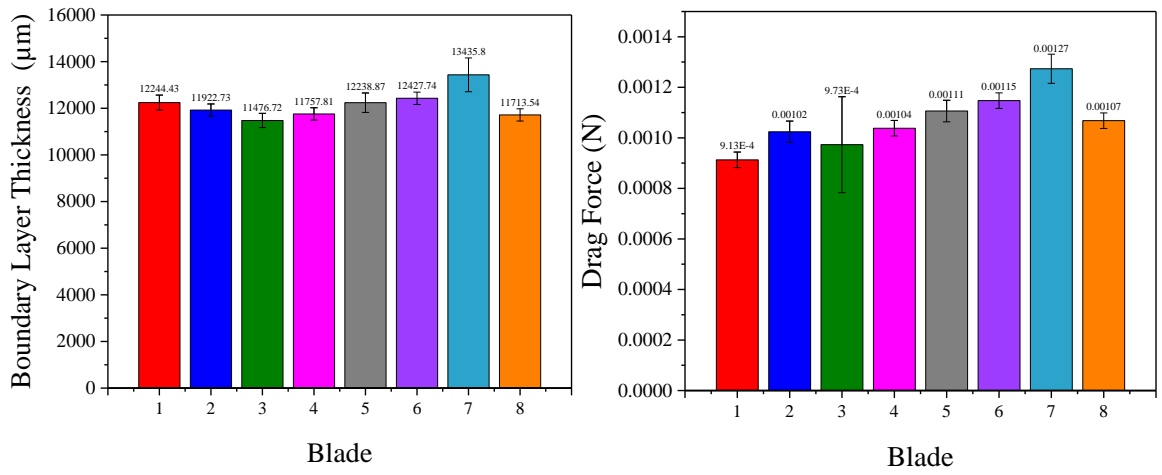


Figure 4.44. Boundary layer thickness and drag force of each blade.

## **Chapter 5 : Performance Evaluation Results of Novel Biphilic Microstructured Surfaces (Stage 4)**

This PhD research aims to explore an alternative passive mechanism for surface topographical modification to enhance heat transfer for energy recovery purposes. To achieve this aim, hydrophobic and hydrophilic structures have been designed, manufactured and tested to aid in the design of an optimal biphilic wettability gradient that can enhance condensation heat transfer. This chapter presents the results of the last stage of this doctoral investigation.

For stage one, based on biomimetic engineering research, a nature-inspired micro-geometry was selected (Scallop) out of the four tested micro-geometries (Lotus, Scallop, Sharkskin and Diamond). This hydrophilic microstructured surface was further studied in stage two, in which the dimensions were varied, resulting in two workpieces (SLC-1 and SLC-2). Additionally, the texturing manufacturing technique was changed to laser micro-processing as it is faster, cleaner and more flexible than Micro-Wire Electrical Discharge Machining ( $\mu$ -WEDM). Moreover, a new hydrophobic microstructured surface was introduced into this research with two variants (HLC-1 and HLC-2) to evaluate both wetting behaviours. SLC-1 and HLC-1 achieved the best and second-best overall performance in stage two.

For the third stage, the hydrophilic scallop variant with the best performance (SLC-1) was selected. Additionally, both hydrophobic variants were chosen to corroborate repeatability. The three workpieces for stage three (SLS-1, HLS-1 and HLS-2) were manufactured by the same texturing technique used in stage two (laser micro-processing). However, in order to expand the scope of the insert manufacture, an additive layer manufacturing technique (selective laser melting) was chosen for this stage. This technique unfurls the opportunity for further research on heat transfer enhancement when more complex workpieces are required. Regarding the results, SLS-1 and HLS-1 presented the best and second-best overall performance.

As a result, SLS-1 and HLS-1 were combined into a biphilic wettability gradient for stage four. For this stage, two variants based on the sequence of the microgeometries manufacturing procedure were tested. For the specimen or workpiece 1 (WLS-1), the hydrophobic features or holes were manufactured first, followed by the hydrophilic or scallop geometries; for specimen 2 (WLS-2), the hydrophilic features were manufactured first, followed by the hydrophobic features using laser micro-processing on additive layer manufactured inserts.

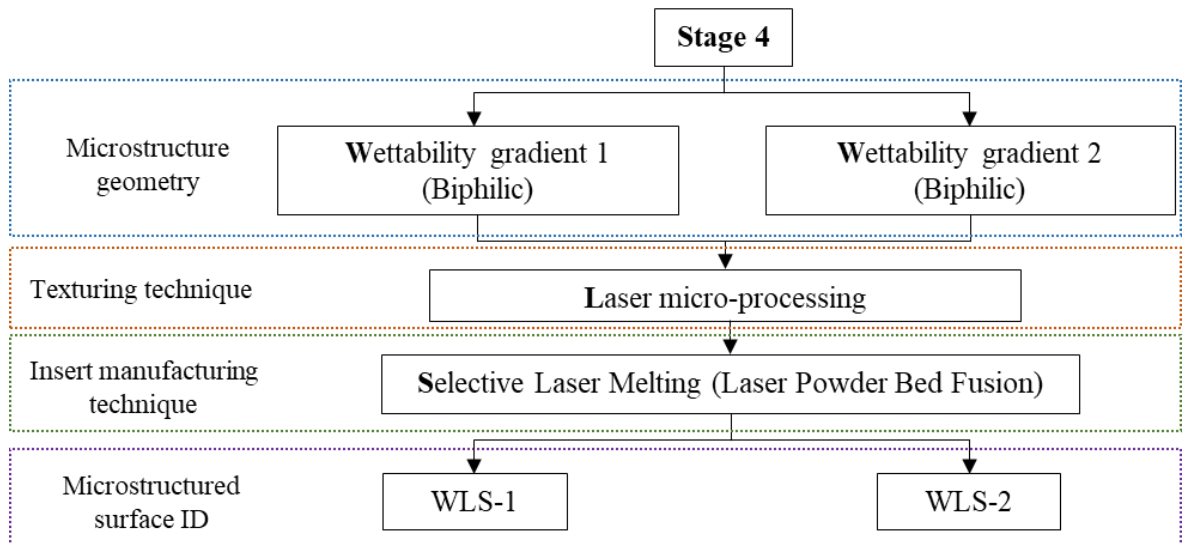


Figure 5.1. Summary of the microstructured surfaces in Stage 4.

## 5.1 Phase 1: Design, Manufacture and Characterisation

### 5.1.1 Design

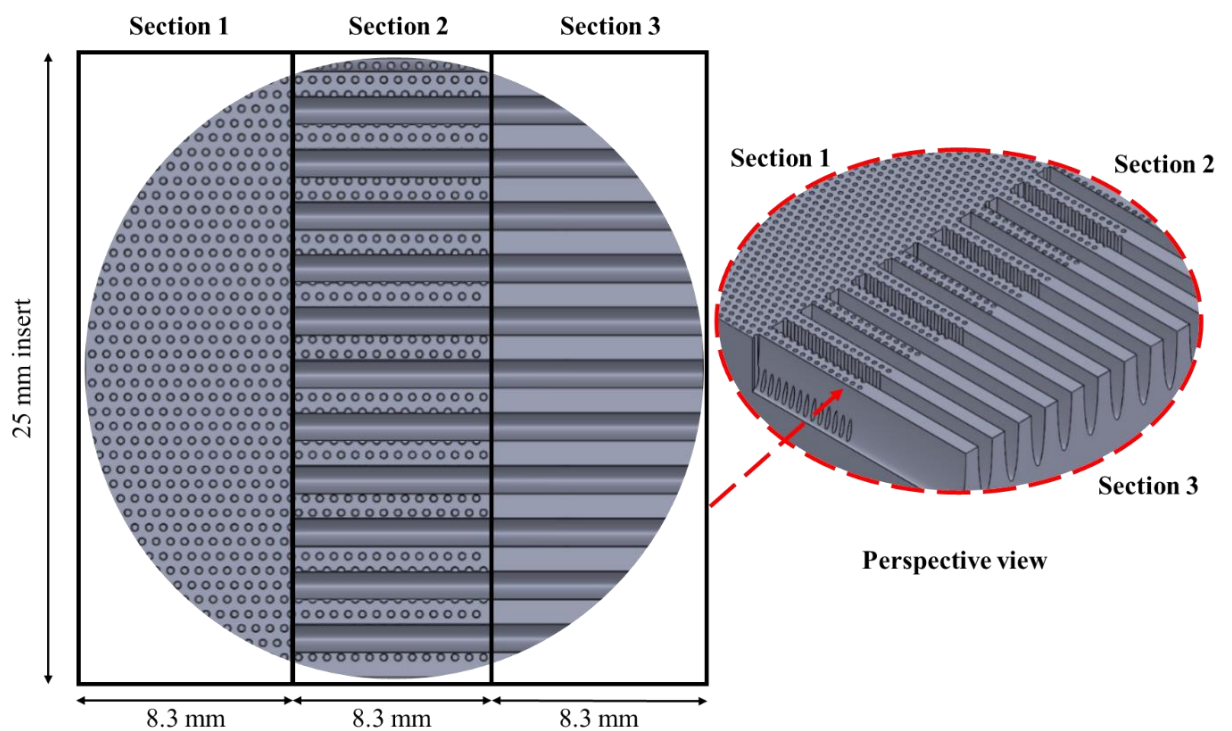
#### 5.1.1.1 Previous Work

Hydrophobic and hydrophilic microstructured surfaces were manufactured and tested in the previous stages of this research. As expected from the literature [99,168,169], nucleation on hydrophobic surfaces requires a higher degree of saturation than what is required when condensing on hydrophilic surfaces; still, dropwise condensation is more desirable for heat transfer applications [48]. The growth and departure of the droplets depend on the size and distribution of the micro geometries that can result in either a hydrophobic or hydrophilic wetting state. Self-removal of condensed droplets depends on the growth rate and the coalescing frequency of condensed droplets; faster growth and more frequent coalescence led to higher self-removal efficiency [72].

Both wetting effects are important during heat transfer to promote dropwise condensation at the nucleation sites; the initial small droplets are mainly formed by direct deposition from the vapour phase onto the surface and grow due to continued condensation by absorbing water molecules. When the droplets become larger, and the distance between neighbouring droplets becomes closer, coalescence starts to be the dominating mechanism for droplet growth until the droplets reach a certain size and slide down, sweeping away other droplets in its path and leaving the condensing surface cleaned and exposed to the vapour to repeat the process [37,55]. As a result, biphilic surfaces that contain a combination of hydrophilic and hydrophobic regions (gradient) can reduce the energy barrier for vapour condensation while promoting droplet departure to enhance dropwise condensation [36].

Therefore, by combining the microstructured surfaces with the overall best performance from previous stages [143,166], a biphilic wettability gradient was designed in order to have both wetting effects. The design is based on the top circular area of 25 mm in diameter the inserts have.

As mentioned in chapter 3, the dimensions of the inserts were designed according to the requirements of the equipment and experiments, i.e. measure the effect of the microstructured surfaces in the boundary layer when the flow is turbulent [19]. The area is divided into three sections, as shown in Figure 5.2, each section provides the necessary area to develop different wetting states in one workpiece.



**Figure 5.2. Concept design.**

The gradient direction would depend on the final workpiece and direction of the flow in order to enhance every stage of the droplet life cycle; for example, Tokunaga and Tsuruta [48] and Sun et al. [87] created biphilic surfaces in which the droplet movement goes from hydrophobic to hydrophilic dominant areas.

The proposed biphilic wettability gradient's characteristics (Figure 5.3 and Figure 5.4) are as follows:

**Section 1:** Hydrophobic features based on HLS-1.

Hole diameter: 17  $\mu\text{m}$

Space between holes: 17.5  $\mu\text{m}$ .

**Section 2:** Hierarchical structures section with a scallop inspired hydrophilic base (grooves) and hydrophobic riblets on the top surface. Based on HLS-1 and SLS-1.

Riblet = 60  $\mu\text{m}$  with hydrophobic holes on the top surface

Groove = 68  $\mu\text{m}$

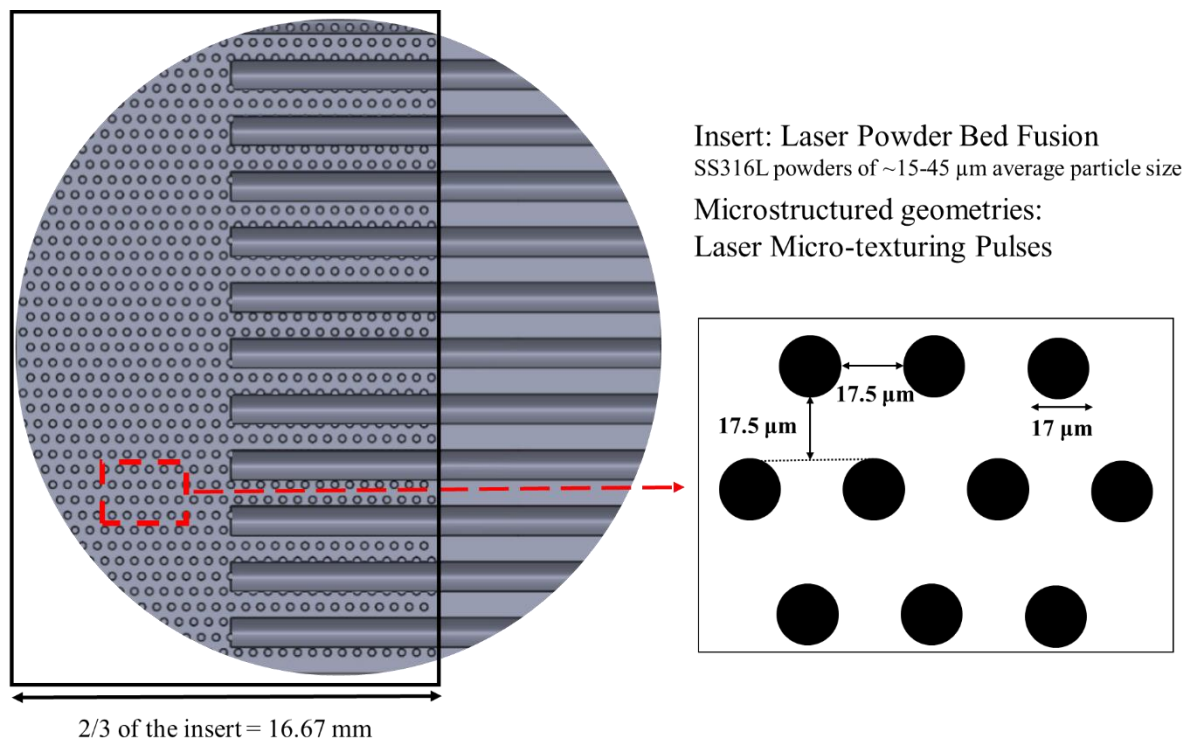
Height/depth = 225  $\mu\text{m}$

**Section 3:** Scallop-inspired hydrophilic features based on SLS-1.

Riblet (unstructured top surface) = 60  $\mu\text{m}$

Groove = 68  $\mu\text{m}$

Height/depth = 225  $\mu\text{m}$



**Figure 5.3. Dimensions of the hydrophobic features in sections 1 and 2.**

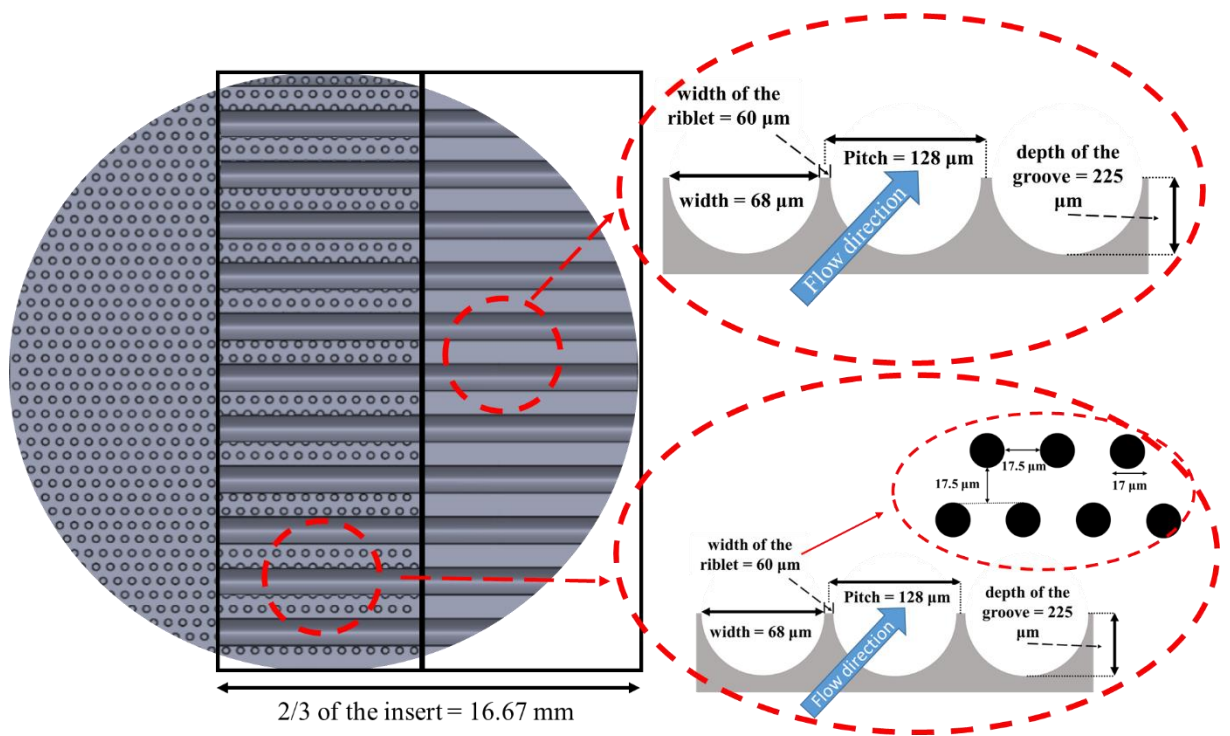


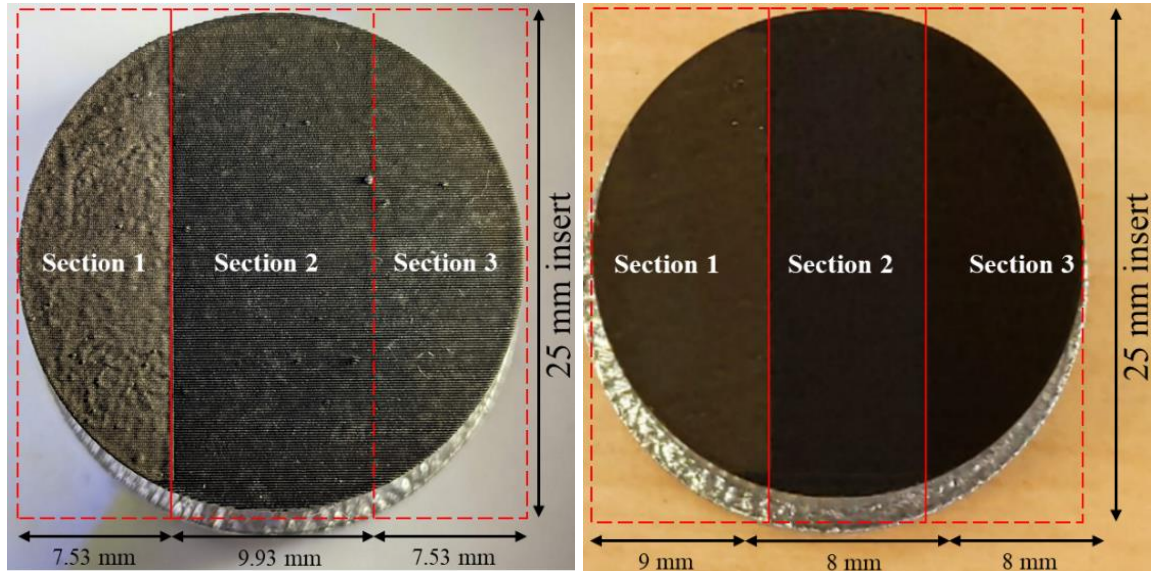
Figure 5.4. Dimensions of the hydrophilic features in sections 2 and 3.

### 5.1.2 Manufacture

Stainless steel inserts were manufactured via laser powder bed fusion. The process utilised SS316L powders of  $\sim 15\text{-}45\ \mu\text{m}$  average particle size, a 200 W laser power, with a beam spot size of  $56\ \mu\text{m}$  (Gaussian profile) and layer thickness of  $50\ \mu\text{m}$ . The point distance between two consecutive laser beam spots was  $60\ \mu\text{m}$  with a laser exposure time of  $80\ \mu\text{s}$ , while the hatch distance was set at  $110\ \mu\text{s}$ . The height of the inserts was 25 mm, while the bottom 10 mm had a diameter of 28 mm and the top 15 mm had a diameter of 25 mm. To manufacture the biphilic wettability gradient on the top surface of the inserts, two laser micro-texturing procedures were chosen in order to see the effect of the manufacturing procedure order on the final workpiece:

- 1) **Specimen WLS-1:** First, hydrophobic features (holes) were created in the first two sections with laser pulses, followed by a scallop pattern (hydrophilic) in sections 2 and 3 with laser as the second step.
- 2) **Specimen WLS-2:** The hydrophilic scallop pattern was manufactured first in sections 2 and 3; as a second step, laser pulses were utilised in sections 1 and 2 to create the hydrophobic microstructures (holes).

The manufactured biphilic specimens are presented in Figure 5.5. The slight difference in the dimension of the sections is attributable to the location and handling of the insert inside the equipment (DMG-Lasertec 40).



**Figure 5.5. Manufactured biphilic wettability gradient. Specimen WLS-1 (left) Specimen WLS-2 (right).**

### 5.1.3 Characterisation

The specimens' roughness values are available in Table 5.1 and the characterisation results obtained from the 3D optical profilometer (Sensofar) and the percentage deviations from the nominal dimensions are shown in Table 5.2. The representation of the scanned areas is shown in Figure 5.6. Considering the scanned data, the manufacturing sequence for creating microstructures presented a percentage difference between 0.21% and 17.66%. Additionally, there were no significant changes in the roughness values when comparing both biphilic workpieces and between sections one with WLS-1 and sections two and three with SLS-1. More details about the characterisation are shown in the following sections.

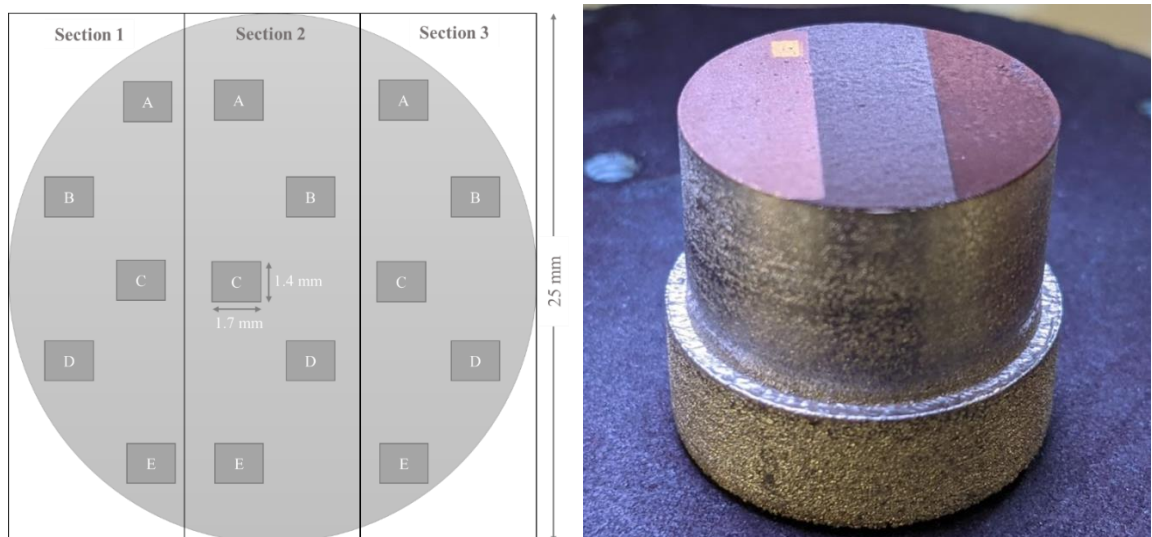
**Table 5.1. Roughness values of WLS-1 and WLS-2 (Stage 4).**

Geometry	Roughness ( $\mu\text{m}$ )	Margin of error ( $\pm$ )	Standard Error
<b>WLS-1 section 1</b>	11.14	0.0445	0.0035
<b>WLS-1 section 2</b>	76.69	0.0762	0.0060
<b>WLS-1 section 3</b>	75.94	0.8005	0.0630
<b>WLS-2 section 1</b>	16.81	1.1866	0.4274
<b>WLS-2 section 2</b>	74.29	3.0059	1.1693
<b>WLS-2 section 3</b>	75.93	2.2278	1.2256



**Table 5.2. Characterisation data of the microstructured surfaces and percentage difference with respect to the nominal dimensions (Stage 4).**

	Parameter	Nominal Dimension ( $\mu\text{m}$ )	WLS-1 ( $\mu\text{m}$ )	Standard Error of the Mean	% Difference with the Nominal Dimension	WLS-2 ( $\mu\text{m}$ )	Standard Error of the Mean	Percentage Difference with the Nominal Dimension (%)	Percentage Difference with WLS-1 (%)
Hydrophobic Features	Hole diameter ( $\mu\text{m}$ )	17	16.42	1.17	3.41%	19.32	1.59	13.65%	17.66%
	Short distance between holes ( $\mu\text{m}$ )	17.5	40.53	4.23	131.60%	41.40	2.91	136.57%	2.15%
	Long distance between holes ( $\mu\text{m}$ )	17.5	77.21	2.43	341.20%	71.35	2.88	307.71%	7.59%
	Height or Depth ( $\mu\text{m}$ )	-	38.76	1.79	-	36.51	1.23	-	5.80%
Hydrophilic Features	Width of the groove ( $\mu\text{m}$ )	68	63.54	1.02	6.56%	59.40	1.65	12.65%	6.52%
	Width of the riblet ( $\mu\text{m}$ )	60	64.29	1.98	7.15%	69.20	1.27	15.33%	7.64%
	Pitch ( $\mu\text{m}$ )	128	128.33	0.57	0.26%	128.60	2.70	0.47%	0.21%
	Depth of the groove ( $\mu\text{m}$ )	225	234.79	2.28	4.35%	225.40	2.19	0.17%	4.00%



**Figure 5.6. Scanned areas representation for characterisation using Sensofar (left). Section 1-A on the insert (right).**

### 5.1.3.1 Section 1: Hydrophobic Features

From the top view scans taken with Sensofar for both specimens, it is possible to see that the hydrophobic section is conformed of evenly distributed holes (Figure 5.7); however, the holes are part of an extruded volcano-shaped features (Figure 5.8) that are formed after the laser pulse melts the stainless steel and this rapidly cools down.

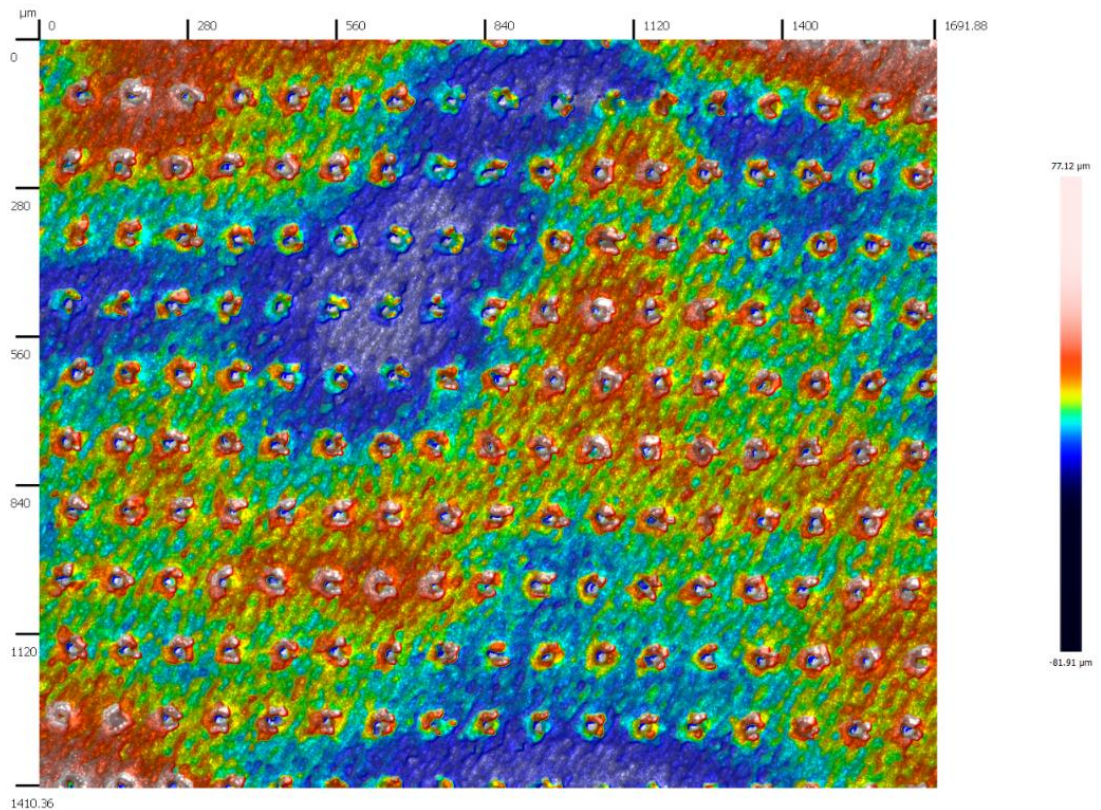


Figure 5.7. Top view scan of section 1, taken with Sensofar.

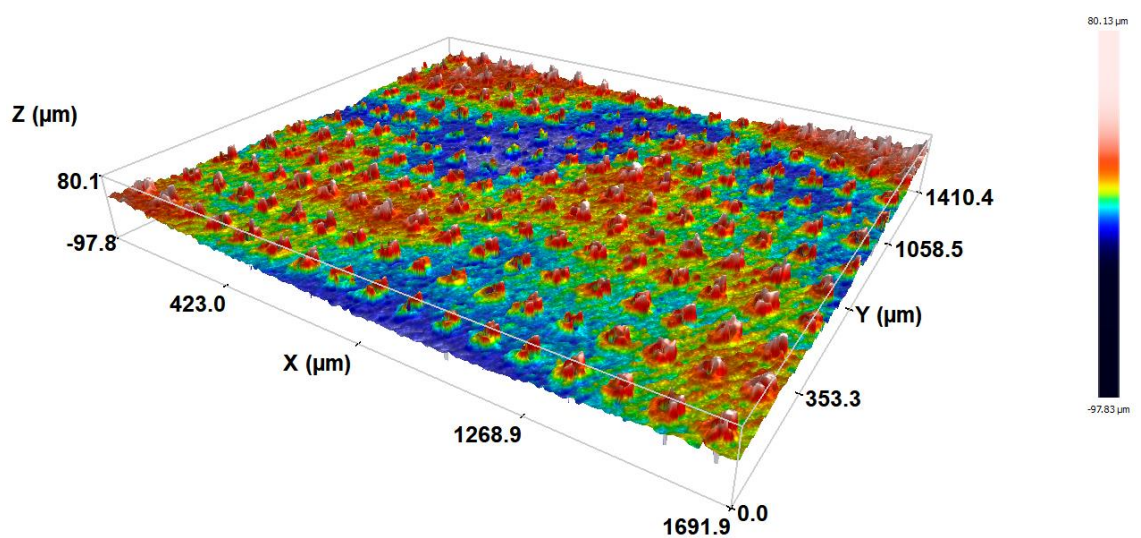


Figure 5.8. Perspective view scan of section 1, taken with Sensofar.

Figure 5.9 shows a representation of the characterisation in section one; from this image is possible to see that the shape of the hydrophobic features slightly differs from each other in both workpieces. Additionally, WLS-1 and WLS-2 present a short-distance (40.53  $\mu\text{m}$  and 41.40  $\mu\text{m}$ , respectively) and a long-distance (77.21  $\mu\text{m}$  and 71.35  $\mu\text{m}$ , respectively) between the features, this significantly differs with the distance of 17.5  $\mu\text{m}$  in both directions that HLS-1 presents in stage three. Percentage difference between 13.65% and up to 341.20% could be attributed to a discrepancy with the parameters used in the software for the laser pulses and its documentation between previous stages and stage four. However, when comparing the hydrophobic features between WLS-1 and WLS-2, the maximum percentage difference is 7.59%, representing the long distance between the micro-features.

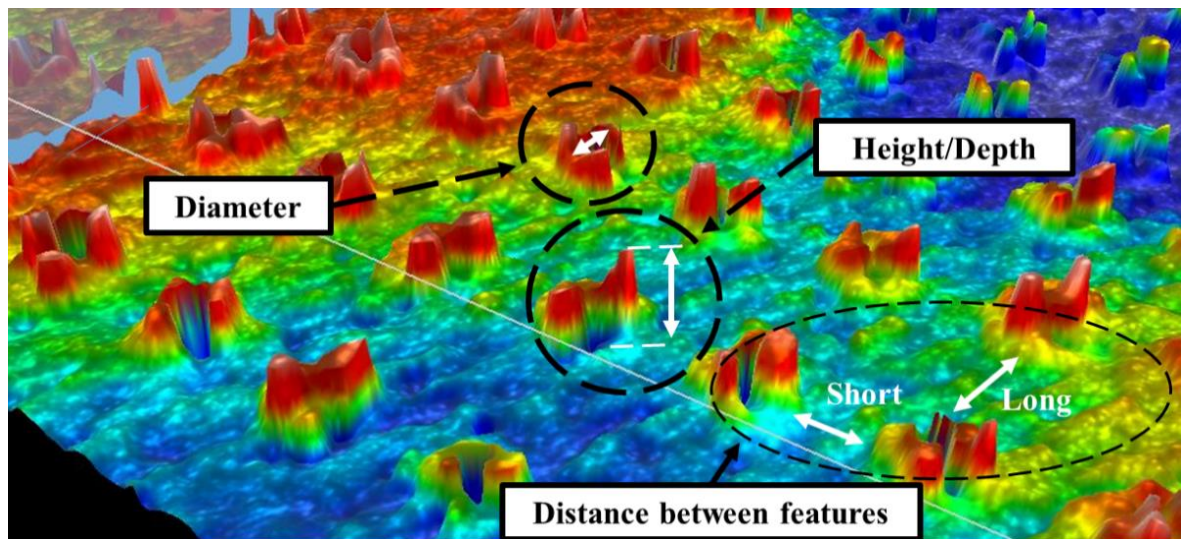


Figure 5.9. Characterisation of section 1 representation.

### 5.1.3.2 Section 2: Hierarchical Structures

Unlike sections one and three, in which WLS-1 and WLS-2 present the same features, section two displays a significant difference between both specimens. In WLS-1, the second step of the manufacturing procedure destroyed the hydrophobic features in section two (Figure 5.10). However, in WLS-2, rows of hydrophobic features were able to be manufactured over the scallops or hydrophilic grooves without damaging them; henceforth, it is possible to see a row of volcano-shaped features in each riblet (Figure 5.11).

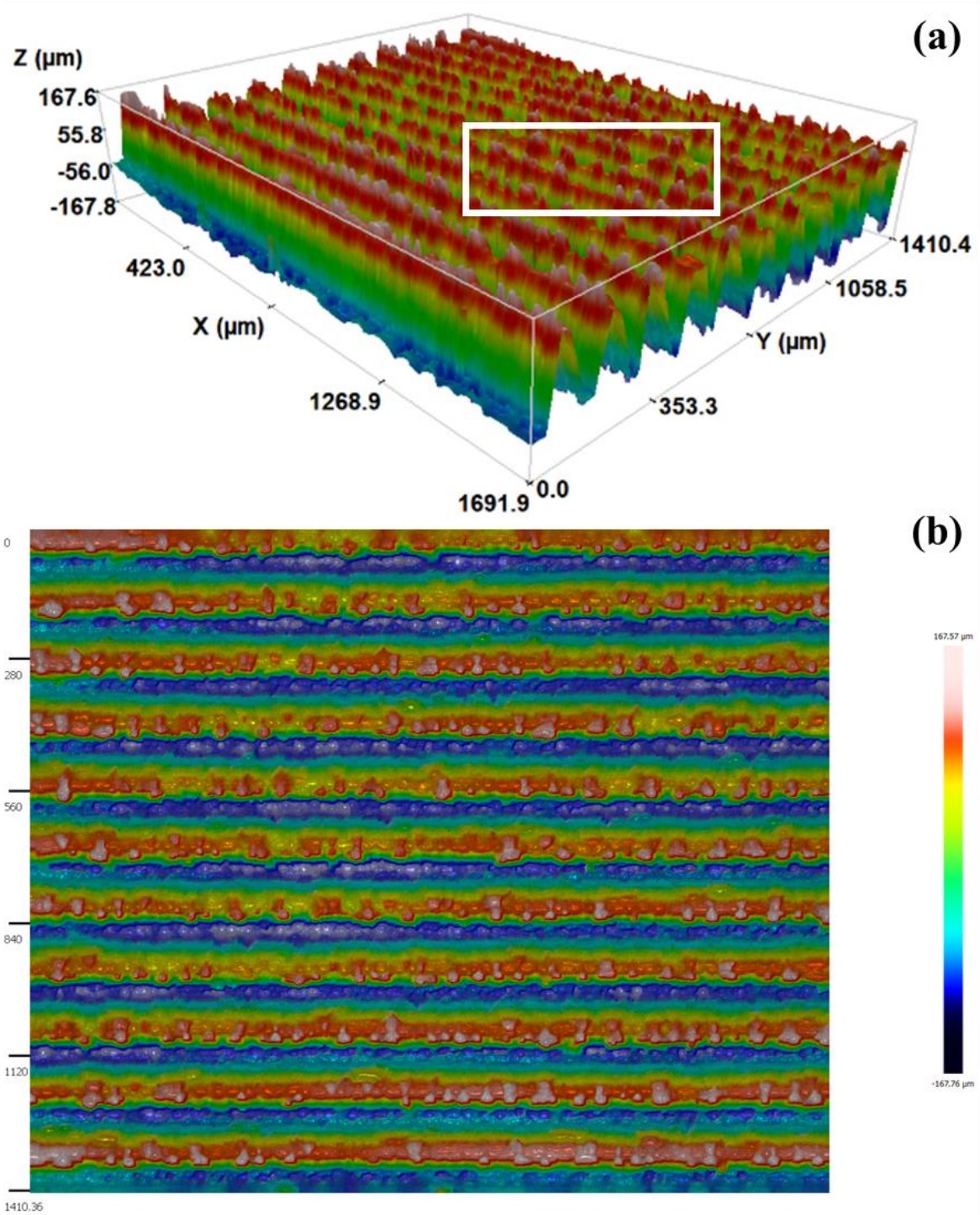


Figure 5.10. Perspective view (a) and top view (b) scans of WLS-1's section 2.

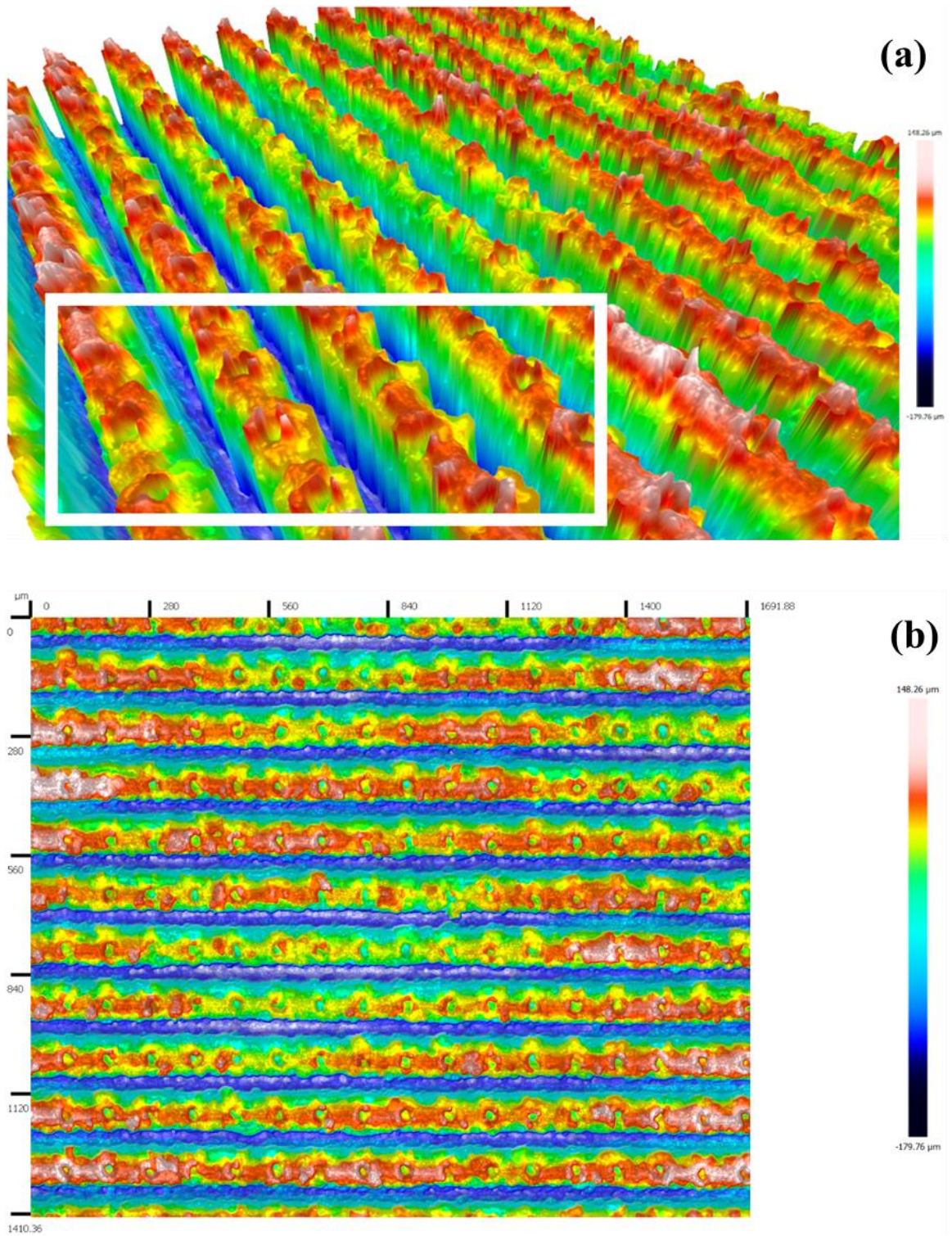


Figure 5.11. Perspective view (a) and top view (b) scans of WLS-2's section 2.

Figure 5.12 represents the measured characteristics of the hydrophilic features in section two of WLS-1. Figure 5.13 shows section two of WLS-2, where the top of the riblets differs from WLS-1.

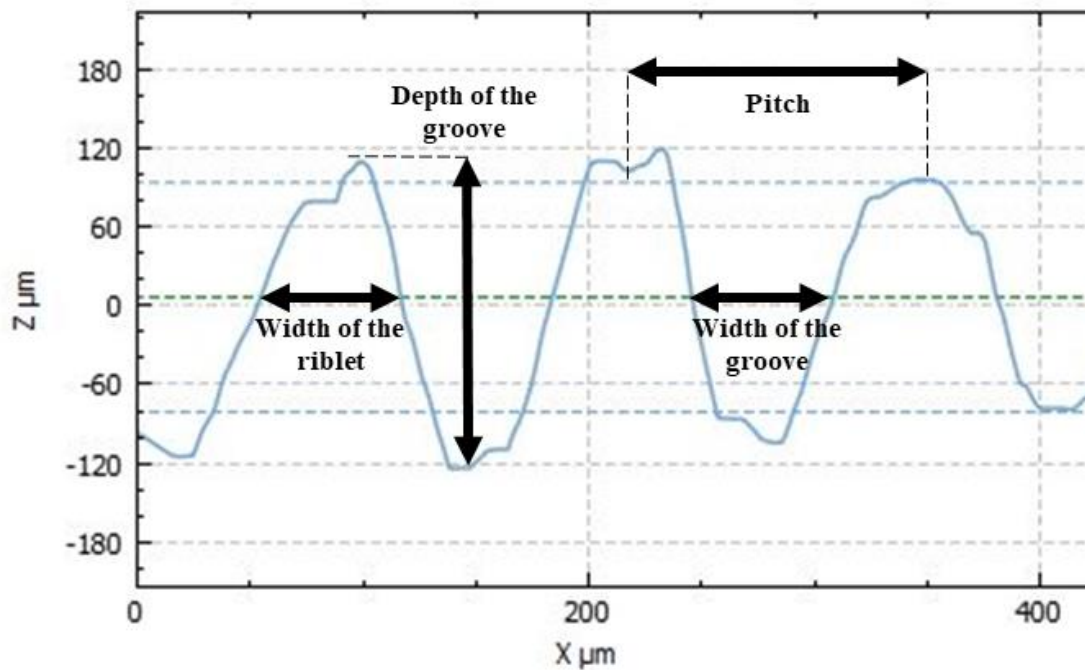


Figure 5.12. Section 2 characterisation of WLS-1.

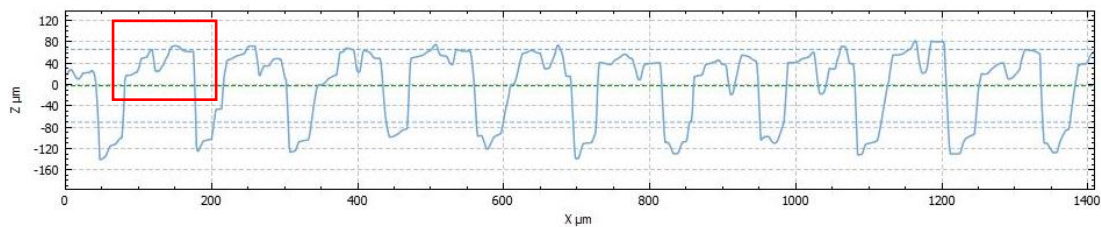


Figure 5.13. Section 2 characterisation of WLS-2.

### 5.1.3.3 Section 3: Hydrophilic Features

Section three scans of the WLS-1 and WLS-2 present the same features as section two of WLS-1; the top of the scallop riblets present extruded semi volcano-shaped features (Figure 5.14). In addition, WLS-2 presents regions of the scallop riblets with unstructured top surfaces (Figure 5.15b). Since the scallop pattern dimensions are virtually the same as those in section two, the information has been combined into Table 5.2 as the hydrophilic features.

Unlike the hydrophobic features, the hydrophilic features achieved the desired dimensions with percentages of difference between 0.17% and 15.33% when compared against SLS-1 and percentages of difference between 0.21% and 7.64% when compared between both biphilic wettability gradient workpieces (WLS-1 and WLS-2).

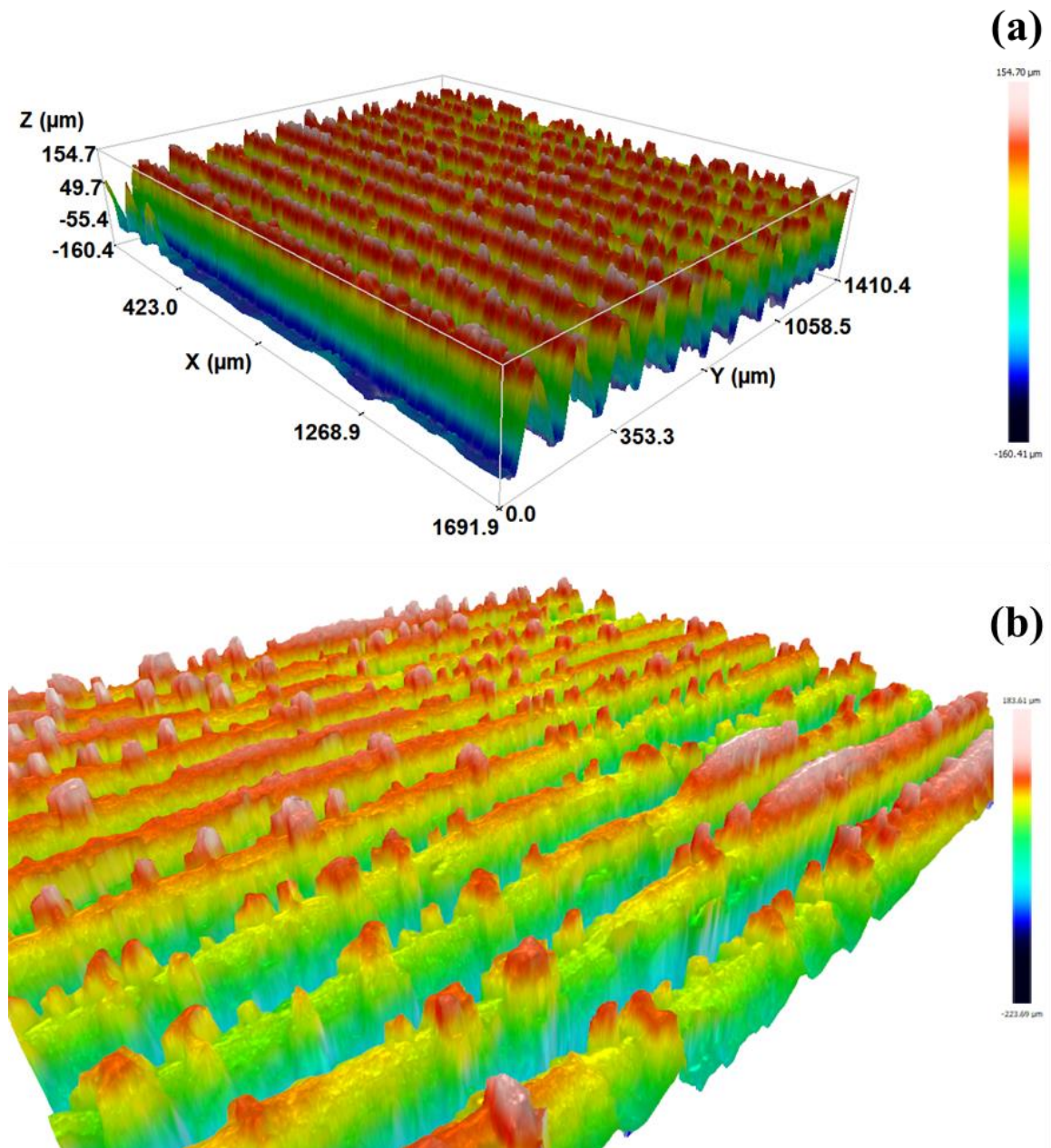


Figure 5.14. Perspective view scan of section 3 (a) WLS-1 and (b) WLS-2.

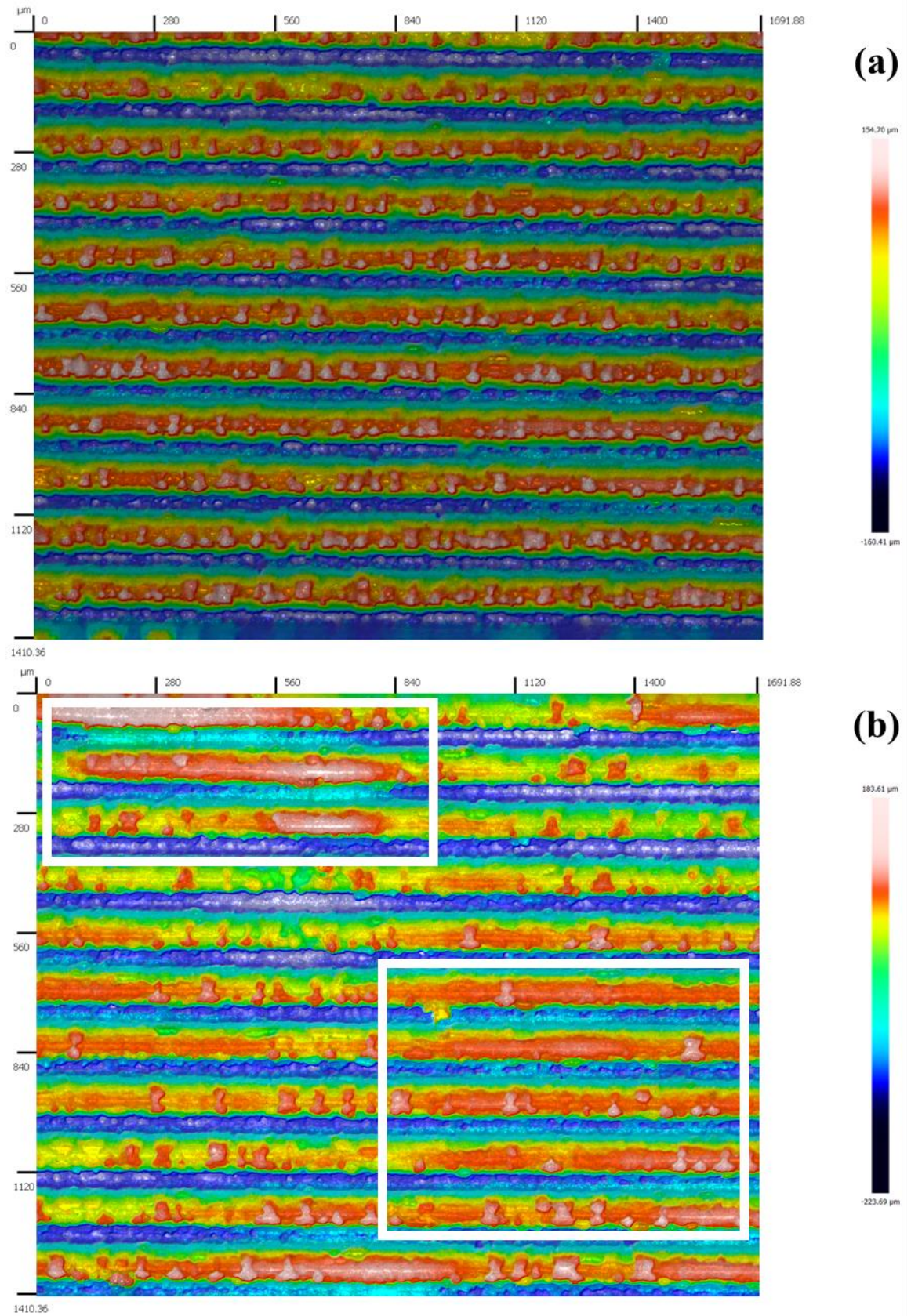


Figure 5.15. Top view scan of section 3 (a) WLS-1 and (b) WLS-2.



### 5.1.3.4 Wettability Characterisation

Images of the contact angle between the water droplets and the different sections of WLS-1 and WLS-2 are presented in Figure 5.16. The microstructure wettability characterisation results (contact angles), together with the margin of errors and the standard error, are shown in Table 5.3. In stage three, the hydrophobic workpiece HLS-1 achieved contact angles of  $128.79^\circ \pm 8.55^\circ$ . In stage four, the hydrophobic behaviour caused by the holes decreased up to 26.60% due to the increased distance between the micro-features in section one. WLS-1 presents contact angles of  $94.53^\circ \pm 5.37^\circ$  and WLS-2 presents contact angles of  $105.43^\circ \pm 4.34^\circ$ . Surprisingly, the extruded semi volcano-shaped features on the riblets of sections two and three in WLS-1 and WLS-2 increased the hydrophilic behaviour up to 33.69% from the  $73.17^\circ \pm 9.44^\circ$  contact angle achieved by SLS-1 in stage three.

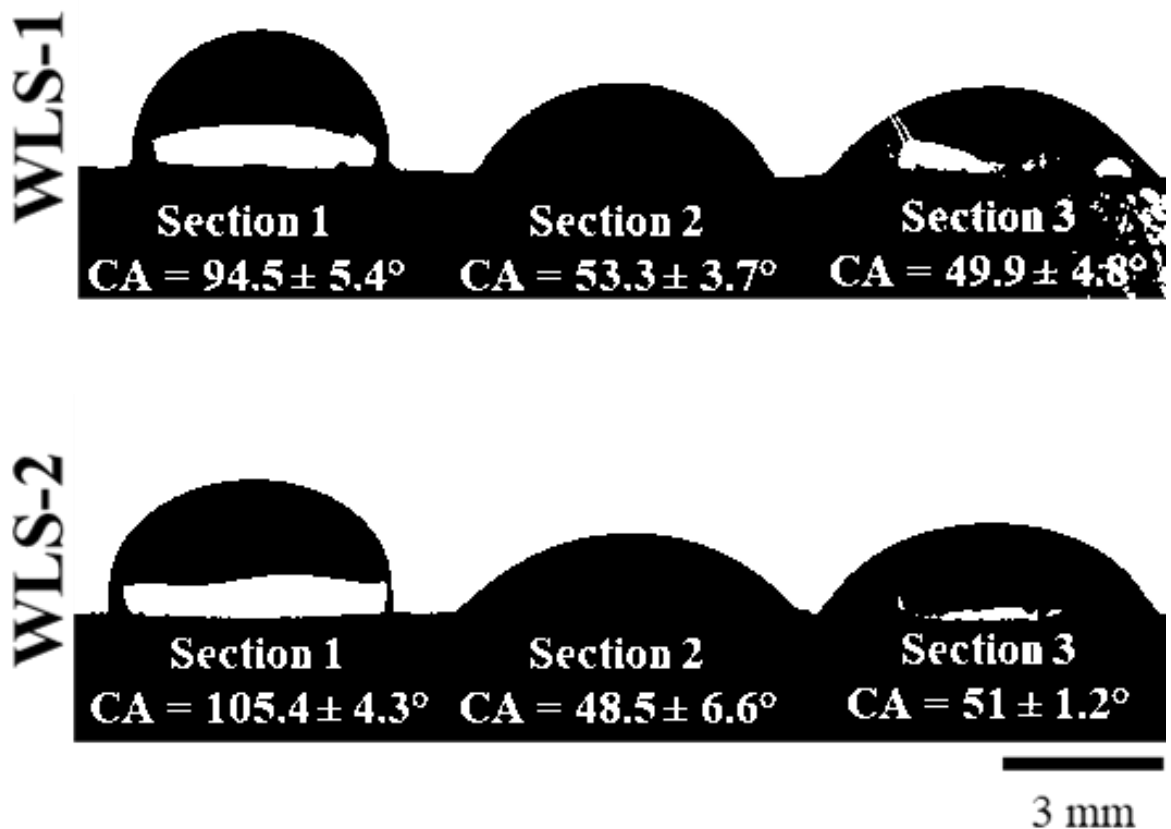


Figure 5.16. Contact angles between water droplets and the unstructured and microstructured surfaces of stage 4.

**Table 5.3. Wettability characterisation data for the microstructured surfaces of stage 4, margin and standard errors.**

<b>Geometry</b>	<b>Contact Angle (°)</b>	<b>Margin of error (<math>\pm</math>)</b>	<b>Standard Error</b>	<b>Wettability</b>
<b>WLS-1 section 1</b>	94.53	5.37	1.93	Hydrophobic
<b>WLS-1 section 2</b>	53.26	3.72	1.34	Hydrophilic
<b>WLS-1 section 3</b>	49.93	4.75	1.71	Hydrophilic
<b>WLS-2 section 1</b>	105.43	4.34	1.56	Hydrophobic
<b>WLS-2 section 2</b>	48.52	6.64	2.39	Hydrophilic
<b>WLS-2 section 3</b>	51.03	1.17	0.37	Hydrophilic

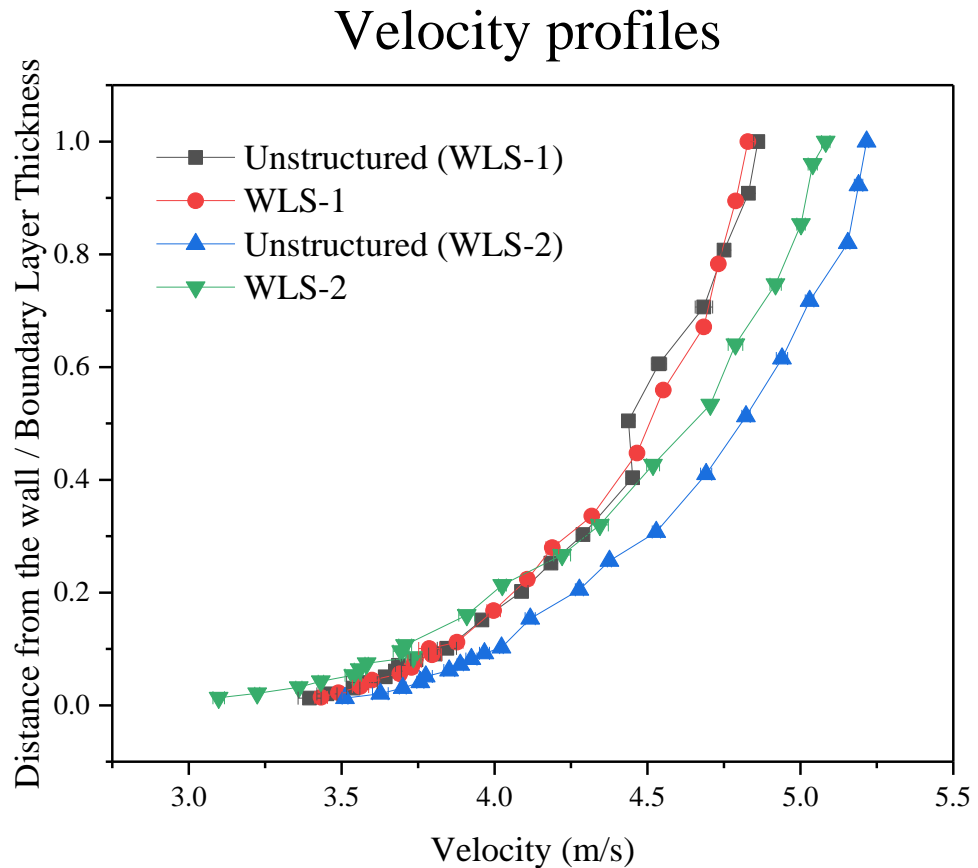
It is important to mention that the biphilic microstructured surface presented a fast drainage effect, as soon as the droplets pass through sections two and section three, the departure stage of the droplet is faster than expected and cannot be captured in pictures, hence slow-motion 1/4x videos were filmed to then export frames to analyse the wettability behaviour based on the contact angle. Figure 5.17 shows the top view of the wettability test. The contact angles of the biphilic wettability gradient surface (section two and three), available in Table 5.3, were obtained at 250 milliseconds; after this, the contact angles decreased to  $0^\circ$ , presenting a complete wetting state.



**Figure 5.17. Top view of the wettability test.**

## 5.2 Phase 2: Fluids Dynamics Evaluation Results (Momentum Transfer)

Due to manufacturing delays and laboratory access restrictions, the velocity experiments for boundary layer control and drag reduction were performed at various times. Every set of experiments was compared against an unstructured surface under the same experimental conditions. Figure 5.18 presents the velocity profiles corresponding to stage four.



**Figure 5.18. Velocity profiles of the stage 4 microstructured surfaces and unstructured surfaces.**

The high velocities observed in the boundary layer of the unstructured surface provided a higher drag force than the biphilic workpieces. Table 5.4 comprises the experimental boundary layer thickness, boundary layer thickness reduction, drag force and drag reduction of the tested surfaces. The smaller velocities profiles presented by WLS-1 and WLS-2 resulted in a 16.99% and 17.23% decrease in drag force and up to 9.77% on boundary layer thickness reduction. When comparing against the performance of the microstructured surfaces in previous stages (reductions up to 17.44% for boundary layer thickness and 18.86% for drag reduction), there are no substantial benefits in the effect the biphilic workpieces have on the fluids dynamics evaluation.

**Table 5.4. Experimental Boundary layer thickness, boundary layer thickness reduction, drag force and drag reduction of stage 4.**

	<b>Boundary Layer Thickness (mm)</b>	<b>Boundary Layer Thickness Reduction (%)</b>	<b>Drag Force (N)</b>	<b>Drag Reduction (%)</b>
<b>Unstructured (WLS-1)</b>	<b>9.91</b>		<b>0.0095</b>	
Standard Error	0.31		0.0002	
<b>WLS-1</b>	<b>8.94</b>	<b>9.77</b>	<b>0.0079</b>	<b>16.99</b>
Standard Error	0.28	1.99	0.0003	2.89
<b>Unstructured (WLS-2)</b>	<b>9.86</b>		<b>0.01244</b>	
Standard Error	0.39		0.00030	
<b>WLS-2</b>	<b>9.37</b>	<b>6.08</b>	<b>0.01237</b>	<b>17.23</b>
Standard Error	0.18	1.26	0.00038	2.51

### 5.3 Phase 3: Heat Transfer Evaluation

Table 5.5 and Figure 5.19 present the results of the condensation experiments after eight minutes in the condensation chamber. This includes surface temperature differential ( $\Delta T_s$ ), specific heat absorbed by the insert ( $Q$ ), heat rate ( $\dot{Q}$ ), heat flux ( $q$ ), heat transfer coefficient ( $h$ ) results with a percentage of improvement with respect to an unstructured surface. The surface temperature differentials ( $\Delta T_s$ ), specific heat ( $Q$ ), heat rate ( $\dot{Q}$ ) and heat flux ( $q$ ) in the WLS-1 and WLS-2 biphilic microstructured surfaces were higher by 62% and 58%, respectively than the unstructured surface, while the heat transfer coefficient ( $h$ ) increased by 65% and 52%, respectively.

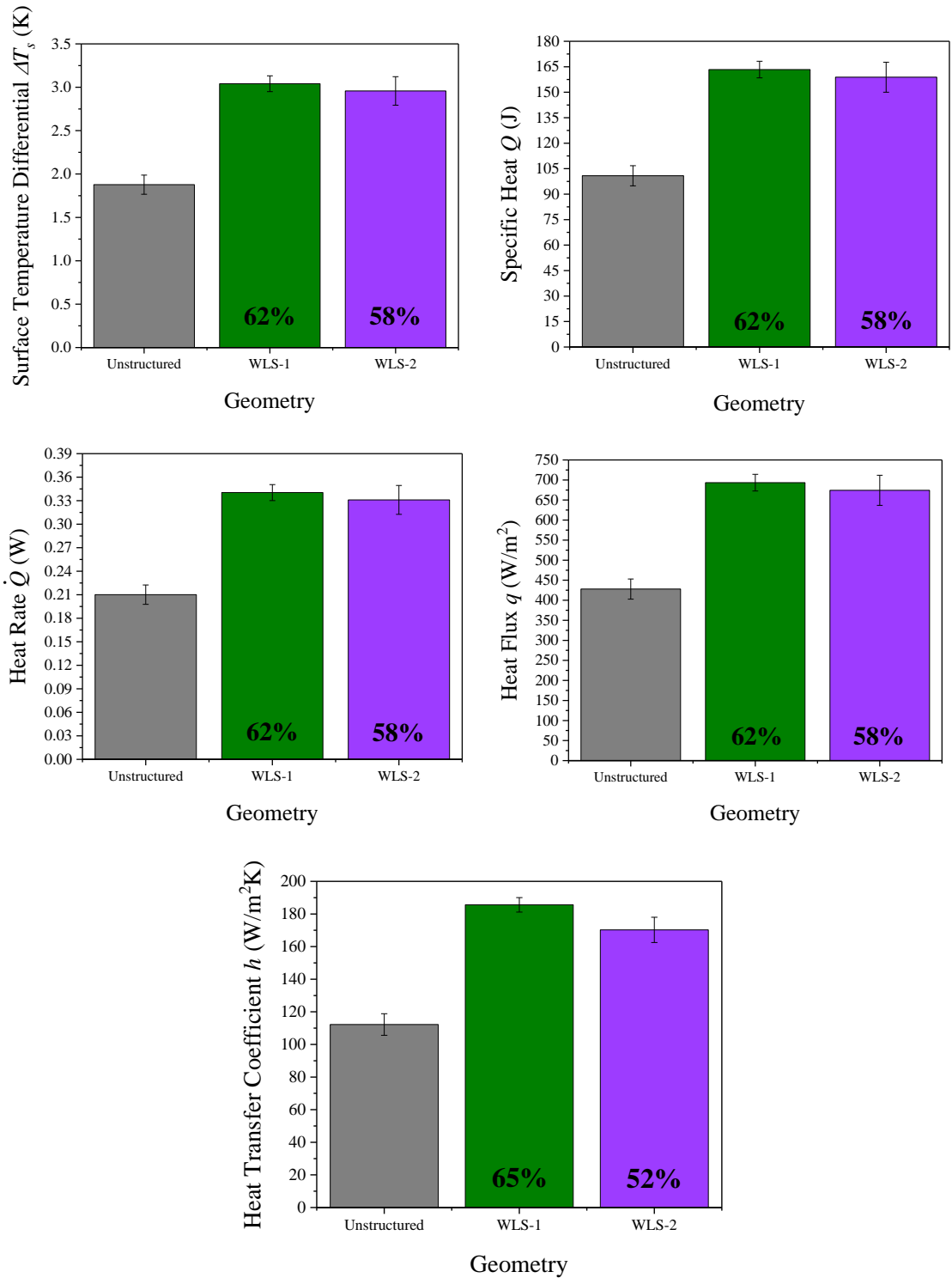
**Table 5.5. Heat transfer results. Surface temperature differential ( $\Delta T_s$ ), specific heat absorbed by the insert ( $Q$ ), heat rate ( $\dot{Q}$ ), heat flux ( $q$ ) and heat transfer coefficient ( $h$ ) results with percentage of improvement with respect to an unstructured surface (Stage 4).**

Specimen	$\Delta T_{\text{surface}} = T_f - T_i$ (°C)			Specific Heat $Q = mC_p\Delta T$ (J)		
	Unstructured	WLS-1	WLS-2	Unstructured	WLS-1	WLS-2
Average	1.88	3.04	2.96	100.83	163	159
Standard Error	0.11	0.09	0.16	5.93	4.89	8.83
% Improvement		<b>62</b>	<b>57.6</b>		<b>62</b>	<b>57.6</b>

Specimen	$\dot{Q}$ Heat rate (W)			Heat flux $q = \dot{Q} / A$ (W/m <sup>2</sup> )		
	Unstructured	WLS-1	WLS-2	Unstructured	WLS-1	WLS-2
Average	0.21	0.34	0.33	427.96	693	674
Standard Error	0.01	0.01	0.02	25.18	20.8	37.49
% Improvement		<b>62</b>	<b>57.6</b>		<b>62</b>	<b>57.6</b>

Specimen	$\Delta T = T_{\text{chamber}} - T_{\text{surface}}$ (°C)			Heat transfer coefficient $h = q / \Delta T$ (W/m <sup>2</sup> °C)		
	Unstructured	WLS-1	WLS-2	Unstructured	WLS-1	WLS-2
Average	3.82	3.74	3.96	112.21	185.61	170.26
Standard Error	0.07	0.10	0.11	6.60	4.46	7.76
% Improvement					<b>65.42</b>	<b>51.74</b>

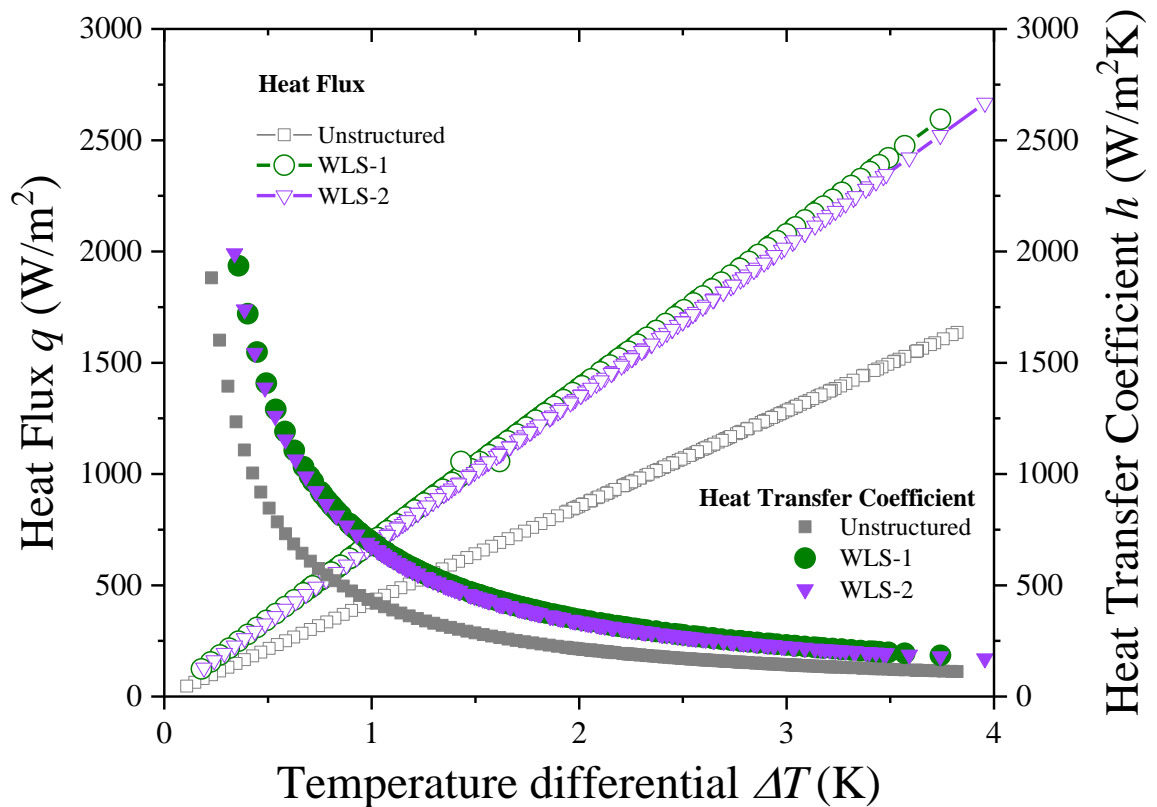
Unlike the average performance on phase two, the novel biphilic wettability gradient approach in stage four provides the best results of this study when considering the four stages. Experimental results achieved two to three times the enhancement provided by single wetting state microstructured surfaces on condensation heat.



**Figure 5.19.** Surface temperature differential ( $\Delta T_s$ ), specific heat absorbed by the insert ( $Q$ ), heat rate ( $\dot{Q}$ ), heat flux ( $q$ ) and heat transfer coefficient ( $h$ ) results with percentage of improvement with respect to an unstructured surface (Stage 4).

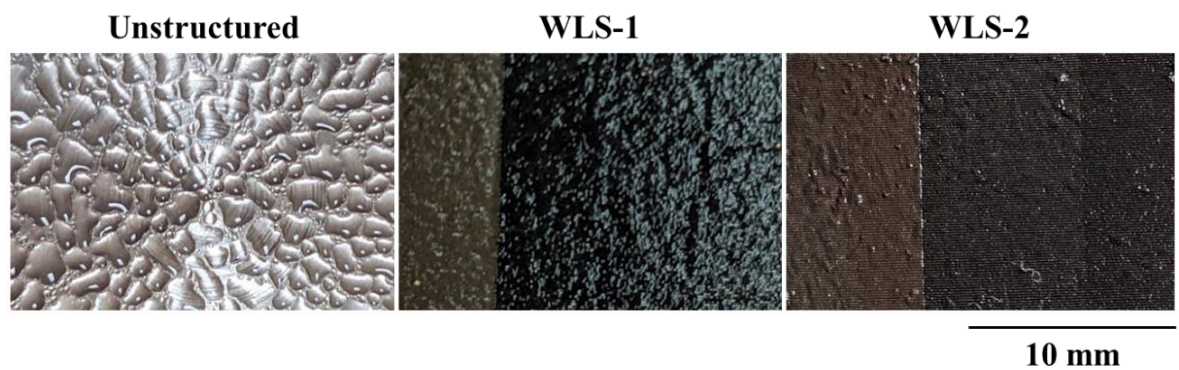
Similar heat transfer enhancement levels were obtained in other studies when using coated surfaces [68]; however, such surfaces lose their effectiveness over time due to fouling, oxidation, and the removal of their coated layer. Hence, the proposed approach provides a passive technique for condensation heat transfer enhancement by modifying the topography of the surface and, therefore, its wettability behaviour without chemical treatments.

Figure 5.20 presents the condensation heat transfer performance based on heat flux ( $q$ ) and heat transfer coefficient ( $h$ ) as a function of the surface subcooling temperature differential ( $\Delta T$ ). Similar to stage one, the coefficient results are comparable with the work carried out by Wen et al. [54], Ghosh et al. [158], and Mahapatra et al. [159]. Additionally, El Fil et al. [46] provide a wide range of experimental heat flux results, encompassing the results of this study.



**Figure 5.20. Condensation heat transfer performance. Heat flux ( $q$ ) and heat transfer coefficient ( $h$ ) as a function of the surface subcooling temperature differential ( $\Delta T$ ).**

Images of the condensate after 8 minutes on each workpiece are shown in Figure 5.21, in which different stages of the droplet life cycle can be visualised between the microstructured surfaces and the unstructured surface. The four stages of this study presented an inversely proportional relationship between the droplet size and the surface temperature differentials, in accordance with what was reported by Chatterjee et al. [160], Peng et al. [47,161] and Xu et al. [162] on condensation heat transfer. Albeit WLS-1 and WLS-2 appear to be at the end of a droplet life cycle when the images were taken, lower droplet density and size can be presumed due to the higher temperature differential they presented when compared to the unstructured surface, the microstructured surfaces from previous stages and the work of Chatterjee et al. [56] and Wen et al. [54] on the topic. Additionally, the biphilic wettability gradient approach used in WLS-1 and WLS-2 achieved faster and more efficient condensate removal in the first droplet life cycle, which promoted higher enhancement of heat transfer due to a significant increase in the interaction between the humid air and the surface [60,163].



**Figure 5.21. Formation of condensates on the unstructured and microstructured surfaces of stage 4.**

The condensation phenomenon is a spatial-temporal cyclic process resulting from a time-dependent sub-process occurring repeatedly. The nucleation stage can take up to 10 seconds, growth between 10 and 100 seconds, coalescence can take between 60 and 1,200 seconds, and sliding ~1 second, giving; as a result, droplet life cycle times between 70 seconds and 1,311 seconds (21.85 minutes) [99]. As mentioned in chapter 4, the proposed qualitative analysis on the number of droplet life cycles is based on the temperature change trend over time of the microstructured surfaces and the condensate state during the experiment. Figure 5.22 presents the droplet life cycles of WLS-1, WLS-2 and the unstructured surface in a surface temperature differential ( $\Delta T_s$ ) vs time plot. The high jump in temperature that WLS-1 and WLS-2 present in the first 100 seconds can be attributable to the fast drainage effect seen during the wettability characterisation, representing shorter droplet life cycles.



Both biphilic workpieces achieved almost six cycles (the last stage of the fifth cycle is visible in Figure 5.21), while the unstructured surface showed  $\sim 5.5$  cycles (halfway through cycle number five). The duration of the droplet life cycles is approximately 80 to 87.27 seconds (Figure 5.22). These results remain in the same range as the previous stages of this study and are comparable to what is reported by Zheng et al. [99].

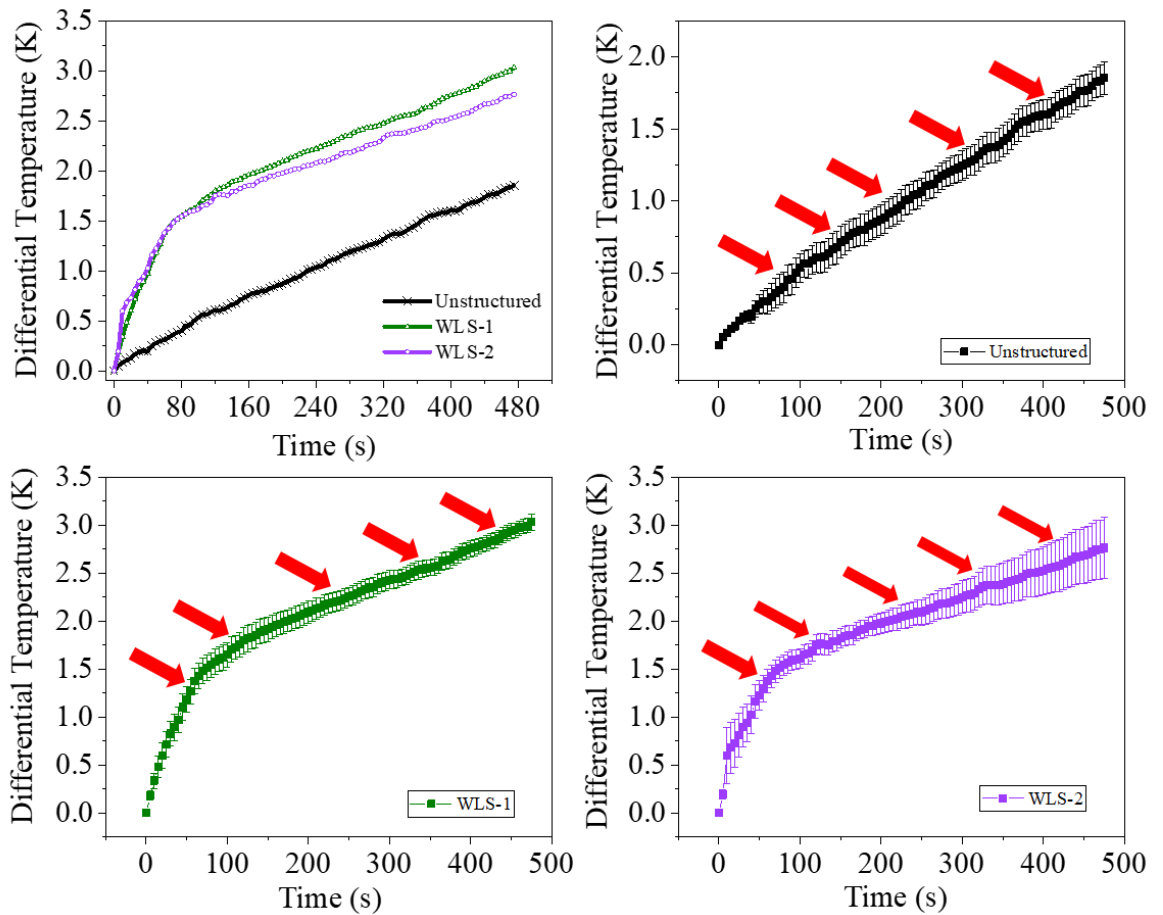


Figure 5.22. Surface temperature differential ( $\Delta T_s$ ) vs time, showing droplet life cycles.

## 5.4 Assessment Summary

In order to select the best-microstructured surface of the final stage, the following components have been considered with a total weight of 100 points:

1. Phase 1: Smallest percentage difference between designed and manufactured workpieces, considering manufacture performance and characterisation data (25 points).
2. Phase 2: Overall performance in experimental boundary layer control and drag reduction results (25 points).
3. Phase 3: Overall performance in condensation heat transfer results (50 points).

Table 5.6 shows a summary of the evaluation carried out in stage four. Even though WSL-2 is the manufactured workpiece closest to the conceptual design, WSL-1 achieved slightly better performance in the experimental components. Overall, the biphilic wettability gradient approach in both workpieces worked as expected in condensation heat transfer enhancement.

**Table 5.6. Assessment summary of stage four.**

Stage 4 - Assessment criteria		Obtained points based on performance	
Component	Value	WLS-1	WLS-2
Manufacture and characterisation (Smallest percentage difference between design and manufactured)	25	12.5	25
Experimental Boundary Layer control and Drag reduction	25	25	12.5
Experimental heat transfer enhancement	50	50	25
<b>Total points</b>	<b>100</b>	<b>87.5</b>	<b>62.5</b>

## Chapter 6 : Discussion

This chapter highlights the main points and challenges that stand out from the conducted research and presents a summary and comparison between stages and evaluation phases. The present study is motivated by the necessity of new alternative energy sources. The novel concept of High Peak Perishable Energy Recovery Systems is based on the enormous amount of energy available in meteorological phenomena, in which condensation heat transfer plays a crucial role. Hence, the purpose of this investigation is to explore an alternative passive mechanism for surface topographical modification, microstructured surfaces, to enhance heat transfer for energy recovery purposes.

### 6.1 Design Challenges and Approach

The design of microstructured surfaces that could enhance condensation heat transfer started by comparing different biomimetic engineering features, i.e. the wetting properties of lotus leaves and the hydrodynamic advantages of shark skin. Even though these microstructures were previously studied for other fluid dynamics applications [19], their use in the condensation experiments of this study showed favourable results for their implementation in energy recovery systems. Four biomimetic-inspired micro-geometries were part of stage one (Lotus, Scallop, Sharkskin, Diamond). Due to the Scallop's overall performance in each of the evaluation phases, its hydrophilic behaviour became the cornerstone for designing the microstructures of the following stages. This wetting state can alleviate many heat transfer issues caused by the lack of contact between droplets and the solid material. However, a novel hydrophobic micro-geometry was also considered for the following stages to compare the effect of both wetting states and ultimately design an optimal biphilic microstructured surface for this study. Additionally, although the same hydrophilic and hydrophobic designs by laser micro-processing were studied in stages two and three, the insert manufacturing technique was varied to optimise the process and facilitate the production of more complex workpieces with microstructured surfaces (e.g. a swirler).

As mentioned in previous chapters, it has been proven that each stage of the droplet life cycle has a preference in wetting state and that the opposite wetting state hinders the performance of said cycle stage. By considering this, in stage four, a novel design approach was developed by combining the hydrophobic and hydrophilic micro-geometries; this biphilic gradient allows droplet nucleation and growth to transition from the required wetting state to the state in which coalescence and sliding can fully perform for and easier droplet removal.

The first challenge was to achieve both wetting states in the 25 mm in diameter top surface inserts. Thus, a biphilic wettability gradient of three sections was designed in which one of the outer sections was fully hydrophilic and the other entirely hydrophobic. Additionally, the middle section was designed to contain hierarchical structures in which the main structure and base are hydrophilic (scallop), and the top of the riblets contains the hydrophobic features. Even though this design is intended to be tested in the available experimental apparatus, hence the 25 mm restriction in diameter, its application in more complex workpieces represents a future challenge due to the flow direction and dimensions of the heat transfer surface area in the HPPE project. This challenge will be easy to overcome once the design of the desiccant resonant swirling tubes by the consortium is finalised to scale up and adapt the biphilic wettability gradient.

Due to this novel biphilic wettability gradient approach and unlike the workpieces in stages one, two and three (presenting one wetting state); the workpieces in stage four successfully demonstrated fast transitions between the gradient sections, achieving the best overall performance in this study by stimulating the surface and humid air interaction with two wetting states.

An important challenge to consider is the lifetime of the microstructured surfaces. Edalatpour, et al. [53] mentioned that some configurations suffer from poor mechanical durability, and their long-term longevity depends on where and how they get used. The lifetime of the manufactured microstructured surfaces may be reduced by deposits from substances and chemical interaction effects. For this reason, recommendations for future work in this area are presented in Chapter 7.

## **6.2 Manufacture and Characterisation of the Textured Workpieces**

The microstructures were designed to be manufactured on the top surface of grade 316L stainless steel inserts to meet the requirements of the experimental equipment available in the engineering school. The inserts of stages one and two were manufactured via casting and conventional turning; additionally, facing operations were included in the procedure to obtain a smooth surface to create the microstructures. Considering further applications with more complex workpieces, a digitally-driven and modern additive manufacturing process, laser powder bed fusion, was chosen for stages three and four in addition to laser pulsations on the top surface to achieve a flat surface for the texturing procedure.

Regarding the manufacture of the microstructured surfaces in stage one, micro-wire electrical discharge machining was used due to availability. The biomimetic-inspired surfaces Lotus and Sharkskin required two and three cuts, respectively, representing a manufacturing challenge for future application.

Simpler micro-geometries (Scallop and Diamond) were considered by reducing the number of cuts to overcome a potential manufacturing issue. As a result, the simplified micro-geometries, Scallop and Diamond, achieved four times higher roughness than their original counterpart, the Lotus and Sharkskin geometries. Furthermore, the dimensions of manufactured Scallop and Diamond workpieces are closer to the proposed design than their counterparts. Scallop shows a maximum percentage difference between the nominal and measured dimensions of 6.12%, Diamond 6.38%, Lotus 33.3% and Sharkskin 45.22%.

These differences can be attributed to the multiple cuts' complexity during the manufacturing stage. When more cuts are required in micro-wire electrical discharge machining, the difference between the design and the final product will be more significant. Additionally, electrical erosion can thin the micro-wire when the speed along its axis is not high enough, reducing the precision of this manufacturing technique [170].

In stages two and three, a faster, cleaner and more flexible manufacturing technique, laser micro-processing, became available. The manufactured hydrophilic workpieces, based on Scallop, of stage two SLC-1, SLC-2 and stage three SLS-1, show a maximum percentage difference between the nominal and measured dimensions of 2.4%, 3.02% and 5.12%, respectively. The reduction in percentage difference values between the designed and manufactured workpieces is in agreement with the benefits that laser micro-processing provides over micro-wire electrical discharge machining. On the other hand, the irregularities in the hydrophobic features, random semi-volcano formations due to the rapid melting and re-solidification of the material, posed their characterisation difficult when using the 3D optical profilometer (Sensofar). For this reason, the scanning electron microscope was employed to obtain the visual representations of the specimens and dimensions. However, due to a discrepancy with the parameters used in the software for the laser pulses and its documentation between these stages and stage four, greater spacing between the hydrophobic features on the biphilic workpieces facilitated data collection when using Sensofar. Furthermore, despite the irregularities the hydrophobic features present, the semi-volcano formations in all workpieces of the last three stages of this study achieved diameters between 16.42  $\mu\text{m}$  and 19.32  $\mu\text{m}$ .

Regarding the effect of the manufacturing procedure order on the final workpieces of stage four, sections one and three of WLS-1 and WLS-2 present the same features with a percentage difference between 0.21% and 17.66%. However, section two displays a significant difference between both specimens. In WLS-1, the second step of the manufacturing procedure destroyed the hydrophobic features in section two, whereas in WLS-2, rows of hydrophobic features were able to be manufactured over the scallops or hydrophilic grooves without damaging them. In regard to the roughness values, there are no significant changes when comparing both biphilic workpieces and when comparing section one with HLS-1 and sections two and three with SLS-1.

### 6.3 Numerical and Experimental Adaptation in Fluids Dynamics

The microstructured surface designs were meant to be optimised through Computational Fluids Dynamics (CFD) analysis to be then manufactured and characterised. The obtained characterisation data would then be fed to the CFD code to optimise the following stages using the actual dimensions of the manufactured microstructures. As mentioned in Chapter 4, despite the fact that the optimisation stage could not be performed for stages two, three and four due to unexpected issues with the CFD code, velocity experiments were successfully carried out for every stage. The experimental velocity profile of the unstructured surface in each stage of this study shows higher velocities than its counterparts in the boundary layer. As mentioned in Chapter 4, higher Reynolds numbers significantly increase the momentum near the wall allowing the boundary layer to withstand a more significant positive pressure gradient (unfavourable pressure), resulting in higher wall shear stress, thus, greater drag force [155].

Regarding stage one, CFD simulations were carried out using the validated model for microstructured surfaces in Hydro3D to replicate the velocity experiments by simulating turbulent flow over different surfaces. These simulations contemplated Lotus, Scallop, Sharkskin and Diamond microgeometries against an unstructured surface. When comparing the microstructured surfaces against the unstructured surface, it is possible to see how the different micro-geometries or riblets influence the dynamics in the boundary layer. As explained in Chapter 4, the micro-geometries create micro-channels that decrease the turbulence; this phenomenon reduces momentum and skin friction values near the wall. Additionally, from the vorticity behaviour results of the different microstructured surfaces, smaller vortices than the ones in the unstructured surface are generated closer to the wall over the riblets; this phenomenon slows down the flow velocity when microstructures are present by blocking the flow entering the valleys between the riblets. Due to the reduction in the lateral and normal velocities the microstructured surfaces caused, the TKE on microstructured surfaces is lower when compared to the unstructured surface at the same distance from the wall in the z-direction.

Even though this stage's numerical and experimental results follow the same tendency, the Lotus workpiece showed twice the expected drag reduction during the experiments. This considerable variation could be attributable to final manufactured microgeometries in which the cuts produced by micro-wire resulted in pyramidal structures that differ from the design and the modelled micro-geometries. Also, when comparing the numerical results against the literature [19], the drag reduction provided by similar microgeometries is between 3% and 76% of what was found in the simulations.

These differences are attributable to the location of the microstructures in the domains and undocumented parameters used for the simulations of the preceding works, such as the Synthetic-Eddy-Method parameters that generate the inflow data.

During the experimental phase in stage one, the angle of action's effect exhibited a minor impact on the experiments when compared to the geometry's contribution, for drag reduction a maximum of 2.9% difference was observed, while the maximum difference between the highest and lowest boundary layer thickness reduction with respect to the angles of action of the geometry was 3%. These results can be attributable to the hotwire anemometer performance and location when measuring the velocities. Due to the potential breakage of the hotwire when working at less than 125  $\mu\text{m}$  from the wall [19], velocities in that location were not considered in this study to avoid damage to the experimental apparatus. Hence velocities in this range could have shown a significant difference when analysing the angle of action. Additionally, as a result of the marginal effect the angle of action against the airflow direction had in stage one, the experimental data for the subsequent stages were collected at what would be equivalent to the angle of action of zero degrees.

The variants SLC-1 and HLC-1 showed the best performance in stage two by achieving low velocities in the boundary layer; as a result, 27.08% and 20.23% decrease in drag force and up to 7% on boundary layer thickness reduction were observed. When comparing against the Scallop microstructured surface from stage one, SLC-1 tripled the drag force reduction; this could be related to the surface topography since SLC-1 presents 2-times the surface area of Scallop and 3-times higher roughness values. In contrast, there was no significant change in boundary layer thickness reduction when compared against stage one results. When comparing stages two and three, stage three workpieces achieved higher boundary layer thickness reduction; on the contrary, stage two workpieces achieved higher drag reduction. In overall, the hydrophilic scallop SLS-1 microstructured surface presented the best performance in stage three, followed by the hydrophobic HLS-1 microstructured surface; the same trend was observed in stage two with similar values in surface area and roughness. A summary of the results is shown in Table 6.1.

As expected, in stage four, the unstructured surface results show higher velocities and greater drag force. The low velocities profiles provided by WLS-1 and WLS-2 resulted in a 16.99% and 17.23% decrease in drag force and up to 9.77% on boundary layer thickness reduction. When comparing against the performance of the microstructured surfaces in previous stages (reductions up to 17.44% for boundary layer thickness and 18.86% for drag reduction), the biphilic workpieces do not offer any significant benefits in the fluids dynamics evaluation.

In addition, scallop micro-geometries were successfully manufactured on the blades of an additive manufactured swirler. However, characterisation of said microstructures was not possible due to the capabilities of the available equipment to perform such task in the swirler. By re-arranging the available burner set-up with the hotwire anemometer apparatus, velocity experiments were used to evaluate the repeatability microstructured surfaces can provide on a complex workpiece. Although the experimental results present low coefficients of variation in boundary layer thickness reduction and drag reduction (5.01 and 10.37, respectively), characterisation data is needed to confirm if the results the swirl showed are due to the manufacturing process efficiency (every blade achieved the identical microstructures' characteristics) or the experimental performance.

#### **6.4 Wettability Effect in Condensation Heat Transfer Performance**

The microstructured surfaces of this study successfully achieved hydrophilic, hydrophobic and biphilic wetting states. Through just physical modification of the surface topography, this innovative passive technique represents a significant achievement for this study because no chemical treatments are required for this approach. The unstructured surface poses a hydrophilic nature with a contact angle of  $81.41^\circ$ . As expected in stage one, Lotus presented a hydrophobic behaviour, similar to Sharkskin and Diamond with contact angles of  $117.60^\circ$ ,  $90.80^\circ$  and  $131.47^\circ$ , respectively. On the other side, the features provided by the Scallop design achieved a more hydrophilic behaviour than the unstructured surface due to the grooves and riblets effect on water droplets. In stages two and three, the hydrophilic workpieces achieved contact angles between  $70.50^\circ$  and  $73.17^\circ$ , while the hydrophobic workpieces achieved contact angles between  $122.78^\circ$  and  $128.79^\circ$ . Both stages present larger surface areas than stage one; thus, a higher number of irregularities contribute to the roughness values and the tendency towards superhydrophobic and superhydrophilic behaviours. Additionally, the experimental results demonstrated that the condensation heat transfer performance was higher for all the microstructured surfaces when compared against the unstructured surface. This study's manufactured hydrophobic and hydrophilic microstructured surfaces achieved up to 30.91% overall condensation heat transfer enhancement.

Furthermore, the novel biphilic wettability gradient approach used for the stage four workpieces achieved up to 62.60% overall enhancement. The results also show that the closer the contact angle to the superhydrophilic or the superhydrophobic wetting state, the greater heat transfer enhancement. In this stage, the extruded semi volcano-shaped features on the riblets of sections two and three in WLS-1 and WLS-2 increased the hydrophilic behaviour up to 33.69%. From the  $73.17^\circ$  contact angle achieved by SLS-1 in stage three, WLS-1 achieved  $53.26^\circ$  and  $49.93^\circ$  in sections two and three, respectively. At the same time, WLS-2 achieved  $48.52^\circ$  and  $51.03^\circ$  in sections two and three, respectively.



On the other hand, the hydrophobic behaviour caused by the holes decreased up to 26.60% due to the increased distance between the micro-features in section one. WLS-1 presents contact angles of  $94.53^\circ \pm 5.37^\circ$  and WLS-2 presents contact angles of  $105.43^\circ \pm 4.34^\circ$ .

In stage one, the Diamond and Scallop geometries exhibit 1.3 and 1.2 times higher surface temperature differentials  $\Delta T_s$ , respectively, when compared to the unstructured counterpart. These results are attributed to the wetting state of the Diamond and Scallop geometries, which were more hydrophobic (CA=131.5°) and more hydrophilic (CA=56.2°) than the unstructured surface (CA=81.4°), additionally, these simplified geometries presented four-time higher roughness than their counterparts and largest surface areas. In stage two, the hydrophilic workpiece (SLC-1) achieved 24.49% enhancement, similar to the 20.34% achieved by its counterpart in stage one. However, SLS-1 in stage three shows the best performance by achieving up to 28.95% enhancement.

On the hydrophobic side, contact angles between  $117.6^\circ$  and  $131.5^\circ$  from stage one showed between 6.6% and 36% enhancement, while contact angles between  $122.8^\circ$  and  $127.1^\circ$  from stage two presented between 11.80% (HLC-2) and 23.80% (HLC-1) enhancement. Higher contact angles were obtained in stage three,  $124^\circ$  and  $128.8^\circ$ , with enhancement percentages when compared against the unstructured surface of 22.6% (HLS-1) and 19% (HLS-2). A summary of the results is shown in Table 6.1. The experimental results show similar tendencies to what is reported in previous experimental and numerical studies [46,99]; in which condensation heat transfer performance has been improved by providing more efficient nucleation sites or higher removal of droplets depending on the wetting state of the surface.

The small droplets that form at the nucleation sites on the surface become larger due to continued condensation. When the distance between neighbouring droplets becomes closer, coalescence starts to be the dominating mechanism for droplet growth until the droplets reach a specific size and slide down, sweeping away other droplets in its path and leaving the condensing surface cleaned and exposed to the vapour to repeat the process [37,55]. In general, hydrophobic surfaces promotes dropwise condensation [48]; however, nucleation on hydrophobic surfaces requires a higher degree of saturation. Consequently, the use of hydrophilic structures, as observed in Chapter 4, can alleviate these heat transfer issues caused by the lack of contact between droplets and the solid material. Moreover, the self-removal of condensed droplets depends on the growth rate and the coalescing frequency of condensed droplets; faster growth and more frequent coalescence led to higher self-removal efficiency [72]. A higher frequency of condensate removal reduces the likelihood of droplets sticking onto the surface, which significantly increases the interaction between the humid air and the surface; thus, a hydrophobic behaviour is more efficient in this stage [60,163].

The benefit of combining both wetting effects was evident in the results of Chapter 5, in which two-thirds of the novel biphilic surfaces achieved an overall hydrophilic state and one-third hydrophobic state. By doubling the enhancement performance, the biphilic microstructured surface represents a viable option for its application in energy recovery systems. Additionally, an inversely proportional relationship between the droplet size and the  $\Delta T$  was observed during the experiments, which is consistent with the studies conducted by Chatterjee et al. [160], Peng et al. [47,161] and Xu et al. [162] in condensation heat transfer. The arrangement and size of the droplets and droplet life cycles were considerably influenced by the design of the microstructure geometries.

The condensation phenomenon is a spatial-temporal cyclic process resulting from a time-dependent sub-process repeatedly [99]. This study proposed a qualitative method for the number of droplet life cycles. The analysis is based on the temperature change trend over time of the microstructured surfaces and the state of the condensate at the end of the experiment; most of the workpieces that achieved more than 24% overall heat transfer enhancement presented between 5 and 6 droplet life cycles, while workpieces that achieved enhancement between 11.80% and 23.80% showed between 3 and 4.5 life cycles. The observed times per droplet life cycle were between 80 and 160 seconds. When compared against the unstructured surface, microstructured surfaces can provide up to 50% shorter droplet life cycles. This means that more cycles can be achieved under a certain amount of time, resulting in more interaction between the fluid and the surface, thus higher heat transfer rates.

These times are comparable to the droplet life cycle times between 70 seconds and 1,311 seconds, reported by Zheng et al. [99]. Other authors reported cycles between 9 and 12 seconds by visualising the condensates on copper patterned surfaces at different flows [56] and cycles between 421.1 and 487.4 seconds for aluminium micro-/nano surfaces with chemical coating [164] by using optical microscopy visualisation. This infers that microstructured surfaces without chemical coating can promote higher heat transfer coefficients than unstructured and chemically treated surfaces. In addition, by validating the temperature change trend method, the quantification of droplet life cycles could optimise the performance of each stage for condensation heat transfer enhancement.

Finally, when analysing the contact angle and the roughness results in Table 6.1, the data did not correlate with Wenzel's model [64] which states that an increase in roughness makes a hydrophilic surface more hydrophilic and a hydrophobic surface more hydrophobic. The texturing technique's role in surface chemistry is a possible reason for this observation. Jiao et al. [171] studied the influence of the surface chemical composition changes induced by laser processing through material vaporisation and chemical reaction with the atmosphere; they found that more hydrocarbons were introduced on the sample surface following the laser texturing process which had a significant influence on wettability. Further research recommendations in this area are presented in Chapter 7.

Table 6.1. Summary of the results of this study.

ID	Research Stage	Texturing Technique	Insert Manufacturing Technique	Wetting State	Contact Angle (°)	Surface Area (m <sup>2</sup> )	Roughness (µm)	Boundary Layer Thickness Reduction (%)	Drag Reduction (%)	Overall Heat Transfer Enhancement (%)	No. of Droplet Life Cycles	Life Cycle Time (s)
<b>Unstructured</b>	1	µ-WEDM	Casting	Hydrophilic	81.41	0.00049	2	-	-	-	3	160.00
<b>Lotus</b>	1	µ-WEDM	Casting	Hydrophobic	117.60	0.00058	5.32	12.59	16.93	20.34	3	160.00
<b>Scallop</b>	1	µ-WEDM	Casting	Hydrophilic	56.20	0.00107	20.17	8.70	9.79	20.34	5	96.00
<b>Sharkskin</b>	1	µ-WEDM	Casting	Hydrophobic	90.80	0.00057	9.72	5.69	6.92	14.65	6	80.00
<b>Diamond</b>	1	µ-WEDM	Casting	Hydrophobic	131.47	0.00070	41.65	7.75	9.40	30.91	6	80.00
<b>SLC-1</b>	2	Laser	Casting	Hydrophilic	70.50	0.00246	63.16	7.00	27.08	24.49	5	96.00
<b>SLC-2</b>	2	Laser	Casting	Hydrophilic	71.18	0.00216	47.31	6.20	13.27	23.80	4.5	106.67
<b>HLC-1</b>	2	Laser	Casting	Hydrophobic	127.13	0.00049	7.69	6.60	20.23	23.98	5	96.00
<b>HLC-2</b>	2	Laser	Casting	Hydrophobic	122.78	0.00049	12.94	10.68	16.82	11.80	4.5	106.67
<b>SLS-1</b>	3	Laser	SLM	Hydrophilic	73.17	0.00226	78.64	17.45	18.86	28.95	5	96.00
<b>HLS-1</b>	3	Laser	SLM	Hydrophobic	128.79	0.00049	8.37	13.10	18.77	22.60	3.5	137.14
<b>HLS-2</b>	3	Laser	SLM	Hydrophobic	124	0.00049	12.27	14.82	15.21	19.00	5.5	87.27
<b>WLS-1</b>	4	Laser	SLM	Biphilic: Section 1	94.53	0.00049	11.14	9.77	16.99	62.60	5.5	87.27
				Biphilic: Section 2	53.26		76.69					
				Biphilic: Section 3	49.93		75.94					
<b>WLS-2</b>	4	Laser	SLM	Biphilic: Section 1	105.43	0.00049	16.81	6.08	17.23	56.80	5.5	87.27
				Biphilic: Section 2	48.52		74.29					
				Biphilic: Section 3	51.03		75.93					

## Chapter 7 : Conclusions

For this PhD research, the ‘biphilic wetting gradient challenge’ was identified as the knowledge gap. On the one hand, biphilic surfaces had been created in the past by chemical and physical modifications. On the other hand, without the use of chemical treatment, surfaces had only been able to achieve one wetting state for energy recovery purposes. This PhD project explored an alternative passive mechanism for surface topographical modification via fabricating microstructured surfaces to achieve a biphilic wetting gradient that could enhance condensation. The experimental results of this investigation demonstrated that the heat rate can be increased by using microstructured surfaces. Moreover, the implementation of the novel biphilic wettability gradient approach in the HPPE recovery system (Desiccant Resonant Swirling Tubes) could increase the amount of energy recovered from hurricanes by 60% due to condensation heat transfer enhancement.

It is important to emphasise that the contribution of this doctoral research acts in two ways regarding climate change and its consequences. By supporting the foundation phase of the High Peak, Perishable Energy Recovery project to add more alternative sources to the renewable energy mix, on the one hand, it supports the reduction of the use of fossil fuels, thus helping to reduce greenhouse gases emissions. On the other hand, by recovering a considerable amount of energy from hurricanes, their power would decrease, thus reducing their adverse environmental, social and economic impacts. Additionally, due to the performance of the microstructured surface in the fluids dynamics and condensation heat transfer evaluations, their application could be expanded to combustion systems, heat exchanges, anti-icing, oil-water separation, self-cleaning and anti-fouling, and water harvesting and treatment [19,172].

In summary, the importance of surface topography in heat transfer and fluids dynamics performance has been demonstrated throughout this work. Microstructures' effects on the surface wetting state and hydrodynamics characteristics (boundary layer control) require extensive work and experiments to understand their characteristics for an optimal design. Consequently, the development of microstructure design, evaluation techniques, and experimental equipment was crucial in this research to achieve its aim.

## 7.1 Findings

The methodology followed in this investigation yielded viable outcomes for the design, manufacture, characterisation, hydrodynamics and thermal evaluation of microstructured surfaces. As a result, a novel biphilic wettability gradient approach via microstructured surfaces was successfully developed as an alternative passive mechanism for surface topographical modification in condensation heat transfer enhancement.

The major findings of this study are presented in this chapter, as well as recommendations for future research based on these findings.

- Hydrophobic, hydrophilic and biphilic wetting states were obtained by manufacturing different micro-geometries on the surface topography without the need of chemical treatments. This achievement represents a viable alternative to the use of chemical coatings that are known for their high cost, low efficiency, and short longevity [53].
- Hydrophobic, hydrophilic and biphilic microstructured surfaces showed similar results in the fluids dynamics evaluation, up to 17.45% boundary layer thickness reduction and up to 27% drag force reduction; their performance was influenced by the dimensions and arrangement of the micro-geometries rather than their wetting state. Furthermore, numerical and experimental results from stage one indicate that this methodology is reliable for optimising the micro-geometries' dimensions and arrangement to improve surface characteristics. In addition, it was possible to test the effect on boundary layer control and drag force of hydrophilic patterns on a complex workpiece (swirler).
- Both hydrophobic and hydrophilic microstructured surfaces showed promising results, up to 30.91% overall condensation heat transfer enhancement. Moreover, the decisive point in performance was the proximity of their contact angle with the superhydrophobic or superhydrophilic states, i.e. the closer the contact angle is to the superhydrophilic or the superhydrophobic wetting state, the more significant heat transfer improvement is achieved.
- The proposed novel design approach resulted in a biphilic wettability gradient that achieved up to 60% better results in the heat transfer evaluation than the unstructured surface and microstructured surfaces with one wetting state. In addition, even when the sequence in the manufacturing procedure of the gradient sections is varied, the overall performance of the microstructured surfaces is virtually the same.

- The experimental apparatus, designed for the condensation heat transfer evaluation (with a total cost of £1,800), successfully achieved the required temperature and relative humidity conditions for the experiments of phase three. The most commonly used apparatus in this type of experiment is the environmental scanning electron microscope (ESEM) with wet mode, which depending on the features and configuration, can cost between \$80,000 (£59,018.80) and \$10,000,000 (£7,376,550.00), with an average cost of \$294,000 (£216,870.57) [173].
- Unlike the ESEM, the different stages of the droplet life cycle could not be visualised with the apparatus used in the condensation heat transfer evaluation. However, a qualitative analysis of the number of droplet life cycles has been proposed to replace the need for the visualisation feature. This approach is based on the temperature change trend of the microstructured surfaces over time and the condensate state at the end of the experiment.
- The boundary layer thickness affects the flow's dynamic and thermal characteristics; with an increase in the boundary layer thickness, the recirculation zone increases, and the maximum heat transfer coefficient decreases [174]. Even though the experimental apparatus in both evaluation phases did not allow data collection under the same conditions for boundary layer analysis, from the fluids dynamics evaluation of this study, all the textured workpieces decreased the boundary layer thickness when compared against an unstructured surface. Moreover, all the textured workpieces achieved a higher heat transfer coefficient, thus higher Nusselt numbers, when compared to the unstructured surface. The higher the Nusselt number, the better is the heat transferred by convection [175]. Therefore, this study qualitatively confirms the theory that supports the relationship between heat and momentum transfer through the boundary layers, as seen in Chapter 2. However, further research is recommended to corroborate it quantitatively.
- This study found the scallop micro-geometry to be the simplest pattern to characterise and manufacture on different object surfaces compared to the other geometries and thus can be adopted for wider applications. This opens up the opportunity for further research in which the design-CFD-manufacture-characterisation loop can be used to optimise workpieces for various applications, beyond the energy sector.

## 7.2 Recommendations for Future Work

The incorporation and use of surface wettability modification for performance improvement of energy recovery systems have a bright and promising future. The results obtained from this investigation indicate that the proposed novel biphilic wettability gradient approach is a viable alternative for condensation heat transfer enhancement via microstructured surfaces. In addition to optimising the droplet life cycles resulting from the biphilic behaviour, the effect the tested microstructured has on hydrodynamics can be applied in combustion, heat exchangers, and water harvesting to improve their performance due to surface and flow interactions. For these reasons, the suggestion is to continue with the research required to implement the biphilic wettability gradient in the HPPE project and for further applications to expand the scope of this research. Future efforts should focus on design and manufacture optimisation and performance evaluation. The recommendations for future work are described below.

- Hydrophobic and hydrophilic surfaces have shown promising results during condensation. However, previous studies [53] have found that some configurations suffer from poor mechanical durability, and their long-term longevity depends on where and how they get used. Microstructured surfaces could lose their effectiveness over time and be vulnerable to abrasion, scratching, corrosion, and eventually fouling, which are common in heat transfer applications. For these reasons, experiments for durability over an extended period of time and under different conditions should be considered to ensure long-term longevity.
- Although the available equipment restricted the microstructured surfaces design of this study for manufacture and experimental evaluation. Their application in more complex workpieces represents a future challenge due to the flow direction, flow characteristics and heat transfer surface area's dimensions. This challenge would be easy to overcome once the final design and conditions are determined; thus, the experimental conditions should be adjusted to this information for full-scale systems testing.
- As mentioned in Chapters 4 and 6, an additional velocity experiment was done with a swirler to test repeatability; however, characterisation of the microstructures was not possible due to the complex shape. Thus, characterisation could be carried out by cutting the blades off the main body. In addition, it is recommended to manufacture at least two workpieces with the same characteristics to analyse the reproducibility regarding the manufacturing technique when creating microstructured surfaces and manufacturing biphilic blades.

- One limitation of the present research was access to funds for experimental equipment. Ideally, the air duct test rig should be capable of controlling pressure, running with humid air, and having temperature measurement points to gather enough data to compare velocity and condensation results for velocity and thermal boundary layers analysis. Additionally, velocities at less than 100  $\mu\text{m}$  from the wall are not possible to measure; consequently, a unislide and hotwire anemometer upgrade is recommended. If the required budget to combine both apparatuses is not available, a device to control the air velocity should be added to the condensation chamber to generate data that can be compared with the velocity experiment results.
- By validating the qualitative temperature change trend analysis, access to an environmental scanning electron microscope (ESEM) would not be needed for this type of experiments, thus reducing the cost of the experiments [173]. Consequently, further work is needed to compare the temperature change trend with each stage of the droplet life cycle for optimisation.
- Once the technical considerations have been carried out, multiple workpieces of the same micro-geometries should be manufactured to consider new sources of uncertainties while a sensitivity analysis should be prepared to obtain sensitivities with respect to the different micro-geometries.
- As mentioned in Chapter 6, the texturing technique could play a significant role in the wettability behaviour by altering the chemical composition of the surface [171]. Therefore, X-ray Photoelectron Spectroscopy (XPS) analysis should be conducted in future studies, before and after the manufacturing process, to investigate the presence of different oxygen-carbon bonds that could contribute to the modification of the wettability.
- Although the open-source Hydro3D code offers the possibility of simulating turbulent flows over different micro-geometries, the lack of documentation and technical support to adapt the code to the current computational requirement represents a significant barrier for the scope of this study. Therefore, it is recommended that any further design optimisation via CFD analysis is carried out with documented and supported commercial software such as STAR-CCM+ or Flow-3D.



- Machine learning has been used in several fields [176]; however, there is a knowledge gap in surface modification to obtain rapid and optimal results. Machine learning has the potential to integrate simulation data into the design process. Further work is needed to explore the scalability and manufacturing with models using several machine learning techniques. These thesis' results can help the development of an accurate and efficient technique to test and validate microstructures design produced via micro-machining technologies. Depending on the micro-machining technology available, a machine learning model could predict the parameters for a particular microstructure design. Currently, the supervisory team of this doctoral project is exploring this point.
- Once the technical considerations have been considered, a cost-benefit analysis of implementing this novel biphilic wettability gradient approach via microstructured surfaces should be done for the High Peak, Perishable Energy Recovery project.

## References

- [1] Arvizu D, Bruckner T, Chum H, Edenhofer O, Estefen S, Faaij A, et al. Technical Summary. IPCC Spec Rep Renew Energy Sources Clim Chang Mitig 2011:158.
- [2] Arvizu D, Bruckner T, Chum H, Edenhofer O, Estefen S, Faaij A, et al. 2011: Technical Summary. In IPCC Special Report on Renewable Energy Sources and Climate Change Mitigation. Cambridge, United Kingdom and New York, NY, USA: 2011.
- [3] REN21. Renewables 2021: Global Status Report. 2021.
- [4] Sawin J, Seyboth K, Sverrisson F. Renewables 2017 Global Status Report. 2017.
- [5] Valera-Medina A. High Peak, Perishable Energy Recovery - Foundation Phase (FP). Cardiff: 2017. <https://doi.org/10.2759/86288>.
- [6] EPA. Global Greenhouse Gas Emissions Data 2017. <https://www.epa.gov/ghgemissions/global-greenhouse-gas-emissions-data> (accessed September 1, 2017).
- [7] NASA. Climate change: How do we know? 2017. <https://climate.nasa.gov/evidence/> (accessed September 1, 2017).
- [8] Edenhofer O, Pichs-Madruga R, Sokona Y, Kadner S, Minx JC, Brunner S, et al. 2014: Technical Summary. In: Climate Change 2014: Mitigation of Climate Change. Contribution of Working Group III to the Fifth Assessment Report of the Intergovernmental Panel on Climate Change. Cambridge, United Kingdom and New York, NY, USA.: 2014.
- [9] IPCC. AR6 Climate Change 2021: The Physical Science Basis. 2021.
- [10] NASA. Scientific consensus: Earth's climate is warming 2017. <https://climate.nasa.gov/scientific-consensus/> (accessed September 7, 2017).
- [11] Kennedy C, Lindsey R. What's the difference between global warming and climate change? Natl Ocean Atmos Adm US 2015. <https://www.climate.gov/news-features/climate-qa/whats-difference-between-global-warming-and-climate-change> (accessed September 1, 2017).
- [12] UKCIP. UK climate impacts map 2013. <http://www.ukcip.org.uk/about-adaptation/climate-impacts/uk-climate-impacts-map/> (accessed September 1, 2017).
- [13] HM Government. UK Climate Change Risk Assessment 2017. 2017.
- [14] World Energy Council. World Energy Resources 2016. World Energy Resour 2016 2016:1–33.
- [15] International Energy Agency. Hydropower. 2021.
- [16] World Energy Council. World Energy Resources Bioenergy 2016 2016:60. [https://doi.org/10.1016/0165-232X\(80\)90063-4](https://doi.org/10.1016/0165-232X(80)90063-4).
- [17] International Energy Agency. Ocean Power. 2021.
- [18] International Energy Agency. Geothermal Power. 2021.

- [19] Al-fahham MAH. A Modelling and Experimental Study to Reduce Boundary Layer Flashback with Microstructure. Cardiff University, 2017.
- [20] Hurricane Research Division. How much energy does a hurricane release? Atl Oceanogr Meteorol Lab 2014. <http://www.aoml.noaa.gov/hrd/tcfaq/D7.html> (accessed January 15, 2017).
- [21] Meteorological Service of New Zealand. Tropical Cyclone Structure in the southern Hemisphere 2018. <http://www.metservice.com/> (accessed May 5, 2020).
- [22] Vos E. How are hurricanes formed? Davidson Inst Sci Educ 2017. <https://davidson.weizmann.ac.il/en/online/askexpert/how-are-hurricanes-formed> (accessed May 5, 2020).
- [23] Kerry A. E. The power of a hurricane: An example of reckless driving on the information superhighway. *Weather* 1999;54:107–8.
- [24] National Oceanic and Atmospheric Administration. Historical Hurricane Tracks. Hurricanes 2020. <https://coast.noaa.gov/hurricanes/#map=4/32/-80> (accessed May 5, 2020).
- [25] Geophysical Fluid Dynamics Laboratory. Global Warming and Hurricanes 2017. <https://www.gfdl.noaa.gov/global-warming-and-hurricanes/>.
- [26] Harper JW. Are Category 6 Hurricanes Coming Soon? *Sci Am* 2011. <http://www.scientificamerican.com/article/are-category-6-hurricanes-coming/>.
- [27] U.S. Department of Energy. How Do Wind Turbines Survive Severe Storms? *Off Energy Effic Renew Energy* 2017. <https://www.energy.gov/eere/articles/how-do-wind-turbines-survive-severe-storms> (accessed May 4, 2020).
- [28] Endress and Hauser. Flow measurement for liquids, gases and steam 2009. <https://www.endress.com/en/Field-instruments-overview/Flow-measurement-product-overview>.
- [29] Vortex Bladeless. First wind turbine without blades nor gears. How it works. 2020. <https://vortexbladeless.com/technology-design/> (accessed May 4, 2020).
- [30] RIA NOVOSTI. Infographic: The Anatomy of a Hurricane. Teach HUB 2010. <http://www.teachhub.com/infographic-anatomy-hurricane> (accessed January 20, 2017).
- [31] NASA. What Are Hurricanes? 2017. <https://www.nasa.gov/audience/forstudents/k-4/stories/nasa-knows/what-are-hurricanes-k4.html> (accessed January 1, 2017).
- [32] Xue Y, Arjomandi M, Richard K. A Critical Review of Temperature Separation in a Vortex Tube. *Exp Therm Fluid Sci* 2010;34:1367.
- [33] Eiamsaard S. No Title. *Renew Sustain Energy Rev* 2008;12:1822–1842.
- [34] Polihronov J. No Title. *Phys Rev Lett* 2012;054504.
- [35] Motoki S. Specific microsurfaces increase heat transfer whilst reducing pressure losses and drag. EFMC11 Seville, Spain 2016.

- [36] Enright R, Miljkovic N, Alvarado JL, Kim K, Rose JW. Dropwise condensation on micro- and nanostructured surfaces. *Nanoscale Microscale Thermophys Eng* 2014;18:223–50. <https://doi.org/10.1080/15567265.2013.862889>.
- [37] Rathakrishnan E. *Elements of Heat Transfer*. First. Taylor & Francis Group; 2012.
- [38] Rudramoorthy R, Mayilsamy K. *Heat Transfer: Theory and Problems*. Pearson Education; 2005.
- [39] Ede AJ. *An Introduction to Heat Transfer: Principles and Calculations*. Pergamon Press; 1967.
- [40] Holman JP. *Heat Transfer*. Tenth. McGraw-Hill; 2010.
- [41] Munson BR, Young DF, Okiishi TH, W. HW, Rothmayer AP, Gerhart PM, et al. *Fundamentals of Fluid Mechanics*. 8th ed. John Wiley & Sons, Inc; 2016.
- [42] McAdams WH. *Heat Transmission*. Third. New York: McGraw-Hill; 1954.
- [43] Kutateladze SS. A hydrodynamics theory of changes in boiling process under free convection. *Iz Akad Nauk SSSR, Otd, TekhNauk* 1951;4:524.
- [44] Labuntsov DA. Heat transfer film condensation of pure steam on vertical surfaces and horizontal tubes. *Teploenergetika* 1957;4:72–80.
- [45] Cengel Y. *Heat Transfer: A Practical Approach*. 2nd ed. New York: McGraw-Hill; 2002.
- [46] El Fil B, Kini G, Garimella S. A review of dropwise condensation: Theory, modeling, experiments, and applications. *Int J Heat Mass Transf* 2020;160. <https://doi.org/10.1016/j.ijheatmasstransfer.2020.120172>.
- [47] Peng B, Ma X, Lan Z, Xu W, Wen R. Experimental investigation on steam condensation heat transfer enhancement with vertically patterned hydrophobic-hydrophilic hybrid surfaces. *Int J Heat Mass Transf* 2015;83:27–38. <https://doi.org/10.1016/j.ijheatmasstransfer.2014.11.069>.
- [48] Tokunaga A, Tsuruta T. Enhancement of condensation heat transfer on a microstructured surface with wettability gradient. *Int J Heat Mass Transf* 2020;156:119839. <https://doi.org/10.1016/j.ijheatmasstransfer.2020.119839>.
- [49] Miljkovic N, Enright R, Nam Y, Lopez K, Dou N, Sack J, et al. Jumping-droplet-enhanced condensation on scalable superhydrophobic nanostructured surfaces. *Nano Lett* 2013;13:179–87. <https://doi.org/10.1021/nl303835d>.
- [50] Rose JW. Dropwise condensation theory and experiment : a review 2002;216:115–28.
- [51] Khan SA, Tahir F, Ali A, Baloch B. Review of Micro – Nanoscale Surface Coatings Application for Sustaining Dropwise Condensation. *Coatings* 2019. <https://doi.org/10.3390/coatings9020117>.
- [52] Birbarah P, Li Z, Pauls A, Miljkovic N. A Comprehensive Model of Electric-Field-Enhanced Jumping-Droplet Condensation on Superhydrophobic Surfaces. *Langmuir* 2015;31:7885–96. <https://doi.org/10.1021/acs.langmuir.5b01762>.

- [53] Edalatpour M, Liu L, Jacobi AM, Eid KF, Sommers AD. Managing water on heat transfer surfaces : A critical review of techniques to modify surface wettability for applications with condensation or evaporation of heat. *Appl Energy* 2018;222:967–92. <https://doi.org/10.1016/j.apenergy.2018.03.178>.
- [54] Wen R, Xu S, Zhao D, Lee YC, Ma X, Yang R. Hierarchical Superhydrophobic Surfaces with Micropatterned Nanowire Arrays for High-Efficiency Jumping Droplet Condensation. *ACS Appl Mater Interfaces* 2017;9:44911–21. <https://doi.org/10.1021/acsami.7b14960>.
- [55] Zhang T, Zhang Z. Droplet growth model for dropwise condensation on concave hydrophobic surfaces. *ACS Omega* 2020;5:22560–7. <https://doi.org/10.1021/acsomega.0c03187>.
- [56] Chatterjee A, Derby MM, Peles Y, Jensen MK. Enhancement of condensation heat transfer with patterned surfaces. *Int J Heat Mass Transf* 2014;71:675–81. <https://doi.org/10.1016/j.ijheatmasstransfer.2013.12.069>.
- [57] Mei M, Yu B, Zou M, Luo L. A numerical study on growth mechanism of dropwise condensation. *Int J Heat Mass Transf* 2011;54:2004–13. <https://doi.org/10.1016/j.ijheatmasstransfer.2011.01.002>.
- [58] Wen R, Lan Z, Peng B, Xu W, Ma X, Cheng Y. Droplet Departure Characteristics and Dropwise Condensation Heat Transfer at Low Steam Pressure. *J Heat Transfer* 2016;138. <https://doi.org/10.1115/1.4032956>.
- [59] Leach RN, Stevens F, Langford SC, Dickinson JT. Dropwise condensation: Experiments and simulations of nucleation and growth of water drops in a cooling system. *Langmuir* 2006;22:8864–72. <https://doi.org/10.1021/la061901+>.
- [60] Anand S, Rykaczewski K, Bengaluru Subramanyam S, Beysens D, Varanasi KK. How droplets nucleate and grow on liquids and liquid impregnated surfaces. *Soft Matter* 2015;11:69–80. <https://doi.org/10.1039/c4sm01424c>.
- [61] Yu DI, Doh SW, Kwak HJ, Kang HC, Ahn HS, Park HS, et al. Wetting state on hydrophilic and hydrophobic micro-textured surfaces : Thermodynamic analysis and X-ray visualization. *Appl Phys Lett* 2015;106. <https://doi.org/10.1063/1.4919136>.
- [62] Whyman G, Bormashenko E, Stein T. The rigorous derivation of Young, Cassie-Baxter and Wenzel equations and the analysis of the contact angle hysteresis phenomenon. *Chem Phys Lett* 2008;450:355–9. <https://doi.org/10.1016/j.cplett.2007.11.033>.
- [63] Brown PS, Bhushan B. Bioinspired materials for water supply and management: Water collection, water purification and separation of water from oil. *Philos Trans R Soc A Math Phys Eng Sci* 2016;374. <https://doi.org/10.1098/rsta.2016.0135>.
- [64] Wenzel RN. Resistance of solid surfaces to wetting by water. *Ind Eng Chem* 1936;28:988–94. <https://doi.org/10.1021/ie50320a024>.
- [65] Cassie ABD, Baxter S. Wettability of porous surfaces. *Trans Faraday Soc* 1944;40:546–51.

- [66] Bikernian JJ. Surface Roughness and Contact Angle. *J Phys Colloid Chem* 1950;54:653–8. <https://doi.org/10.1021/j150479a008>.
- [67] Liu T, Sun W, Sun X, Ai H. Thermodynamic Analysis of the Effect of the Hierarchical Architecture of a Superhydrophobic Surface on a Condensed Drop State 2010;26:14835–41. <https://doi.org/10.1021/la101845t>.
- [68] Webb RL, Kim N-H. Principles of Enhanced Heat Transfer. 2nd ed. Taylor & Francis Routledge; 2005.
- [69] Bergles AE, Nirmalan V, Junkhan GH, Webb RL. Bibliography on augmentation of convective heat and mass transfer II, Heat Transfer Laboratory Report HTL-31, ISU--ERI--Ames--84221. Ames: 1983.
- [70] Schmidt E, Schurig W, Sellschopp W. Versuche über die Kondensation von Wasserdampf in Film- und Tropfenform. *Forsch Ing* 1930;1:53–63.
- [71] Yao CW, Garvin TP, Alvarado JL, Jacobi AM, Jones BG, Marsh CP. Droplet contact angle behavior on a hybrid surface with hydrophobic and hydrophilic properties. *Appl Phys Lett* 2012;101. <https://doi.org/10.1063/1.4752470>.
- [72] He M, Zhang Q, Zeng X, Cui D, Chen J, Li H, et al. Hierarchical Porous Surface for Efficiently Controlling Microdroplet's Self-Removal. *Adv Mater* 2013;2291–5. <https://doi.org/10.1002/adma.201204660>.
- [73] Parin R, Del Col D, Bortolin S, Martucci A. Dropwise condensation over superhydrophobic aluminium surfaces. *J Phys Conf Ser* 2016;745. <https://doi.org/10.1088/1742-6596/745/3/032134>.
- [74] Guo Z, Zhou F, Hao J, Liu W. Effects of system parameters on making aluminum alloy lotus. *J Colloid Interface Sci* 2006;303:298–305. <https://doi.org/10.1016/j.jcis.2006.06.067>.
- [75] Boreyko JB, Chen CH. Self-propelled dropwise condensate on superhydrophobic surfaces. *Phys Rev Lett* 2009;103:2–5. <https://doi.org/10.1103/PhysRevLett.103.184501>.
- [76] Kumagai S, Tanaka S, Katsuda H, Shimada R. On the Enhancement of Filmwise Condensation Heat Transfer by Means of the Coexistence with Dropwise Condensation Sections. *Exp Heat Transf* 1991;4:71–82. <https://doi.org/10.1080/08916159108946406>.
- [77] Drelich J, Wilbur JL, Miller JD, Whitesides GM. Contact angles for liquid drops at a model heterogeneous surface consisting of alternating and parallel hydrophobic/hydrophilic strips. *Langmuir* 1996;12:1913–22. <https://doi.org/10.1021/la9509763>.
- [78] Morita M, Koga T, Otsuka H, Takahara A. Macroscopic-wetting anisotropy on the line-patterned surface of fluoroalkylsilane monolayers. *Langmuir* 2005;21:911–8. <https://doi.org/10.1021/la0485172>.
- [79] Raj R, Enright R, Zhu Y, Adera S, Wang EN. Unified model for contact angle hysteresis on heterogeneous and superhydrophobic surfaces. *Langmuir* 2012;28:15777–88. <https://doi.org/10.1021/la303070s>.

- [80] Varanasi KK, Hsu M, Bhate N, Yang W, Deng T. Spatial control in the heterogeneous nucleation of water. *Appl Phys Lett* 2009;95:2007–10. <https://doi.org/10.1063/1.3200951>.
- [81] Mishchenko L, Khan M, Aizenberg J, Hatton BD. Spatial control of condensation and freezing on superhydrophobic surfaces with hydrophilic patches. *Adv Funct Mater* 2013;23:4577–84. <https://doi.org/10.1002/adfm.201300418>.
- [82] Boreyko JB, Chen C. Restoring Superhydrophobicity of Lotus Leaves with Vibration-Induced Dewetting 2009:1–4. <https://doi.org/10.1103/PhysRevLett.103.174502>.
- [83] Quéré D. Non-sticking drops. *Reports Prog Phys* 2005. <https://doi.org/10.1088/0034-4885/68/11/R01>.
- [84] Lv C, Hao P. Driving droplet by scale effect on microstructured hydrophobic surfaces. *Langmuir* 2012;28:16958–65. <https://doi.org/10.1021/la3040769>.
- [85] Zhang J, Han Y. Shape-gradient composite surfaces: Water droplets move uphill. *Langmuir* 2007;23:6136–41. <https://doi.org/10.1021/la063376k>.
- [86] Shastry A, Case MJ, Böhringer KF. Directing droplets using microstructured surfaces. *Langmuir* 2006;22:6161–7. <https://doi.org/10.1021/la0601657>.
- [87] Sun C, Zhao XW, Han YH, Gu ZZ. Control of water droplet motion by alteration of roughness gradient on silicon wafer by laser surface treatment. *Thin Solid Films* 2008;516:4059–63. <https://doi.org/10.1016/j.tsf.2008.01.011>.
- [88] Motoki S, Kawahara G, Shimizu M. Optimal heat transfer enhancement in plane Couette flow 2017:1--38. <https://doi.org/10.1017/jfm.2017.779>.
- [89] Bixler GD, Bhushan B. Shark skin inspired low-drag microstructured surfaces in closed channel flow. *J Colloid Interface Sci* 2013;393:384–96. <https://doi.org/10.1016/j.jcis.2012.10.061>.
- [90] Bixler GD, Bhushan B. Fluid drag reduction with shark-skin riblet inspired microstructured surfaces. *Adv Funct Mater* 2013;23:4507–28. <https://doi.org/10.1002/adfm.201203683>.
- [91] Bixler GD, Bhushan B. Rice and butterfly wing effect inspired low drag and antifouling surfaces: A review. *Crit Rev Solid State Mater Sci* 2015;40:1–37. <https://doi.org/10.1080/10408436.2014.917368>.
- [92] Marschewski J, Brechbühler R, Jung S, Ruch P, Michel B, Poulikakos D. Significant heat transfer enhancement in microchannels with herringbone-inspired microstructures. *Int J Heat Mass Transf* 2016;95:755–64. <https://doi.org/10.1016/j.ijheatmasstransfer.2015.12.039>.
- [93] Fronk BM, Zada KR. Evaluation of Heat and Mass Transfer Models for Sizing Low-Temperature Kalina Cycle Microchannel Condensers. *J Energy Resour Technol* 2016;139:022002. <https://doi.org/10.1115/1.4034229>.
- [94] Zheng S, Eimann F, Philipp C, Fieback T, Gross U. Modeling of heat and mass transfer for dropwise condensation of moist air and the experimental validation. *Int J Heat Mass Transf* 2018;120.

- [95] Li G, Alhosani M, Yuan S, Liu H, Al Ghaferi A, Zhang T. Microscopic droplet formation and energy transport analysis of condensation on scalable superhydrophobic nanostructured copper oxide surfaces. *Langmuir* 2014;30.
- [96] Sikarwar B, Battoo N, Khandekar S, Muralidhar K. Dropwise condensation underneath chemically textured surfaces: simulation and experiments. *Heat Transf* 2011;133.
- [97] Aili A, Ge Q, Zhang T. How nanostructures affect water droplet nucleation on superhydrophobic surfaces. *Heat Transf* 2017;139.
- [98] Khandekar S, Muralidhar K. Drop dynamics and dropwise condensation on textured surfaces. Switz AG Springer 2020.
- [99] Zheng SF, Gross U, Wang XD. Dropwise condensation: From fundamentals of wetting, nucleation, and droplet mobility to performance improvement by advanced functional surfaces. *Adv Colloid Interface Sci* 2021;295:102503. <https://doi.org/10.1016/j.cis.2021.102503>.
- [100] Attinger D, Frankiewicz C, Betz AR, Schutzius TM, Ganguly R, Das A, et al. Surface engineering for phase change heat transfer : A review. *MRS Energy Sustain A Rev J* 2014;1–40. <https://doi.org/10.1557/mre.2014.9>.
- [101] Romano JM, Garcia-Giron A, Penchev P, Gulcur M, Whiteside BR, Dimov S. Lotus-Leaf Inspired Surfaces: Hydrophobicity Evolution of Replicas Due to Mechanical Cleaning and Mold Wear. *J Micro Nano-Manufacturing* 2020;8. <https://doi.org/10.1115/1.4046097>.
- [102] The Physics Classroom. Methods of Heat Transfer. *Therm Phys* 2016. <http://www.physicsclassroom.com/class/thermalP/Lesson-1/Methods-of-Heat-Transfer> (accessed April 15, 2017).
- [103] Nicol AA, Medwell JO. The effect of surface roughness on condensing steam. *J Chem Eng* 1966;66:170–3.
- [104] Medwell JO, Nicol AA. Surface roughness on condensing films. *ASME Pap* 65-HT-43, New York 1965.
- [105] Sculpteo. Metal 3D printing vs metal casting: How to choose? *3D Learn Hub* 2021. <https://www.sculpteo.com/en/3d-learning-hub/3d-printing-technologies-and-processes/metal-casting-vs-metal-3d-printing/> (accessed September 15, 2021).
- [106] Orejon D, Shardt O, Gunda NSK, Ikuta T, Takahashi K, Takata Y, et al. Simultaneous dropwise and filmwise condensation on hydrophilic microstructured surfaces. *Int J Heat Mass Transf* 2017;114:187–97. <https://doi.org/10.1016/j.ijheatmasstransfer.2017.06.023>.
- [107] Zheng Y, Han D, Zhai J, Jiang L. In situ investigation on dynamic suspending of microdroplet on lotus leaf and gradient of wettability micro- and nanostructure from water condensation 2008;084106. <https://doi.org/10.1063/1.2887899>.
- [108] Bhushan B. Biomimetics: lessons from nature – an overview. *Philos Trans R Soc A Math Phys Eng Sci* 2009;367:1445–86. <https://doi.org/10.1098/rsta.2009.0011>.



- [109] Bhushan B, Jung YC, Koch K. Micro-, nano- And hierarchical structures for superhydrophobicity, self-cleaning and low adhesion. *Philos Trans R Soc A Math Phys Eng Sci* 2009;367:1631–72. <https://doi.org/10.1098/rsta.2009.0014>.
- [110] Dean B, Bhushan B. Shark-skin surfaces for fluid-drag reduction in turbulent flow: a review. *Philos Trans R Soc A Math Phys Eng Sci* 2010;368:5737–5737. <https://doi.org/10.1098/rsta.2010.0294>.
- [111] Jin Y, Herwig H. Turbulent flow and heat transfer in channels with shark skin surfaces: Entropy generation and its physical significance. *Int J Heat Mass Transf* 2014;70:10–22.
- [112] Wen L, Weaver JC, Lauder G V. Biomimetic shark skin: design, fabrication and hydrodynamic function. *J Exp Biol* 2014;217:1656–66. <https://doi.org/10.1242/jeb.097097>.
- [113] Al-fahham MAH, Bigot S, Medina AV. A study of fluid flow characteristics using micro structured surfaces produced by WEDM. *4M / IWMMF* 2016;708.
- [114] W. Rodi, G. Constantinescu TS. *Large-Eddy Simulation in Hydraulics*. London: CRC Press; 2013.
- [115] Ouro P. *Large-Eddy Simulation of Tidal Turbines*. Cardiff University, 2017. <https://doi.org/10.5281/zenodo.1340658>.
- [116] Fraga B, Stoesser T. Influence of bubble size, diffuser width, and flow rate on the integral behavior of bubble plumes. *J Geophys Res Ocean* 2016;121:3887–904.
- [117] Al-fahham M, Medina AV, Marsh R. Experimental Study to Enhance Resistance for Boundary Layer Flashback in Swirl Burners Using Microsurfaces 2017:1–10.
- [118] Stoesser T, Nikora V. Flow structure over square bars at intermediate submergence: Large Eddy Simulation study of bar spacing effect. *Acta Geophys* 2008:876.
- [119] Cevheri M, McSherry R, Stoesser T. A local mesh refinement approach for large-eddy simulations of turbulent flows. *Int J Numer Methods Fluids* 2016;82:261–85. <https://doi.org/10.1002/flid.4217>.
- [120] Nicoud F, Ducros F. Subgrid-scale stress modelling based on the square of the velocity gradient tensor. *Flow, Turbul Combust* 1999;62:183–200.
- [121] Huang S., Li Q. A new dynamic one-equation subgrid.scale model for large eddy simulations. *Int J Numer Methods Eng* 2010;81:835–65.
- [122] Martin S, Bhushan B. Fluid flow analysis of continuous and segmented riblet structures. *RSC Adv* 2016;6:10962–78.
- [123] Martin S, Bhushan B. Modeling and optimization of shark-inspired riblet geometries for low drag applications. *J Colloid Interface Sci* 2016;474:206–15. <https://doi.org/10.1016/j.jcis.2016.04.019>.
- [124] Fu YF, Yuan CQ, Bai XQ. Marine drag reduction of shark skin inspired riblet surfaces. *Biosurface and Biotribology* 2017;3:11–24. <https://doi.org/10.1016/j.bsbt.2017.02.001>.

- [125] Abbas A, Bugada G, Ferrer E, Fu S, Periaux J, Pons-Prats J, et al. Drag reduction via turbulent boundary layer flow control. *Sci China Technol Sci* 2017;60:1281–90. <https://doi.org/10.1007/s11431-016-9013-6>.
- [126] Machining. CustomPartNet 2007. <https://www.custompartnet.com/wu/machining> (accessed September 1, 2021).
- [127] Cardiff University invests in Renishaw additive manufacturing machine. Renishaw 2014. <https://www.renishaw.com/en/cardiff-university-invests-in-renishaw-additive-manufacturing-machine--29087> (accessed September 1, 2021).
- [128] Ramirez-Cedillo E, García-López E, Ruiz-Huerta L, Rodriguez CA, Siller HR. Reusable unit process life cycle inventory (UPLCI) for manufacturing: laser powder bed fusion (L-PBF). *Prod Eng* 2021;15:701–16. <https://doi.org/10.1007/s11740-021-01050-6>.
- [129] Wire EDM. Manuf Guid n.d. <https://www.manufacturingguide.com/en/wire-edm> (accessed September 1, 2021).
- [130] Schaefer Technologie GmbH. Innovative Solutions for Science and Engineering. Sensofar Metrol 2021. <https://www.sensofar.com/metrology/>.
- [131] Sensofar Metrology. S mart & S onix. Dimensions 2021.
- [132] Sensofar Metrology. SensoScan. S Mart S OnixIn-Line 3D Surf Sensors 2021.
- [133] Metrology Products. Sensofar. S Mart Launch – A High-Resolution 3D Sens Autom Prod Syst 2015.
- [134] Scanning Electron Microscope. Purdue Univ 2019. [https://www.purdue.edu/ehps/rem/laboratory/equipment\\_safety/Research\\_Equipment/sem.html](https://www.purdue.edu/ehps/rem/laboratory/equipment_safety/Research_Equipment/sem.html).
- [135] Quetzeri-Santiago MA, Yokoi K, Castrejón-Pita AA, Castrejón-Pita JR. Role of the Dynamic Contact Angle on Splashing. *Phys Rev Lett* 2019;122:228001. <https://doi.org/10.1103/PhysRevLett.122.228001>.
- [136] Stalder AF, Kulik G, Sage D, Barbieri L, Hoffmann P. A Snake-Based Approach to Accurate Determination of Both Contact Points and Contact Angles. *Colloids Surfaces A Physicochem Eng Asp* 2006;286:92–103.
- [137] Stalder AF, Melchior T, Müller M, Sage D, Blu T, Unser M. Low-Bond Axisymmetric Drop Shape Analysis for Surface Tension and Contact Angle Measurements of Sessile Drops. *Colloids Surfaces A Physicochem Eng Asp* 2010;364:72–81.
- [138] Stadler A, Sage D. Drop Shape Analysis 2020. <http://bigwww.epfl.ch/demo/dropanalysis/> (accessed June 1, 2021).
- [139] Martin S, Bhushan B. Fluid flow analysis of a shark-inspired microstructure. *J Fluid Mech* 2014;756:5–29. <https://doi.org/10.1017/jfm.2014.447>.

- [140] Özahi E, Çarpınlioğlu MT, Gündoğdu MY. Simple methods for low speed calibration of hot-wire anemometers. *Flow Meas Instrum* 2010;21:166–70. <https://doi.org/10.1016/j.flowmeasinst.2010.02.004>.
- [141] Jørgensen FE. How to measure turbulence with hot-wire anemometers a practical guide. *Dantec Dyn* 2002:3244. [https://doi.org/Publication no.: 9040U6151](https://doi.org/Publication%20no.:%209040U6151).
- [142] Qi B, Wei J, Li X. Enhancement of condensation heat transfer on grooved surfaces: Numerical analysis and experimental study. *Appl Surf Sci* 2017;115:1287–97.
- [143] Martinez-Zavala H, Bhaduri D, Valera-Medina A, Bigot S. Experimental study on heat transfer enhancement during condensation using microstructured surfaces. *Int. Conf. Appl. Energy* 2019, Västerås, Sweden: 2019.
- [144] Cione JJ. The Relative Roles of the Ocean and Atmosphere as Revealed by Buoy Air–Sea Observations in Hurricanes. *Mon Weather Rev* 2014;143:904–13. <https://doi.org/10.1175/mwr-d-13-00380.1>.
- [145] Ramalingam S, Rajendran S, Viswanathan M, Duraisamy V. Effect of antioxidant additives on oxides of nitrogen (NO<sub>x</sub>) emission reduction from annona biodiesel operated diesel engine. Elsevier Ltd; 2019. <https://doi.org/10.1016/B978-0-08-102791-2.00010-6>.
- [146] Lighthouse Prep. Arithmetic Mean (Average). *Arith Mean* 2015. [http://www.platinumgmat.com/gmat\\_study\\_guide/statistics\\_mean](http://www.platinumgmat.com/gmat_study_guide/statistics_mean) (accessed August 20, 2011).
- [147] Lighthouse Prep. Standard Deviation. *Stand Deviat* 2015. [http://www.platinumgmat.com/gmat\\_study\\_guide/statistics\\_standard\\_deviation](http://www.platinumgmat.com/gmat_study_guide/statistics_standard_deviation) (accessed August 20, 2011).
- [148] Kalla S, Wilson LT. Standard Error of the Mean. *Stand Error Mean* 2018.
- [149] Niloy A. How to Calculate Margin of Error 2022. [https://www.exceldemy.com/calculate-margin-of-error-in-excel/#5\\_Applying\\_CONFIDENCET\\_Function](https://www.exceldemy.com/calculate-margin-of-error-in-excel/#5_Applying_CONFIDENCET_Function) (accessed August 1, 2022).
- [150] Cardiff University. Our supercomputer. *Adv Res Comput* 2019. <https://www.cardiff.ac.uk/advanced-research-computing/about-us/our-supercomputers> (accessed December 1, 2021).
- [151] Università Degli Studi di Parma. Lotus leaf inspires scientists to create world’s first self-cleaning metals 2016. <https://phys.org/news/2016-06-lotus-leaf-scientists-world-self-cleaning.html>.
- [152] University of Twente. Self cleaning Lotus leaf imitated in plastic by using a femtosecond laser 2007. <https://phys.org/news/2007-01-lotus-leaf-imitated-plastic-femtosecond.html>.
- [153] Laskari A. Pressure and velocity fluctuations in wall-bounded turbulent flows. UNIVERSITY OF SOUTHAMPTON, 2017.

- [154] Hutchins N, Marusic I. Large-scale influences in near-wall turbulence. *Philos Trans R Soc A Math Phys Eng Sci* 2007;365:647–64. <https://doi.org/10.1098/rsta.2006.1942>.
- [155] Schlichting H. *Boundary layer theory*. 8TH ed. 2000.
- [156] Handwiki. Turbulence kinetic energy 2021. [https://handwiki.org/wiki/Physics:Turbulence\\_kinetic\\_energy](https://handwiki.org/wiki/Physics:Turbulence_kinetic_energy).
- [157] Bechert DW, Bruse M, Hage W, Van Der Hoeven JGT, Hoppe G. Experiments on drag-reducing surfaces and their optimization with an adjustable geometry. *J Fluid Mech* 1997;338:59–87. <https://doi.org/10.1017/S0022112096004673>.
- [158] Ghosh A, Beaini S, Zhang BJ, Ganguly R, Megaridis CM. Enhancing Dropwise Condensation through Bioinspired Wettability Patterning. *Langmuir* 2014. <https://doi.org/10.1021/la5028866>.
- [159] Mahapatra PS, Ghosh A, Ganguly R, Megaridis CM. Key design and operating parameters for enhancing dropwise condensation through wettability patterning. *Int J Heat Mass Transf* 2016;92:877–83. <https://doi.org/10.1016/j.ijheatmasstransfer.2015.08.106>.
- [160] Chatterjee A, Derby MM, Peles Y, Jensen MK. Enhancement of condensation heat transfer with patterned surfaces. *Int J Heat Mass Transf* 2014;71:675–81. <https://doi.org/10.1016/j.ijheatmasstransfer.2013.12.069>.
- [161] Peng B, Ma X, Lan Z, Xu W, Wen R. Analysis of condensation heat transfer enhancement with dropwise-filmwise hybrid surface: Droplet sizes effect. *Int J Heat Mass Transf* 2014;77:785–94. <https://doi.org/10.1016/j.ijheatmasstransfer.2014.05.052>.
- [162] Xu W, Lan Z, Liu Q, Du B, Ma X. Droplet size distributions in dropwise condensation heat transfer: Consideration of droplet overlapping and multiple re-nucleation. *Int J Heat Mass Transf* 2018;127:44–54. <https://doi.org/10.1016/j.ijheatmasstransfer.2018.07.020>.
- [163] Grooten MH, Geld CW. The importance of drainage in dropwise condensation from flowing air–steam mixtures. 14th Int. Heat Transf. Conf., 2010, p. 51–60.
- [164] He M, Zhang Q, Zeng X, Cui D, Chen J, Li H, et al. Hierarchical porous surface for efficiently controlling microdroplets self-removal. *Adv Mater* 2013;25:2291–5. <https://doi.org/10.1002/adma.201204660>.
- [165] Garden-Cuesta RD. *Surface texturing of electrodes for electrosurgery*. Cardiff University, 2019.
- [166] Martinez-Zavala H, Bhaduri D, Petkov P, Valera-Medina A. Effects of laser microtextured surfaces in condensation heat transfer. 20th CIRP Conf Electro Phys Chem Mach 2020.
- [167] Dowling L, Kennedy J, O’Shaughnessy S, Trimble D. A review of critical repeatability and reproducibility issues in powder bed fusion. *Mater Des* 2020;186:108346. <https://doi.org/10.1016/j.matdes.2019.108346>.

- [168] Ji X, Zhou D, Dai C, Xu J. Dropwise condensation heat transfer on superhydrophilic-hydrophobic network hybrid surface. *Int J Heat Mass Transf* 2019;132:52–67. <https://doi.org/10.1016/j.ijheatmasstransfer.2018.11.139>.
- [169] Shang Y, Hou Y, Yu M, Yao S. Modeling and optimization of condensation heat transfer at biphilic interface. *Int J Heat Mass Transf* 2018;122:117–27. <https://doi.org/10.1016/j.ijheatmasstransfer.2018.01.108>.
- [170] Slătineanu L, Dodun O, Coteață M, Nagiț G, Băncescu IB, Hrițuc A. Wire electrical discharge machining - a review. *Machines* 2020;8:1–28. <https://doi.org/10.3390/machines8040069>.
- [171] Jiao Y, Brousseau E, Shen X, Wang X, Han Q, Zhu H, et al. Investigations in the fabrication of surface patterns for wettability modification on a Zr-based bulk metallic glass by nanosecond laser surface texturing. *J Mater Process Technol* 2020;283:116714. <https://doi.org/10.1016/j.jmatprotec.2020.116714>.
- [172] Zhang S, Huang J, Chen Z, Yang S, Lai Y. Liquid mobility on superwetable surfaces for applications in energy and the environment. *J Mater Chem A* 2019;7:38–63. <https://doi.org/10.1039/c8ta09403a>.
- [173] Ward B. Electron Microscope Cost. *Microsc Clarity* 2022. <https://microscopeclarity.com/electron-microscope-cost/> (accessed January 21, 2022).
- [174] Terekhov VI, Bogatko T V. Effect of boundary layer thickness before the flow separation on aerodynamic characteristics and heat transfer behind an abrupt expansion in a round tube. *Thermophys Aeromechanic* 2008;15:91–7.
- [175] Schaller M. *Free and Forced Convection*. Gerätebau: 2016.
- [176] JavaTpoint. *Applications of Machine learning* 2021. <https://www.javatpoint.com/applications-of-machine-learning> (accessed February 6, 2022).

## Appendix A

**Table A.1. Summary of the current research on surface wettability modification. Adaptation from Edalatpour, et al. [53].**

Researcher	Surface Modification Technique	Surface Materials	Results
Al-Khayat et al.	Chemical & Physical	Copper	$\theta = 81 \pm 1^\circ$ nanopattern $\theta = 85 \pm 2^\circ$ micropattern $\theta = 88 \pm 3^\circ$ macropattern $\theta = 45 \pm 1^\circ$ flat P4 VP
Bai et al.	Chemical	Glass	MWC <sup>a</sup> = 2.78 (g/cm <sup>2</sup> h) (5-pointed star-shaped pattern)
Bikerman	Physical	Stainless steel	Grooved surfaces: Droplet spreaded along the Grooves. Ridge: Droplet spreaded over surfaces of any kind and degree of roughness. Hybrid surface: The behavior of the droplet was difficult to predict.
Chatterjee et al.	Chemical	Copper	Condensation heat transfer coefficient of the patterned surface was either higher or lower than the completely hydrophobic one depending on the pattern.
Chen et al.	Chemical	Aluminum	$\theta = 134 (\pm 1.1^\circ) - 154.8^\circ (\pm 1.6^\circ)$
Cieśliński & Krygier	Chemical	Stainless steel	$\theta \approx 80^\circ$
Extrand	Physical & Chemical	Silicon	$\theta_R < 2^\circ$ $\theta_A = 7 \pm 3^\circ$
Gao & McCarthy	Physical & Chemical	Silicon	$\theta_R = 81 - 134^\circ, \theta_A = 117 - 168^\circ$ (smooth field) $\theta_R = 11 - 111^\circ, \theta_A = 33 - 120^\circ$ (hydrophobic field) $\theta_R = 82 - 132^\circ, \theta_A = 116 - 168^\circ$ (rough field)
Garrod et al.	Chemical	Silicon	$152^\circ < \theta_A < 154^\circ$ $151^\circ < \theta_R < 152^\circ$
Guo et al.	Physical & Chemical	Aluminum Copper	$\theta \approx 160 - 162.5^\circ$ pH = 1 $\theta \approx 155 - 168^\circ$ pH = 14 $\theta \approx 160^\circ$ (coating)
Hou et al.	Chemical	Silicon	$\theta = 161 \pm 4^\circ$ MWC $\approx 10+7$ ( $\mu\text{m}^2$ ) in 5 min
Hu et al.	Chemical	Copper	$\theta_{\max} \approx 160^\circ (\pm 2^\circ)$ $\theta_{\max} \approx 157^\circ (\pm 2^\circ)$ after 5 months
Huang et al.	Chemical	Copper	$\theta_{\max} \approx 153^\circ (\pm 2^\circ)$

Note:  $\theta$  = contact angle,  $\theta_A$  = advancing angle;  $\theta_R$  = receding angle;  $\theta_H$  = hysteresis.

(Continuation) Table A.1. Summary of the current research on surface wettability modification.

Adaptation from Edalatpour, et al. [53].

Researcher	Surface modification technique	Surface materials	Results
Huang & Leu	Chemical	Copper	$\theta_{\max} \approx 151.69^\circ (\pm 5.11^\circ)$
Kashaninejad et al.	Physical	Silicon	$\theta_R \approx 118 - 126^\circ$ $\theta_A \approx 140 - 144^\circ$
Lee et al.	Chemical	Silicon	$\theta = 162^\circ$ superhydrophobic $\theta = 105^\circ$ moderate hydrophobic $\theta = 3^\circ$ hydrophilic $\theta = 1^\circ$ super hydrophilic
Li et al.	Chemical	Aluminum	$\theta_{\max} \approx 90 - 137^\circ$ (unmodified) $\theta_{\max} \approx 96 - 152^\circ$ (with ODT)
Lei et al.	Chemical	Silicon	$\theta = 148.5 \pm 3.5^\circ$
Lu et al.	Chemical	Aluminum	$\theta_{\max} \approx 170^\circ$
Meng et al.	Chemical	Copper	$\theta_{\max} \approx 151^\circ$
Narhe & Beysens	Chemical	Silicon	$\theta = 138^\circ$
Ou et al.	Chemical	Copper	$\theta_{\max} = 152^\circ (\pm 1.5^\circ)$
Peng et al.	Chemical & Physical	Copper	$120.4^\circ < \theta < 121.3^\circ$ hydrophobic region $51.5^\circ < \theta < 53.2^\circ$ hydrophilic region
Qian & Shen	Chemical	Copper & Aluminum	$\theta = 156^\circ, \theta_A = 158^\circ, \theta_R = 153^\circ$ (Al) $\theta = 153^\circ, \theta_A = 155^\circ, \theta_R = 145^\circ$ (Cu)
Raj et al.	Chemical	Silicon	$\theta_A = 20 - 38^\circ$ SiO <sub>2</sub> -based $\theta_A = 44 - 58^\circ$ photoresist-based $\theta_A = 34 - 53^\circ$ pattern-based
Ren et al.	Physical & Chemical	Aluminum	$\theta < 5^\circ$ (Al), $\theta = 166^\circ$ (STA) $\theta \approx 120^\circ$ (monolayer), $\theta < 5^\circ$ (PEI)
Safaei et al.	Chemical	Copper	$\theta_{\max} \approx 156^\circ$
Seo et al.	Chemical	Silicon	Guiding tracks ability of water droplet ( $\theta > 150^\circ$ )
Shirtcliffe et al.	Physical & Chemical	Copper	$\theta \approx 136 (\pm 3^\circ)$ electrodeposited Cu $\theta \approx 160 (\pm 3^\circ)$ chocolate chip cookie texture
Shirtcliffe et al.	Physical & Chemical	Copper	$\theta \approx 155^\circ, \theta_H = 22^\circ$ (rough tops and pits) $\theta \approx 152^\circ, \theta_H = 37^\circ$ (smooth tops and rough pits)
Sun et al.	Chemical	Copper	$\theta_{\max} = 162^\circ$
Tenjimbayashi et al.	Chemical	-	Dynamic analysis of the water droplet ( $73.59^\circ < \theta < 96.93^\circ$ ) adhesion on the patterned surfaces.

Note:  $\theta$  = contact angle;  $\theta_A$  = advancing angle;  $\theta_R$  = receding angle;  $\theta_H$  = hysteresis.

(Continuation) Table A.1. Summary of the current research on surface wettability modification.

Adaptation from Edalatpour, et al. [53].

Researcher	Surface modification technique	Surface materials	Results
Thickett et al.	Chemical & Physical	Silicon	$\theta = 91.3 \pm 1.8^\circ$ PS $\theta = 36 \pm 2.7^\circ$ P4 VP $\theta = 90.2 \pm 1.9^\circ$ dewetted
Wan et al.	Physical	Aluminum	$\theta_{\max} = 155.98^\circ$
Wang & Zhang	Chemical	Copper	$\theta_{\max} \approx 165^\circ (\pm 2^\circ)$
Wong et al.	Chemical & Physical	Silicon	$\theta < 89 \pm 1^\circ$ PS $44 \pm 3^\circ < \theta < 57 \pm 2^\circ$ patterned
Wu et al.	Chemical	Stainless Steel	$\theta_{\max} \approx 166.3^\circ$
Xiu et al.	Physical & Chemical	Silicon	$\theta_R = 142.6 - 158.6^\circ$ $\theta_A = 163.1 - 167.6^\circ$
Yang et al.	Chemical & Physical	Aluminum	Parallel and perpendicular water droplet contact angles on patterned surfaces are discussed.
Yao et al.	Chemical	Silicon	$\theta = 112.1^\circ$
Yoon et al.	Chemical & Physical	Silicon	Honeycomb, and circular-shaped pattern surfaces.
Zhang et al.	Chemical	Silicon	$\theta = 157^\circ$ Sliding angle $< 1^\circ$
Zheng et al.	Chemical	Aluminum	$\theta = 160^\circ$ perpendicular to the 0.5mm track $\theta = 110^\circ$ parallel to the 0.5mm track
Zhu et al.	Chemical	Silicon	$120.8^\circ < \theta < 121.9^\circ$ no pillars $140.5^\circ < \theta < 165.1^\circ$ with pillars
Zhu et al.	Chemical	Copper	$155.2^\circ < \theta < 159.5^\circ$
Zorba et al.	Chemical	Silicon	Achievement of $66^\circ < \theta < 130^\circ$ by tailoring the surface micro and nanometer scale via femtosecond laser irradiation.

Note:  $\theta$  = contact angle,  $\theta_A$  = advancing angle;  $\theta_R$  = receding angle;  $\theta_H$  = hysteresis.



## Appendix B

User manual for microstructured surfaces simulations using Hydro3D in the Hawk supercomputer from a Windows environment. Version October 2020 by HMZ.

### 1. Modify configuration files to run Hydro3D.

- control.cin: fluid solver variables and choice of additional tools.
- mdmap.cin: sub-domain descriptions.
- infodom.cin: assignation of sub-domains to CPUs.
- geom.cin: immersed boundary method variables.

### 2. Connect to Global Protec

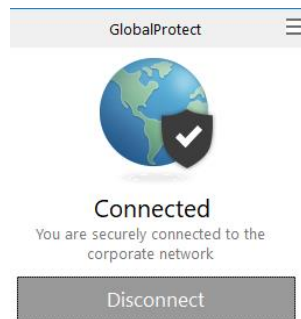


Figure B.1. Global Protect.

### 3. Access WinSCP

- host name: hawklogin.cf.ac.uk
- username: c.studentID (Example: c.c1655148)

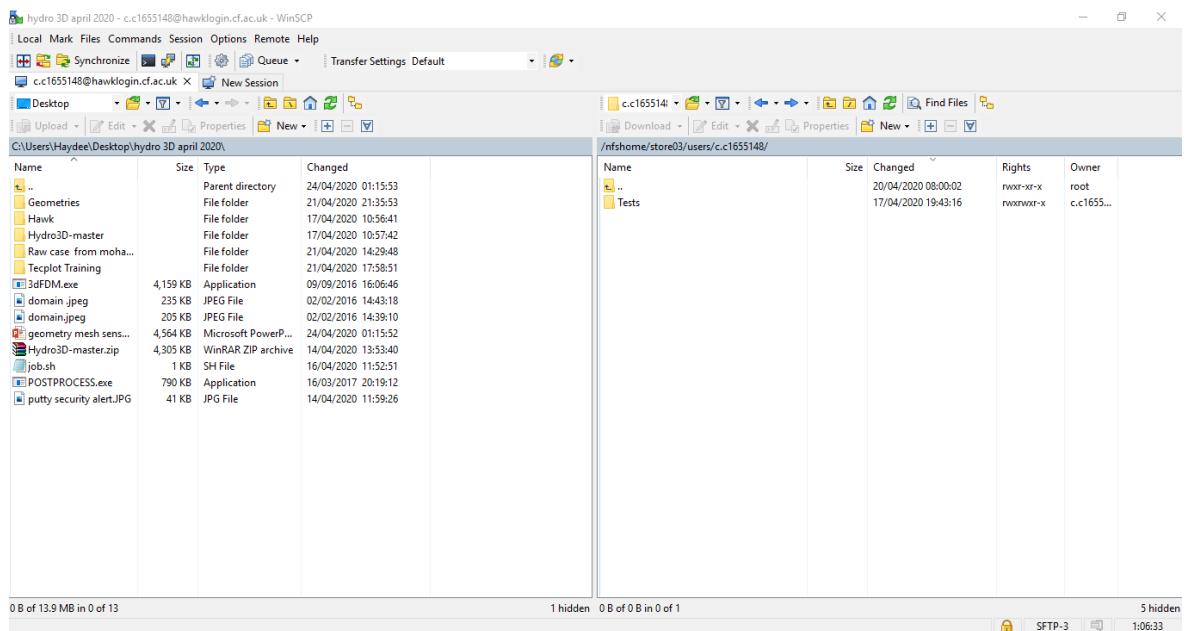


Figure B.2. WinSCP interface.

## 4. Access PuTTY

- Host name: c.studentID@hawklogin.cf.ac.uk
- Example: c.c1655148@hawklogin.cf.ac.uk

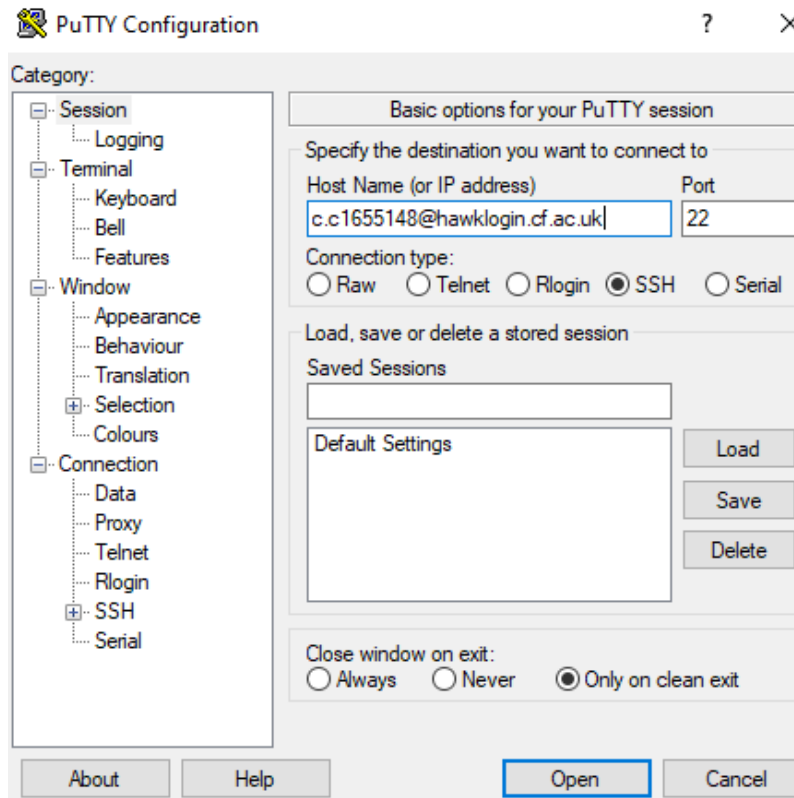


Figure B.3. PuTTY interface.

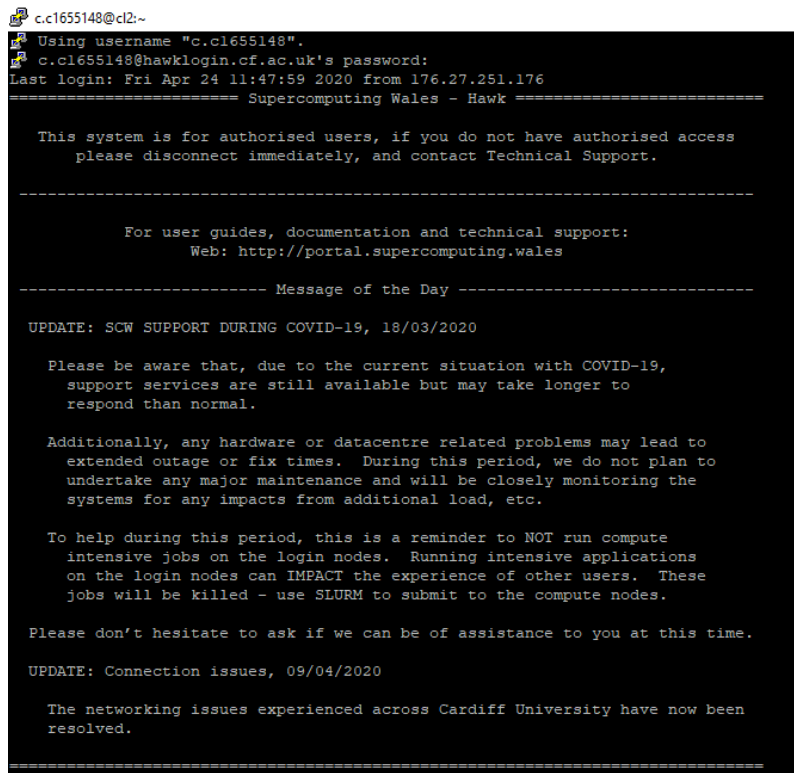


Figure B.4. Hawk supercomputer interface.

## 5. Ensure all files are in Unix (LF) language using Notepad++

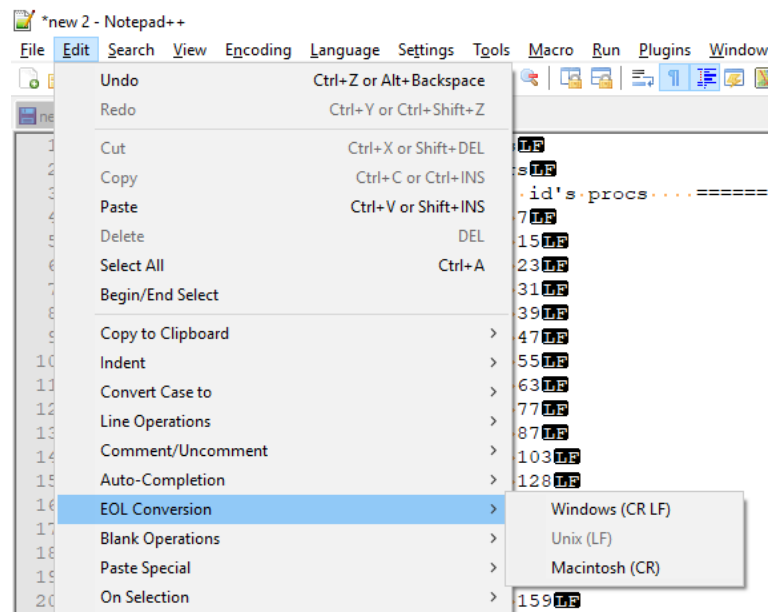


Figure B.5. Notepad++ interface.

## 6. From PC pass Hydro3D files to the server in WinSCP (SCRATCH)

## 7. Make sure all the files have permissions set to 0777

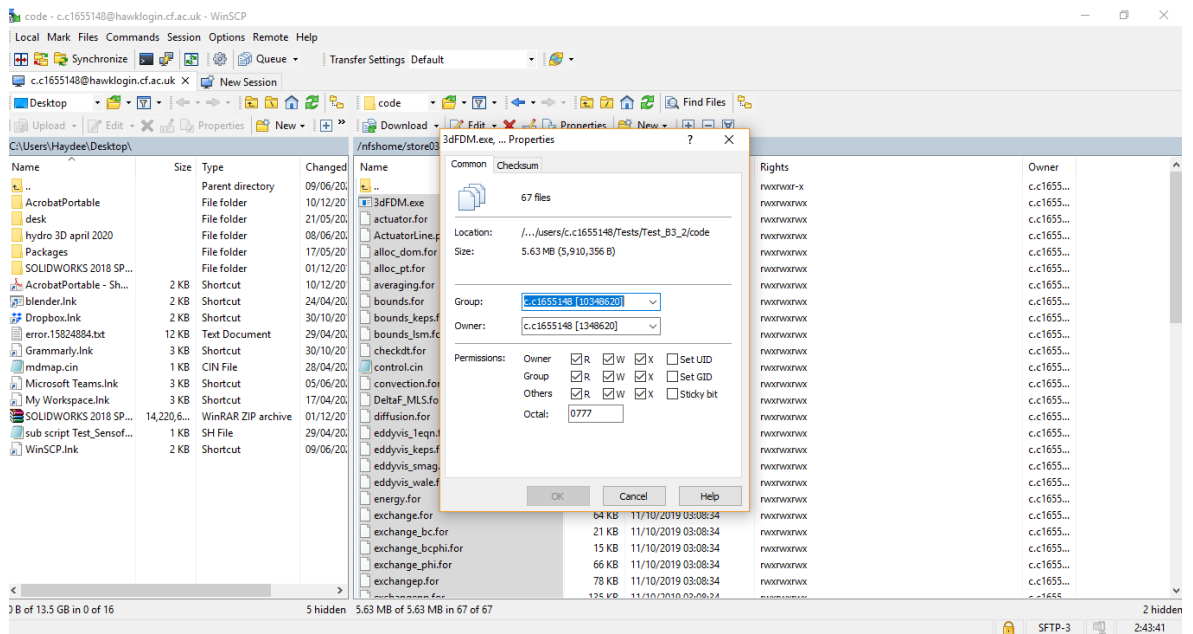


Figure B.6. Permissions set-up.

8. Make sure the submission job script has the address of the server

```

#!/bin/bash --login
#SBATCH -n 32                #Number of cores to use
#SBATCH --ntasks-per-node=32 #40 is the maximum cores per node
#SBATCH --exclusive          #Exclusive access to node
#SBATCH -o output.%J.txt     #Output file
#SBATCH -e error.%J.txt      #Error file
#SBATCH -J TMS2              #Job name
#SBATCH --qos=maxtime7d
#SBATCH -t 0-168:00          #Running time<72h
#SBATCH -p htc               #Queue name -- htc for 1 node; compute >1
#SBATCH --account=scw1257    #060

module purge
module load hpcw
module load compiler/intel/2018/4
module load mpi/intel/2018/4
module load lustre_getcwd_fix

#make -j 32

executable=/scratch/c.c1655148/TMS2/CODE/3dFDM.exe
WDPATH=/scratch/c.c1655148/TMS2/CODE

cd ${WDPATH}

NCPUS=32

mpirun -np $NCPUS $executable -traceback

```

Figure B.7. Submission job script

9. In PuTTY:

Change directory to the one where the source code and 3dFMD are:

```
cd /scratch/c.c1655148/TMS2/CODE
```

10. Load modules from the submission job script to the terminal:

- make clean
- module purge
- module load hpcw
- module load compiler/intel/2018/4
- module load mpi/intel/2018/4
- module load lustre\_getcwd\_fix
- #make -j 32

```

c.c1655148@c2:~$ cd /nfshome/store03/users/c.c1655148/TMS2/CODE
[c.c1655148@c2:~]$ module purge
[c.c1655148@c2:~]$ module load hpcw
[c.c1655148@c2:~]$ module load compiler/intel/2018/4
[c.c1655148@c2:~]$ module load mpi/intel/2018/4
[c.c1655148@c2:~]$ module load lustre_getcwd_fix
[c.c1655148@c2:~]$ make -j 32
mpif90 -> -real-size 64 -O2 -qpperm -traceback -> module_vars.o module_vars.for
mpif90 -> -real-size 64 -O2 -qpperm -traceback -> module_multisdata.o module_multisdata.for
mpif90 -> -real-size 64 -O2 -qpperm -traceback -> module_mpi.o module_mpi.for
mpif90 -> -real-size 64 -O2 -qpperm -traceback -> module_vars_pt.o module_vars_pt.for
mpif90 -> -real-size 64 -O2 -qpperm -traceback -> module_phi.o module_phi.for
mpif90 -> -real-size 64 -O2 -qpperm -traceback -> delta_func.o delta_func.for
mpif90 -> -real-size 64 -O2 -qpperm -traceback -> post.o post.for
mpif90 -> -real-size 64 -O2 -qpperm -traceback -> bounds_kps.o bounds_kps.for
mpif90 -> -real-size 64 -O2 -qpperm -traceback -> conversion_for.o conversion_for.for
mpif90 -> -real-size 64 -O2 -qpperm -traceback -> mpisolver.o mpisolver.for
mpif90 -> -real-size 64 -O2 -qpperm -traceback -> wall_function.o wall_function.for
mpif90 -> -real-size 64 -O2 -qpperm -traceback -> log_law.o log_law.for
mpif90 -> -real-size 64 -O2 -qpperm -traceback -> alloc_pt.o alloc_pt.for
mpif90 -> -real-size 64 -O2 -qpperm -traceback -> MPI_pt.o MPI_pt.for
mpif90 -> -real-size 64 -O2 -qpperm -traceback -> LFT.o LFT.for
mpif90 -> -real-size 64 -O2 -qpperm -traceback -> timesig.o timesig.for
mpif90 -> -real-size 64 -O2 -qpperm -traceback -> wmo.o wmo.for
mpif90 -> -real-size 64 -O2 -qpperm -traceback -> energy.o energy.for
mpif90 -> -real-size 64 -O2 -qpperm -traceback -> press.o press.for
mpif90 -> -real-size 64 -O2 -qpperm -traceback -> roughness_function.o roughness_function.for
mpif90 -> -real-size 64 -O2 -qpperm -traceback -> rungek.o rungek.for
mpif90 -> -real-size 64 -O2 -qpperm -traceback -> averaging.o averaging_for
mpif90 -> -real-size 64 -O2 -qpperm -traceback -> eddyvis_mag.o eddyvis_mag_for
mpif90 -> -real-size 64 -O2 -qpperm -traceback -> eddyvis_wala.o eddyvis_wala_for
mpif90 -> -real-size 64 -O2 -qpperm -traceback -> eddyvis_leq.o eddyvis_leq_for
mpif90 -> -real-size 64 -O2 -qpperm -traceback -> eddyvis_kps.o eddyvis_kps_for
mpif90 -> -real-size 64 -O2 -qpperm -traceback -> exchange_bc.o exchange_bc_for
mpif90 -> -real-size 64 -O2 -qpperm -traceback -> exchangepp.o exchangepp_for
mpif90 -> -real-size 64 -O2 -qpperm -traceback -> exchangephi.o exchangephi_for
mpif90 -> -real-size 64 -O2 -qpperm -traceback -> exchangepsi.o exchangepsi_for
mpif90 -> -real-size 64 -O2 -qpperm -traceback -> exchange.o exchange_for
mpif90 -> -real-size 64 -O2 -qpperm -traceback -> exchangev.o exchangev_for
mpif90 -> -real-size 64 -O2 -qpperm -traceback -> exchangep.o exchangep_for
mpif90 -> -real-size 64 -O2 -qpperm -traceback -> sedim.o sedim_for
mpif90 -> -real-size 64 -O2 -qpperm -traceback -> imb.o imb_for
mpif90 -> -real-size 64 -O2 -qpperm -traceback -> fdrac.o fdrac_for
mpif90 -> -real-size 64 -O2 -qpperm -traceback -> initial.o initial_for
mpif90 -> -real-size 64 -O2 -qpperm -traceback -> init_particle.o init_particle_for
mpif90 -> -real-size 64 -O2 -qpperm -traceback -> localparameters.o localparameters_for
mpif90 -> -real-size 64 -O2 -qpperm -traceback -> alloc_dom.o alloc_dom_for
mpif90 -> -real-size 64 -O2 -qpperm -traceback -> flocal.o flocal_for
mpif90 -> -real-size 64 -O2 -qpperm -traceback -> checkin.o checkin_for
mpif90 -> -real-size 64 -O2 -qpperm -traceback -> signal.o signal_for
mpif90 -> -real-size 64 -O2 -qpperm -traceback -> diffusion.o diffusion_for
mpif90 -> -real-size 64 -O2 -qpperm -traceback -> newly_mpi.o newly_mpi_for
mpif90 -> -real-size 64 -O2 -qpperm -traceback -> shapes.o shapes_for
mpif90 -> -real-size 64 -O2 -qpperm -traceback -> shapes.o shapes_for
mpif90 -> -real-size 64 -O2 -qpperm -traceback -> bounds_lm.o bounds_lm_for
mpif90 -> -real-size 64 -O2 -qpperm -traceback -> exchange.o exchange_for
mpif90 module_vars.o module_multisdata.o module_mpi.o module_vars_pt.o module_phi.o delta_func.o LFT.o timesig.o wmo.o energy.o press.o roughness_function.o rungek.o averaging.o eddyvis_mag.o eddyvis_wala.o eddyvis_leq.o eddyvis_kps.o conversion.o dif
function.o newly_mpi.o mpisolver.o wall_function.o log_law.o alloc_pt.o MPI_pt.o delta_func.o LFT.o timesig.o wmo.o energy.o press.o SEM.o sedim.o -O2 -qpperm -traceback -> 34FM.exe \
[c.c1655148@c2:~]$

```

Figure B.8. Modules.

11. Change directory to the one where the submission job script:

```
cd /scratch/c.c1655148/TMS2
```

12. Submit job:

```
sbatch Test_Sensofar_1.sh
```

```

c.c1655148@c2:/nfshome/store03/users/c.c1655148/Tests/Test_Sensofar_1
UPDATE: SCW SUPPORT DURING COVID-19, 18/03/2020

Please be aware that, due to the current situation with COVID-19,
support services are still available but may take longer to
respond than normal.

Additionally, any hardware or datacentre related problems may lead to
extended outage or fix times. During this period, we do not plan to
undertake any major maintenance and will be closely monitoring the
systems for any impacts from additional load, etc.

To help during this period, this is a reminder to NOT run compute
intensive jobs on the login nodes. Running intensive applications
on the login nodes can IMPACT the experience of other users. These
jobs will be killed - use SLURM to submit to the compute nodes.

Please don't hesitate to ask if we can be of assistance to you at this time.

UPDATE: Connection issues, 09/04/2020

The networking issues experienced across Cardiff University have now been
resolved.

=====
[c.c1655148@c2:~]$ sacct
JobID JobName Partition Account AllocCPUS State ExitCode
-----
15755589 Test MS 1 htc scw1257 32 RUNNING 0:0
15755589.ex+ extern scw1257 32 RUNNING 0:0
15755589.0 pmi_proxy scw1257 1 RUNNING 0:0
[c.c1655148@c2:~]$ cd /nfshome/store03/users/c.c1655148/Tests/Test_Sensofar_1/code
-bash: cd: /nfshome/store03/users/c.c1655148/Tests/Test_Sensofar_1/code: No such file or directory
[c.c1655148@c2:~]$ cd /nfshome/store03/users/c.c1655148/Tests/Test_Sensofar_1/code/
[c.c1655148@c2:~]$ module purge
[c.c1655148@c2:~]$ module load hpcw
[c.c1655148@c2:~]$ module load compiler/intel/15.0/3.187
[c.c1655148@c2:~]$ module load mpi/intel/5.1/3.210
[c.c1655148@c2:~]$ module load lustre_getcwd_fix
[c.c1655148@c2:~]$ #make -j 32
[c.c1655148@c2:~]$ cd /nfshome/store03/users/c.c1655148/Tests/Test_Sensofar_1/
[c.c1655148@c2:~]$ sbatch Test_Sensofar_1.sh
Submitted batch job 15771153

```

Figure B.9. Job submission.

13. To see status of the submitted jobs:

```
[c.cl655148@cl2 ~]$ sacct
      JobID      JobName  Partition      Account  AllocCPUS      State  ExitCode
-----
16562051      Test_B3_2    htc          scw1257      36      FAILED      1:0
16562051.ba+      batch          scw1257      36      FAILED      1:0
16562051.ex+      extern          scw1257      36      COMPLETED  0:0
[c.cl655148@cl2 ~]$
```

Figure B.10. sacct.

```
[c.cl655148@cl2 Test_B3]$ squeue
      JOBID PARTITION      NAME      USER  ST      TIME  NODES NODELIST(REASON)
-----
16559392    highmem  tide_ptm  b.ucs40b  CG      9:33      1  ccs1001
16560046    highmem  tide_ptm  b.ucs40b  PD      0:00      1  (QOSMaxMemoryPerUser)
16560047    highmem  tide_ptm  b.ucs40b  PD      0:00      1  (QOSMaxMemoryPerUser)
16560053    highmem  tide_ptm  b.ucs40b  PD      0:00      1  (QOSMaxMemoryPerUser)
16560061    highmem  tide_ptm  b.ucs40b  PD      0:00      1  (QOSMaxMemoryPerUser)
16560062    highmem  tide_ptm  b.ucs40b  PD      0:00      1  (QOSMaxMemoryPerUser)
```

Figure B.11. squeue.

```
[c.cl655148@cl2 Test_B3]$ slurmtop
slurmtop - Tue Jun 09 14:20:10 2020 - 79 users, 23 starving
Jobs: 483 total, 184 running, 299 waiting, 0 suspended
Nodes: 440 total, 297 allocated, 142 idle, 1 down, 125571 watts, 582398099 joules consumed
CPUs: 19300 total, 12793 allocated load 66.28%
Memory: 61756190m allocated, 74362130m free

      USER      ACCOUNTS  NB JOBS  NB NODES  PARTITIONS
-----
c.sacmq      scw1510      12      21      compute_amd,highmem,htc
c.scezx      scw1072      3      30      compute,highmem
c.cl316097scw116...  3      17      compute_amd
c.cl220629  scw1103      3      24      compute
c.sacmd5      scw1514      8      18      compute,compute_amd,dev
c.cl519156  scw1510      2      20      compute
c.cl858059  scw1039      6      12      compute_amd
c.scejz7      scw1589      4      16      compute
c.cl773828  scw1599      1      5      compute_amd
c.cl851936  scw1592      8      8      gpu,gpu_v100
```

Figure B.12. slurmtop.

14. To cancel a submitted job:

```
[c.cl655148@cl2 Test_B3_TG]$ sacct
      JobID      JobName  Partition      Account  AllocCPUS      State  ExitCode
-----
16562051      Test_B3_2    htc          scw1257      36      FAILED      1:0
16562051.ba+      batch          scw1257      36      FAILED      1:0
16562051.ex+      extern          scw1257      36      COMPLETED  0:0
16563095      Test_B2      compute      scw1257      51      PENDING      0:0
16563930      Test_B3_TG    htc          scw1257      51      PENDING      0:0
[c.cl655148@cl2 Test_B3_TG]$ scancel 16563930
[c.cl655148@cl2 Test_B3_TG]$ sacct
      JobID      JobName  Partition      Account  AllocCPUS      State  ExitCode
-----
16562051      Test_B3_2    htc          scw1257      36      FAILED      1:0
16562051.ba+      batch          scw1257      36      FAILED      1:0
16562051.ex+      extern          scw1257      36      COMPLETED  0:0
16563095      Test_B2      compute      scw1257      51      PENDING      0:0
16563930      Test_B3_TG    htc          scw1257      51      CANCELLED+  0:0
```

Figure B.13. scancel jobnumber.

15. To change output files from .bin to .dat use ./3POSTPROCESS.exe to be opened in Tecplot.

16. Enter the number of domains to generate the files.

17. Tecplot installation:

In order to activate the license, please follow the next instructions:

- Download the software: <https://www.tecplot.com/products/tecplot-360/>
- Install it and choose the "Network license server" Licensing option.
- Indicate the following:  
License server name. (Example: 131.251.239.239)  
Port number. (Example: 27100)
- In Help>License Roaming select the latest date available. This is optional but allows you to work with Tecplot outside the university.

\*As of February 2022, Tecplot is no longer supported by Cardiff University.

## Appendix C

Technical guide to process characterisation data from Sensofar Smart into Hydro3D input files.

1. Open the C# application for Sensofar point cloud file processing.
2. Click “Select Sensofar data”.
3. Covert unit from  $\mu\text{m}$  to cm in the “scale” box.
4. Adjust the coordinates, x, y, and z, of the microstructured surface to be inside the computational domain.
5. Expand the scanned area by duplicating it in the x and y direction in the Grid X and Grid Y boxes.
6. If there are empty spaces in the microstructured surface, select “Add borders”.
7. Save the adjusted file.

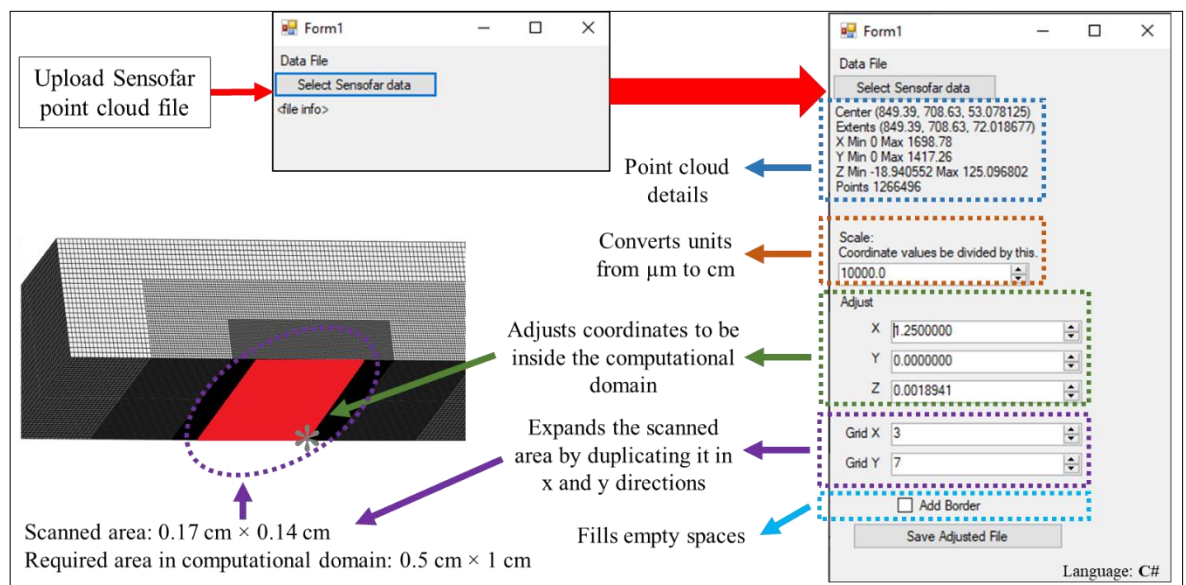

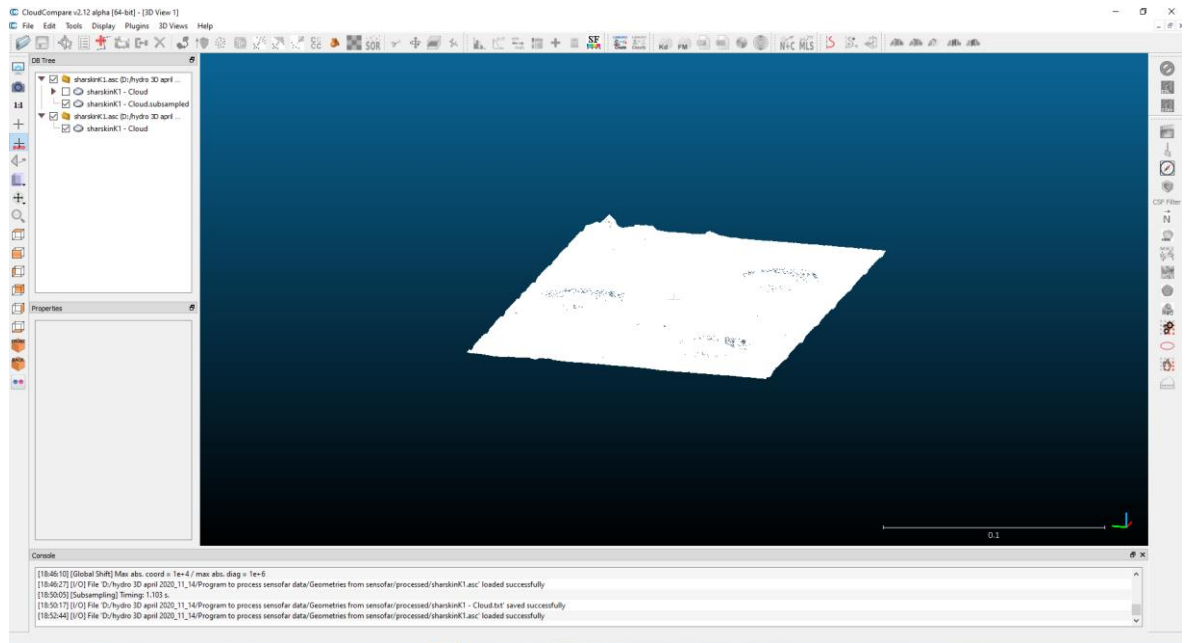


Figure C.1. C# application for Sensofar point cloud file processing.

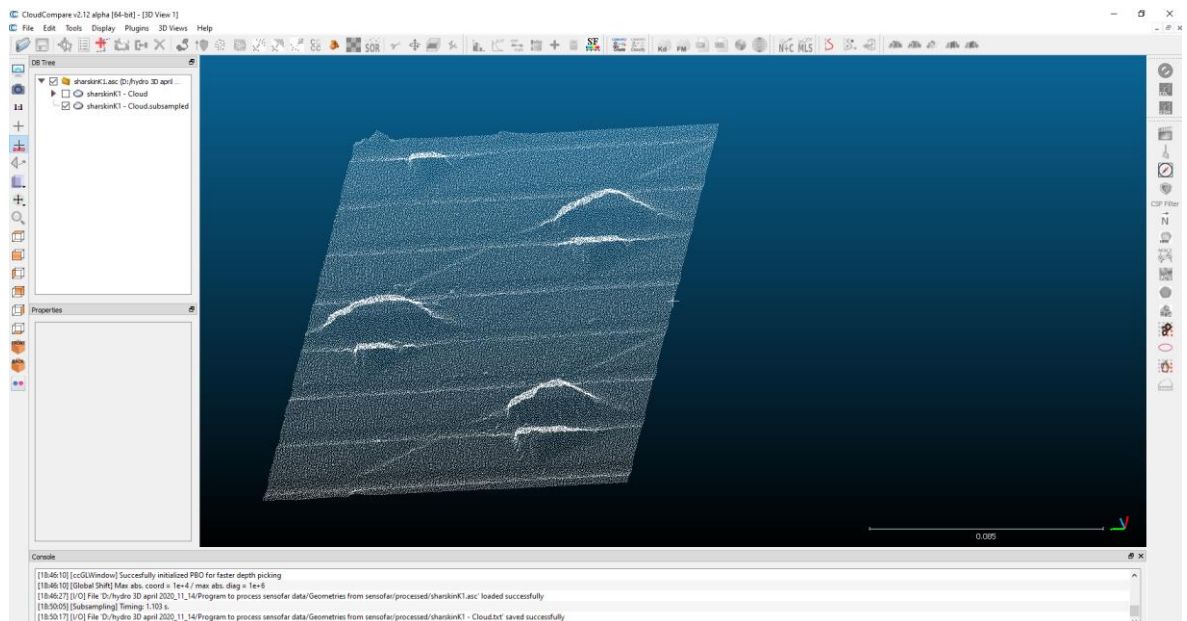
8. Convert the file to .asc to be open in cloudcompare to reduce the point cloud density.



9. Select from the menu: Edit > Subsample > 'spatial' mode, or via the  icon in the upper main toolbar.
10. Set the minimum space between points to be 0.001 or 0.0005 to have points every 10  $\mu\text{m}$  and 5  $\mu\text{m}$  to meet the Hydro3D requirements for the ghost cell method without affecting the scanned geometry.



**Figure C.2. Cloudcompare interface before data processing.**



**Figure C.3. Cloudcompare interface after data processing.**

## Appendix D

This appendix presents more detailed results of Chapter 4.

**Table D.1. Experimental Boundary layer thickness, boundary layer thickness reduction, drag force and drag reduction of stage 1.**

Angle of Action: 0°	Boundary Layer Thickness (mm)	Boundary Layer Thickness Reduction (%)	Drag Force (N)	Drag Reduction (%)
<b>Unstructured</b>	<b>9.68</b>		<b>0.0259</b>	
Standard Error	0.19		0.0116	
<b>Lotus</b>	<b>8.46</b>	<b>12.59</b>	<b>0.0219</b>	<b>16.93</b>
Standard Error	0.19	0.38	0.0085	2.11
<b>Scallop</b>	<b>8,836.31</b>	<b>8.70</b>	<b>0.0228</b>	<b>9.79</b>
Standard Error	0.28	1.54	0.0086	1.67
<b>Sharkskin</b>	<b>9.12</b>	<b>5.69</b>	<b>0.0240</b>	<b>6.92</b>
Standard Error	0.1	0.87	0.0092	0.98
<b>Diamond</b>	<b>8.93</b>	<b>7.75</b>	<b>0.0238</b>	<b>9.40</b>
Standard Error	0.39	1.94	0.0097	0.96
Angle of action: 30°	Boundary Layer Thickness (mm)	Boundary Layer Thickness reduction (%)	Drag force (N)	Drag reduction (%)
<b>Unstructured</b>	<b>9.68</b>		<b>0.0259</b>	
Standard Error	0.20		0.0116	
<b>Lotus</b>	<b>7.11</b>	<b>10.58</b>	<b>0.0181</b>	<b>14.03</b>
Standard Error	0.16	0.32	0.0071	0.10
<b>Scallop</b>	<b>8.53</b>	<b>8.40</b>	<b>0.0222</b>	<b>9.52</b>
Standard Error	0.27	1.49	0.0084	1.62
<b>Sharkskin</b>	<b>8.63</b>	<b>5.39</b>	<b>0.0217</b>	<b>6.26</b>
Standard Error	0.095	0.82	0.0083	2.59
<b>Diamond</b>	<b>8.46</b>	<b>7.33</b>	<b>0.0198</b>	<b>7.82</b>
Standard Error	0.38	1.83	0.0081	0.80

(Continuation) Table D.1. Experimental Boundary layer thickness, boundary layer thickness reduction, drag force and drag reduction of stage 1.

Angle of action: 45°	Boundary Layer Thickness $\delta$ (mm)	Boundary Layer Thickness $\delta$ reduction (%)	Drag force (N)	Drag reduction (%)
<b>Unstructured</b>	<b>9.68</b>		<b>0.0259</b>	
Standard Error	0.2		0.0116	
<b>Lotus</b>	<b>7.19</b>	<b>10.70</b>	<b>0.0179</b>	<b>13.87</b>
Standard Error	0.16	0.32	0.0070	0.10
<b>Scallop</b>	<b>9.21</b>	<b>9.07</b>	<b>0.0227</b>	<b>9.74</b>
Standard Error	0.3	1.61	0.0086	1.66
<b>Sharkskin</b>	<b>8.23</b>	<b>5.13</b>	<b>0.0196</b>	<b>5.66</b>
Standard Error	0.09	0.79	0.0075	2.34
<b>Diamond</b>	<b>9.01</b>	<b>7.81</b>	<b>0.0213</b>	<b>8.41</b>
Standard Error	0.4	1.95	0.0087	0.86
Angle of action: 60°	Boundary Layer Thickness $\delta$ (mm)	Boundary Layer Thickness $\delta$ reduction (%)	Drag force (N)	Drag reduction (%)
<b>Unstructured</b>	<b>9.68</b>		<b>0.0259</b>	
Standard Error	0.2		0.0116	
<b>Lotus</b>	<b>6.66</b>	<b>9.91</b>	<b>0.0171</b>	<b>13.21</b>
Standard Error	0.15	0.30	0.0067	0.09
<b>Scallop</b>	<b>8.16</b>	<b>8.03</b>	<b>0.0159</b>	<b>6.83</b>
Standard Error	0.26	1.42	0.0060	1.17
<b>Sharkskin</b>	<b>7.89</b>	<b>4.92</b>	<b>0.0184</b>	<b>5.30</b>
Standard Error	0.09	0.75	0.0070	2.19
<b>Diamond</b>	<b>8.93</b>	<b>7.74</b>	<b>0.0224</b>	<b>8.82</b>
Standard Error	0.4	1.93	0.0091	0.90

(Continuation) Table D.1. Experimental Boundary layer thickness, boundary layer thickness reduction, drag force and drag reduction of stage 1.

Angle of action: 90°	Boundary Layer Thickness $\delta$ (mm)	Boundary Layer Thickness $\delta$ reduction (%)	Drag force (N)	Drag reduction (%)
<b>Unstructured</b>	<b>9.68</b>		<b>0.0259</b>	
Standard Error	0.2		0.0116	
<b>Lotus</b>	<b>6.35</b>	<b>9.45</b>	<b>0.0168</b>	<b>13.01</b>
Standard Error	0.14	0.28	0.0066	0.09
<b>Scallop</b>	<b>8.49</b>	<b>8.36</b>	<b>0.0226</b>	<b>9.71</b>
Standard Error	0.27	1.48	0.0086	1.66
<b>Sharkskin</b>	<b>7.26</b>	<b>4.53</b>	<b>0.0152</b>	<b>4.38</b>
Standard Error	0.08	0.69	0.0058	1.81
<b>Diamond</b>	<b>8.83</b>	<b>7.66</b>	<b>0.0209</b>	<b>8.22</b>
Standard Error	0.39	1.91	0.0085	0.84

Table D.2. Experimental Boundary layer thickness, boundary layer thickness reduction, drag force and drag reduction of stage 2.

	Boundary Layer Thickness (mm)	Boundary Layer Thickness Reduction (%)	Drag Force (N)	Drag Reduction (%)
<b>Unstructured</b>	<b>9.48</b>		<b>0.0126</b>	
Standard Error	0.14		0.0003	
<b>SLC-1</b>	<b>8.81</b>	<b>7.00</b>	<b>0.0092</b>	<b>27.08</b>
Standard Error	0.076	0.57	0.0003	2.00
<b>SLC-2</b>	<b>8.89</b>	<b>6.23</b>	<b>0.0109</b>	<b>13.27</b>
Standard Error	0.26	1.94	0.0003	2.63
<b>HLC-1</b>	<b>8.85</b>	<b>6.60</b>	<b>0.0100</b>	<b>20.23</b>
Standard Error	0.11	0.80	0.0002	1.51
<b>Unstructured (HCL-2)</b>	<b>9.91</b>		<b>0.0095</b>	
Standard Error	0.31		0.0002	
<b>HLC-2</b>	<b>8.85</b>	<b>10.68</b>	<b>0.0079</b>	<b>16.82</b>
Standard Error	0.29	2.05	0.0002	2.12

**Table D.3. Experimental Boundary layer thickness, boundary layer thickness reduction, drag force and drag reduction of stage 3.**

	<b>Boundary Layer Thickness (mm)</b>	<b>Boundary Layer Thickness Reduction (%)</b>	<b>Drag Force (N)</b>	<b>Drag Reduction (%)</b>
<b>Unstructured</b>	<b>9.91</b>		<b>0.0095</b>	
Standard Error	0.31		0.0002	
<b>SLS-1</b>	<b>8.18</b>	<b>17.45</b>	<b>0.0077</b>	<b>18.86</b>
Standard Error	0.21	1.49	0.0001	0.54
<b>HLS-1</b>	<b>8.61</b>	<b>13.10</b>	<b>0.0078</b>	<b>18.77</b>
Standard Error	0.16	1.18	0.0001	0.85
<b>HLS-2</b>	<b>8.44</b>	<b>14.82</b>	<b>0.0081</b>	<b>15.21</b>
Standard Error	0.09	0.63	0.0001	0.30

**Table D.4. Repeatability analysis based on boundary layer thickness and drag force (swirl flow experiments).**

<b>Blade</b>	<b>Boundary Layer Thickness (mm)</b>	<b>Drag Force (N)</b>
1	12.24	0.000913
2	11.92	0.001024
3	11.48	0.000973
4	11.76	0.0010383
5	12.24	0.0011062
6	12.43	0.0011474
7	13.44	0.0012736
8	11.71	0.00106795
<b>Average</b>	<b>12.15</b>	<b>0.00106794</b>
<b>Standard Deviation</b>	<b>0.61</b>	<b>0.000110766</b>
<b>Standard Deviation of the Mean</b>	<b>0.22</b>	<b>0.000039616</b>
<b>Margin of error</b>	<b>0.51</b>	<b>0.000092602</b>
<b>Coefficient of variation</b>	<b>5.01</b>	<b>10.37</b>